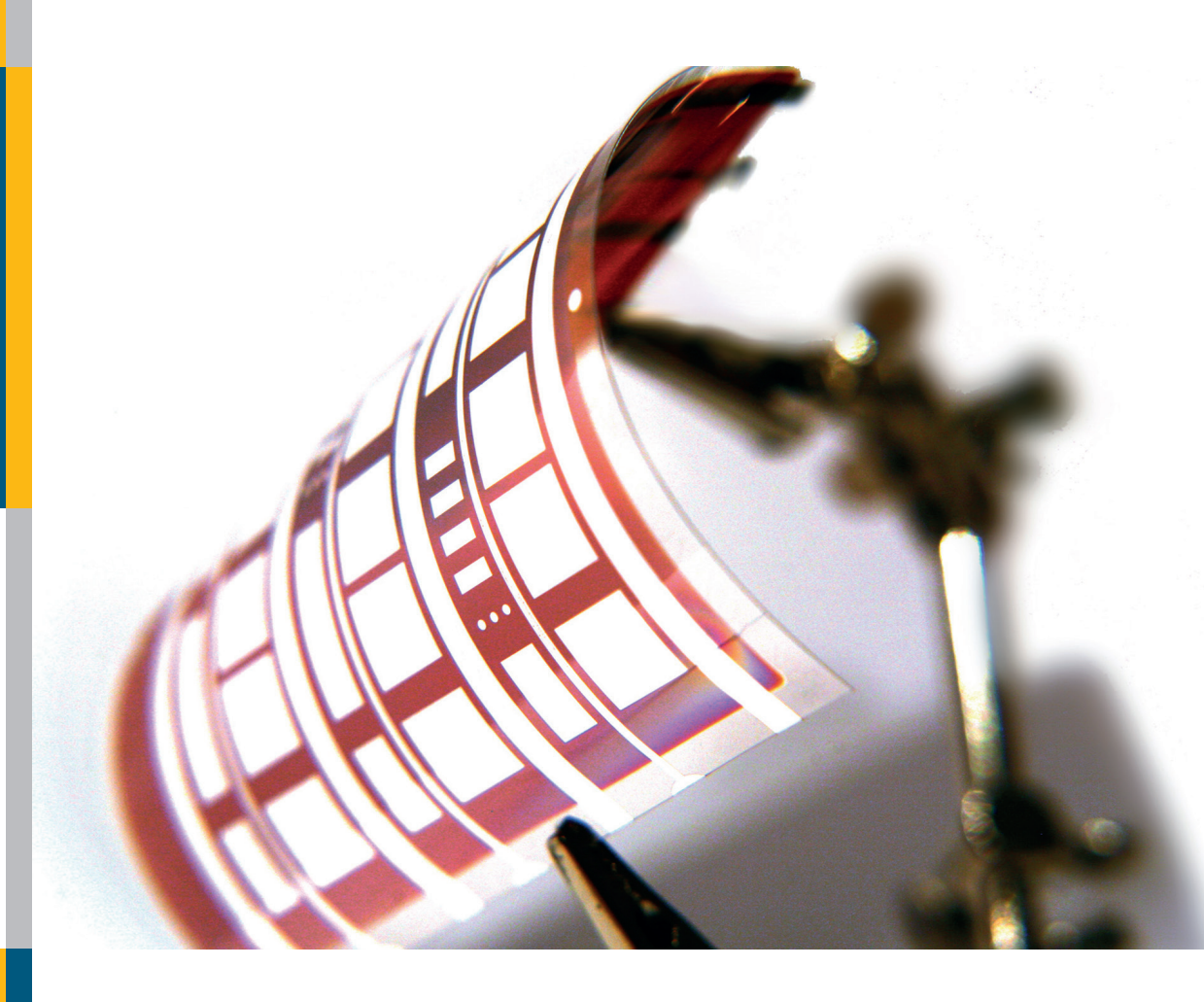
Low Temperature Thin-Film Silicon Solar Cells on Flexible Plastic Substrates

Karen Wilken



Energie & Umwelt/ Energy & Environment Band/Volume 377 ISBN 978-3-95806-235-1



Forschungszentrum Jülich GmbH Institute of Energy and Climate Research IEK-5 Photovoltaics

Low Temperature Thin-Film Silicon Solar Cells on Flexible Plastic Substrates

Karen Wilken

Schriften des Forschungszentrums Jülich Reihe Energie & Umwelt / Energy & Environment Bibliographic information published by the Deutsche Nationalbibliothek. The Deutsche Nationalbibliothek lists this publication in the Deutsche Nationalbibliografie; detailed bibliographic data are available in the Internet at http://dnb.d-nb.de.

Publisher and Forschungszentrum Jülich GmbH

Distributor: Zentralbibliothek

52425 Jülich

Tel: +49 2461 61-5368 Fax: +49 2461 61-6103

Email: zb-publikation@fz-juelich.de

www.fz-juelich.de/zb

Cover Design: Grafische Medien, Forschungszentrum Jülich GmbH

Printer: Grafische Medien, Forschungszentrum Jülich GmbH

Copyright: Forschungszentrum Jülich 2017

Schriften des Forschungszentrums Jülich Reihe Energie & Umwelt / Energy & Environment, Band / Volume 377

D 82 (Diss. RWTH Aachen University, 2017)

ISSN 1866-1793 ISBN 978-3-95806-235-1

The complete volume is freely available on the Internet on the Jülicher Open Access Server (JuSER) at www.fz-juelich.de/zb/openaccess.



This is an Open Access publication distributed under the terms of the <u>Creative Commons Attribution License 4.0</u>, which permits unrestricted use, distribution, and reproduction in any medium, provided the original work is properly cited.

Abstract

Providing energy for a steadily increasing world population is one of the major tasks of our time. Solar energy has the ability to satisfy this demand in a clean, sustainable and environmentally friendly manner. Though solar module prices have fallen considerably within the last years, costs need to be further reduced to achieve comprehensive grid-parity. A possible approach for reduced module costs is provided by thin-film technologies and the use of low cost polymer substrates. In addition, this research field offers the opportunity to provide flexible and lightweight solar modules, gaining increasing attention for applications in building integrated photovoltaics, flexible electronics and mobile power applications. Roll-to-roll manufacturing in turn provides an additional tool for possible cost reductions by high-throughput production.

The use of low cost transparent plastic films enables to produce solar cells in the so-called superstrate concept, where sunlight enters through the substrate. However, these types of substrates limit the applicable process temperature range. The aim of this thesis is to investigate the influence of low deposition temperatures (120 °C) on the properties of functional layers and to establish a link between material properties and the performance of thin-film silicon solar cells on plastic substrates. This work demonstrates that the deterioration in electrical properties of amorphous silicon (a-Si:H) layers, due to a lower deposition temperature, can be compensated by careful adjustment of deposition gas flow mixtures, resulting in an efficiency of 9.1% for an a-Si:H solar cell on glass substrate. Microcrystalline silicon (μ c-Si:H) layers are less sensitive to a reduction in deposition temperature and by implementation in an a-Si:H/ μ c-Si:H tandem solar cell, an efficiency of 9.8% was achieved with great potential for future improvement.

The low temperature a-Si:H solar cells exhibit a strong improvement in all photovoltaic parameters, particularly in the fill factor, after post-deposition annealing at 120 °C. Extensive studies were carried out to understand the underlying physical processes and to link the changes in individual layers upon annealing to changes in solar cell performance. Changes in layer properties were investigated as a function of annealing time and consequent influence on the solar cell performance was analyzed. Measurements of external quantum efficiencies of p- as well as n-side illuminated solar cells in addition to variable intensity measurements revealed a strong positive effect of the post-deposition annealing on the charge carrier collection efficiency. Possible contributions from the $\mu\tau$ -products of electrons and holes in the intrinsic absorber layer, as well as the built-in field in the solar cell were analyzed and discussed, and supported by computer simulations. Annealing effects present in a-Si:H solar cells on PET substrates and μ c-Si:H solar cells on glass substrates were treated as well.

The utilization of light management concepts represents one of the most important factors to enhance solar cell performance while keeping absorber layers sufficiently thin. By using transparent polymer films for solar cells in the superstrate concept, light management approaches need to be maintained at low temperatures and should not impair the substrate transparency. Two approaches were investigated: (i) wet-chemical etching of aluminum doped zinc oxide in HCl solution and (ii) nanoimprint lithography. A significant improvement in light scattering properties of the TCO covered substrates was found by implementation of each of the approaches compared to the flat reference. Applied in an a-Si:H solar cell, an enhanced external quantum efficiency and thus short-circuit current density as well as fill factor of the flexible solar cell was found. Furthermore, it could be shown that similar solar cell efficiencies can be achieved on PET and glass substrates for amorphous silicon solar cells deposited at 120 °C.

Finally, the angular dependence of the photovoltaic parameters of a-Si:H solar cells on imprint-textured PET substrates was investigated to analyze the influence of various bent states on the performance of flexible devices. A model was introduced to calculate efficiencies for solar cells in various bent states and the largest deterioration was found to result from a reduction in effective solar cell area and thus reduced number of collected photons.

Zusammenfassung

Die ausreichende Energieversorgung der stetig wachsenden Weltbevölkerung ist wohl eine der größten Aufgaben unserer Zeit und die von der Sonne zur Verfügung gestellte Energie ist grundsätzlich ausreichend, um dieser Nachfrage nachhaltig und umweltfreundlich nachzukommen. Obwohl die Preise für Solarmodule in den letzten Jahren erheblich gefallen sind, sind weitere Kosteneinsparungen notwendig, um umfassende Netzparität zu erreichen. Ein möglicher Ansatz für reduzierte Modulkosten bieten die sogenannten Dünnschichttechnologien sowie die Verwendung von kostengünstigen Polymersubstraten: Hierdurch können flexible und sehr leichte Solarmodule entwickelt werden, die zunehmend in den Fokus für Anwendungen wie gebäudeintegrierte Photovoltaik, flexible Elektronik und mobile Stromversorgung rücken. Die Möglichkeit der Rolle-zu-Rolle Prozessierung von flexiblen Solarzellen birgt zudem weiteres Potential für mögliche Kosteneinsparungen.

Die Verwendung von kostengünstigen transparenten Plastikfolien ermöglicht es Solarzellen im sogenannten Superstrat-Konzept zu entwickeln, bei dem das Sonnenlicht durch das Substrat in die Solarzelle eintritt. Diese Plastikfolien limitieren jedoch auch die anwendbaren Prozesstemperaturen. Das Ziel dieser Arbeit ist daher den Einfluss von niedrigen Depositionstemperaturen (120 °C) auf die Eigenschaften der funktionalen Schichten sowie deren Zusammenhang mit der Leistung von Dünnschichtsilizium-Solarzellen auf Polymersubstraten zu untersuchen. Diese Arbeit zeigt, dass die Verschlechterung der elektrischen Eigenschaften von amorphen Silizium (a-Si:H)-Schichten, aufgrund der verringerten Depositionstemperatur, durch sorgfältige Anpassung der Depositionsparameter kompensiert werden kann, und es werden Wirkungsgrade von 9.1 % für eine a-Si:H Solarzelle auf Glassubstrat erzielt. Mikrokristallines Silizium (μ c-Si:H) ist weniger empfindlich gegenüber niedrigen Depositionstemperaturen und durch Implementierung in eine a-Si:H/ μ c-Si:H Tandemsolarzelle kann ein Wirkungsgrad von 9.8 % auf Glassubstrat erreicht werden, mit großem Potential für weitere Verbesserungen.

Die bei niedrigen Temperaturen hergestellten a-Si:H Solarzellen weisen eine erhebliche Verbesserung der photovoltaischen Parameter, speziell des Füllfaktors, durch nachträgliches Tempern bei 120°C auf. Umfangreiche Studien wurden durchgeführt, um die zugrundeliegenden physikalischen Prozesse des Temperns zu verstehen und Veränderungen in den Schichteigenschaften mit der Verbesserung der Solarzellenleistung in Zusammenhang zu bringen. Schichteigenschaften wurden als Funktion der Temperzeit evaluiert und daraus folgende Einflüsse auf die photovoltaischen Parameter der Solarzelle auf Glassubstrat untersucht. Durch Messungen von externer Quantenausbeute von p- und n-Seiten beleuchteten Solarzellen, sowie Strom-Spannungs-Kennlinien unter variabler Intensität, wurde eine stark positive Wirkung des nachträglichen Temperns auf die Ladungsträgersammlung festgestellt. Mögliche Beiträge durch Verbesserung des Mobilität-Lebensdauer-Produkts

der Elektronen und Löcher in der intrinsischen Absorberschicht, sowie des eingebauten Feldes in der Solarzelle wurden analysiert und diskutiert, sowie durch Computersimulationen unterstützt. Tempereffekte in a-Si:H Solarzellen auf PET Substrat sowie μ c-Si:H Solarzellen auf Glassubstrat wurden ebenfalls untersucht.

Lichtmanagement-Systeme zur verbesserten Lichteinkopplung und Lichtstreuung stellen einen der wichtigsten Faktoren zur Verbesserung der Wirkungsgrade von Solarzellen mit dünnen Absorberschichten dar. Die Verwendung von transparenten Polymersubstraten für Solarzellen im Superstrat-Konzept erfordert die Entwicklung von Lichtmanagement-Konzepten bei niedrigen Prozesstemperaturen, ohne Beeinträchtigung der Transparenz des Substrates. In dieser Arbeit wurden zwei Ansätze verfolgt: (i) nasschemisches Ätzen von Aluminium-dotiertem Zinkoxid in Salzsäure und (ii) Nanoimprint-Lithografie. Es konnte eine erhebliche Verbesserung der lichtstreuenden Eigenschaften der mit Zinkoxid beschichteten Substrate durch beide Lichtmanagement-Konzepte gegenüber der flachen Referenz festgestellt werden. Durch Implementierung in eine a-Si:H Solarzelle wurde eine Verbesserung in der externen Quantenausbeute und somit Kurzschlussstromdichte, sowie im Füllfaktor der flexiblen Solarzelle erzielt. Des Weiteren konnte gezeigt werden, dass ähnliche Solarzellen-Wirkungsgrade für bei 120 °C hergestellten a-Si:H Solarzellen auf Glas- und PET-Substrat erreicht werden können.

Schließlich wurde die Abhängigkeit der photovoltaischen Parameter von a-Si:H Solarzellen auf geimprinteten PET Substraten vom Lichteinfallswinkel untersucht, um den Einfluss des Biegezustandes auf die Leistung von flexiblen Solarzellen zu analysieren. Ein Model zur Berechnung von Wirkungsgraden von Solarzellen in verschiedenen Biegezuständen wurde entwickelt und die größte Minderung durch die Reduzierung der effektiven Solarzellenfläche, und somit reduzierten Anzahl von gesammelten Photonen, identifiziert.

Contents

| 1. | Intro | troduction | | | |
|----|--------------|------------|--|------|--|
| 2. | Fundamentals | | | | |
| | 2.1. | Transp | parent Conductive Oxides | 15 | |
| | | 2.1.1. | | | |
| | | 2.1.2. | Optical Properties | 16 | |
| | | 2.1.3. | | | |
| | 2.2. | Thin-F | Film Silicon | . 19 | |
| | | 2.2.1. | Amorphous Silicon | . 19 | |
| | | 2.2.2. | Microcrystalline Silicon | . 23 | |
| | | 2.2.3. | Film Growth by PECVD | 24 | |
| | | 2.2.4. | Low Temperature Deposition of Thin-Film Silicon | 26 | |
| | 2.3. | Solar (| Cells | . 28 | |
| | | 2.3.1. | Main Principle of a Thin-Film Silicon based Solar Cell | . 28 | |
| | | 2.3.2. | Tandem Solar Cells | . 30 | |
| | 2.4. | Annea | ling of Thin-Film Silicon Films and Solar Cells | . 31 | |
| | | Management | . 34 | | |
| | | 2.5.1. | Etching of ZnO:Al | 34 | |
| | | 2.5.2. | Nanoimprint Lithogaphy | . 35 | |
| | 2.6. | Flexib | le Thin-Film Silicon Solar Cells | 36 | |
| 3. | Prep | paration | and Characterization | 39 | |
| | 3.1. | Cluste | rtool Deposition System | | |
| | | 3.1.1. | PECVD Process Chamber (PC1-PC3) | 40 | |
| | | 3.1.2. | | 41 | |
| | | 3.1.3. | Deposition on Flexible Substrates | 42 | |
| | 3.2. | Deposi | ition Processes for Layers and Solar Cells | 44 | |
| | | 3.2.1. | Substrates | 44 | |
| | | 3.2.2. | Deposition of Transparent Conductive Oxides | 45 | |
| | | 3.2.3. | Light Management | 45 | |
| | | 3.2.4. | Deposition of Thin-Film Silicon Layers and Solar Cells | 46 | |
| | | 3.2.5. | Annealing | 49 | |
| | | Charac | cterization of Individual Layers | 50 | |
| | | 3.3.1. | Layer Thickness | 50 | |
| | | 3.3.2. | | | |
| | | 3.3.3. | Characterization of Silicon Layers | | |

| | 3.4. | Charac | cterization of Solar Cells | 63 |
|----|---|--------|--|-----|
| | | 3.4.1. | Current-Voltage Characteristic | 63 |
| | | 3.4.2. | Quantum Efficiency | 64 |
| | | 3.4.3. | Variable Intensity Measurement (VIM) | 65 |
| | | 3.4.4. | Secondary Ion Mass Spectrometry (SIMS) | 67 |
| 4. | Low | • | erature Thin-Film Silicon on Glass Substrate | 69 |
| | 4.1. | _ | phous Silicon | 69 |
| | | 4.1.1. | Boron-Doped a-Si(C):H Window Layers $\ \ \ldots \ \ \ldots \ \ \ldots$. | 69 |
| | | 4.1.2. | Intrinsic a-Si:H Absorber Layers | 78 |
| | | 4.1.3. | T T T T T T T T T T T T T T T T T T T | 82 |
| | | 4.1.4. | | 84 |
| | | 4.1.5. | | 94 |
| | 4.2. | | crystalline Silicon and Tandem Solar Cells | 96 |
| | | 4.2.1. | Microcrystalline Silicon | 97 |
| | | 4.2.2. | Tandem Solar Cells | |
| | | 4.2.3. | Conclusion and Outlook | 102 |
| 5. | | _ | | 103 |
| | | | uction | |
| | 5.2. | Annea | ling of Individual Silicon Layers | |
| | | 5.2.1. | | |
| | | 5.2.2. | | |
| | | 5.2.3. | 8 | |
| | | 5.2.4. | | |
| | 5.3. | | ling of a-Si:H Solar Cells | |
| | | 5.3.1. | Effect of Individual Layers on the Annealing Behavior of Solar Cells | |
| | | 5.3.2. | | |
| | | 5.3.3. | | |
| | | 5.3.4. | Summary | |
| | 5.4. | | sion | |
| | | 5.4.1. | Built-In Field | |
| | | 5.4.2. | Mobility-Lifetime Product | |
| | | 5.4.3. | Structural Processes | |
| | | | ling of Flexible Solar Cells | |
| | 5.6. Annealing of μc -Si:H Solar Cells | | | |
| | 5.7. | Conclu | sion and Outlook | 138 |
| 6. | Sola | | on Flexible Substrates | 141 |
| | 6.1. | | | 141 |
| | 6.2. | - | Management on PET Substrate | |
| | | 6.2.1. | Introduction | |
| | | 6.2.2. | Texture-Etching of ZnO:Al Layers | |
| | | 6.2.3. | Nanoimprint Lithography | |
| | | 6.2.4. | Comparison and Discussion of Light Management Approaches | 163 |

| | 6.3. | 6.3.1. 6.3.2. | mance under Bending | 166 |
|--|---|------------------|---------------------|-----|
| 7. | Con | clusion | | 177 |
| Α. | Арр | endix t | o Chapter 4 | 181 |
| В. | B. Appendix to Chapter 6 | | | |
| C. | C. Solar Cells with ITO and IO:H Layers | | | |
| D. Effects of Barrier Layers on PET Substrates | | | | 188 |
| E. Deposition Parameters for Individual Layers and Solar Cells | | | | 192 |
| Bil | bliog | raphy | | 195 |
| Lis | st of | Abbrev | iations | 219 |
| Lis | st of | Publica | tions | 225 |
| Αc | know | /ledgm | ent | 229 |

1. Introduction

In a world marked by a rising population and industrialization of developing countries, the global energy demand is steadily increasing, attaining a consumption of 108170 TWh in 2013 [1]. Though increased attention is given to low-carbon sources of energy, emitting little or no greenhouse gases, fossil fuels such as oil, coal and natural gas continuously dominate the global energy mix, having a share of 81% on the total energy use in 1989 and still in 2014 [2]. Natural consequences on the economy, environment as well as society are for example economic dependence, imponderable influence on the climate and global warming by emission of greenhouse gases, as well as a negative impact on human health by air pollution. Accordingly, a clean and sustainable energy supply is needed to meet the rising energy demand (also called the Terawatt Challenge [3]) on one hand and to comply with the target of the Paris Agreement to hold the increase in global average temperature well below 2°C, compared to pre-industrial levels, on the other hand.

A solution is provided by renewable energy sources and among these, solar energy is by far the most abundant source of energy. The yearly earth-reaching energy provided by the sun is around 1×10^9 TWh, thus a thousand times as much as the world energy consumption per year. This means that the energy demand can easily be satisfied, provided that the energy can be collected in a feasible way. Photovoltaic (PV) devices, such as solar cells, are able to collect the sunlight and convert it into electrical power. In recent years, the deployment of solar modules was significantly increased, inducing a drop in market prices by 80 % from 2008 to 2015 [4]. As a result, solar energy is starting to meet "grid-parity" in a growing number of countries, meaning that the levelized cost of electricity is equal to or less than the price of purchasing power from the electricity grid. The lowest reported price for a solar PV project so far is 0.0299 US\$/kWh for a 800 MW project in Dubai [5]. Costs are even predicted to decline further as deployment increases and technology improves [6].

Among commercially available technologies, solar modules based on crystalline silicon (c-Si), having best efficiencies of more than 22% [7], represent the largest photovoltaic market share of around 90%. Thin-film technologies based on copper indium gallium selenide (CIGS), cadmium telluride (CdTe) and thin-film silicon (amorphous (a-Si:H) and microcrystalline (μ c-Si:H) silicon) exhibit lower module efficiencies with best values of around 16-18%, 19% and 12%, respectively [7]. Though thin-film technologies had been predicted to attain an increasing market share despite lower efficiencies [8], the share actually decreased from 15% in 2009 to 10% in 2013 [6]. This may be related to significant cost reductions for c-Si solar modules due to huge investments in production capacity, especially in China, in the last few years [6]. Furthermore, as the balance of system (including all components other than the photovoltaic panels) accounts for rising proportions

of PV generation costs, high efficiencies become increasingly important. As a result, thin-film technologies were left behind regarding utility-scale PV deployment. Nevertheless, there is still a huge potential for thin-film technologies regarding special applications such as building integrated photovoltaic (BIPV) systems, flexible electronics and mobile power applications [6, 9, 10]. The possibility for thin-film photovoltaics to be processed on flexible substrates in roll-to-roll manufacturing provides not only possible cost reductions by high throughput production, but also enables new markets where flexible and lightweight products are needed. In fact, the market forecast for flexible photovoltaics is estimated to be 70 billion US\$ by 2030 [11]. However, the level of maturity in flexible photovoltaics is considerably lower compared to its rigid counterpart [12].

Among thin-film technologies, thin-film silicon has the advantage of relatively low process temperatures below 200 °C by using plasma-enhanced chemical vapor deposition (PECVD) from the gas phase. This enables a wider choice of substrates, especially the use of low cost plastic films. The PECVD process can easily be scaled up enabling large area and high throughput production by roll-to-roll processing. Most thin-film silicon solar cells are produced in the so-called superstrate concept where sunlight enters through the substrate (typically glass). Consequently, transparent polymer films such as polyethylene naphthalate (PEN), polyethylene terephthalate (PET) or polycarbonate (PC) are required for flexible devices. They are also essential in the case of flexible (semi-)transparent BIPV products. On the other hand, due to their low glass transition temperatures, these types of substrates impose a limited temperature of <150 °C for all fabrication processes. This work therefore aims at the investigation and development of thin-film silicon solar cells entirely deposited at temperatures below 150 °C, including amorphous and microcrystalline silicon films as well as transparent conductive oxide (TCO) layers.

The electronic transport properties in amorphous and microcrystalline silicon are considerably deteriorated compared to its crystalline counterpart. A thin absorber layer is therefore desired to ensure effective collection of photo-generated charge carriers. Furthermore, low material consumption and short deposition times may save costs. Yet light absorption and thus the photocurrent generated by the solar cell is significantly reduced in the case of thin solar cells. For this reason, so-called light management concepts have been developed, aiming at enhanced light absorption without increasing the absorber layer thickness. This includes increased incoupling of sunlight as well as prolongation of the optical light path inside the absorber layer. In fact, the improvement of light management concepts has been suggested as one of the most important factors in the development of thin-film silicon modules as well as other photovoltaic technologies [9]. Usually, prolongation of the optical path is achieved by inserting textured interfaces, to scatter or diffract the light, in combination with a highly reflective back contact. If the scattering angle is large enough, light may even be trapped in the device due to multiple reflections, thereby significantly enhancing absorption in accordance with the Lambert-Beer law. In the case of devices in superstrate configuration, these textured interfaces are typically implemented at the front side of the device between the substrate and photoactive layers. Using transparent polymer films, several of the commonly used light management approaches may not be applicable anymore as temperature limits are imposed here as well. Consequently, there is a strong need for advanced light management concepts that can be obtained at low temperature. Moreover, for the case of superstrate solar cells or (semi-)transparent devices, a negative influence on the substrate transparency due to the light management concept should be avoided. This work therefore also investigates different light management approaches realized at low process temperatures regarding the influence on the performance of flexible amorphous silicon solar cells.

This work was embedded in the joint research project "FlexSol" and was supported by the German Federal Ministry for Economic Affairs and Energy (BMWi) (funding code 0325442D) and part of the results have been published in the final report [13]. The present work is organized as follows:

- Chapter 2 comprises the fundamentals of transparent conductive oxides (TCO) as well as thin-film silicon and their implementation in single junction and multi-junction solar cells. Particular focus is thereby placed on the effect of low deposition temperature as well as post-deposition annealing treatment of silicon layers and solar cells. Basic principles of light management concepts are introduced and a short review about flexible thin-film silicon solar cells is given.
- **Chapter 3** provides details about the deposition processes of TCO and silicon films in addition to the characterization methods used for layers and solar cells.
- Chapter 4 presents the results on the influence of reduced deposition temperature on thin-film silicon layers and solar cells. Though results on microcrystalline layers and solar cells as well as a-Si:H/ μ c-Si:H tandem devices are also presented, the main focus is placed upon the effect of low deposition temperatures on the material properties of amorphous silicon layers and solar cells.
- Chapter 5 elaborates the results on the effect of post-deposition annealing on low temperature a-Si:H material properties as well as solar cells on glass substrates. Silicon layers are investigated with respect to changes in their electrical and optical properties as well as bonding structure upon annealing. Accordingly, the influence of varying material properties of silicon layers on the device performance is investigated. Furthermore, links between changes in layer properties and charge carrier collection in the solar cell upon annealing are addressed applying computer simulations using a simplified device model. A short outlook on the annealing effects in a-Si:H solar cells on PET substrates as well as μ c-Si:H solar cells on glass substrates is given as well.
- Chapter 6 presents the results of a-Si:H layers and solar cells on flexible substrates. Special attention is paid to the investigation of light management approaches that may be applied at low temperature on PET substrates. Two light management approaches are investigated, (i) etching of zinc oxide, where a texture evolves when treated in acidic solution after deposition and (ii) nanoimprint lithography where a rough texture is imprinted on the PET substrate. The effects of these textured interfaces on the performance of a-Si:H solar cells is examined and both approaches are compared. Moreover, this chapter addresses issues that arise from the flexibility, particularly bending of the substrate. For this reason, the performance of a-Si:H solar cells operating in bent conditions is analyzed by measurements under various angles of light incidence and subsequent calculations.

Chapter 7 summarizes the conclusions drawn in the individual chapters.

2. Fundamentals

2.1. Transparent Conductive Oxides

Several device applications require materials that exhibit a high optical transparency in the visible and near infrared (NIR) spectrum as well as a high electrical conductivity. The applications in focus are multifunctional windows as well as contact electrodes for optoelectronic devices such as displays, light-emitting diodes (LED) and solar cells [14]. Possible materials include thin (few nm) metal films like Al, Ag and Cu, metallic nanowires or particles, carbon based nanotubes and graphene, conductive polymers like PEDOT:PSS as well as metal oxides called transparent conductive oxides (TCO) [15–17]. Among these, TCOs still provide the highest market share [15]. So far most important TCOs for electrode applications are In₂O₃, SnO₂ and ZnO typically doped with Sn, F and Al, respectively. These materials provide a large optical band gap (typically above 3 eV) while exhibiting a nearly metallic conductance when appropriately doped.

In this chapter, the basic electrical and optical properties of TCOs will be addressed, although the focus will specifically be put upon aluminum doped zinc oxide (ZnO:Al) which will be the most intensively investigated TCO in this work. An overview of various TCO materials and their applications can be found in [18]. Further details about ZnO and ZnO:Al can be found in [19].

2.1.1. Electrical Properties

For application as electrical contact, a high conductivity is a key parameter for TCO materials. The conductivity of a material can be described as follows:

$$\sigma = q(N_{\rm n}\mu_{\rm n} + N_{\rm p}\mu_{\rm p}) \tag{2.1}$$

where q is the elementary charge, $N_{n/p}$ and $\mu_{n/p}$ are the density and mobility of electrons and holes, respectively. Accordingly, the conductivity of a TCO can be increased by enhancing the density and/or the mobility of charge carriers in the material. As the majority of TCOs is n-type [18], the contribution from positive charges, and thus the right term in the bracket, can be neglected.

Due to the large band gap, the charge carrier density of undoped zinc oxide is relatively low with 10^{17} cm⁻³ [19], but can be increased by either extrinsic and/or intrinsic doping. In the case of intrinsic doping, free electrons can be generated by changing the stoichiometry of the film. Resulting oxygen vacancies or interstitial metal atoms lead

to excess electrons with low energies for excitation to the conduction band. However, an increasing number of oxygen vacancies reduces the transparency of the film and is therefore undesirable. The most common way to increase the charge carrier density in TCOs is extrinsic doping by impurity atoms. For this purpose, metal atoms in the lattice are substituted by higher-valence impurity atoms (such as Al in the case of ZnO) that provide additional electrons for conduction. The dopant concentration is limited by the solubility of the impurity atom in the metal oxide lattice. Above a certain carrier concentration, the donor levels are shifted into the conduction band and the material becomes degenerated. In this case, no energy is needed to excite electrons into the conduction band and the electrons can be treated as a free electron gas such as in metals. For zinc oxide this is the case for $N > 5 \times 10^{18} \, \mathrm{cm}^{-3}$ [20], and all films investigated in this work can be treated as such.

Another possibility to enhance the conductivity is the improvement of electron transport by increasing the mobility of charge carriers in the film. Though designed for the description of metals, the Drude model [21] provides an appropriate description for the electron transport in degenerated semiconductors. In this model the conductivity of a film can be described by

$$\sigma = \frac{Nq^2\tau}{m_{\rm e}} \tag{2.2}$$

where q is the elementary charge, N the charge carrier density, $m_{\rm e}$ the effective mass of an electron and τ the average time between two scattering events. Accordingly, scattering processes limit the electronic transport. Amongst others, the main mechanisms in zinc oxide are (i) scattering at ionized impurities such as intrinsic lattice defects or extrinsic dopants and (ii) scattering at grain boundaries. In (i), the electrical field of ionized impurities disturbs the electronic transport and correspondingly scattering increases with increasing dopant concentration and thus N. In case (ii), grain boundaries consist of a disordered phase and thus present a potential barrier for charge carriers. The probability of overcoming this barrier, and consequently the mobility of charge carriers increases, with increasing N. Due to the opposing trends with N, ionized impurity scattering dominates the electronic transport and thus mobility for ZnO films exhibiting $N > 10^{20} \,\mathrm{cm}^{-3}$, while at lower charge carrier densities, scattering at grain boundaries dominates the mobility in polycrystalline TCO films [22].

2.1.2. Optical Properties

In optoelectronic applications such as solar cells or LEDs, the transparency is important for sufficient coupling of light in- or out of the device. An incoming electromagnetic wave has three options to interact with a certain material. Reflection occurs at interfaces between materials with different refractive indexes. Inside the material, the electromagnetic wave can either be absorbed or transmitted. The resulting measures of transmittance T, reflectance R and absorptance A each describe the portion of interaction relative to

the total amount of incoming intensity. For reasons of energy conversion the following equation applies:

$$A + T + R = 1 \tag{2.3}$$

In Fig. 2.1, typical curves for A, T and R of a TCO are plotted as a function wavelength of the incident light. In this case, the measurements were conducted on a 800 nm thick

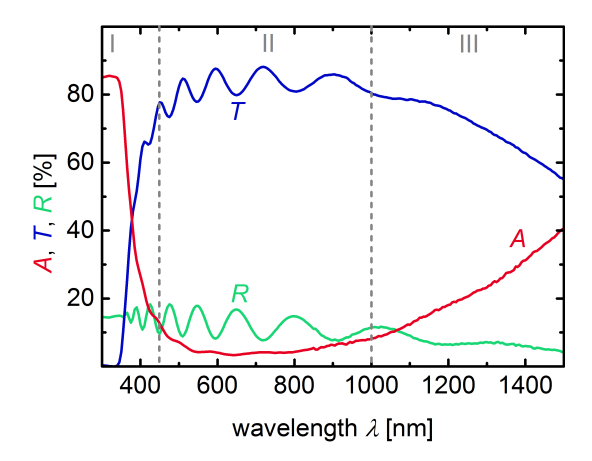


Figure 2.1.: Spectra of transmittance T (blue), reflectance R (green) and absorptance A (red) as a function of wavelength λ for a ZnO:Al layer with a thickness of 800 nm. Three regions I-III can be distinguished (see text for explanation), as approximately indicated by dashed grey lines.

layer of ZnO:Al deposited by magnetron sputtering on a glass substrate. The spectra can be divided into three regions I-III which are explained in the following.

Region I - Fundamental Absorption In this region, the energy of incident photons $E_{\rm ph}$ is larger than the optical band gap $E_{\rm g}$ of the TCO and electrons are excited from the valence into the conduction band. Towards lower energies (longer wavelengths), A abruptly decreases and T increases when the energy becomes too low for direct excitation. The transition wavelength depends on the optical band gap but is also influenced by the so-called Burstein-Moss effect [23, 24], which describes the shift of absorption edge towards shorter wavelength with increasing charge carrier density.

Region II - Transparent Region In this region, $E_{\rm ph}$ is not sufficient for direct excitation of electrons from the valence into the conduction band and a high transparency of around or more than 80 % is evident for the visible and near-infrared (NIR) range between 450 and 1000 nm. In this region, the transmittance is mainly reduced by reflections at glass/ZnO:Al and ZnO:Al/air interfaces (depending on the refractive indexes and roughness of the interfaces) and absorption due to defects that induce states within the optical band gap. Interference fringes in T and R are visible due to constructive and destructive interference in the thin-film resulting from reflections at smooth interfaces.

Region III - Free Carrier Absorption With further increase in λ , the frequency of the incoming light is lowered and free electrons in the conduction band of the TCO may follow the oscillation of the incoming electromagnetic wave. This free carrier absorption increases with increasing wavelength and consequently reduces the transmittance in this region. With increasing carrier concentration in the TCO, the onset of free carrier absorption shifts to shorter wavelengths [19]. For applications such as thin-film silicon solar cells, the transparency in the relevant wavelength range up to 1200 nm may then already be affected by a reduction in T. This directly indicates a fundamental trade-off between the electrical conductivity and optical transparency in the long wavelength region of a TCO layer and each material needs to be tailored regarding its specific application.

2.1.3. Fabrication by Magnetron Sputtering

In this work, ZnO:Al is used as TCO layer for the application in solar cells on flexible substrates. Although various deposition techniques exist, such as e.g. chemical vapor deposition, spray pyrolysis, electrochemical deposition, pulsed laser deposition, sol-gel processes and evaporation (see [22, 25, 26] and references herein), the focus in this chapter will be on magnetron sputtering. Advantages of this technique are the low deposition temperature due to the plasma assistance, suitable for flexible polymer substrates, and the possibility of large area deposition, as needed for roll-to-roll processing.

The sputter process is schematically drawn in Fig. 2.2. Two electrodes are placed

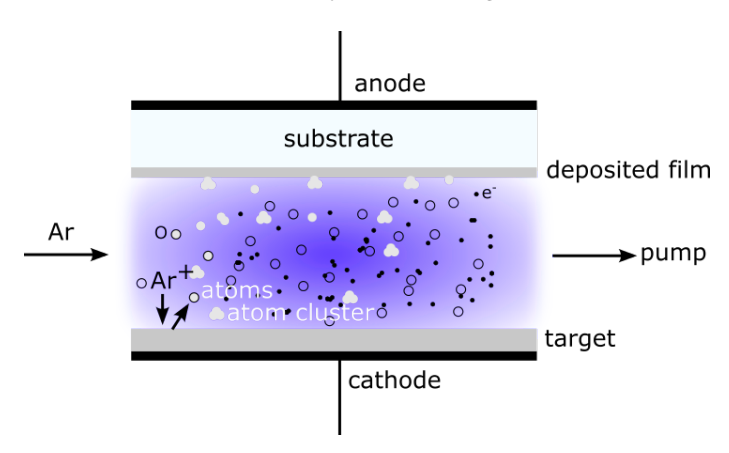


Figure 2.2.: Schematic drawing of the sputtering process. Argon atoms are ionized and Ar⁺ ions are accelerated towards the target. Upon impact atoms or atom clusters are released and veered towards the substrate where they form a film upon deposition.

in a ultrahigh vacuum (UHV) chamber. The target material is positioned on the cathode and the substrate for film deposition is positioned on the anode, respectively. In the simple case, a DC power is applied to the electrodes, building up a static electrical field between the electrodes. An inert sputtering gas such as e.g. argon provides the particles for ionization. Some particles in the Ar gas volume are inherently ionized and are thus accelerated. Due to collisions with neutral atoms, more ionized particles are generated, setting off collision cascades and ignite the plasma. Due to the electrical field, Ar⁺ ions are accelerated towards the cathode and impinge on the target under high velocity. Upon impact, apart from other interactions, atoms or atom clusters are ejected (so-called "sputtered") from the target with a certain amount of kinetic energy. Upon contact with the (substrate) surface, the particles are deposited and form a film.

Target materials such as $\rm ZnO:Al_2O_3$ are not conductive and the charge transfer from $\rm Ar^+$ ions would lead to charging of the target. In the extreme case, this leads to compensation of the electrical field and the plasma extinguishes. Alternating electrical fields (with e.g. radio frequency RF) are therefore applied. The frequency is chosen in such way that electrons can follow the field and reach the target, while $\rm Ar^+$ ions are virtually static in the plasma due to their inertia. As a result, the negative charge at the cathode induces an electrical field, that accelerates the ions and induces ion bombardment of the target.

The deposition rate depends on the number of collision events of the sputtered particles and a low pressure is thus desired to ensure short deposition times. However, if the pressure is too low, less particles are available for sustaining the plasma and the plasma may extinguish. The placement of a permanent magnet under the target confines electrons on helical paths close to the surface of the sputter target due to the Lorentz force. The effect on the argon ions can be neglected due to their inertia. This way the probability for ionization of argon atoms is enhanced and the plasma is stable also at low pressures. Further references about the sputtering process and its variations can be found in [26].

2.2. Thin-Film Silicon

Thin-film silicon, that is amorphous and microcrystalline silicon, is a widely applied material for thin-film electronics and in particular for solar cells. It can be cost effectively deposited from the gas phase by chemical vapour deposition at relatively low substrate temperatures ($<200\,^{\circ}$ C), enabling the deposition on temperature-sensitive but low-cost polymer substrates. In this section, the structural and resulting electrical and optical properties of hydrogenated amorphous (a-Si:H) and microcrystalline (μ c-Si:H) silicon are presented. Plasma enhanced chemical vapor deposition (PECVD) is used for the fabrication of the silicon layers and solar cells in this work and will thus be introduced. More detailed information about the material and processes can be found in e.g. [27–29].

2.2.1. Amorphous Silicon

Structure Like in its crystalline equivalent, Si-atoms in amorphous silicon are bonded in a tetrahedrally and mainly fourfold coordinated network. However, no long range or-

der exists in the material, as the bond distances and especially angles are distorted up to 1% and 10%, respectively [30]. As a result, highly strained and in some cases even non-saturated bonds, so-called dangling bonds, are present within the network. Another consequence, resulting from the lack of long range order, is that crystalline directions for indirect minima in the band structure are undefined. Thus amorphous semiconductors always have effectively direct band gaps, leading to higher absorption coefficients compared to the crystalline phase [27, 30]. Without a band structure in the common sense being available, the electronic structure of amorphous silicon is described by the density of states N(E), as shown in Fig. 2.3.

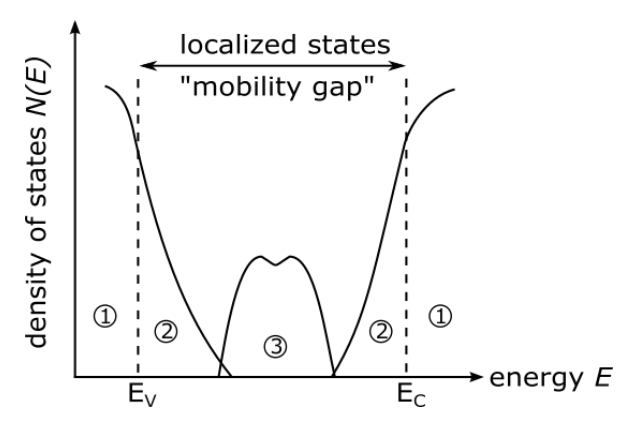


Figure 2.3.: Electronic structure in amorphous silicon described by the density of states as function of energy N(E). Three types of states are available: 1) extended band-like states, 2) localized band-like states, 3) localized defect states in the energy gap. Indicated by dashed lines are the valence band and conduction band edge E_V and E_C , respectively, that define the mobility gap.

In general, three types of states can be identified: 1) extended band-like states, similar to the conduction and valence band in crystalline silicon, resulting from overlapping electronic wavefunctions of non- or only slightly distorted bonds in the network. Charge carriers can move freely in these states [30]. 2) Localized band-like states or tail states, resulting from more strongly distorted and thus weak bonds, where no overlapping of wavefunctions occurs. At room temperature, charge carriers in these states are frequently excited to the conduction band and recaptured, resulting in a reduced mobility. Consequently, mobility edges are defined at the transition from localized to extended states, as indicated in Fig. 2.3. In between the mobility edges, the mobility gap serves as an equivalent to the band gap in crystalline silicon. As the edge from extended to localized states is not abrupt, the value for the mobility gap depends on the definition or evaluation, impeding a direct comparison of absolute values. Though mobility gap is the correct terminology here, it will be named in a more common way as band gap in the following sections. 3) Localized defect states resulting from highly distorted or mostly non-saturated bonds, so-called dangling bonds. These build up a distribution of defect

states inside the band gap, which act as recombination centres for charge carriers and thus impede the lifetime of excess carriers [27, 30].

In unhydrogenated amorphous silicon the density of such defect states is rather high (above 10^{19} cm⁻³ [27, 31]), making the application in optoelectronic devices unattractive. However, dangling bonds can be saturated by incorporation of hydrogen (typically without changing the amorphous structure [27]), resulting in a significantly reduced defect density around 10^{15} - 10^{16} cm⁻³ [27, 32]. Furthermore, only the reduction in defect density allowed the significant increase in dark conductivity by p- and n-type doping of amorphous silicon [33]. Accordingly, only *hydrogenated* amorphous silicon (a-Si:H) will be suitable for the application in solar cells.

A short notice on the stability of amorphous silicon shall be given here. In 1977, Staebler and Wronski discovered that the conductivity of a-Si:H films is reduced upon illumination [34]. This so-called Staebler-Wronski-Effect (SWE) is due to an increased defect density resulting from broken Si-H bonds under illumination of the samples [35]. This in turn results in a deterioration of the photovoltaic performance which stabilizes after a certain time of illumination. The effect is metastable and initial efficiencies of solar cells can nearly be retrieved upon annealing at temperatures below the deposition temperature, typically at 160 °C for deposition temperatures of 180-200 °C.

Electronic Transport The electronic properties of a-Si:H are only briefly presented here, a more detailed discussion can be found in [27]. In general, when a conducting material is placed into an electric field E, a current density J can be observed given by Ohm's law:

$$J = \sigma E \tag{2.4}$$

where σ is the conductivity of the material, that can be described by the following equation (see also Section 2.1.1).

$$\sigma = q \left(N_{\rm n} \mu_{\rm n} + N_{\rm p} \mu_{\rm p} \right) \tag{2.5}$$

where q is elementary charge, $\mu_{\rm n/p}$ the mobility and $N_{\rm n/p}$ the charge carrier density of electrons and holes, respectively. In amorphous semiconductors different transport mechanisms can take place, as mentioned in the section above, but at room temperature the transport in the extended states is dominating [27]. As the hole mobility is low in amorphous silicon, primarily electrons contribute to the current transport. The conductivity in a-Si:H is thermally activated, so that the dark conductivity can be estimated by equation 2.6:

$$\sigma_{\rm d} = \sigma_0 \exp\left(-\frac{E_{\rm A}}{kT_0}\right) = \sigma_0 \exp\left(-\frac{E_{\rm C} - E_{\rm F}}{kT_0}\right)$$
 (2.6)

where k is the Boltzmann constant, T_0 the absolute temperature and E_A is the activation energy, that the charge carriers have to overcome to contribute to the current transport. For the material investigated in this work, this is the energy difference between Fermi level E_F and conduction band edge E_C and the value for the conductivity prefactor σ_0 is $150 \,\mathrm{S/cm}$ [36].

Under illumination, additional energy is provided by photons that excite charge carriers into the extended states. For the resulting photo conductivity, which is evaluated from the conductivity measured under illumination minus σ_d , the charge carrier density is determined by the generation rate G and lifetime τ until recombination of the charge carriers. Therefore the photo conductivity can be described by

$$\sigma_{\rm ph} = qG\mu\tau \tag{2.7}$$

The generation rate, and therefore the photo conductivity, depends on the energy and intensity of the photons the material is exposed to. A large mobility-lifetime ($\mu\tau$) product of charge carriers, and thus a large $\sigma_{\rm ph}$, usually indicates a high material quality. Other influences like the position of the Fermi level will be discussed later.

Optical Properties The optical properties of absorber materials in solar cells are crucial, since after all the absorption of the sunlight plays a significant role for the efficiency of the photovoltaic device. In Fig. 2.4, the absorption coefficient α of intrinsic a-Si:H is plotted as a function of photon energy $E_{\rm ph}$ (black solid line). For comparison, the

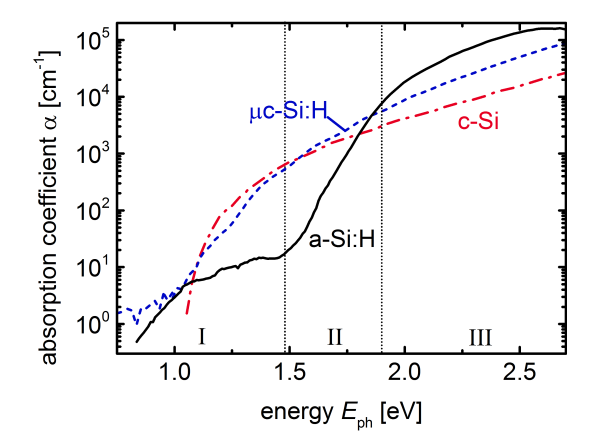


Figure 2.4.: Exemplary absorption spectrum of an a-Si:H sample (black solid line). Three areas can be distinguished: (I) the defect absorption in the low energy range. The photon energy is just enough to enable transitions between extended and defect states, (II) transitions between band tails and extended states, (III) transitions between extended states in the valence and conduction band. The curves for crystalline silicon c-Si (red dash-dotted line) and microcrystalline silicon μ c-Si:H (blue dashed line) are shown for comparison.

absorption spectrum of crystalline silicon is also plotted in the figure (red dash-dotted line). The a-Si:H spectrum can be divided into three regions: (I) for photons with low energy ($E_{\rm ph} < 1.5 \, {\rm eV}$), only transitions between the extended states and defect states are possible. Therefore the absorption coefficient in this range is dominated by the defect density and can be used for the evaluation of the electronic quality of the material. In the second region (II, $1.5 \, {\rm eV} < E_{\rm ph} < 1.9 \, {\rm eV}$), excitations from the valence band tail into

the conduction band or from the conduction band tail into the valence band are dominating for electrons and holes, respectively. Light absorption by charge carriers in defect states still takes place but is superimposed by tail state transitions. A strong increase in absorption occurs in this range, as with more energy the number of states available for excitations increases exponentially (see also Fig. 2.3). Finally, when the energy of photons is sufficiently high (III, $E_{\rm ph} > 1.9\,{\rm eV}$), band-band transitions take place in the third region. Due to the quasi-direct band gap in a-Si:H, the absorption coefficient is considerably larger than for crystalline silicon in this region.

2.2.2. Microcrystalline Silicon

Microcrystalline silicon is a mixed phase material that consists of crystalline grains, amorphous silicon phase, grain boundaries and voids. A detailed description of this material can be found in [37, 38]. The size and volume fraction of the crystallites strongly depends on the conditions during PECVD deposition. In Fig. 2.5, the schematic model developed by Vetterl et al. is presented, showing the microstructure of μ c-Si:H film as a function of the crystalline volume fraction [37]. On the left and right hand side of the figure, material

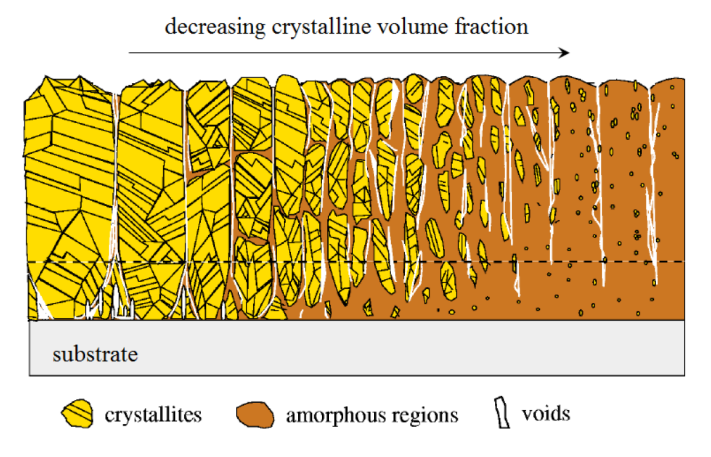


Figure 2.5.: Schematic model showing the microstructure of μ c-Si:H film as a function of the crystalline volume fraction. The picture is taken from [37].

exhibiting a highly crystalline and a low volume fraction of crystallites, respectively, is shown. For most deposition conditions, the layer growth starts with an incubation zone before the actual growth of microcrystals begins. The diameter of the crystalline grains increases with deposition time, resulting in a conical shape of crystallites before columnar growth continues. The space between grains is filled with amorphous tissue, but also voids or cracks can be present there, depending on the deposition conditions. With decreasing crystalline volume fraction (towards the right side in Fig. 2.5), grains are interrupted and more amorphous silicon is present in between, until only nanocrystals distributed in the amorphous tissue are present. The main parameter influencing the crystallinity of films

is the silane concentration, that is the share of silane flow in total gas flow during the deposition [37, 39].

The electrical and optical properties are strongly affected by structural changes. The absorption coefficient of intrinsic microcrystalline silicon is presented in Fig. 2.4, along with the absorption curves for a-Si:H and crystalline silicon. In the range $1.3\,\mathrm{eV} < E_\mathrm{ph} < 1.7\,\mathrm{eV}$, the absorption coefficient of $\mu\mathrm{c}$ -Si:H mainly follows the fundamental absorption curve for crystalline silicon with its nominal band gap of $1.1\,\mathrm{eV}$. For $E_\mathrm{ph} > 1.7\,\mathrm{eV}$, contribution from the amorphous phase with quasi-direct band gap enhances α over c-Si [40]. For $E_\mathrm{ph} < 1.3\,\mathrm{eV}$, defect absorption increases α compared to c-Si and consequently these defects also deteriorate the electrical properties such as mobility and lifetime of charge carriers compared to crystalline silicon. Regarding light-induced degradation due to the SWE, $\mu\mathrm{c}$ -Si:H solar cells are generally more stable compared to a-Si:H [41], and the magnitude of degradation depends on the amount of amorphous volume fraction [42].

2.2.3. Film Growth by PECVD

The predominant deposition technique for thin-film silicon is by plasma enhanced chemical vapor deposition (PECVD), in which the film is deposited on a substrate from the gas phase. In the case of amorphous silicon, silane is the main precursor gas and hydrogen gas is added to improve the material quality. The thermal dissociation of silane would require temperatures around 400 °C [43], which is energy-intensive and restricts the choice of substrates. For thin-film silicon deposition, PECVD offers a more cost-effective way, as due to collisions with electrons, accelerated by an alternating field, silane molecules will dissociate without additional thermal energy. Nevertheless, the substrate temperature is usually around 200 °C to ensure sufficient surface mobility of growth radicals, which is important to gain reasonable material quality [29].

A schematic illustration of the deposition process for thin-film silicon is shown in Fig. 2.6. An alternating voltage with frequencies in the range from 10-100 MHz is applied to two parallel electrodes, while silane and hydrogen are introduced into and pumped through the deposition chamber. Owing to the inelastic collisions with electrons in the plasma, the gas molecules are dissociated or ionized, forming various types of radicals, atoms and ions. The substrate is placed on the grounded electrode and growth precursor molecules such as SiH₃ bind to silicon dangling bonds on the growing film. The surface dangling bonds are generated from reactions abstracting hydrogen, either thermal desorption of hydrogen or reaction of the hydrogen atoms with other SiH₃ or hydrogen molecules, as it is depicted in Fig. 2.7.

The material quality of the growing film sensitively depends on the surface mobility and diffusion of growth precursors on the film surface and the growing film will be more compact if the silicon precursor is able to find an energetically favorable site for bond formation. The surface mobility of the atoms or molecules in turn depends on the substrate temperature and surface properties. Adding hydrogen to the gas mixture leads to

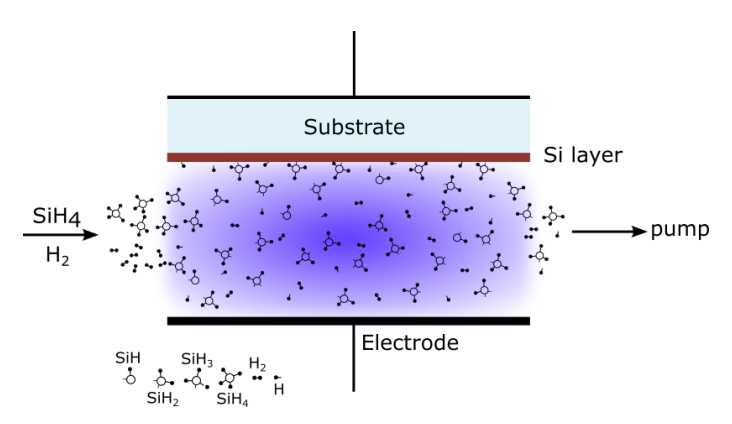


Figure 2.6.: Schematic illustration of the PECVD process. Silane and hydrogen molecules are dissociated to form various types of radicals that interact with the growing film on the substrate surface.

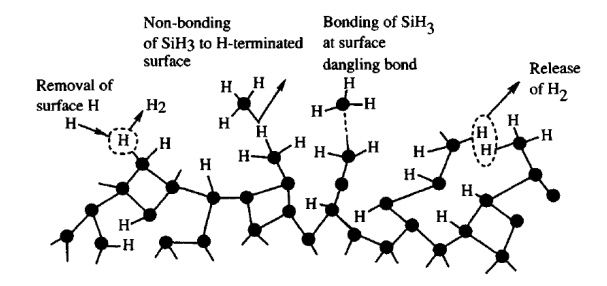


Figure 2.7.: Mechanisms possible for the binding of SiH_3 to the growing surface. The picture is taken from [27].

a coverage of the surface with atomic hydrogen by saturation of surface dangling bonds, thereby enhancing the diffusion of growth precursors [44, 45]. Furthermore, it provides local heating of the film surface by hydrogen exchange reactions, thereby providing additional energy for the surface diffusion of growth radicals [29]. The silicon film formation is a balance between deposition and etching by hydrogen atoms as indicated by the idealized reaction equation 2.8 [39], although there are many complex processes and secondary reactions in between.

$$SiH_x(plasma) \rightleftharpoons Si(solid) + xH(plasma)$$
 (2.8)

The forward reaction represents film deposition and the reverse reaction describes the etching process. The hydrogen gas, which is added to the deposition, promotes the deposition of high quality material, likely due to etching of the growing surface. It is expected that weak Si-Si bonds (in energetically unfavorable configurations) in disordered regions are preferentially etched, so that ordered regions remain, resulting in a reduced defect density. In the extreme case, this leads to the growth of microcrystalline silicon. Ions are also considered to influence the material properties, in such way that the energy impact upon (moderate) ion bombardment on the growing surface results in an enhancement of the surface mobility of growth precursors [46].

The growth mechanism for microcrystalline silicon is still under discussion and several growth models have been proposed. A common basis is the key role of atomic hydrogen covering the surface of the growing film. Details and an overview can be found in [47].

2.2.4. Low Temperature Deposition of Thin-Film Silicon

As mentioned above, the material quality sensitively depends on the surface mobility of growth precursors. The higher the surface mobility, the higher the probability to find an energetically favorable binding site and thus more ordered material is produced. Apart from surface properties that can be influenced by adding hydrogen, the substrate temperature during the PECVD process plays an important role. In general, more energy for the diffusion of precursors is available at higher substrate temperatures. It should be mentioned here that the diffusion mechanism of adsorbed precursor radicals are still under discussion and a summary of existing models is provided by Collins and Ferlauto [48].

Matsuda investigated the defect density in a-Si:H films as a function of substrate temperature $T_{\rm s}$ during deposition and observed that minimal defect densities are obtained at temperatures around 250 °C [29], as shown in Fig. 2.8. The explanation is based on the idea that the dangling bond density in the bulk film is mainly governed by the dangling bond density at the film surface during growth [44]. While the abstraction rate of hydrogen by SiH₃ radicals is assumed to be temperature independent, additional thermal desorption of hydrogen from the surface begins at temperatures above 300 °C, thus increasing the surface defect density. At low temperatures below 200 °C on the other hand, the surface

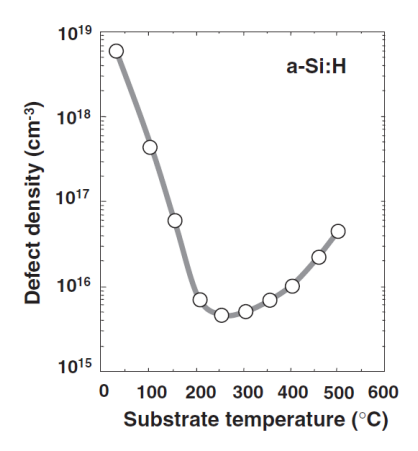


Figure 2.8.: Defect density as a function of substrate temperature for a-Si:H films grown by PECVD according to Matsuda [29].

dangling bond density increases due to the slow surface diffusion of SiH₃ radicals, resulting in the U-shaped defect density as function of substrate temperature shown in Fig. 2.8. A controversial hypothesis was given by Robertson, who attributed the increase in bulk defect density towards low deposition temperatures to an increased fraction of weak Si-Si bonds generated in the subsurface of the growing film rather than the surface defect density [49]. A detailed overview of various models may be found in [48, 50].

A common approach to reduce the defect density at low deposition temperatures is the increase in hydrogen gas flow during deposition [51]. As a result, the etching effect explained above is likely to increase, thereby enhancing the structural order in the film and resulting in a more stable network with lower defect densities [39]. In the case of microcrystalline silicon, the defect density is less sensitive to the reduction in deposition temperature, as shown by Matsuda [29]. A possible explanation is related to the high hydrogen flux in the plasma and the consequent local heating effect from hydrogen exchange reactions that provide additional energy for the surface diffusion of growth precursors, even at low temperatures [29].

Typical hydrogen contents in device quality a-Si:H films are around 5-20% [49], significantly more than needed for the passivation of dangling bonds. It has been demonstrated that the hydrogen content in the film decreases with increasing substrate temperature [27, 51–53]. This is usually interpreted as an increased desorption of hydrogen from the film surface at higher substrate temperatures [54]. Resulting from the higher hydrogen content at low deposition temperatures, an increase in the band gap of a-Si:H can be observed [55–60]. Though not clearly understood, an explanation is often related to the reduction of weak Si-Si bonds by hydrogen. These weak Si-Si bonds create states near the valence band edge, while stronger Si-H bonds induce states deeper in the valence band. As a result, the valence band edge shifts down and as the conduction band remains unaffected the band gap increases [27, 53, 58, 61]. Therefore low deposition temperatures

have been utilized to reduce the parasitic absorption of doped layers and also to increase the open-circuit voltage of solar cells by tuning the band gap of intrinsic layers [51, 62], for example for photo electrochemical water splitting [63].

In summary, low deposition temperatures increase the defect density in thin-film silicon films, which need to be compensated by process optimization by e.g. increasing the percentage of hydrogen in the gas mixture during deposition.

2.3. Solar Cells

2.3.1. Main Principle of a Thin-Film Silicon based Solar Cell

The operating principle of silicon wafer-based solar cells is based on the diffusion of generated charge carriers in a pn-junction. The key is a diffusion length of charge carriers around $200\,\mu\mathrm{m}$. The defect density in doped a-Si:H layers is significantly larger and diffusion lengths of charge carriers are very low. Therefore, an intrinsic absorber layer with lower defect density is embedded between a p-type window layer and an n-type layer in a so-called p-i-n configuration (see Fig. 2.9). Incident photons are absorbed in the intrinsic layer and generate, or more precisely excite, charge carriers (electrons to the conduction band and holes to the valence band). The p- and n-type layer built up an electrical field through the intrinsic absorber layer that leads to separation of charge carriers and transport to the electrodes, where they can be collected (as shown in Fig. 2.10).

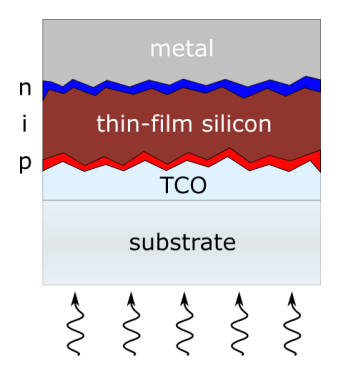


Figure 2.9.: Structure of a p-i-n solar cell in superstrate configuration. As the light comes through the substrate and front contact, both must be transparent.

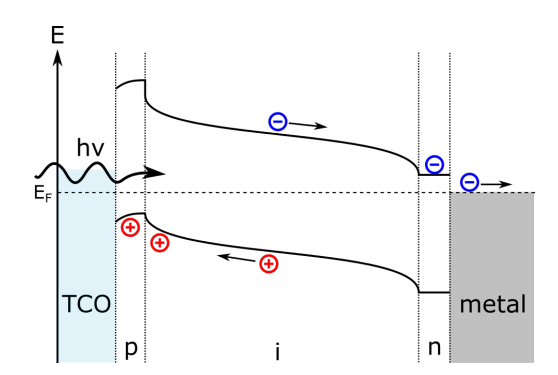


Figure 2.10.: Schematic band diagram of a p-i-n solar cell for short-circuit conditions. The p- and n-type layer produce an electric field in which the charge carriers are separated and transported to the electrodes.

Due to the higher absorption coefficient, resulting from the quasi-direct band gap, thin-film silicon layers need considerably less material to absorb the same amount of light: typical absorber layer thicknesses are in the range of $300\,\mathrm{nm}$ (a-Si:H) and $1\text{-}2\,\mu\mathrm{m}$

(μ c-Si:H), compared to several hundreds of micrometers in the case of c-Si solar cells. The lifetime of charge carriers that are generated in the doped layers is very low and usually do not contribute to the photocurrent [27]. A trade-off exists regarding the thickness of the absorber layer: the thinner the intrinsic layer, the larger the built-in field and thus enhanced charge carrier collection from the device. Due to this, solar cells with thin absorber layers are also considered to be less sensitive to light-induced degradation [28]. On the other hand, a reduced layer thickness also reduces the absorption of light and thus the photogenerated current provided by the solar cell. Accordingly, light-trapping concepts have been introduced that prolong the light path inside the absorber layer. These will be discussed later in this chapter (Section 2.5). The drift lengths are significantly larger in microcrystalline silicon but on the other hand the absorption coefficient is also lower, thus the absorber layer thickness is typically larger compared to amorphous silicon solar cells.

There are different configurations regarding the deposition sequence of the layers in solar cells. In the *substrate* configuration, which is mainly used for opaque substrates, the deposition sequence is n-i-p on top of a contact layer. In the *superstrate* concept, exclusively used in this work, the substrate material and contact layer on top needs to be transparent and is followed by a p-i-n deposition sequence (as in Fig. 2.9). In both configurations, the device is illuminated through the p-type layer of the device, and is called p-side illuminated. This is preferable due to the short drift length of holes as minority carriers compared to electrons, especially in a-Si:H. The larger amount of photons is absorbed in the front part of the absorber layer and correspondingly holes have a shorter way to drift when the p-type layer is positioned at the front. Accordingly, n-side illuminated devices usually exhibit lower photovoltaic performance [46], but can be used to separately investigate effects on the charge carrier extraction of electrons and holes, as will be shown in Section 5.3.

The performance of a photovoltaic device is evaluated by its current density-voltage (J-V) curve under illumination. In Fig. 2.11, a typical J-V curve of a solar cell is shown. The short-circuit current density $J_{\rm SC}$ is the maximum current density and is obtained in short-circuit condition at V=0. In the ideal case, it should equal the photo-generated current density $J_{\rm ph}$, assuming that the dark current at short-circuit conditions can be neglected. The open-circuit voltage $V_{\rm OC}$ is the maximum voltage generated by the solar cell and is obtained at J=0, when no net current is flowing. At any point of the J-V curve, the power density that is delivered by the solar cell is defined by

$$P = V \times J \tag{2.9}$$

The point where the power reaches its maximum P_{max} is called the maximum power point (MPP) with its corresponding current density J_{MPP} and voltage V_{MPP} . The fill factor FF is defined as

$$FF = \frac{P_{\text{max}}}{J_{\text{SC}} \times V_{\text{OC}}} = \frac{J_{\text{MPP}} \times V_{\text{MPP}}}{J_{\text{SC}} \times V_{\text{OC}}}$$
(2.10)

which corresponds to the ratio of the grey rectangle to the rectangle with the dashed border in Fig. 2.11. Linked to the fill factor are the series and shunt resistance $R_{\rm s}$ and $R_{\rm sh}$

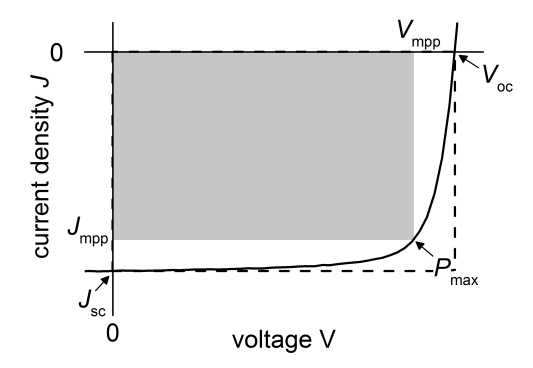


Figure 2.11.: Current density-voltage J-V curve of a solar cell and the parameters that can be evaluated: short-circuit current density $J_{\rm SC}$, open-circuit voltage $V_{\rm OC}$, current density and voltage at the maximum power point (MPP) $J_{\rm MPP}$ and $V_{\rm MPP}$, respectively.

of the solar cell, that are calculated from the slope ${}^{dV}/{}_{dJ}$ at $V=V_{\rm OC}$ and V=0, respectively. The resistances arise from losses that occur in different regions of the solar cells, and $R_{\rm s}$ and $R_{\rm sh}$ should be as low and as high as possible, respectively. Finally the efficiency η is defined as the ratio of maximum power $P_{\rm max}$ provided by the solar cell to the power of the incident light $P_{\rm ill}$, and can be calculated from

$$\eta = \frac{P_{\text{max}}}{P_{\text{ill}}} = \frac{J_{\text{SC}} \times V_{\text{OC}} \times FF}{P_{\text{ill}}} \qquad (2.11)$$

Solar cells in this work are characterized by four photovoltaic parameters: short-circuit current density J_{SC} , open-circuit voltage V_{OC} , fill factor FF and efficiency η .

2.3.2. Tandem Solar Cells

The efficiency of single-junction solar cells is limited by its fundamental trade-off between voltage and light absorption, which both depend on the band gap [64]: thermalization losses occur for photons with energy $E_{\rm ph}$ larger than the band gap $E_{\rm g}$ of the absorber material, while photons with $E_{\rm ph} < E_{\rm g}$ can not be absorbed at all. As a result, a maximum efficiency of around 30 % can be achieved in the ideal case using a band gap between 1.3 eV and 1.4 eV [65]. By employing multijunction solar cells with absorber layers exhibiting different band gaps, a better utilization of the solar spectrum can be achieved as high energy photons are absorbed by a large band gap absorber and thus allow high voltages, while a low band gap material provides the utilization of low energy photons. Accordingly, the efficiency limit can be extended, in the case of four junctions up to 50 % [65].

In the case of thin-film silicon, the availability of amorphous and microcrystalline silicon with differing band gaps provides an intruding multijunction device concept and the so-called "micromorph" a-Si:H/ μ c-Si:H tandem solar cell was developed [66]. The tandem

cells are composed of two p-i-n solar cells stacked upon one another and connected in series. The amorphous silicon sub cell is positioned at the front of the device, filtering the incident light by absorbing high energy photons and transmit low energy photons that can be absorbed in the microcrystalline sub cell (see Fig. 2.12). Accordingly, both cells

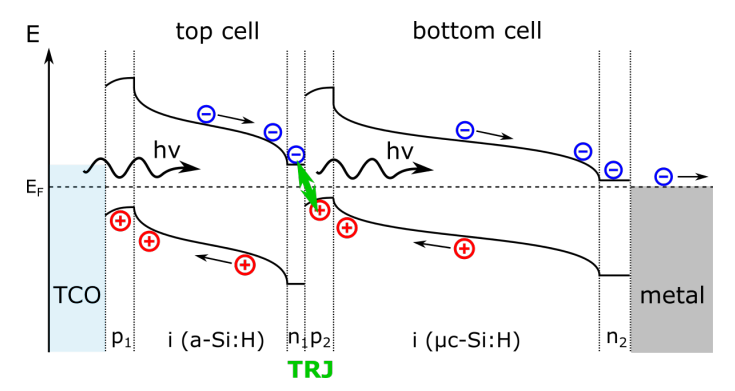


Figure 2.12.: Band diagram of a p-i-n-p-i-n tandem solar cell for short-circuit conditions. Holes and electrons from top and bottom cell, respectively, have to recombine at the n-/p-interface to ensure a continuity in current transport. The interface is therefore called tunnel recombination junction (TRJ).

absorb light, leading to the generation of charge carriers, and for both an electric field is provided by respective p- and n-type layers. Holes are transported to the front contact (p-type layer), whereas electrons are transported to the n-type layer, and electrons from the top cell recombine with holes provided by the bottom cell to ensure a continuous current transport. For the recombination, charge carriers have to tunnel through the n_1 -/ p_2 -interface. This is called tunnel recombination junction (TRJ) and a good contact must build up, so that there is no accumulation of charge carriers that disables further excitation. For this purpose, highly doped n- and p-type layers forming a defect rich interface are usually needed to reduce the tunnel distance and to increase the density of states available for recombination [67]. Due to the series connection, the photovoltages of the sub cells sum up, while the overall photocurrent is limited by the sub cell with the lowest current. Accordingly, the photocurrents of the sub cells should preferably be similar to avoid electrical losses (so called "current-matched").

2.4. Annealing of Thin-Film Silicon Films and Solar Cells

As a typical, empirically deduced procedure, thin-film silicon solar cells are annealed at temperatures below deposition temperature after back contact evaporation, mainly to remove uncontrollable light-induced degradation which may occur during the deposition or handling of the sample [68–70]. On the other hand, it is well known that prolonged annealing, especially at temperatures above the deposition temperature, may lead to outdiffusion of hydrogen [71]. This in turn results in a significant increase in the defect

density as dangling bonds remain when Si-H bonds are broken, and thus layer and device properties are considerably deteriorated [72–74].

However, significant improvements are sometimes found in amorphous silicon solar cells upon post deposition annealing, especially when the layers are deposited at low temperatures: Brinza et al. have studied a-Si:H solar cells deposited at 100°C and have shown that upon post-deposition annealing at 100 °C, the efficiency considerably increases by up to 40% relative [75]. They ascribed this improvement mainly to an increase in $V_{\rm OC}$. Studies of Koch et al. reported an even stronger increase in efficiency up to a factor of 5 for a deposition temperature of 75 °C and subsequent annealing at 110 °C, caused by a strong increase in short-circuit current density [76, 77]. An efficiency improvement of 50% relative was found by Wang et al. for amorphous silicon germanium solar cells prepared at 200 °C for different annealing temperatures up to 230 °C [78]. They correlated the improvement in FF and J_{SC} to an increase and decrease of the shunt and series resistance, respectively. Mittal et al. [79] investigated the effect of post-deposition annealing on complete a-Si:H modules and found an increase in module performance. In literature, the reasons for the improvements were manifold, such as a reduced sheet resistance of the TCO covered substrate [78], but most often the improvement in device performance was ascribed to an improvement in intrinsic layer properties [78, 79].

Annealing of amorphous silicon solar cells was deeply investigated in the past decades, predominantly with regards to the recovery of the device performance after light-induced degradation. After discovery of the Staebler-Wronski-Effect (SWE) in 1977 [34], much research was conducted to understand the mechanism of degradation, as well as of the subsequent annealing process. Light exposure deteriorates the optoelectronic properties of a-Si:H, which correspondingly reduces the performance of the photovotaic device. Explanations and models are numerous [80], yet the reason is often related to the recombination of electron-hole-pairs, generated by illumination, which induce the creation of dangling bonds [35]. The underlying processes are still under discussion and an overview can be found in [80]. These light-induced defects were found to be metastable, meaning that they can be removed by subsequent annealing [34]. Accordingly, many studies were performed to investigate the annealing kinetics of light-induced degradation [81–83].

On the other hand, annealing may also remove so-called "native" defects present in the as-deposited state and it is under discussion whether the two types of defects have the same origin and/or annealing kinetics [84–88]. Several studies have been performed on various types of amorphous silicon layers, deposited by different PECVD techniques, sputter deposition, as well as for material with deposition temperatures ranging between room temperature and 250 °C [86, 89]. Even when keeping only to studies for low deposition temperatures ($<150\,^{\circ}$ C), the results of post-deposition annealing of intrinsic a-Si:H layers are manifold:

• Concerning electrical properties of the intrinsic layer, the photo response - that is the ratio of photo to dark conductivity - increases in most cases (up to several orders

- of magnitude) upon post-deposition annealing, mainly due to an increase in $\sigma_{\rm ph}$ [76, 86, 89–93].
- Kunst et al. [94], Neitzert et al. [95] and Koch et al. [77] have shown that the $\mu\tau$ -product of electrons improve upon post-deposition annealing. They assigned this to a reduction in defect density in the intrinsic absorber layer upon annealing, as detected from CPM measurements [76] as well as ESR spin density [95]. Indeed, many authors find a reduction in defect density (between 20 % and orders of magnitude) upon post-deposition annealing at various temperatures and for various durations [77, 86–89, 92, 93, 96–98].
- Indication for a reduction in structural disorder is found by a reduction in Urbach energy upon annealing [87, 89, 93].
- Regarding doped a-Si:H layers, several authors have found the dark conductivity of doped a-Si:H layers significantly increases upon post-deposition annealing [99–102].
 This is often ascribed to activation of dopant atoms, for example due to a reduction in defect density of the films [100]. Especially in p-type layers, activation of dopants may also occur by breaking boron-hydrogen complexes that keep the boron atoms in a non-active three-fold coordination [101, 102].

In intrinsic as well as doped a-Si:H layers, the effects of deposition temperatures and post-deposition annealing are often related to thermal equilibrium models introduced by Smith and Wagner [103] as well as Street et al. [104, 105]: Smith et al. explained the defect density for films deposited at 250 °C by glow-discharge with the formation of dangling bonds due to the recombination of thermally excited charge carriers similar to what happens during Staebler-Wronski effect [106]. This defect density may be frozen-in during cooling down of the layers after deposition and relaxation may occur upon post-deposition annealing. Street et al. introduced another thermal equilibrium model first for doped layers [104, 105] which was later extended also for intrinsic a-Si:H layers [84]. It was shown that the material properties of a-Si:H sensitively depend on the deposition temperature, as well as annealing temperatures and corresponding cooling rates. According to their theory, above an equilibrium temperature $T_{\rm E}$, the material is in thermal equilibrium with $T_{\rm E}$ being around 80 °C and 130 °C for p- and n-type layers respectively, and 200 °C for intrinsic a-Si:H layers. For annealing temperatures below $T_{\rm E}$, thermally activated equilibration occurs to bring the structure of a-Si:H in direction of thermal equilibrium.

Stutzmann on the other hand suggested that thermal defect equilibration is of minor importance for the overall defect density in a-Si:H and that structural transitions only occur at the highest temperature in thermal history of the material [74]. Parsons et al. [86] concluded that for intrinsic a-Si:H films with low defect density, annealing at $T_{\rm ann}$ for a time $t_{\rm ann}$ is essential after deposition to relax the intrinsic electronic defects incorporated during film deposition. At $T_{\rm s}$ of 225-325 °C, relaxation occurs during deposition, while for lower $T_{\rm s}$ annealing at e.g. 170 °C for more than 2 h is necessary to reach equilibrium.

Microscopically, Street et al. assigned the above described effect to the motion of hydrogen in the silicon network, and introduced the "hydrogen glass model" [104]. In this model, the hydrogen sublattice can be considered as a glass where the glass transition

temperature (= $T_{\rm E}$) is between the metastable equilibrium and the frozen-in state of a glass. They suggest that hydrogen atoms diffuse well below the deposition temperature and close to the equilibrium temperature. A detailed overview of various equilibrium models can also be found in [50].

Overall, amorphous silicon deposited at low deposition temperatures below $150\,^{\circ}$ C is considered to be far away from thermal equilibrium and relaxation processes need to be taken into account when post-deposition annealing treatments are carried out.

2.5. Light Management

Light management in a solar cell comprises the incoupling to as well as trapping of light inside the absorber layer of the device. Light incoupling can be improved by e.g. introduction of rough surfaces at the front side of the solar cell that serve as refractive index grading [107]. Other possibilities are antireflection layers between the TCO and silicon layers [108] or anti-reflection coatings on the glass substrate [109]. Trapping of the light leads to a prolongation of the optical path inside the absorber layer and is usually achieved by introduction of textured surfaces that scatter or diffract the light in combination with a highly reflective back contact. Light trapping enhances the absorption of photons and thus increases the short-circuit current of the solar cell. Besides, it allows a reduction of the absorber layer thickness, which may lead to an increased open-circuit voltage, reduction in manufacturing costs and/or reduced degradation as e.g. in the case of amorphous silicon absorber layers [28].

Several light management concepts exist, which can exhibit periodic or random concepts, including as-grown textured SnO_2 :F, wet-chemically etched ZnO:Al, as-grown textured low-pressure chemical vapor deposition (LPCVD) ZnO:B, textured silver layers, imprinted photo resists, hot embossed plastic foils, etched glass substrates, nanoparticles or photonic crystals (see [110–112] and references herein). An overview of state-of-the-art light management approaches in thin-film silicon solar cells can be found in [110]. The light trapping performance of a textured surface can be evaluated by the haze value and the angular intensity distribution and several approaches have been made to describe a relation between these measures and the surface morphology [113–115].

In this chapter, the two light management approaches on flexible substrates applied in this work are introduced. First, the well established etching of aluminum doped zinc oxide ZnO:Al is introduced. Second, the nanoimprint lithography approach is presented that can be used to create arbitrary nanotextures on various types of substrates.

2.5.1. Etching of ZnO:Al

Layers of sputter deposited zinc oxide develop an inherent texture when they are wetchemically etched in acidic or alkaline solutions [116, 117]. The evolving surface morphology depends strongly on the microstructure of the initial films and accordingly on the

growth conditions during deposition, as well as on the etching process through the type of etchant, its concentration, temperature and time. For example, different textures evolve by etching in KOH, HCl or HF solution [19, 20]. A well established process is the etching of sputtered aluminum doped zinc oxide (ZnO:Al) in HCl solution, which can lead to well designed surface morphologies that enhance the light trapping in thin-film silicon solar cells [118].

Several models have been developed to relate the growth conditions of ZnO:Al films to the surface texture after etching in HCl solution, which are briefly presented in the following. Kluth et al. [119] presented an approach to relate the evolving surface morphology of the film to the temperature and pressure during growth of the ZnO:Al. It is based on the Thornton model [120], which was originally developed to correlate the microstructure of sputtered films to deposition conditions. The model is based on the general idea that the energy available for adsorbed atoms on the substrate surface increases with increasing substrate temperature and reduced pressure, respectively. In the model of Kluth et al., three types of material named A, B and C were found for sputtered ZnO:Al films, deposited in the temperature range from room temperature to 270 °C. Type A material, which is deposited at low temperature and high pressure, thus low energy available for adsorbed atoms, is isotropically etched with hardly any change in surface morphology. Type B material, which evolves at intermediate temperature and pressure, is more compact and anisotropic etching leads to homogeneously distributed craters on the surface of the etched film. Type C material, deposited at high temperatures, was found to be very compact and upon etching only a few large craters evolve. This model was extended by Berginski et al. to include also the target dopant concentration of the ceramic ZnO:Al₂O₃ target [118].

Owen investigated the influence of various types of etchants as well as their concentration and temperature and postulated a connection to the resulting crater size and distribution [20]. Horizontal and vertical etching rates and thus the size and depth of etched craters depend on the nature of the grain boundary as well as the mobility and size of the etchant. If large etchants can not penetrate deeply into the grain boundary, the vertical etching rate is limiting and reactions are limited to the surface. Sharper features are observed when the horizontal etching rate is limiting, as in the case of small HF etchants which can more easily penetrate deep into grain boundaries.

Application of this light management approach to thin-film silicon solar cells was early presented by Löffl et al. [121] and is now widely applied in state-of-the-art solar cells.

2.5.2. Nanoimprint Lithogaphy

Nanoimprint lithography was first developed in 1996 by Chou et al. for the replication of nanotextured surfaces [122]. Since then, the technique has been further developed and optimized, and sub 5 nm features are possible by now [123]. In general, nanoimprint lithography (NIL) describes the replication of nanoscale textures from a textured mold

on the surface of a substrate. Among this technique, several variations exist: the mold can consist of a soft or hard material, the textures can be pressed directly into a polymer substrate via hot embossing or utilizing a photo sensitive polymer cast, that can be cured by UV light, laser light, and/or temperature. A great advantage is the possibility of a high throughput production on large scale substrates by roll-to-roll frabrication [124]. Applications range from electrical devices [125, 126], optical devices [127, 128] and optoelectronic devices [129, 130] to magnetic applications [131]. An overview of the various techniques of NIL can be found in [132, 133]. Regarding the implementation in thin-film silicon solar cells, the approach was successfully applied at the IEK-5 in Jülich [134, 135] as well as the Neuchâtel group [136, 137] and several other [138, 139].

2.6. Flexible Thin-Film Silicon Solar Cells

Due to their special characteristics, flexible solar cells offer many advantages: the flexibility and light weight make them suitable for building integration as well as mobile applications. Using roll-to-roll production, a high throughput may allow a cost reduction, not only regarding the deposition process [140], but also for storage and transport when the solar cells are space-savingly rolled up. More costs can be avoided considering the rejects due to breakage of fragile glass substrates. The glass substrate actually contributes to more than $20\,\%$ to the overall module cost, supporting the economic advantage of cheaper substrates [141].

Thin-film silicon is especially suited for the application on flexible substrates, as the PECVD deposition process can easily be applied on large area in roll-to-roll deposition systems [142], and the process temperature is relatively low to enable the use of polymer films. Already in the 1980s, flexible a-Si:H solar cells have been deposited in roll-to-roll deposition on stainless steel, polyimide (PI) and polyethylene terephthalate (PET) substrates [142–144]. The choice of the substrate defines the boundary conditions for the fabrication of thin-film silicon solar cells, and several flexible substrates will therefore be discussed in the following.

Metal and PI films In the case of metal foils or temperature-resistant polymer films like polyimide (PI), optimal process conditions with substrate temperatures of around 200 °C can be applied. Most developments have so far been conducted on these opaque substrates at high temperatures by several groups [139, 142, 143, 145–157], and maximum initial efficiencies of 16.3 % were achieved with a triple-junction structure of a-Si:H/a-SiGe:H/μc-Si:H by United Solar [158]. Low temperature (≤150 °C) a-Si:H solar cells on stainless steel substrates were fabricated by Brinza et al. as well as Ma et al. [75, 159]. Using opaque substrates however, monolithic series connection of a large area module can not easily be performed by laser scribing but needs more advanced techniques [148]. As a result, considerable losses occur by upscaling to modules.

Flexible glass Recently, flexible glass substrates show presence in the market and solar cells deposited on these substrates show initial efficiencies of 9.3% using tandem junctions of a-Si:H/ μ c-Si:H [160]. However, the cost of these substrates is relatively high [161], and its intrinsic brittleness may cause problems during handling.

Transparent polymer films On the other hand, low-cost polymer films like polyethylene terephthalate (PET), polyethylene naphthalate (PEN) or polycarbonate (PC) can be used to reduce the costs of the device and allow lighter weight compared to metal films. However, these plastic films have low glass transition temperatures and maximum process temperatures are limited to 150 °C [162, 163]. Accordingly, considerable effort is needed to develop low temperature silicon films with appropriate material quality. Three concepts were considered in the past:

- In order to avoid the temperature limitation imposed by cheap polymer films, the Helianthos consortium developed an advanced concept, in which the deposition was carried out on aluminum foil at high deposition temperatures (around 200 °C) and subsequently transferred to a transparent polyester substrate. Finally, the temporary aluminum substrate was removed by chemical etching [164]. Solar cells deposited with this approach achieved initial efficiencies of 9.4 % and 8.1 % in the case of a-Si:H/µc-Si:H and a-Si:H solar cells, respectively [165, 166]. However, the use of a temporary substrate and its chemical etching causes additional production costs.
- Most of the research on transparent polymer films was conducted on solar cells in the substrate or n-i-p configuration, where opaque or less transparent substrates can be used as well [137, 144, 166–172]. Without any light management textures, efficiencies of thin-film silicon solar cells were low, with maximum initial efficiencies of 6.3%. In the substrate configuration, the transparency of the substrate does not need to be considered for light management approaches and best efficiencies for a-Si:H and a-Si:H/µc-Si:H tandem solar cells of 9.9% and 11.2%, respectively, were achieved by the Neuchâtel group, using hot embossing and UV NIL technique on PEN substrates and deposition temperatures below 180 °C [137, 170–172]. Though initially transparent, the polymer substrates need to be covered with a reflecting layer to ensure trapping of light in the absorber layer in the case of n-i-p configuration.
- On the other hand, considerably less work was done on flexible solar cells in p-i-n configuration with illumination through the transparent polymer substrate. Most groups have not been using light management textures, resulting in low efficiencies [77, 173–177]. The group at Utrecht University utilized light trapping for a p-i-n a-Si:H solar cell on transparent polymer substrates, thus achieving higher efficiencies. They developed a microstructuring process of PC substrates by hot embossing a periodically pyramidal texture, thereby achieving initial 7.4% efficiency for an a-Si:H solar cell deposited at low substrate temperature of 130 °C [111, 178, 179].

Overall, the crucial elements to develop flexible solar cells in superstrate configuration with appropriate efficiencies on cost-efficient polymer films are (i) the development of high quality thin-film silicon layers and solar cells at low deposition temperatures ($<150\,^{\circ}\mathrm{C}$) and (ii) the application of advanced light management schemes that improve light incoupling and trapping, that do not impair the transparency of the substrate and can be fabricated at low temperature.

3. Preparation and Characterization

3.1. Clustertool Deposition System

The clustertool deposition system, used for the fabrication of transparent conductive oxide (TCO) and silicon layers as well as solar cells, is a multichamber deposition system consisting of nine chambers, as depicted in Fig. 3.1. In addition to five process chambers

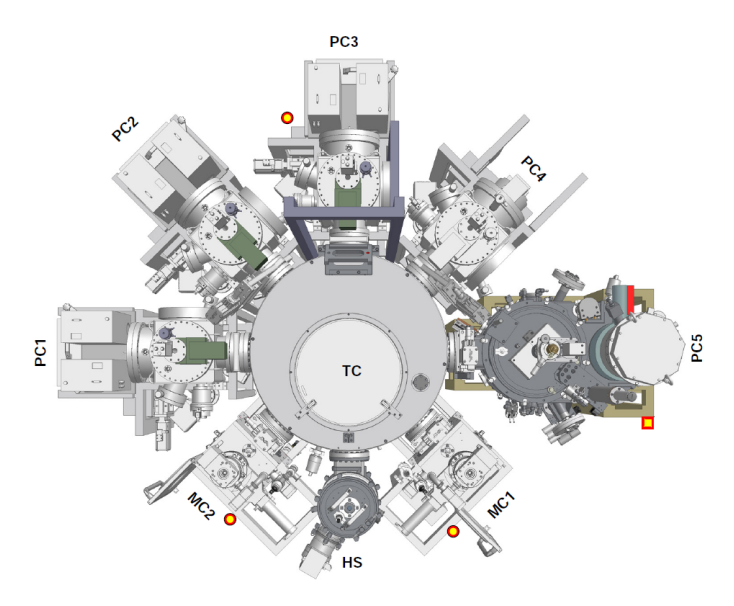


Figure 3.1.: Schematic drawing of the clustertool deposition system. The labels indicate the name of the respective chambers. Extracted from: Manual of the Clustertool Deposition System CS 300 PS, VON ARDENNE Anlagentechnik GmbH.

(PC1-PC5), two loading chambers (MC1, MC2) and a heater station (HS) are present, which are connected by the transfer chamber (TC) thus allowing a transport between the chambers without vacuum break. Except for the heater station, each chamber is divided from the TC by valves. The transport of substrates between the chambers is provided by an automated robot arm that is located in the transfer chamber. Among the process chambers are three identically designed PECVD chambers, one each for p-type, intrinsic and n-type silicon layers (PC1, PC2 and PC3, respectively), to avoid cross contamination of the doping gases, which may deteriorate the quality of the individual layers. The other

process chambers are a hot-wire CVD chamber (PC4), as well as a sputter chamber for the deposition of front and back contacts (PC5). The system is designed for a maximum substrate size of $10 \times 10 \text{ cm}^2$. Further details about the deposition system can be found in [180].

3.1.1. PECVD Process Chamber (PC1-PC3)

A schematic drawing of a PECVD process chamber is presented in Fig. 3.2. The substrate

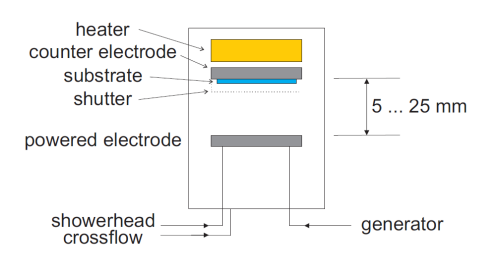


Figure 3.2.: Schematic drawing of the PECVD process chambers PC1-PC3 in the clustertool deposition system. All chambers have the same construction. The drawing is adapted from [181] and not drawn to scale.

is transferred into the chamber by the robot arm and positioned into the holder for the substrate carrier. The substrate is heated directly by the heater, which is brought into contact with the substrate. The temperature controller allows to adjust the heater temperature up to $500\,^{\circ}$ C. In order to obtain information about the actual substrate temperature, calibration measurements were carried out using a thermocouple [182] as well as temperature data logger SL55T from Signatrol Ltd. Under ultrahigh vacuum ($< 10^{-7}$ mbar), the substrate temperature resulting from heat conduction and radiation is significantly lower than the aimed temperature. Upon inlet of the process gases, the substrate temperature considerably increases resulting from convective heat transfer. Accordingly, a preheating procedure of 10 minutes under process conditions but without ignited plasma was conducted prior to the first deposition on the substrate.

In this work, the indicated temperature values are nominal substrate temperatures during the deposition after the preheating step, though one has to keep in mind that the temperature measurements are accompanied by a large error bar of up to $\pm 15\,^{\circ}\mathrm{C}$ at a substrate temperature of 120 °C. In this work, heater temperatures were set between 140 °C and 200 °C for the deposition of silicon layers, corresponding to nominal substrate temperatures of 120 °C and 180 °C.

The holder along with the substrate serves as grounded electrode for the PECVD process. The powered circular electrode with a diameter of 164 mm is underneath, consequently the deposition of material occurs in face-down configuration. The distance between the two electrodes can be varied between 5 mm and 25 mm by moving the heater,

which in turn pushes down the substrate towards the powered electrode in the desired position. Each chamber is equipped with two generators operating at 13.56 MHz (radio frequency RF) and 81.36 MHz (very high frequency VHF), respectively, which are connected to the chamber via a matchbox for impedance matching, i.e. optimal power coupling. The process gases are regulated by mass flow controllers and introduced into the chamber through the powered electrode positioned on the bottom of the chamber (so-called "showerhead electrode"). A shutter protects the substrate from irregularities during the plasma starting process and deposition starts when the shutter is opened after stabilization of the plasma. The transport, valves, shutter and also the deposition parameters such as heater temperature, pressure, gas flows, electrode distance, etc. as well as the power and impedance matching are controlled by a fully computer based system.

3.1.2. Sputter Chamber (PC5)

The schematic drawing of the sputter chamber PC5 is presented in Fig. 3.3. Similar to



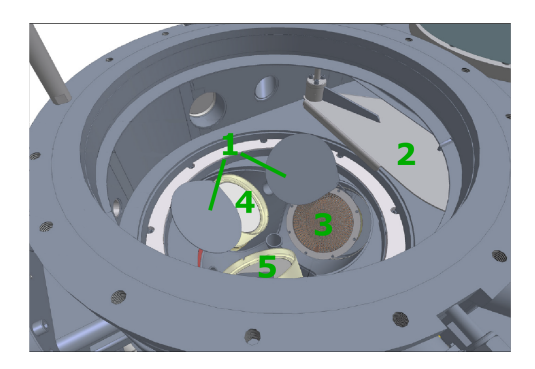


Figure 3.3.: Principle design of the sputter chamber PC5 in the clustertool deposition system. 1: target shutter, 2: substrate shutter, 3: RF cathode with ZnO:Al target, 4: DC cathode, 5: DC/RF cathode with ITO target, 6: substrate holder, 7: heater. The picture is taken from the manual of the Clustertool deposition system.

the case of PECVD process chambers, the substrate is transferred into the chamber by the robot arm and positioned into the holder for the substrate carrier (6) which is located in the center of the chamber. During deposition, the substrate can be rotated to improve the homogeneity of the deposited layers. In this case, the substrate is heated by a graphite heater (7), which is positioned 7 cm above the substrate. Likewise, the actual substrate temperature was related to the set heater temperature by calibration measurements with the temperature data logger SL55T from Signatrol Ltd. The indicated temperatures in this work are thus also nominal substrate temperatures. The heating of the substrate upon particle bombardment of the sputtering process have been found to be small within 10 °C for the power values used in this work when the deposition is started at room temperature and is thus neglected.

Three cathodes with a diameter of 96 mm are placed at the bottom of the sputtering chamber, each tilted by 45° to the substrate normal, as depicted in Fig. 3.3. Consequently, the deposition occurs in face down configuration as well. The target positions used in this work are cathode 3 and 5, where a ZnO:Al₂O₃ (99/1 wt.%) and a In₂O₃:SnO₂ (95/5 wt.%) target is placed, respectively. Both targets are powered by an RF generator, while an additional DC generator is connected to the ITO target on cathode 5. The targets are each covered with a shutter (1) if not in use to protect them against contamination resulting from other sputter processes. A pre-sputtering process is carried out for 10 minutes prior to each deposition with the substrate shutter (2) closed to ensure a contamination free deposition. Sputtering gases connected to the chamber are argon as well as oxygen (1% diluted in argon).

3.1.3. Deposition on Flexible Substrates

Due to the face down deposition configuration, the flexible $10 \times 10 \text{ cm}^2$ substrate needs to be carried in a special holder in order to avoid dropping of the substrate into the chamber. Furthermore, the electrode distance in the PECVD reactor is adjusted by the heater pushing the substrate down towards the powered electrode, implying that the holder needs to exhibit a certain stability. One possibility is the use of a metallic mask, on which the substrate is positioned and fixed with a metallic backing plate. However, supportive grids of the mask would always reduce the area available for deposition and may also influence the plasma conditions at the substrate surface. Another solution was developed in a preceding project and is shown in Fig. 3.4. The holder consists of a twopiece metal frame; the flexible substrate is inserted into the first frame (indicated A in Fig. 3.4) and is fixed when the second metal frame (B) is placed on top. The second metal frame is secured by four set screws indicated by red arrows. Besides the uninterrupted deposition area, this holder has the additional advantage that also parts of the layer and solar cell characterization can be performed while the flexible substrate is fixed in the holder. This prevents curling up of the sample after deposition, which arises due to the residual stress resulting from different thermal expansion coefficients of the deposited layers and the polymer substrate.

A few points need to be considered regarding the deposition process of silicon and TCO layers using this substrate holder. First, the electrode distance in the PECVD chambers is set by the heater position. The thickness of the metal frame is 5 mm, thus

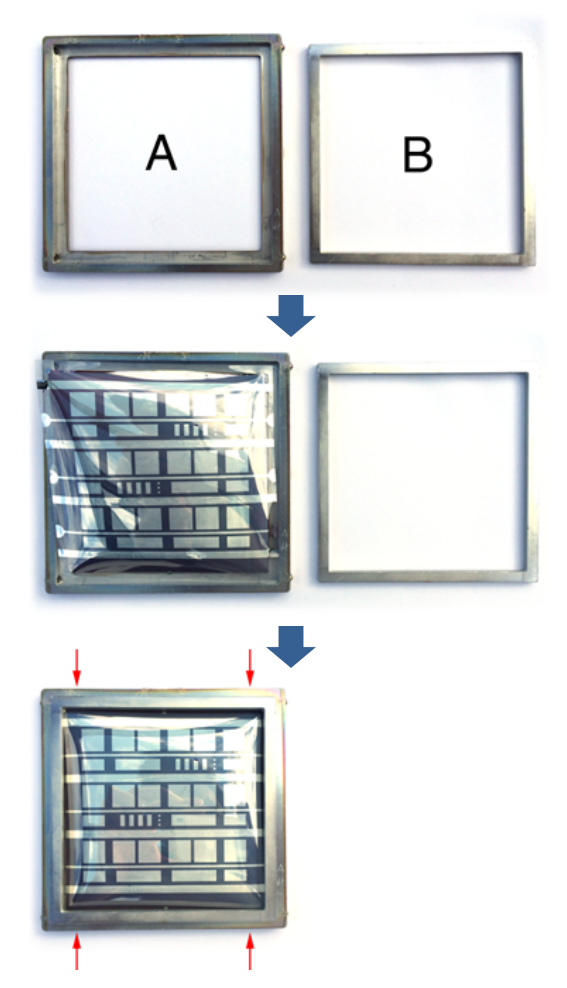


Figure 3.4.: Photographs of the substrate holder used in this work for the deposition and characterization of layers and solar cells on flexible substrates. A: supporting metal frame in which the substrate is placed, B: fixing metal frame. Frame B is fixed by four set screws indicated by red arrows.

significantly larger as a typical glass substrates (around 1 mm). Considering that the flexible substrate is not positioned at the bottom of the holder but slightly closer to the center, the electrode distance was estimated to be around 2 mm less than set by the heater. In order to have approximately similar deposition parameters for glass and flexible substrates, the electrode distance thus needs to be set 2 mm larger when the flexible substrate holder is used. Another significant difference is the temperature transfer to the substrate. In case of glass substrates, the heater in the PECVD chamber is directly in contact with the substrate allowing an appropriate heat transfer by radiation as well as conduction. In case of the flexible substrate holder, the heater is only in contact with the metal frame, diminishing heat conduction to the substrate. Accordingly, the substrate temperature of the polymer substrate is expected to be lower. On the other hand, a significant portion of the heat transfer occurs via convection of the process gases which should be similar for both glass and polymer substrates. Apart from that, a difference in emissivity for the two types of substrates may also influence the actual substrate temperature. The accurate temperature difference between glass and PET substrate could not be determined within the scope of this work and a possible difference needs to be considered when results for layers and solar cells on PET substrates are discussed. In case of the sputtering process, the heat transfer occurs mainly by radiation, meaning that a possible difference would primarily arise due to varying emissivities of the substrates.

3.2. Deposition Processes for Layers and Solar Cells

3.2.1. Substrates

Several types of substrates were used during the preparation of this work. Commercially available SnO₂:F covered glass substrates exhibiting a pyramidal surface structure type U and VU from Asahi Glass Co., Ltd. were used for a-Si:H single junction and a-Si:H/µc-Si:H tandem solar cell deposition, respectively. These are named Asahi-U and Asahi-VU in the following. Alternatively, Corning Eagle XG glass substrates covered with ZnO:Al layers were used. In the case of μ c-Si:H single junction solar cells, in-house optimized ZnO:Al deposited at 300 °C on Corning Eagle XG glass substrates in an inline sputtering system were used [118]. These ZnO:Al layers were texture-etched for 40s in 0.5 % HCl solution before deposition of the silicon layers. For selected a-Si:H solar cells, ZnO:Al layers deposited at lower substrate temperatures were used as TCO. Corning Eagle XG glass substrates with a thickness of 1.1 mm were also used for the deposition and characterization of individual TCO and silicon layers as well as solar cells. In some cases the glass was coated with a 10 nm layer of electron beam evaporated SiO₂ to improve the adhesion of layers. In addition, individual silicon layers were deposited on doubleside polished Czochralski (CZ) grown silicon wafers for the characterization by infrared spectroscopy.

In the case of deposition of TCO as well as silicon layers and solar cells on flexible substrates, heat stabilized polyethylene terephthalate (PET) film Melinex[®] ST504 with a

thickness of 125 μ m from DuPont Teijin Films was used. The film has an upper processing temperature of 150 °C [163]. PET films covered with a thin (20 nm) layer of zinc tin oxide (ZnSnO_x) as barrier layer were provided by Fraunhofer-Institut für Elektronenstrahl- und Plasmatechnik FEP. After deposition of the barrier layer, the films have been sent between clean paper sheets to protect them from contamination and dust. Alternatively, an inhouse developed silicon oxynitride (SiO_xN_y) layer with a thickness of 70 nm deposited by sputtering was used as barrier layer [183]. No further cleaning steps were conducted on the substrates before loading into the deposition system.

3.2.2. Deposition of Transparent Conductive Oxides

Besides Asahi-U and VU substrates, ZnO:Al is the most used TCO in this work. For the deposition of ZnO:Al layers, a ZnO:Al₂O₃ (99/1 wt.%) target is used. The substrate temperature $T_{\rm s}$ was varied between room temperature and 320 °C and the substrate was rotating with 5 rpm during the deposition. Argon was used as process gas with a flow of 30 sccm and the deposition pressure was 1.3 or 4.7 μ bar. The powered electrode was operated in RF mode with a power of 100 W. Prior to each deposition, the substrate is loaded into the sputter chamber and kept for at least 1 hour under vacuum for preheating, and removal of moisture from the substrate to assure a base pressure of around 10^{-7} mbar. Afterwards, a 10 minutes pre-sputtering process is conducted, as described in Section 3.1.2.

3.2.3. Light Management

In order to achieve appropriate incoupling and trapping of the light in the solar cell, two light management approaches were investigated during this work. The experimental procedures to achieve the textured interfaces are described in the following.

Etching of ZnO:Al A relatively simple light management approach but which is limited to only zinc oxide material is by a wet-chemical etching treatment. Details about chemical texturing can be found elsewhere [20]. In this work, etching was performed by dipping the ZnO:Al covered substrate in $0.5\,\%$ diluted solution of hydrochloric acid (HCl). The etching time was varied between $10\,\mathrm{s}$ and $40\,\mathrm{s}$.

Nanoimprint Lithography The preparation of light management textures by ultra violet nanoimprint lithography (UV NIL) is a two step process, as presented in Fig. 3.5.

First, the inverse of an arbitrary surface texture ("master") is transferred into a soft polymer mold via hot embossing (a). For this purpose, a UV-transparent polymer (polyolefin plastomer, POP) is heated up above its glass transition temperature to 90 °C and pressed into the master texture. Due to the reduced viscosity at high temperature, the polymer flows into the texture and after cooling down the inverse master texture is

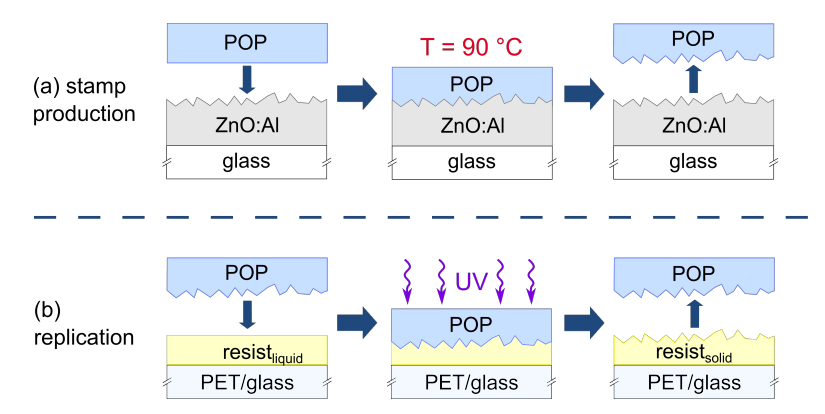


Figure 3.5.: Process flow for the replication of light trapping textures. (a) Polyolefin plastomer (POP) stamp production from a high temperature ZnO:Al master texture, (b) replication of the master texture on the glass/PET substrate via the resist layer.

sustained in the POP. Afterwards the POP stamp and master texture are mechanically separated.

Second, the original texture is replicated into a photo resist layer on the glass or PET substrate (b). For this, the UV sensitive photo resist layer Ormocorp from the *Microresist Technology GmbH* is spin-coated on the substrate (3000 rpm). This photo resist is explicitly designed for optoelectronic devices which require high transparencies [136]. The previously produced and UV-transparent POP stamp is pressed into the liquid photo resist which is then hardened by UV illumination. Thus, the original master texture is sustained after removal of the stamp. After UV exposure, the photo resist has a refractive index similar to glass.

For the nanoimprint process, the commercially available system Nanonex NX2000 was used and further details about the process and replication quality can be found in the literature [134, 135, 184]. The maximum substrate diameter is 10 cm. In the case of PET substrates, a short cleaning step in acetone and isopropanol is conducted in advance.

3.2.4. Deposition of Thin-Film Silicon Layers and Solar Cells

Prior to each deposition, the substrate is loaded to the process chamber and preheated for at least 1 hour to remove moisture from the substrate and assure a base pressure of around 10^{-8} mbar. Afterwards, additional 10 minutes pre-heating process in the presence of process gases is conducted to ensure an appropriate substrate temperature, as described in Section 3.1.1. An important point regarding the PET substrates here is its hygroscopic nature which leads to the absorption of moisture from the ambient atmosphere [185]. For this reason, the preheating procedure in vacuum needs to be significantly longer in the case of PET substrates, in order to achieve base pressures in the range of 10^{-8} mbar.

Preheating times took up to several hours and was usually conducted over night before the deposition was started.

For the deposition of thin-film silicon layers, silane (SiH₄) and hydrogen (H₂) gases were used as process gases. In case of p-type and n-type layers, trimethylborane (B(CH₃)₃ TMB, 2.54% diluted in helium) and phosphine (PH₃, 5% diluted in silane) are added as doping gases to PC1 and PC3, respectively. In the case of amorphous silicon p-type layers, methane (CH₄) can be added as alloying gas to the p-type layer deposition to widen the band gap of the material. When the gas composition is varied in order to change the material properties, results are given as a function of TMB concentration $c_{\rm TMB}$, phosphine concentration $c_{\rm PH3}$, CH₄ concentration $c_{\rm CH4}$ as well as silane concentration SC, which are defined as follows:

$$c_{\text{TMB}} = \frac{[\text{TMB}] \times 0.0254}{[\text{SiH}_4]}$$

$$c_{\text{PH3}} = \frac{[\text{PH3}] \times 0.05}{[\text{SiH}_4]}$$

$$c_{\text{CH4}} = \frac{[\text{CH}_4]}{[\text{CH}_4] + [\text{SiH}_4]}$$

$$SC = \frac{[\text{SiH}_4]}{[\text{SiH}_4] + [\text{H}_2]}$$

The flows of respective gases are indicated in brackets and are given as absolute gas flows including the dilution gas in the case of TMB and PH₃. The deposition parameters including the gas flows for the various types of layers presented in this work are listed in Table 3.1.

After deposition of the silicon layers, the gas supply and generator were switched off and the chamber was purged with argon for three minutes to ensure that no residual deposition gases remain. After transfer to one of the loading chambers, the sample was cooled down for at least 30 minutes before exposition to ambient air and further processing.

Finally, the back contact needed to be prepared. In most cases, a $700\,\mathrm{nm}$ silver (Ag) layer was thermally evaporated on the substrate through a shadow mask, which simultaneously defines the individual active solar cell area of $0.1..1.0\,\mathrm{cm}^2$. The front contact is connected by scribing through the silicon layer and subsequent evaporation of silver stripes. The typical cell design forming 36 solar cells and front contact stripes on a $10\times10\,\mathrm{cm}^2$ glass substrate is shown in Fig. 3.6. In order to reduce plasmonic absorption losses at the silicon/silver interface, in some cases a 70 nm layer of ZnO:Al (1% dopant concentration) was sputtered on the silicon layer before silver evaporation [107]. After silver deposition, the sample was dipped in $0.25\,\%$ hydrochloric acid solution to remove

 $^{^1{\}rm Some}$ intrinsic a-Si:H layers with ${\rm CH_4}$ gas added during deposition were prepared for comparison purposes in Section 4.1.1

Table 3.1.: Parameters for the deposition of silicon layers in this work: power P, excitation frequency f, electrode distance $d_{\rm el}$, deposition pressure p, substrate temperature $T_{\rm s}$, as well as process gas flows. Dopant gas flow corresponds to TMB and PH₃ in the case of p-type and n-type layers, respectively. The flows are given as absolute values including dilution gases (2.54 % TMB in helium and 5 % PH₃ diluted in silane, respectively). A more detailed sample list of deposition parameters can be found in the appendix.

| Layer | P [W] | f [MHz] | $d_{\rm el}$ [mm] | p [mbar] | <i>T</i> _s [°C] | SiH ₄ flow [sccm] | H_2 flow [sccm] | CH ₄ flow [sccm] | dopant flow [sccm] |
|-------------------------------------|----------|----------------|-------------------|------------|----------------------------|------------------------------------|-------------------|-----------------------------------|--------------------------|
| p-type | | | | | | | | | |
| a-Si(C):H | 4 | 13.56 | 12 | 1.6 | 120 - 180 | 9 | 90 | 0-5 | 5-25 |
| $\mu \text{c-Si:H}$ | 30 | 81.36 | 22 | 1.0 | 120,180 | 1.5 | 200 | _ | 1.2 |
| intrinsic a-Si:H μ c-Si:H | 4 20 | 13.56 81.36 | 12 11 | 1.6 1.0 | 120-180 120 | 5-30 4-11 | 90-115 200-207 | 0-10 ¹ | _ _ |
| n-type a-Si:H μ c-Si:H | 4 10 | 13.56 81.36 | 12 10 | 1.6 1.0 | 120 120 | 5-50 2.7 | 100-140 200 | - - | 2-50 1.2 |

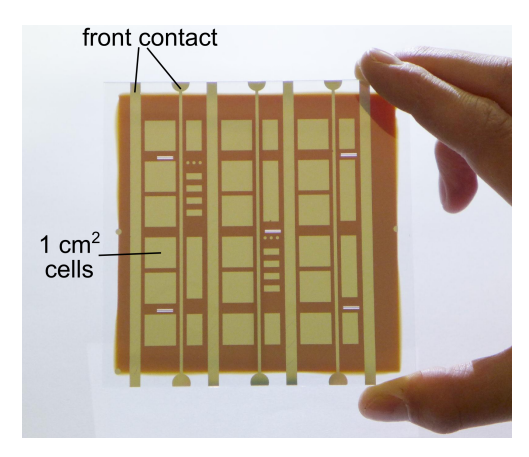


Figure 3.6.: Picture of a typical solar cell design deposited on a $10 \times 10 \,\mathrm{cm}^2$ substrate. The silver back contact determines the cell areas of the 36 solar cells. The front contact is connected to the silver stripes through scratches in the deposited silicon layers.

the ZnO:Al layer where it is not covered by Ag. Apart from the preheating process due to the outgasing of PET sustrates and the adjustment in heater distance discussed in Section 3.1.3, procedures are similar for glass and PET substrates.

In Fig. 3.7, the various types of solar cells investigated in this work are presented, that is (a) amorphous silicon (a-Si:H) single junction solar cell, (b) microcrystalline (μ c-Si:H) single junction solar cell as well as (c) amorphous/microcrystalline silicon (a-Si:H/ μ c-Si:H) tandem solar cell. All devices were deposited in p-i-n or p-i-n-p-i-n depo-

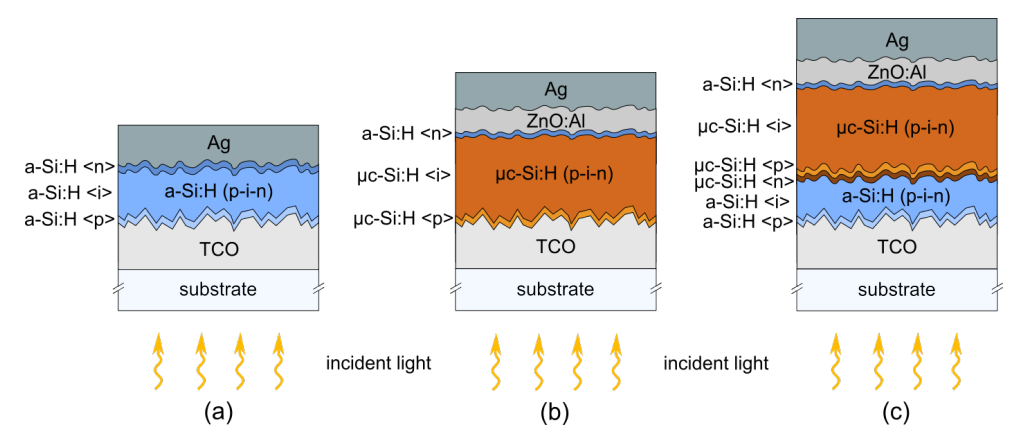


Figure 3.7.: Schematic drawing of the layer stacks used for (a) a-Si:H single junction, (b) μ c-Si:H single junction and (c) a-Si:H/ μ c-Si:H tandem solar cells.

sition sequence. In case of microcrystalline intrinsic absorber layers, a highly microcrystalline p-type layer was used to improve nucleation for the development of microcrystals in the intrinsic absorber layer. The application of an amorphous n-type layer on top of the microcrystalline intrinsic absorber layer minimizes the effect of current collection from outside the defined solar cell area, which may falsify the measured current density during J-V measurements (see Section 3.4). The tunnel recombination junction between the amorphous top and microcrystalline bottom cell in case of the tandem device was realized by a contact of μ c-Si:H n-type to μ c-Si:H p-type layer, which has been shown to ensure a low electrical resistance [186].

3.2.5. Annealing

In the case of standard deposition temperatures of 180-200 °C, a short annealing step of 30 minutes at 160 °C in ambient air is typically applied. Though exact reasons are not precisely known, this procedure slightly improves the solar cell efficiency and helps to avoid uncontrollable degradation by the Staebler-Wronski-Effect during solar cell manufacturing. During this work, a substantial increase in the photovoltaic performance of the solar cells deposited at low temperature upon post-deposition annealing was observed. In Chapter 5, results will be shown and intensively discussed. Unless stated differently, the

annealing is carried out in ambient air at an annealing temperature $T_{\rm ann}$ of 120 °C, similar to the substrate temperature during deposition.

3.3. Characterization of Individual Layers

Before implemented in solar cells, the material properties of individual layers were investigated and optimized. The utilized characterization methods for both TCO and silicon layers are presented in this section. In some cases, adjustments in the measurement procedure or sample preparation are necessary for the application on PET substrates. Unless stated differently, the method can be applied just the same as on glass substrates.

3.3.1. Layer Thickness

Knowledge of the thickness of the deposited layers is important to evaluate the deposition rate as well as for the comparability of various films. Many experiments and evaluations require the knowledge of the actual layer thickness. The film thickness was measured by a DEKTAK 6M profilometer from Vecco company. In the case of silicon layers, a sharp step was produced by either a small dot of silver paste on the substrate before deposition that could be scratched away afterwards, or by laser ablation. In the case of ZnO:Al layers, a sharp step was produced by locally removing the ZnO:Al layer with 2% diluted HCl solution. By drawing a circle with hydrophobic ink, the drop of solution could be isolated within this circle and the ink is subsequently removed by isopropanol. For each sample, this was carried out at several locations on the substrate to gain additional statistics and information about the homogeneity of the film over the substrate area. The thickness was determined by averaging these values and the inaccuracy of the film thickness was typically about 10% over a substrate area of $10 \times 10 \, \mathrm{cm}^2$.

The profilometer measurement as described above does not work in the case of flexible substrates due to possible bending of the substrate and sinking of the probe tip into the PET substrate. Another possibility is scanning of the step by atomic force microscopy (AFM). However, the reliability of this method could not be verified so far.

In this work, the layer thickness d on flexible substrates was only determined in the case of smooth films, where d may be evaluated from interference fringes in transmission and reflection curves [187]:

$$d = \frac{\lambda_1 \lambda_2}{2n\left(\lambda_2 - \lambda_1\right)} \tag{3.1}$$

where $\lambda_{1,2}$ are the wavelengths of two neighboring extremes (maxima or minima) and n the refractive index of the film which is assumed to be constant in the wavelength range $\lambda_1 < \lambda < \lambda_2$.

3.3.2. Characterization of TCO Layers

After deposition on glass and/or PET substrates, the TCO layers were characterized regarding their electrical and optical properties. Images were taken by atomic force microscopy and scanning electron microscopy to get information about the surface texture, which is an important aspect when light management schemes are investigated.

Electrical Characterization

A relatively simple and fast approach to evaluate the sheet resistance of a conducting layer is by four point probe measurements. Another technique, which additionally gives information about the density and mobility of charge carriers in the films but needs sample preparation, is the Hall effect measurement. In the case of PET substrates, it is important for both measurements that a glass substrate is used as a hard basis under the PET film to ensure proper contact between layer and probe.

Four Point Probe The probe consist of four equidistant lined-up contact pins which are in contact with the TCO layer. A current I is applied to the outer pins, while the resulting voltage V is measured between the two inner pins. Assuming that contact resistances can be neglected, the corresponding sheet resistance R_{\square} can be calculated by

$$R_{\square} = \frac{\pi}{\ln(2)} \times \frac{V}{I} \tag{3.2}$$

where $\pi/\ln(2)$ is a calibration factor determined by the sample geometry, assuming an infinite layer whose thickness is small compared to the probed distance. A detailed description of this method can be found in [188].

Hall effect Measurement Hall effect measurements allow for the evaluation of the density N and mobility μ of charge carriers in the TCO layer. In this technique, four contact pins are placed to the edges of a $11 \times 11 \,\mathrm{mm^2}$ sized sample. A current I is applied to two opposing contacts and due to a magnetic field B, applied normal to the substrate surface, the Lorentz force will affect the moving charge carriers in the TCO film having a known thickness d. A counteracting electrical field induces a voltage $V_{\rm H}$ between the contacts perpendicular to the current-applying pins which is proportional to the charge carrier density N:

$$V_{\rm H} = \frac{IB}{qdN} \tag{3.3}$$

By additionally measuring the sheet resistance R_{\square} , the resistivity ρ and thus carrier mobility μ can be extracted from the measurement through the following equations:

$$\rho = R_{\square} \times d \tag{3.4}$$

$$\mu = \frac{1}{Nq\rho} \tag{3.5}$$

where q is the elementary charge.

In this work, a commercially available Hall Effect Measurement System RH2030 from the company *PhysTech GmbH* applying the van-der-Pauw method [189] was used. This method has the advantage of not being affected by the sample geometry. However, in order to minimize the measurement error, the contact pins should preferably be placed in the edges of the sample. Before each measurement, the ohmic contact between contact pins and sample was verified. The measurements were performed at room temperature in ambient air.

Optical Characterization

Transmittance, Reflectance and Haze For the optical characterization of the TCO layers, the dual beam spectrophotometer LAMBDA 950 from *PerkinElmer* was used. It covers a wavelength range from 250 nm (UV) to 2500 nm (NIR). Light is emitted from a deuterium lamp (UV) and a tungsten halogen lamp (visible VIS and NIR) and a certain wavelength is selected by a double monochromator. Using mirrors, one beam is lead past the sample and serves as reference while the other is focused on the substrate side of the sample. This helps compensating for fluctuations in the light beam intensity.

For measuring the total transmittance T, the sample is positioned directly in front of an integrating sphere that ensures that independent of the angle all transmitted light is collected by one of the detectors. The detectors are located at the bottom of the integrating sphere and depending on the wavelength range, either a photomultiplier (UV/VIS) or a cooled PbS photodetector is used. For the measurement of total reflectance R, the sample is positioned in the back of the integrating sphere, where an opening opposite the entry opening can be unclenched. An absorber is placed behind the sample ensuring that only light reflected at the substrate side of the sample enters the integrating sphere and thus the detector. Both T and R are normalized to the total irradiation.

In order to characterize the light scattering properties of textured surfaces, the diffuse transmittance $T_{\rm diff}$ can be measured. In that case, the sample is positioned in front of the integrating sphere, similar to the case of T measurement, but this time the outlet opening opposite the sample is kept open. Thus only diffusely transmitted light (scattering angle $>5^{\circ}$ to the substrate normal) is detected. The haze in transmission $H_{\rm T}$ serves as a measure for the light scattering behavior of the layer and is defined by the ratio of diffusely transmitted of totally transmitted light:

$$H_{\rm T} = \frac{T_{\rm diff}}{T} \tag{3.6}$$

A detailed description of the spectrophotometer and measurement technique can be found in [190].

In this work, only the wavelength range between 300 nm and 1100 nm, relevant for solar cells, was investigated. Regarding the measurement on PET substrates, additional attention needs to be paid to the adjustment of the sample. Bending or tilting can be avoided by fixing the substrate with adhesive tape to the sample holder.

Angle Resolved Scattering (ARS) Haze measurement was introduced above to characterize the light scattering properties of a TCO layer. However, it only gives the percentage of scattered light. In order to gain more detailed information about the angles light is scattered into, angle resolved scattering (ARS) measurements are performed. The inhouse developed setup consist of a laser beam with a wavelength of 550 nm that is split into two beams after passing through a polarization filter, chopper and lense. One beam serves as a reference to compensate for fluctuations in the laser beam intensity and the other is focused on the substrate side of the sample. In case of textured TCO surfaces, the laser beam is scattered at the TCO side of the sample. A schematic drawing of the detection setup is shown in Fig. 3.8. While the light is scattered in all directions (dashed

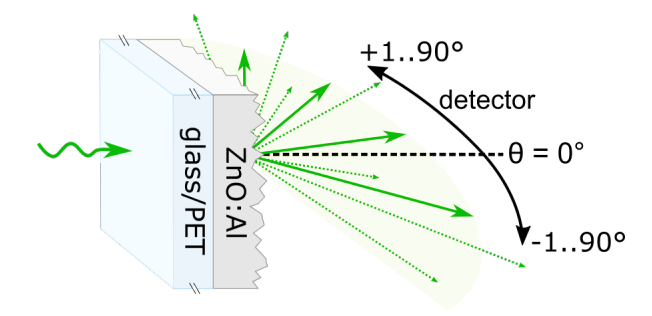


Figure 3.8.: Schematic drawing of detection principle in the angle resolved scattering (ARS) measurement setup.

arrows), the movable detector only detects the light in one plane over a scattering angle θ from -90° to +90° to the substrate normal (solid arrows). Assuming isotropic scattering (which is valid for the random textures investigated in this work), the angular intensity distribution AID is calculated by integration of the scattered light intensity over the θ -dependent scattering cone multiplied by an area correction factor. The error bar of the AID values is around 6% [183]. The detector consists of a silicon photodiode, measures with a resolution of 1° and any measured detector signal is normalized to the base signal without sample, recorded at the beginning of the measurement. A detailed description of the setup and measurement technique can be found in [183].

An important source of error in this measurement is the adjustment of the sample to the laser beam. In order to ensure that the light is scattered in the plane of the laser beam, in which also the detector operates, the sample needs to be positioned accurately perpendicular to the laser beam. A tilting of the sample would lead to an underestimation of the AID. Bending in the case of PET substrates results in a similar effect. Therefore the PET substrate is fixed between to aperture plates each with an opening of $15\times15\,\mathrm{mm}^2$. However, a slight tilting or bending of the substrate in this aperture can not be completely ruled out.

Surface Morphology

The surface of textured TCO layers can be evaluated by various techniques. While Scanning Electron Microscopy (SEM) produces an image of the sample by detecting emitted electrons from the surface material, Atomic Force Microscopy (AFM) analyzes the surface by interaction of a small tip with the sample surface. The latter method provides quantitative information on morphological properties of the surface such as distribution of heights or angles, in contrast to SEM. It is however more time consuming and the scan size is limited to a few tens of micrometers.

Scanning Electron Microscopy (SEM) During SEM measurements, a (primary) electron beam is focused on the sample. The electrons interact with the atoms in the sample and among other reactions, back scattering of secondary electrons (SE) occurs which can be detected by an appropriate detector. SE have a small kinetic energy and therefore only those that have their origin atom near the surface can leave the sample and are detected. The amount of detected SE determines the brightness value and thus by scanning the sample a visual 2D image of the sample surface is obtained. It should be noted here that the number of SE also depends on the investigated material which may affect the SEM image if material contrasts are existent in the sample. In order to avoid influences from the environment, the measurements are performed under vacuum.

In this work, the field emission SEM Gemini from the LEO company was used. The images were taken by applying an acceleration voltage between 5 and $20\,\mathrm{kV}$ and the sample was tilted by 60° to the electron beam to enhance the number of SE leaving the surface. The maximum resolution is dependent on the investigated material and is between 1 and $10\,\mathrm{nm}$.

Atomic Force Microscopy (AFM) During AFM measurements, the sample surface is scanned in x- and y-direction while detecting the surface height with a measurement tip. The small silicon tip has a radius of 10 nm and is attached to a cantilever. In this work the measurement was performed in the non-contact mode, in which the tip is brought close to the sample surface without actually touching it. The tip oscillates close to its resonance frequency and when the tip approaches the sample surface van-der-Waals forces reduce the oscillation amplitude. While scanning, a piezo element adjusts the tip-to-sample distance such that the oscillation amplitude stays constant. The position of the cantilever in z-axis (height) is detected by the reflection of a laser beam from the cantilever to a position-sensitive photodiode. Thus a three dimensional surface image of the sample is obtained.

The used system was the Nanostation 300 from Surface Imaging Systems GmbH (SIS) and the measurement was performed in ambient air. The probed area was $10\times10\,\mu\text{m}^2$ including 512×512 data points. Typical imaging errors result e.g. from deep craters with small lateral size, in which the tip can not penetrate due to its finite diameter. In that case, the diameter of the tip will be mapped. Another issue is also the

presence of very steep edges. The piezo elements exhibit a certain inertia limiting the speed of height adjustment, which may result in an incorrect illustration of the surface. In the case of PET substrates, electrostatic charges significantly influence the measurement and the resulting image of the surface topography. Therefore an Ionizing Air Blower AEROSTAT® PC from Simco-Ion was directed at the sample during the measurement. Even with applied deionization, measurement artifacts occur regularly for ZnO:Al layers on PET substrate. Accordingly, results from AFM measurements on PET substrates should be treated with care.

The resulting AFM images have been evaluated using the software Gwyddion [191]. After a plane correction, which compensates for tilting of the substrate or drifts in the piezo elements, the normalized surface area A_{norm} was evaluated. This was done by evaluation of the total surface area and normalization to the reference area of a smooth substrate, which is assumed to be $100 \,\mu\text{m}^2$. An overview of AFM applications to analyze the surface topography of solar cells is given by [20].

3.3.3. Characterization of Silicon Layers

For the characterization of silicon layers, individual films were deposited on Corning glass substrates and silicon wafers. The layer thickness was between 180 nm and 500 nm and was kept similar within a given series of samples.

Structural Properties

Infrared Scpectroscopy Infrared (IR) spectroscopy is a tool to detect IR active bonding configurations and molecules in a material. Under irradiation with infrared light, absorption at characteristic wavelengths can be detected resulting from these oscillations. The absorption intensity is proportional to the occurrence of the chemical bond and can therefore be quantitatively evaluated. Further details about the method can be found in [192].

In this work, this technique was used to detect hydrogen as well as carbon bonded in the amorphous silicon network. The absorption spectrum is evaluated from transmittance T measurements as a function of wave number ν by knowledge of the layer thickness d:

$$\alpha_{\rm IR}(\nu) = -\frac{1}{d} \ln \left(T(\nu) \right) \tag{3.7}$$

This method was extensively applied to p-type a-Si:H and a-SiC:H layers in this work, and in Fig. 3.9 a typical absorption spectrum of a p-type a-SiC:H sample is shown. The corresponding bonds and vibrational modes are listed in Table 3.2.

The strongest absorption peaks result from vibrations of Si-H bonds: the Si-H and Si-H₂ wagging and/or rocking mode at $620\text{-}640\,\mathrm{cm}^{-1}$, the Si-H stretching mode in compact material $(2000\,\mathrm{cm}^{-1})$ and the stretching mode of dihydride-bonds Si-H₂ [194] or Si-H located at internal surfaces or voids [196] at $2080\text{-}2100\,\mathrm{cm}^{-1}$. Additionally, the Si-H

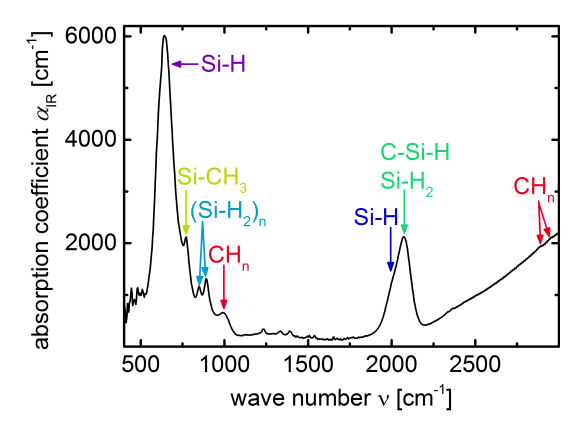


Figure 3.9.: Typical infrared absorption spectrum $\alpha_{\rm IR}(\nu)$ of a p-type a-SiC:H sample. The various types of oscillating bonds and their frequencies are indicated and also listed in Table 3.2.

Table 3.2.: Peak positions of the absorption bands for bonds present in a typical p-type a-SiC:H layer along with the type of vibration according to [193–197], with CH_n corresponding to a carbon atom attached to 1, 2 or 3 hydrogen atoms.

| wave number $\nu \ [\mathrm{cm}^{-1}]$ | bond | vibration mode |
|--|-------------------------------------|------------------|
| 620-640 | $Si-H, Si-H_2$ | wagging, rocking |
| 780, 800 | $\mathrm{Si}\text{-}\mathrm{CH}_3$ | wagging, rocking |
| 845, 890 | $(Si-H_2)_n$ | bending |
| 1000 | CH_{n} | wagging, rocking |
| 2000 | Si-H | stretching |
| 2080-2100 | $Si-H_2$, $Si-H_{void}$, $C-Si-H$ | stretching |
| 2880, 2960 | CH_{n} | stretching |

stretching mode at $2000\,\mathrm{cm^{-1}}$ may be shifted to the $2080\text{-}2100\,\mathrm{cm^{-1}}$ range in the presence of carbon attached to the Si-H bond [195]. Further absorption peaks result from vibrations of dihydride bonds (Si-H₂)_n (845 and 890 cm⁻¹) [194], Si-CH₃ (780 and $800\,\mathrm{cm^{-1}}$), as well as CH_n at $1000\,\mathrm{cm^{-1}}$ and $2880/2960\,\mathrm{cm^{-1}}$. An overview of other oscillation modes present in amorphous silicon and -alloys can be found in [192].

The integrated absorption peak intensity I_{ν} of a certain bond vibration located at ν serves as a measure for the number of bonds present in the sample and is calculated by integration over the absorption peak after subtraction of a straight baseline:

$$I_{\nu} = \int \frac{\alpha(\nu)}{\nu} d\nu = \frac{1}{\nu_0} \int \alpha(\nu) d\nu \tag{3.8}$$

For simplicity, it is assumed that the small variation in wave number can be neglected, and the integrated area is divided by the wave number of the peak maximum ν_0 . In the case of the two overlapping Si-H stretching modes located at 2000 and 2080-2100 cm⁻¹,

two Gaussian peaks are fitted to the data to determine the integrated area for each of the two peaks.

A quantitative analysis of hydrogen and carbon content can be conducted by application of an appropriate proportionality factor, which is called absorption strength. In this work, this was done for the hydrogen content $c_{\rm H}$, evaluated from the absorption peak at 2000-2100 cm⁻¹. According to Brodsky et al. [193], the number of bonded hydrogen atoms $N_{\rm H}$ in the sample can be calculated by multiplying the integrated absorption peak intensity I_{2000} with the absorption strength k_{2000} of the oscillation mode:

$$N_{\rm H} = k_{2000} \cdot I_{2000} \tag{3.9}$$

In literature, typical values of k_{2000} are shown to be between $0.9 - 3.3 \times 10^{20}$ cm⁻² [198–200], and were in this work determined for each sample by an iterative method suggested by Beyer and Ghazala [201].

Maley and Szafranek [202] reported that a film thickness lower than $1 \mu m$ leads to an overestimation of the hydrogen content as the difference in refractive indexes at the a-Si:H/c-Si interface leads to multiple reflections. Thus a correction for thin films has to be taken into account [202]. The hydrogen content is then determined using Eq. 3.10.

$$c_{\rm H} = \frac{N_{\rm H}}{N_{\rm H} + N_{\rm Si}} \tag{3.10}$$

in which N_{Si} is taken to be a fixed value of $5.0 \times 10^{22} \, \mathrm{cm}^{-3}$ [198]. Please note that the evaluation from IR measurements is only an estimate for the hydrogen content in the film as only bonded hydrogen is considered.

Information about the microstructure can also be obtained from IR measurement in the case that no peaks related to carbon are detected in IR spectra of the sample (intrinsic and n-type a-Si:H films). Under these conditions, the presence of the $2090\,\mathrm{cm^{-1}}$ mode indicates a void-rich material [195, 196]. The more porous a sample, the higher the intensity of the $2090\,\mathrm{cm^{-1}}$ mode. A microstructure factor R_{m} is therefore introduced as a quantitative measure for material quality:

$$R_{\rm m} = \frac{I_{2090}}{I_{2000} + I_{2090}} \tag{3.11}$$

where $I_{2000/2090}$ is the integrated absorption peak intensity at $2000 \,\mathrm{cm^{-1}}$ and $2090 \,\mathrm{cm^{-1}}$, respectively. As material with good quality is usually compact, it is desired to yield a low R_{m} value [203].

As normal infrared spectroscopy is a time consuming method because the intensity of infrared sources is very low, usually Fourier Transform Infrared Spectroscopy (FTIR) is applied. This method does not detect the transmission spectrally but from an interferogram that is taken within a few minutes. A more detailed description of the method can be found in [192].

The measurements were performed on silicon layers deposited on double-side polished CZ wafer pieces with a size of $15 \times 15 \,\mathrm{mm}^2$. One piece of the original wafer was

withhold and served as a reference sample. The measurements were performed with a Nicolet 5700 Fourier Transform Infrared spectrometer in the wave number range from 400 to 4000 cm⁻¹. Each spectrum was normalized to the reference measurement of the uncoated wafer to eliminate influences from the substrate, detector or infrared source. In order to avoid absorption by other compounds, for example by gaseous water in the air, the sample chamber was continuously purged with nitrogen. The Fourier transformation was done by OMNIC software on the measuring computer.

Raman Spectroscopy Raman spectroscopy offers the possibility to get information about the microstructure of a material. This method utilizes Raman scattering, that is the inelastic scattering of electromagnetic waves with molecules or atoms. Monochromatic light from a laser is focused on a sample and a certain fraction of this light interacts inelastically with the material by emission or annihilation of phonons. Accordingly, the spectrum of scattered photons contains information about the phonon spectrum in the solid and may be used for the investigation of the structural features of a given material. Raman spectroscopy is commonly applied to determine the crystalline volume fraction in mixed phase μ c-Si:H [204].

In a Raman spectrum, the intensity of scattered light is plotted as a function of the Raman shift resulting from the interaction with phonons. In Fig. 3.10, typical Raman spectra for amorphous and microcrystalline silicon layers are shown. The prominent peak

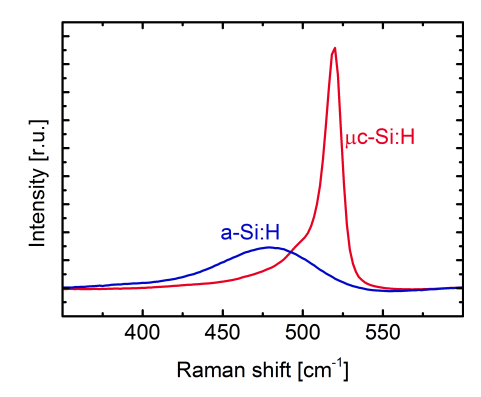


Figure 3.10.: Typical Raman spectra of an a-Si:H (blue line) and μ c-Si:H layer with a crystalline volume fraction of 83 % (red line).

located at $520\,\mathrm{cm^{-1}}$ can be attributed to the crystalline phase of the material, whereas the peak correlated with the amorphous phase is located around $480\,\mathrm{cm^{-1}}$ and broadened due to the lack of long range order. By subtraction of a scaled reference a-Si:H spectrum, the crystalline peak intensity can be evaluated and a semi-quantitative value for the crystalline volume fraction $I_{\rm crs}$ can be calculated by

$$I_{\rm crs} = \frac{I_{\rm c}}{I_{\rm c} + I_{\rm a}} \tag{3.12}$$

where $I_{\rm c}$ and $I_{\rm a}$ correspond to the integrated intensities attributed to the crystalline and amorphous silicon phase, respectively.

Additionally, information about the structural disorder in amorphous silicon layers can be obtained using Raman spectroscopy. For this purpose the transverse optical (TO) phonon mode located at $480 \,\mathrm{cm^{-1}}$ is evaluated in more detail. In literature, the position x_{TO} and width ω_{TO} of the TO peak are regarded as a measure for the short range order in a-Si:H material [205, 206]. The evaluation of x_{TO} from the Raman spectrum is illustrated in Fig. 3.11. First, the Raman spectrum is normalized to the maximum at $480 \,\mathrm{cm^{-1}}$

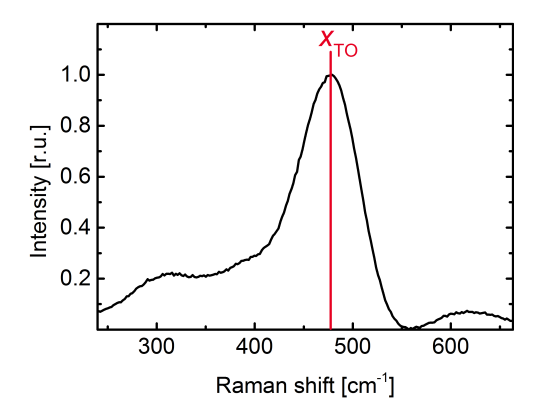


Figure 3.11.: Typical Raman spectrum of an intrinsic a-Si:H layer. A straight line that symmetrically divides the upper part of the peak determines the TO phonon position x_{TO} .

and the minimum at $560 \,\mathrm{cm^{-1}}$ (corresponding to 1 and 0, respectively). Towards small wavenumbers, the TO phonon peak is superimposed by the neighboring peak. Therefore, a straight line is drawn parallel to the y-axis and positioned in such way that the upper part of the TO peak is symmetrically divided. The position of the line determines x_{TO} . Further information about the evaluation of short and medium range order from Raman scattering measurements can be found in [207].

In this work, the measurements were performed with an inVia Raman microscope from *Renishaw*, that uses a green laser with a wavelength of 532 nm. The spectrometer was calibrated with a crystalline silicon wafer before each measurement.

Electrical Properties

Electrical Conductivity For the measurement of dark and photo conductivities, coplanar silver contacts were evaporated onto the silicon films on glass and/or PET substrates as illustrated in Fig. 3.12. Applying a voltage V induces a lateral current I between the contacts and thereby the conductivity σ can be determined from the geometric dimensions by the following equation.

$$\sigma = J \times \frac{1}{E} = \frac{I}{bd} \times \frac{h}{V} \tag{3.13}$$

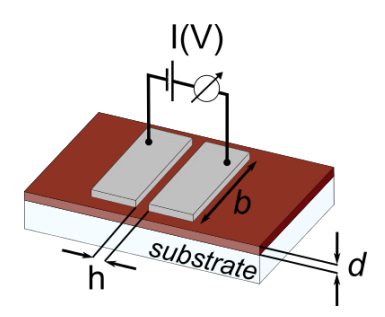


Figure 3.12.: Configuration of the samples prepared for conductivity measurements. The size of the samples was about $10 \times 15 \text{ mm}^2$. Conductivity values can be evaluated from the measured current I and the applied voltage V using the geometric dimensions: film thickness of the silicon layer d, distance between the contacts h and the length of the contacts b.

where J is the current density, E the electrical field between the contacts, h and b are the distance and length of the contacts and d the thickness of the deposited film.

In order to avoid a possible influence of adsorbed atmospheric species on the conductivity of the silicon films [208], the samples were annealed in vacuum at their deposition temperature (but maximum 160 °C) for 30 minutes and subsequently measured at room temperature in the vacuum. The samples had a size of $10\times15~\mathrm{mm}^2$ and the contacts had a geometry resulting in $h=1~\mathrm{mm}$ and $b=10~\mathrm{mm}$. The voltage was $100~\mathrm{V}$, applied by a 6517A Electrometer from Keithley, which simultaneously measured the current. The conductivity measurements took place in darkness (dark conductivity σ_{d}) as well as under illumination provided by a halogen lamp (σ_{ill}), from which the photo conductivity σ_{ph} is evaluated by

$$\sigma_{\rm ph} = \sigma_{\rm ill} - \sigma_{\rm d} \tag{3.14}$$

The halogen lamp had a light intensity calibrated with a c-Si diode to be effectively equal to Air-Mass (AM)1.5 illumination with respect to the photogenerated current. The photo response serves as a measure for the material quality of intrinsic absorber layers and is determined by the ratio of photo to dark conductivity $\sigma_{\rm ph}/\sigma_{\rm d}$. It should be noted that the conductivity is measured parallel to the surface, whereas the current transport in a solar cell occurs in the growth direction of the deposition.

Steady-State Photocarrier Grating Technique (SSPG) In amorphous silicon, electrons are majority carriers and the photo conductivity is mainly dominated by electron transport thus reflecting the mobility-lifetime product of electrons. In order to get access to the properties of holes as minority carriers, steady-state photocarrier grating technique (SSPG) was carried out. This method was first developed by Ritter, Zeldov and Weiser in 1986 [209] and serves as a complementary technique to the measurement of photo conductivity. The sample structure is similar to that used for conductivity measurements, i.e. with evaporated coplanar silver contacts on top of the sample. During the measurement, a He-Ne laser beam is split into two coherent light beams that both impinge the sample

in the probe area between the silver contacts. A certain angle is adjusted between the two laser beams resulting in an interference pattern that leads to a spatial sinusoidally modulated photogeneration rate of excess charge carriers in the silicon layer. This in turn leads to a so-called photo carrier grating with a modulation in the excess charge carrier densities. From measurement of the photocurrent at different grating periods and assuming ambipolar transport and charge neutrality, the ambipolar diffusion length $L_{\rm amb}$ can be evaluated [209]. The ambipolar diffusion length is dominated by minority carriers and correlates to the mobility-lifetime ($\mu\tau$)_h-product according to equation 3.15 [210]:

$$L_{\rm amb} = \sqrt{2\frac{q}{kT_0} \left(\mu\tau\right)_{\rm h}} \tag{3.15}$$

where q is the elementary charge, k the Boltzmann constant and T_0 the absolute temperature. The measurements were performed by M. Güneş at the Mugla Sitki Kocman University in Turkey and a detailed description of the measurement setup can be found in [211]. An extensive review on the basic theory, experimental setups and applications is given by Brüggemann [210].

Optical Absorption

In this work, two methods were used to determine absorption coefficients α of silicon films. For the evaluation of the band gap, Photothermal Deflection Spectroscopy (PDS) was performed. The other technique is the Constant Photocurrent Method (CPM), which is especially useful for detecting the sub-gap absorption which serves as a measure for the defect density in the films.

Photothermal Deflection Spectroscopy (PDS) The absorption spectra, from which the band gap was evaluated in this study, were measured by PDS. The experimental setup is illustrated in Fig. 3.13. This method utilizes the fact that the absorption of light leads to heating in a semiconductor, when no charge carriers are extracted. The temperature difference is very small, as the illumination is usually provided by a halogen lamp through a monochromator, resulting in a low intensity. In order to detect the weak heat dissipation, the sample is inserted into liquid carbon tetrachloride CCl_4 , which has a strongly temperature dependent refractive index n [212]. As a result, a graded refractive index is present near the surface of the sample, depending on the amount of absorbed monochromatic light. A laser beam is placed parallel to the sample and is deflected due to the difference in n. The deflection serves as a measure for the amount of the absorbed light which can then be translated into the absorption coefficient. Simultaneously, the light that is not absorbed is detected behind the sample in transmission, so that interference fringes in the spectra can be eliminated.

The optical E_{04} gap is used as band gap, which is defined as the energy corresponding to an absorption coefficient α of 10^4 cm⁻¹.

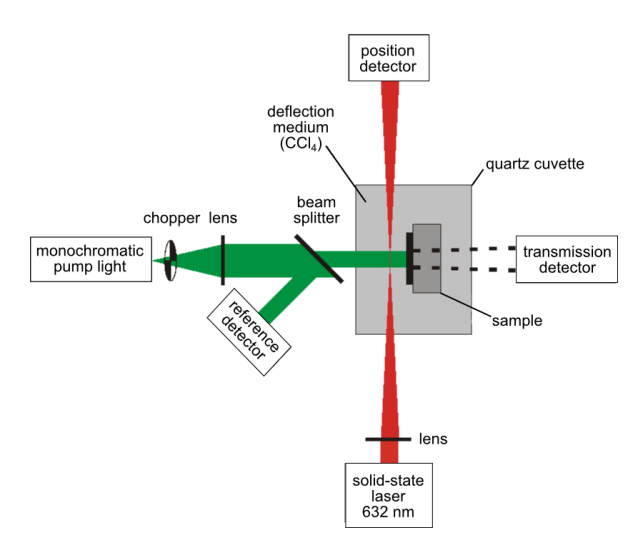


Figure 3.13.: Experimental setup of the photothermal Deflection Spectroscopy (PDS) measurement used in this work for the evaluation of band gaps. The illustration is taken from [212].

Constant Photocurrent Method (CPM) For the evaluation of the density of states in the band gap of the silicon layer, CPM measurements were performed. This method is able to detect very low absorption coefficients down to $10^{-2} \, \mathrm{cm}^{-1}$ [213]. The absorption coefficient is evaluated from the photocurrent that occurs due to illumination with monochromatic light of known intensity. As this is a conductivity measurement and electrons are majority carriers in a-Si:H, mainly the excitation of electrons into the conduction band is considered. Correct evaluation of the absorption coefficient in CPM is expected for the case of homogeneous absorption over the whole thickness of the film, i.e. for low absorption coefficients and thin films ($\alpha d \ll 1$). For the samples investigated during this study, this condition was fulfilled as the thickness was approximately 500 nm and absorption coefficients for photon energies <1.7 eV were very low. The measured photocurrent $I_{\rm ph}$ is proportional to the number of incident photons $N_{\rm ph}$, the lifetime τ of the electrons and the absorption coefficient α :

$$I_{\rm ph} \propto N_{\rm ph} \left(E_{\rm ph} \right) \times \tau \left(E_{\rm ph} \right) \times \alpha \left(E_{\rm ph} \right)$$
 (3.16)

During the spectral measurement, the intensity of the light, i.e. the number of incident photons, is regulated in such way that the photocurrent is kept constant. This means that the generation rate of charge carriers is fixed, aiming to keep the occupation of the states and thus the lifetime τ of the charge carriers constant. The absorption coefficient is then evaluated from the adjusted photon flux, that is needed to keep the photocurrent constant at a given wavelength:

$$\alpha (E_{\rm ph}) \approx {\rm const} \times \frac{1}{N_{\rm ph} (E_{\rm ph})}$$
 (3.17)

As CPM gives only relative values of α , the absorption curves have to be calibrated. In this work this is done by adjustment to the absolute absorption spectra obtained from PDS measurements. The CPM measurements were performed using the same experimental setup as for the conductivity measurements.

In a-Si:H, the defect density $N_{\rm d}$ is approximately proportional to the absorption coefficient in the sub-gap region and can be estimated by Equation 3.18 [214]

$$\alpha(E_{\rm ph}) = C \times N_{\rm d} \tag{3.18}$$

where C is a constant. For simplicity, the absorption coefficient at a single energy value is taken. The most common procedure is to read out the defect absorption $\alpha_{1.2\text{eV}}$, which is the absorption coefficient corresponding to a photon energy of 1.2 eV [214].

3.4. Characterization of Solar Cells

The performance of solar cells under illumination is described by the so-called photovoltaic parameters, that are evaluated from current density-voltage (J-V) curves of the solar cell. More detailed and especially spectral information can be obtained from spectrally resolved quantum efficiencies of the solar cells which are measured by the differential spectral response technique. The method will only be briefly presented here, detailed information about the experimental setup can be found in [215]. Additional measurements of the collection voltage and chemical composition are conducted to deeper investigate the influence of post-deposition annealing on the photovoltaic device. Unless stated differently, the results presented later were measured on solar cells with an active area of $1\,\mathrm{cm}^2$.

3.4.1. Current-Voltage Characteristic

Current-voltage measurements in this work were performed using a class A Wacom-WXS-140S sun simulator that provides a calibrated AM1.5 spectrum with a power density of $1000\,\mathrm{W/m^2}$. The temperature was held constant by a heater and cooling circuit at $25\,^{\circ}\mathrm{C}$. The intensity and homogeneity of the illumination was calibrated prior to each measurement. The sample is fixed on a vacuum chuck in the completely illuminated measuring station and each cell is contacted individually. The J-V curves are measured by a computer program, that controls a Keithley 196 System Digital Multimeter that can apply voltage and measure current at the same time. The software controls the contacting and automatically measures all cells on one substrate. For solar cells on PET substrates, fixing on the vacuum chuck and automated contacting was not possible. Therefore these solar cells were measured while fixed in the holder for flexible substrates (as described in Section 3.1.3) and connected manually by individual contact pins. In addition, no temperature control could be applied for the measurement in the flexible substrate holder.

The photovoltaic parameters $J_{\rm SC}$, $V_{\rm OC}$, FF and η , as well as the series resistance $R_{\rm s}$ are evaluated from J-V measurements under illumination according to Section 2.3.1, while the shunt resistance $R_{\rm sh}$ is evaluated from J-V curves measured in the dark.

3.4.2. Quantum Efficiency

The external quantum efficiency EQE describes the number of electron-hole pairs that are extracted from the solar cell for each incident photon and is defined as

$$EQE(\lambda) = \frac{J_{\text{ph}}(\lambda)}{q \times \Phi(\lambda)}$$
(3.19)

where $J_{\rm ph}$ is the photo-generated current density, $\Phi\left(\lambda\right)$ the photon flux per time and unit area of the incident light for a certain wavelength and q the elementary charge. The measurement is performed by illuminating a solar cell with monochromatic light and measuring the photo-generated current for a given wavelength. The measurements are performed in short-circuit conditions. In order to improve the signal-to-noise ratio, the probe light was chopped and changes in photocurrent were detected using a lock-in amplifier.

Two different quantum efficiencies are considered in this work. The external quantum efficiency EQE considers all incident photons, while in the internal quantum efficiency IQE only photons that are absorbed in the device are taken into account. This is done by excluding the part that is reflected back from the solar cell, as measured by the LAMBDA 950 spectrometer presented in Section 3.3.2:

$$IQE = \frac{EQE}{1 - R} \tag{3.20}$$

The external quantum efficiency was measured in an in-house differential spectral response (DSR) setup, consisting of a xenon lamp and a monochromator [216]. The investigated wavelength range was 320-800 nm and 320-1150 nm in the case of a-Si:H and μ c-Si:H or tandem solar cells, respectively. In order to measure the sub cells of tandem solar cells separately, the sub cell that is not being probed is saturated using red or blue bias illumination provided by light emitting diodes. The solar cells on PET substrates were measured either in the flexible substrate holder or fixed between two aperture plates similar to the case of ARS measurements in Section 3.3.2.

By integration of the EQE curve over the investigated wavelength range between λ_1 and λ_2 , the current density J_{QE} of the device can be calculated:

$$J_{\text{QE}} = q \int_{\lambda_1}^{\lambda_2} EQE(\lambda) \Phi_{\text{AM1.5}}(\lambda) d\lambda$$
 (3.21)

where q is the elementary charge and $\Phi_{\text{AM1.5}}(\lambda)$ the photon flux density of the AM1.5 solar spectrum. This value is considered for the determination of the sub cell currents in tandem

solar cells, as well as in the case of highly conductive n-type layers in microcrystalline solar cells to avoid parasitic current collection from outside the cell area [217].

In this work, EQE curves were measured under various incident angles γ of the light to investigate the effects of bending on the flexible solar cell performance. The tilting of the substrate was executed by a step motor controlled by a computer program and the incident angles were varied from normal incidence (0°) to 60° in steps of 2°.

3.4.3. Variable Intensity Measurement (VIM)

Variable intensity measurement is an effective tool to distinguish between the three main effects influencing the fill factor of a thin-film silicon solar cell: series resistance $R_{\rm s}$, shunt resistance $R_{\rm sh}$ as well as the collection of charge carriers [28]. As already indicated by the name, VIM describes the measurement of J-V curves under various illumination intensities. Here, only a short overview will be given, further details about the method, evaluation and results can be found in [218–220].

Under the assumption that bulk recombination in the intrinsic silicon layer is determined by neutral dangling bonds and the diffusion of charge carriers in the intrinsic layer is negligible, the voltage-dependent current density of thin-film silicon solar cells can be described as a superposition of the photo-generated current density $J_{\rm ph}$, diode current density from the drift-diffusion model $J_{\rm diode}$, current density through physical shunts $J_{\rm sh}$ and the recombination current density $J_{\rm rec}$ [221]:

$$J(V) = -J_{\rm ph} + J_{\rm diode} + J_{\rm sh} + J_{\rm rec}$$

$$= -J_{\rm ph} + J_0 \left[\exp \left(\frac{qV}{n_{\rm ideal} kT_0} - 1 \right) \right] + \frac{V}{R_{\rm sh}} + J_{\rm ph} \frac{d^2 \Psi}{(\mu \tau)_{\rm eff} (V_{\rm bi} - V)}$$
(3.22)

with J_0 the reverse saturation current density, V the voltage, q the elementary charge, k the Boltzmann constant, T_0 the absolute temperature, $n_{\rm ideal}$ the ideality factor, $R_{\rm sh}$ the shunt resistance, d the thickness of the intrinsic absorber layer and $V_{\rm bi}$ the built-in voltage of the solar cell. The parameter Ψ is a correction factor that considers the deformation of the electrical field due to charged defects or ionized contaminations in the absorber layer. According to Shah et al., probable values are $\Psi=1$ in the case of a thin absorber layer around 250 nm and $\Psi\approx 2$ for d=400 nm [218]. The effective mobility-lifetime product $(\mu\tau)_{\rm eff}$ combines the $\mu\tau$ -products of electrons and holes and is defined as [221]:

$$(\mu\tau)_{\text{eff}} = 2\frac{\mu_{\text{n}}^{0}\tau_{\text{n}}^{0} \times \mu_{\text{p}}^{0}\tau_{\text{p}}^{0}}{\mu_{\text{n}}^{0}\tau_{\text{n}}^{0} + \mu_{\text{p}}^{0}\tau_{\text{p}}^{0}}$$
(3.24)

where $\tau_{\rm n/p}^0$ and $\mu_{\rm n/p}^0$ are the capture times by neutral dangling bonds and the band mobility of electrons/holes, respectively.

The short-circuit resistance $R_{\rm SC}$ is introduced as the inverse slope of the J-V curve at V=0:

$$R_{\rm SC} = \left(\frac{dJ}{dV}\right)_{V=0}^{-1} \tag{3.25}$$

along with Equation 3.23 this results in

$$R_{\rm SC} = \left(J_0 \frac{q}{n_{\rm ideal} k T_0} + \frac{1}{R_{\rm sh}} + \frac{J_{\rm ph}}{V_{\rm coll}}\right)^{-1} \approx \left(\frac{1}{R_{\rm sh}} + \frac{J_{\rm SC}}{V_{\rm coll}}\right)^{-1}$$
(3.26)

with

$$V_{\text{coll}} = \frac{(\mu \tau)_{\text{eff}} V_{\text{bi}}^2}{\Psi d^2} = L_{\text{d}} \times \frac{E_{\text{bi}}}{\Psi}$$

$$(3.27)$$

being the so-called collection voltage, with the collection (or drift) length $L_{\rm d}$ and the built-in field $E_{\rm bi} = V_{\rm bi}/d$. Thereby it is assumed that the diode current is negligible compared the the contribution from shunt and recombination current and thus $J_{\rm ph} \approx J_{\rm SC}$.

As stated before, the J-V curve is measured under various illumination intensities which is realized by using grey filters that allow a reduction in intensity without modifying the illumination spectrum. The values of $V_{\rm coll}$ and $R_{\rm sh}$ can be evaluated by plotting $R_{\rm SC}$ as a function of $J_{\rm SC}$, as illustrated in Fig. 3.14. At very low $J_{\rm SC}$ values, the photo-generated

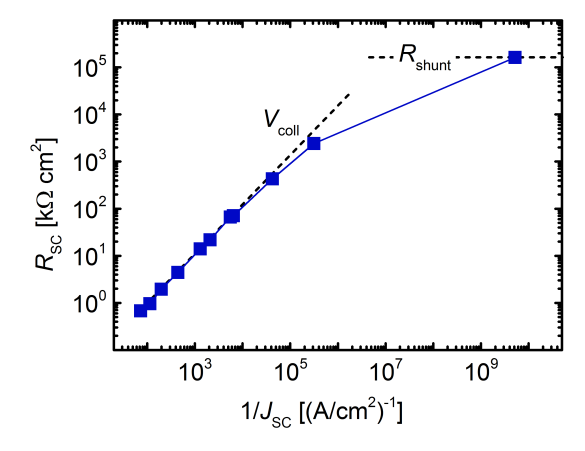


Figure 3.14.: Short-circuit resistance $R_{\rm SC}$ as a function of the inverse short-circuit current density $J_{\rm SC}^{-1}$ measured under various illumination intensities for a low temperature a-Si:H solar cell. The diagonal line corresponds to a linear fit of the first part of the curve in the non-logarithmic plot and correlates to $V_{\rm coll}$ through Eq. 3.26. The $R_{\rm SC}$ measured at very low $J_{\rm SC}$ values corresponds to the shunt resistance in the device.

current is negligible and according to Equation 3.26, $R_{\rm SC}$ then corresponds to the shunt resistance $R_{\rm sh}$ of the device. In general, the curve should asymptotically approach $R_{\rm sh}$. It should be noted that $R_{\rm sh}$ is given in $\Omega {\rm cm^2}$ consistent with the short-circuit current density instead of current. In the region of medium light intensity and thus medium $J_{\rm SC}$, the influence of the shunt resistance can be neglected and $R_{\rm SC}$ is limited by the recombination term. Thus $V_{\rm coll}$ can be calculated from the slope of the $R_{\rm SC}$ ($J_{\rm SC}^{-1}$) curve. In principle, the curve should also asymptotically approach the series resistance at very high illumination intensities above 1 sun. However, these measurement conditions are not convenient as amorphous silicon degrades rather quick under high light intensities.

3.4.4. Secondary Ion Mass Spectrometry (SIMS)

By SIMS measurements the spatially resolved chemical composition of a material can be analyzed. Primary ions are directed on the sample surface and secondary ions are emitted upon impact and accompanied ionization. The secondary ions originating from the sample are subsequently analyzed by a mass spectrometer and can provide information on the chemical composition of the sample. This method is destructive and a depth profile can be obtained as a function of erosion time due to the sputtering by primary ions. Further information about the method can be found e.g. in [222].

In this work, SIMS was used to investigate the influence of post-deposition annealing on the depth-dependent chemical composition of a-Si:H solar cells. For this purpose, a-Si:H solar cells were deposited on double-side polished CZ wafers and analyzed with the SIMS system ATOMIKA 4000 that uses a quadrupole mass filter.

4. Low Temperature Thin-Film Silicon on Glass Substrate

Previous developments carried out at the Clustertool deposition system demonstrated that an optimal a-Si:H and μ c-Si:H solar cell performance in terms of efficiency is obtained at a deposition temperature of 180 °C and under the deposition parameters of the individual layers specified in Table E.1 in Appendix E [223]. It has been shown that a reduction in deposition temperature below 180 °C leads to a deterioration in electrical properties, especially dark conductivities of doped layers, resulting in losses in fill factor and overall efficiency [224, 225]. At the same time, also the defect density in intrinsic a-Si:H continuously increases with decreasing substrate temperature below 180 °C [50, 226]. However, the use of low temperatures below 150 °C is mandatory for the deposition of solar cells and layers if low cost transparent polymer films such as PET are intended to be used as substrate material [163]. Accordingly, the influence of the deposition temperature on the material properties of thin-film silicon layers, as well as on the solar cell performance is investigated in this chapter. The deposition parameters in Table E.1 are taken as a reference throughout this chapter and were the starting point for the investigation of temperature effects. The deposition parameters are then adjusted to maintain sufficiently conductive doped layers as well as intrinsic a-Si:H layers with low defect density even at low temperature. The results presented below have partly been published in [224].

4.1. Amorphous Silicon

Electrical and optical characterization of individual layers was carried out by measurements of dark and photo conductivity, absorption coefficient by means of PDS, FTIR spectra as well as Raman scattering. The layers are optimized by variation of deposition parameters and are subsequently applied in single junction solar cells, aiming to high efficiencies for solar cells deposited at 120 °C.

4.1.1. Boron-Doped a-Si(C):H Window Layers

Temperature Series In the following, the effect of the deposition temperature on the electrical and optical properties as well as on the chemical bonding structure of p-type a-SiC:H layers is investigated. Information about the chemical bonding configuration can be obtained from FTIR absorption measurements. A typical FTIR spectrum for a p-type

a-SiC:H layer and frequencies of typical bond vibrations can be found in Section 3.3.3. The absorption peak of the Si-H stretching mode at $2000-2100 \,\mathrm{cm}^{-1}$ for various substrate temperatures between $120\,^{\circ}\mathrm{C}$ and $180\,^{\circ}\mathrm{C}$ of the p-type layer is shown in Fig. 4.1. It can

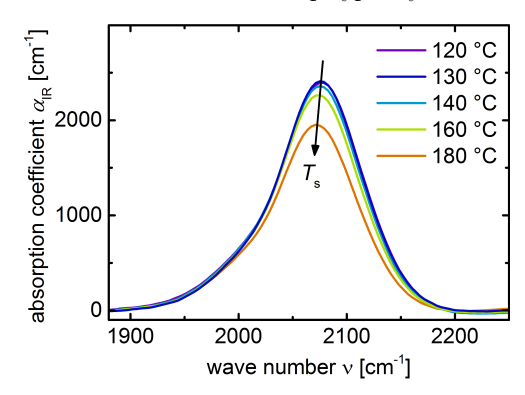


Figure 4.1.: Infrared absorption peak of the Si-H stretching vibration in p-type layers deposited at various substrate temperatures T_s between 120-180 °C.

be seen that the absorption intensity of the Si-H stretching mode in the FTIR absorption spectrum decreases with increasing substrate temperature, which implies that the hydrogen content in the films is reduced [193]. A likely explanation, often discussed in the literature, is related to an increased amount of energy available for desorption of hydrogen during the deposition process, due to the higher substrate temperature. As a consequence, less hydrogen is incorporated in a-Si:H films [54].

Integrated absorption peak intensities I_{ν} for the absorption bands located at $2000 \,\mathrm{cm^{-1}}$, $2090 \,\mathrm{cm^{-1}}$, $845/900 \,\mathrm{cm^{-1}}$ as well as $780/800 \,\mathrm{cm^{-1}}$ are shown as a function of substrate temperature in Fig. 4.2. The integrated peak intensities serve as a measure for the number of bonds in the films and can be translated into contents of e.g. bonded hydrogen or carbon by using approriate absorptions strengths [201]. It should be noted here that the carbon-related absorption bands at 1000 cm⁻¹ and 2880/2960 cm⁻¹ show similar trends as the Si-CH₃ wagging mode at $780/800\,\mathrm{cm}^{-1}$ and are thus not presented. It is visible from the Si-H stretching modes in (a) and (b), that both I_{2000} and I_{2090} decrease slightly from 15.2 to 11.4 cm⁻¹ and 110 to 87 cm⁻¹, respectively, when the temperature is raised from 120 °C to 180 °C. As derived qualitatively from Fig. 4.1 above, this indicates a reduction in hydrogen content c_H . Absolute values for c_H can be calculated from the integrated peak intensities, as described in Section 3.3.3. Correspondingly, c_H decreases from $12.7\pm1.5\,\%$ to $10.4\pm1.5\,\%$ when the temperature is raised from $120\,^{\circ}\mathrm{C}$ to $180\,^{\circ}\mathrm{C}$. The fact that the absorption peak intensity $I_{780+800}$ of the Si-CH₃ wagging mode in (d) is constant over the investigated temperature range suggests that no change in the number of Si-CH₃ bonds occurs, thus the effect of temperature on the carbon content can be neglected. From (c), a reduction in silicon dihydride bonds with increasing temperature can be deduced, which also accounts for the reduction in I_{2090} . This implies a decreased number of voids or hydrogen clusters present in the film and thus less defective material when the substrate temperature is increased [39].

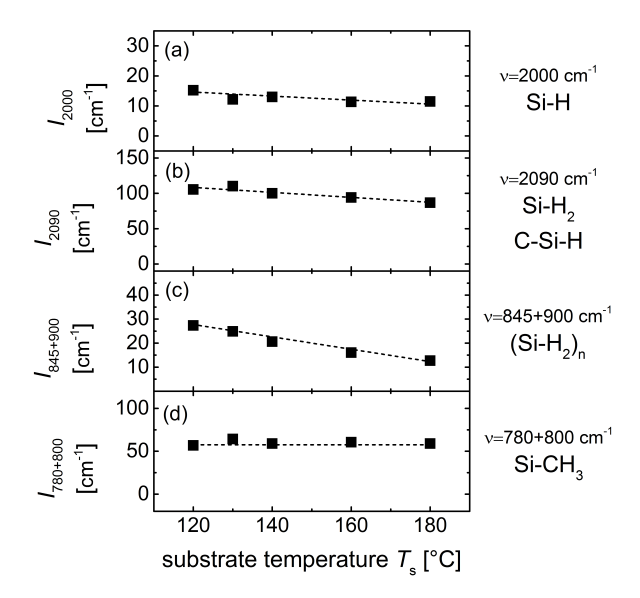


Figure 4.2.: Integrated FTIR absorption peak intensities of Si-H stretching modes I_{2000} (a) and I_{2090} (b), (Si-H₂)_n bending mode $I_{845+900}$ (c) and Si-CH₃ wagging mode $I_{780+800}$ (d) for varied substrate temperature $T_{\rm s}$ of the p-type layer. Lines are guides to the eye.

For the application as doped window layer in a solar cell, the band gap as well as the conductivity of the p-type layer should be as high as possible to reduce parasitic absorption losses and ensure efficient charge carrier collection [28]. In Fig. 4.3(a), the dark conductivity σ_d is plotted as a function of optical gap E_{04} for the layers deposited under various substrate temperatures. Furthermore, the sub-gap absorption $\alpha_{1.2\text{eV}}$ of the films, which serves as a measure for the defect density in the layers, is presented in Fig. 4.3(b). The absorption spectra from which $\alpha_{1.2\text{eV}}$ was derived can be found in Fig. A.1 in the Appendix. The error bar in E_{04} gap for the p-type layers was determined from several measurements on samples of various deposition runs. It can be seen from Fig. 4.3(a) that the E_{04} gap tends to decrease from 2.1 eV to 2.0 eV with an increase in temperature, accompanied by an increase in dark conductivity by two orders of magnitude from around 2×10^{-8} S/cm at 120 °C to 1×10^{-6} S/cm at 180 °C. At the same time, the sub-gap absorption in (b) increases by a factor of two from around 200 cm^{-1} to 400 cm^{-1} .

The decrease in band gap with increasing temperature can presumably be related to the reduced hydrogen content, which is in accordance with literature, where an empirical correlation between hydrogen content and optical band gap is found [55–59]. Although the correlation is not clearly understood, a possible explanation is related to the reduction of weak Si-Si bonds by hydrogen. These weak Si-Si bonds create states near the valence band edge, while stronger Si-H bonds induce states deeper in the valence band. As a result, the valence band edge shifts down and as the conduction band remains unaffected the band gap increases [27, 53, 58, 61]. The increase in $\alpha_{1.2\text{eV}}$ may at least partly be induced by the shift of absorption curve towards lower photon energies with increasing

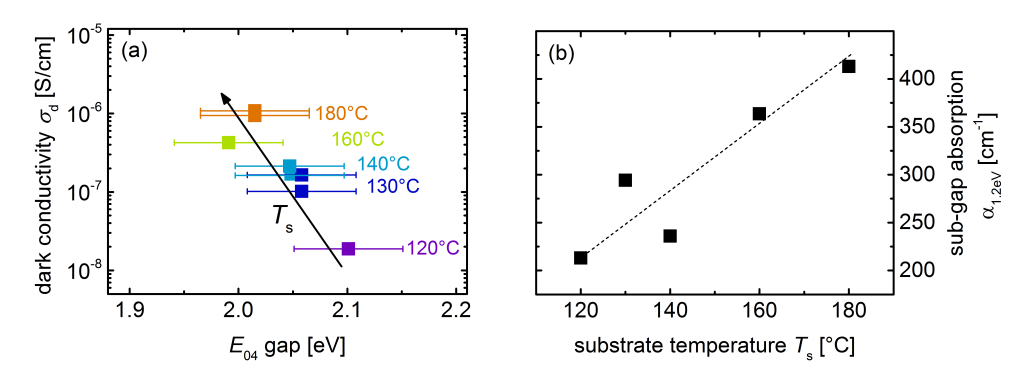


Figure 4.3.: (a) Dark conductivity $\sigma_{\rm d}$ versus E_{04} gap for p-type a-SiC:H layers deposited at various substrate temperatures $T_{\rm s}$, (b) sub-gap absorption $\alpha_{1.2{\rm eV}}$ as a function of substrate temperature $T_{\rm s}$. The arrow in (a) shows the direction of increasing $T_{\rm s}$. The dashed line in (b) is a guide to the eye.

substrate temperature (see also Fig. A.1). Besides, it is well known that in doped a-Si:H layers additional dangling bonds are created by dopant atoms [27]. As a result, a high defect density may be related to an enhanced doping level, which would lead to an increase in dark conductivity [33]. On the other hand, a high defect density resulting from poor material quality will induce a Fermi level shift towards midgap, thereby increasing the activation energy which lowers the conductivity of the films. As the increase in defect density with increasing temperature is accompanied by a rise in $\sigma_{\rm d}$, it seems likely that a higher number of dopant atoms is activated in the high temperature film. Another possible reason for the increase in $\sigma_{\rm d}$ with $T_{\rm s}$ might be related to the reduction in band gap [227].

TMB Series In order to improve the material quality of the p-type layer at low temperature (here: 120°C), two series of samples were investigated: a-Si:H layers prepared with trimethylborane B(CH₃)₃ (TMB) as dopant gas, and a-SiC:H layers prepared with TMB as well as methane (CH₄) gases. The TMB concentration c_{TMB} was varied and corresponding changes in the chemical bonding structure were again derived from integrated absorption peak intensities I_{ν} of FTIR spectra. The substrate temperature was kept constant at 120 °C and $c_{\rm CH4}$ of 36 % was used for the <p> a-SiC:H layers. The results are shown in Fig. 4.4. It can be seen from (a) and (b), that I_{2090} increases at the expense of I_{2000} with increasing c_{TMB} for both <p> a-Si:H (blue triangles) and <p> a-SiC:H layer (black squares). No clear trend with increasing c_{TMB} is observable for $I_{845+900}$ in (c). Simultaneously, a distinct increase in $I_{780+800}$ is visible, suggesting that a larger amount of carbon is incorporated into the films by adding more TMB to the gas mixture. Consequently, the shift of the Si-H stretching band from 2000 cm⁻¹ to 2090 cm⁻¹ with increasing $c_{\rm TMB}$ is most likely related to the increased presence of carbon. A higher integrated absorption intensity of the Si-CH₃ wagging mode at $780/800 \,\mathrm{cm}^{-1}$ for a-SiC:H layers compared to $\langle p \rangle$ a-Si:H layers is evident from (d) and can be related to an

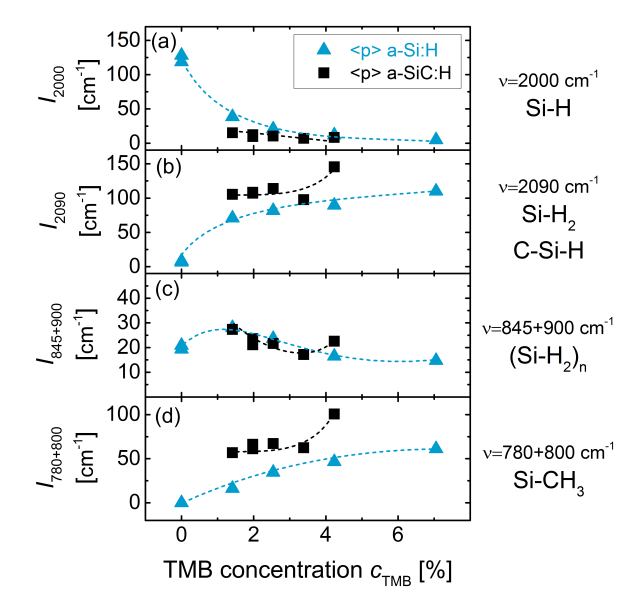


Figure 4.4.: Integrated FTIR absorption peak intensities of Si-H stretching modes I_{2000} (a) and I_{2090} (b), (Si-H₂)_n bending mode $I_{845+900}$ (c) and Si-CH₃ wagging mode $I_{780+800}$ (d) for varied TMB concentration $c_{\rm TMB}$ during deposition for <p> a-Si:H (blue triangles) as well as <p> a-SiC:H (black squares) layers deposited at 120 °C. Lines are guides to the eye.

increased amount of carbon in the <p> a-SiC:H films due to additional methane in the gas mixture during deposition.

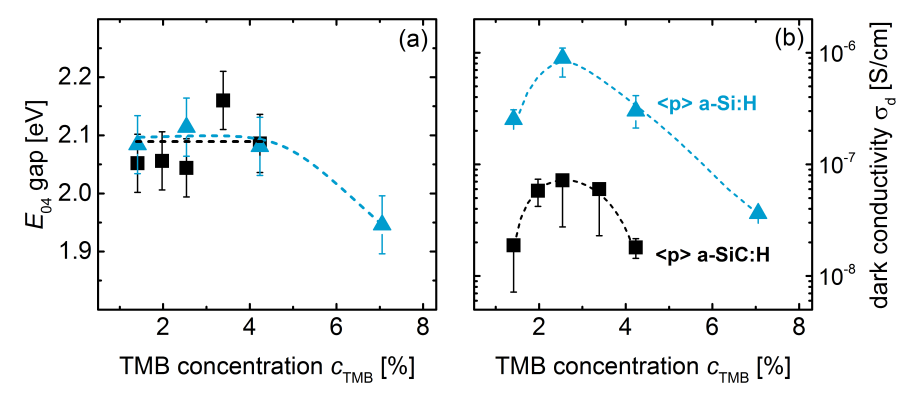


Figure 4.5.: (a) Optical E_{04} gap and (b) dark conductivity $\sigma_{\rm d}$ for <p> a-SiC:H (black squares) and <p> a-Si:H (blue triangles) layers deposited at 120 °C as function of TMB concentration $c_{\rm TMB}$ during deposition. Lines are guides to the eye.

Values for E_{04} and $\sigma_{\rm d}$ of the layers are shown in Fig. 4.5(a) and (b), respectively, as a function of TMB concentration. In the case of optical E_{04} gap, no distinct trend with $c_{\rm TMB}$ can be observed and E_{04} is $2.1\pm0.1\,{\rm eV}$ for both types of layers between $1.5\,\% < c_{\rm TMB} < 4.2\,\%$, when the error bar of the measurement is considered. This is slightly surprising, as one may expect an increase in band gap with additional carbon, either due to increased $c_{\rm TMB}$ or $c_{\rm CH4}$ in the gas mixture [228]. At higher $c_{\rm TMB}$ of 7.1%, some effect can be observed for the <p> a-Si:H layer, which reduces E_{04} down to a value of 1.95 eV. The dark conductivity on the other hand is around one order of magnitude lower for <p> a-SiC:H layers in the investigated $c_{\rm TMB}$ range and peaks at about 2.5% for varied TMB concentration, at $(9.0\pm2.5)\times10^{-7}\,{\rm S/cm}$ for <p> a-Si:H and $(7.2\pm2.5)\times10^{-8}\,{\rm S/cm}$ for <p> a-SiC:H layers.

The defect density is again estimated by the sub-gap absorption $\alpha_{1.2\mathrm{eV}}$ which is shown in Fig. 4.6 as a function of c_{TMB} . The absorption spectra from which $\alpha_{1.2\mathrm{eV}}$ was derived can be found in Fig. A.2 in the Appendix. While $\alpha_{1.2\mathrm{eV}}$ is constant at 229±48 cm⁻¹ for a-SiC:H layers over the investigated c_{TMB} range between 1.4% and 4.2%, $\alpha_{1.2\mathrm{eV}}$ for a-Si:H layers increases continuously with increasing c_{TMB} from 75 cm⁻¹ at 1.4% to 508 cm⁻¹ at 7.1%.

Most of the above presented results on layer properties do not reveal very distinct tendencies, resulting from several effects that compete with each other: With regards to the band gap, it was shown that the presence of boron in the films can lead to a reduction in band gap. A possible explanation is often related to higher degree of disorder and a broadening of the band tails by incorporation of dopant atoms into the film [229, 230]. Furthermore, as shown above, an increase in $c_{\rm TMB}$ leads to an increase in carbon content in the films, which usually leads to an increase in the band gap due to alloying effect [228]. These two counteracting effects, taking place when $c_{\rm TMB}$ is increased, might then

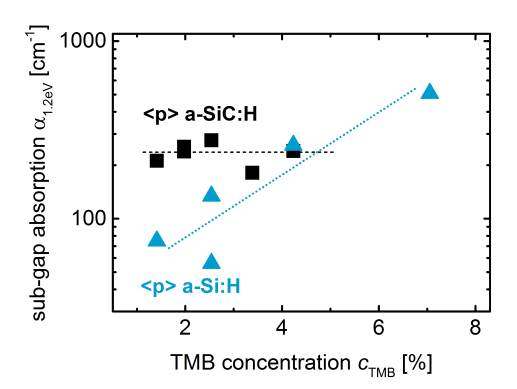


Figure 4.6.: Sub-gap absorption $\alpha_{1.2\text{eV}}$ as a function of TMB concentration c_{TMB} for <p>a-SiC:H (black) and <p>> a-Si:H (blue) layers deposited at 120 °C. Lines are guides to the eye.

result in the more or less constant E_{04} up to $c_{\rm TMB}$ of 4.2%, before at higher $c_{\rm TMB}$ the optical band gap finally decreases, possibly due to a high amount of boron in the films. Concerning the defect density, an increase in doping level also increases the number of defects in the films, as discussed above. It was also shown that besides a widening of the band gap, an increase in carbon content in a-Si:H films induces additional defects [231]. In case of $\langle p \rangle$ a-Si:H, both effects may account for the linear increase in $\alpha_{1.2 {\rm eV}}$ with increasing $c_{\rm TMB}$. In case of $\langle p \rangle$ a-SiC:H, the defect density is already high at low $c_{\rm TMB}$, probably due to the higher carbon content resulting from added methane gas. Dopant activation is more difficult for materials with a high defect density [33], and might thus be an explanation why no significant increase in $\alpha_{1.2 {\rm eV}}$ is visible with further increase in $c_{\rm TMB}$ for the case of $\langle p \rangle$ a-SiC:H layers.

The dark conductivity, related to the position in Fermi level, is affected by the doping level, band gap as well as defect density, and is a result from the effects discussed above. Since the first discovery of doping in a-Si:H, shown by Spear and LeComber in 1975, it is known that an increased doping level (in this case by adding TMB) leads to an increase in conductivity by several orders of magnitude [33]. However, effective doping is only possible in materials with relatively low defect density [33]. The peak-shaped dependence of $\sigma_{\rm d}$ on $c_{\rm TMB}$ for both types of p-type layers (Fig. 4.5(b)) might therefore be related to a first increase due to an increase in doping level, but the increased amount of carbon in the film from increased $c_{\rm TMB}$ induces defects that may result in a reduction of $\sigma_{\rm d}$. This might also account for the significantly higher $\sigma_{\rm d}$ in the case of <p> a-Si:H, when due to the added methane for <p> a-SiC:H dopant activation is impeded by a large number of defects. Please note that the band gap is similar for both types of layers and can thus not be the reason for the difference in $\sigma_{\rm d}$.

Carbon Incorporation by CH₄ and **TMB** In the following, the incorporation of carbon atoms into the film is investigated in more detail. In order to separate the effects resulting from TMB and CH₄ gases, intrinsic a-Si:H layers are taken and TMB only is added in

one case, while CH₄ only is added in the other, resulting in a p-type a-Si:H and intrinsic a-SiC:H layer, respectively. FTIR absorption peak intensities for these two series are shown in Fig. 4.7. It is evident from the increased intensity of the Si-CH₃ vibration in

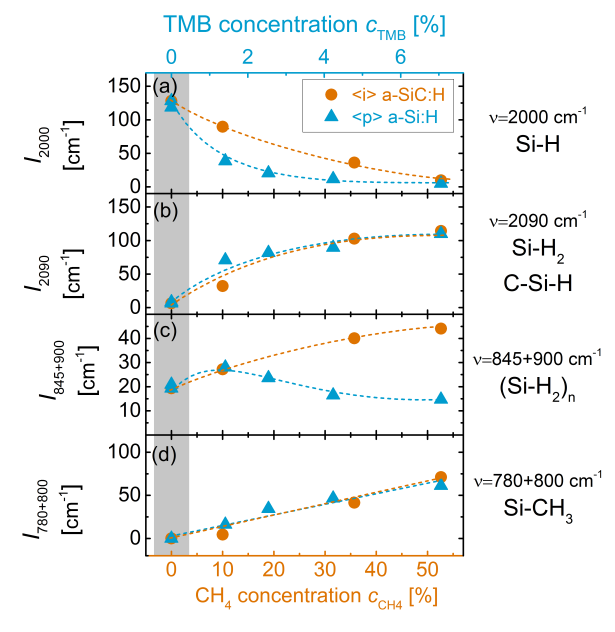


Figure 4.7.: Integrated FTIR absorption peak intensities of Si-H stretching modes I_{2000} (a) and I_{2090} (b), (Si-H₂)_n bending mode $I_{845+900}$ (c) and Si-CH₃ wagging mode $I_{780+800}$ (d). Shown are data for intrinsic a-SiC:H layers as a function of $c_{\rm CH4}$ (orange circles, lower x-axis) as well as for p-type a-Si:H layers as a function of $c_{\rm TMB}$ (blue triangles, upper x-axis), both deposited at 120 °C. The upper x-axis is scaled by a factor of 7.4 compared to the lower x-axis. The shaded area indicates $c_{\rm TMB} = c_{\rm CH4} = 0$, which represents data for an intrinsic a-Si:H layer. Lines are guides to the eye.

(d) that carbon atoms are incorporated by both TMB and CH_4 gas during deposition. Interestingly, TMB and CH_4 concentrations can be scaled as such that the magnitude of carbon incorporation is quite similar, meaning that similar integrated peak intensities of the Si-CH₃ wagging mode of $66.2\pm5.0\,\mathrm{cm^{-1}}$ can be obtained by adding either $7.1\,\%$ TMB or $52.6\,\%$ CH₄. This indicates a higher carbon incorporation efficiency by TMB compared to CH_4 , more precisely higher by a factor of 7.4. Due to the presence of three carbon atoms in the TMB molecule (B(CH₃)₃), a factor of 3 would be expected. The fact that the actual factor is even larger than 3 implicates that C atoms originating from TMB are more favorably incorporated than C atoms originating from CH₄, which is in accordance with previous work [230].

In both types of layers the increase in I_{2090} at the expense of I_{2000} is similar (see Fig. 4.7(b) and (a), respectively). For $\langle i \rangle$ a-SiC:H (orange circles), this shift from I_{2000} to I_{2090} with increasing c_{TMB} is probably caused by both the increased presence of carbon

as well as an increased amount of silicon dihydride bonds, as evident from Fig. 4.7(c). The increase in (Si-H₂)_n bending mode intensity matches those of earlier studies, where it was suggested that carbon promotes the creation of Si-H₂ bonds [197]. For a-Si:H (blue triangles), the shift of the Si-H stretching mode with increasing $c_{\rm TMB}$ (Fig. 4.7(a)) is clearly due to the increased presence of carbon as no significant increase in $I_{845+900}$ (Fig. 4.7(c)) could be detected. On the contrary, the $I_{845+900}$ value slightly decreases with $c_{\rm TMB}$, suggesting that the presence of boron in the film reduces the number of dihydride bonds that might be created by carbon.

Summary A higher deposition temperature for p-type a-Si:H layers leads to a reduced hydrogen content in the films, mainly due to reduction of silicon dihydride bonds, implying that less voids are present in the film at high temperatures. Along with the reduction of hydrogen content, the optical gap decreases with increasing temperature. The dark conductivity of the p-type layer is significantly increased by two orders of magnitude by raising the substrate temperature from 120 °C to 180 °C, which might partly be due to the reduced band gap. On the other hand, this might also be attributed to an increased activation of dopants, suggested by the increase in sub-gap absorption with raising temperature.

In case of low temperature (120 °C) p-type layers, it was shown that carbon is incorporated into the films from CH₄ as well as TMB gas. Due to the carbon alloying effect resulting from TMB, as well as the low deposition temperature, $\langle p \rangle$ a-Si:H layers, for which no methane was added during deposition, exhibit already a sufficiently large band gap for use as window layer in a solar cell. Further carbon incorporation by adding methane to the deposition gas mixture only reduces the dark conductivity without increasing E_{04} , likely due to an increased defect density induced by high amounts of carbon in the film. Optimal material properties were found at medium TMB concentrations of 2.5 %, indicating a trade-off between doping by boron atoms and increasing density of recombination centers due to boron and/or carbon incorporation. The band gap varies only slightly with TMB concentration over the investigated range. Only at high values above 7 % a reduction is found, possibly due to the increased presence of boron.

Comparing the effects of CH_4 and TMB on contents of hydrogen and carbon in the films, quite similar values were found when c_{TMB} is multiplied by a factor of around 7.4. This implies that during PECVD deposition the incorporation of carbon originating from TMB is preferred over that stemming from CH_4 .

Overall, the deterioration in electrical properties of the p-type layer, resulting from the inevitable reduction in substrate temperature, could be compensated by leaving out methane and optimizing the TMB concentration during the deposition. Even more, the optimized films deposited at $120\,^{\circ}\mathrm{C}$ exhibit a slightly increased optical gap of $2.1\,\mathrm{eV}$ compared to $2.0\,\mathrm{eV}$ for the reference p-type layer deposited at high temperature.

4.1.2. Intrinsic a-Si:H Absorber Layers

Effect of Substrate Temperature The influence of the substrate temperature on the material properties of intrinsic amorphous silicon layers have been the subject of a preceding diploma thesis [51]. In that work, a large variation in substrate temperature between 70 and 250 °C was investigated and a detailed discussion about the resulting electrical and optical properties can be found there.

In the present work, the difference between intrinsic a-Si:H layers deposited at $120\,^{\circ}$ C and $180\,^{\circ}$ C is briefly addressed, before the effect of the deposition gas mixture on low temperature intrinsic absorber layers is studied.

The FTIR absorption spectrum between 1900 and 2200 cm⁻¹, where the vibration of the Si-H stretching mode appears, is shown in Fig. 4.8. Similar to the case of p-type a-Si:H

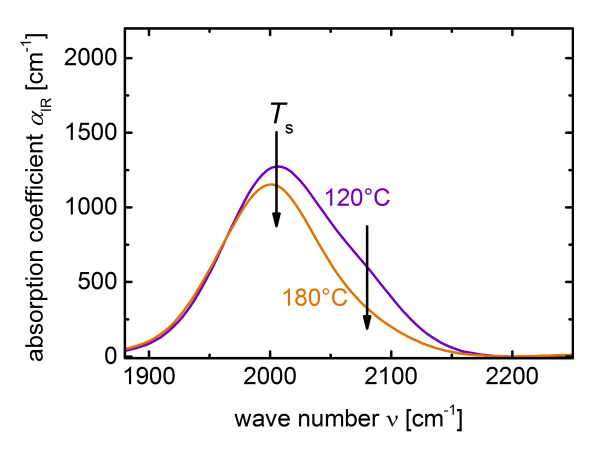


Figure 4.8.: Infrared absorption peak of the Si-H stretching mode for intrinsic a-Si:H deposited at substrate temperatures $T_{\rm s}$ of 120 °C (purple) and 180 °C (orange).

layers, the absorption peak is reduced with increasing substrate temperature, indicating a decrease in hydrogen content $c_{\rm H}$. Indeed, calculated $c_{\rm H}$ values, which are presented in Tab. 4.1, are 7.8% and 9.5% for the layers deposited at high and low temperature, respectively. Furthermore, the microstructure factor $R_{\rm m}$, that can be taken as a measure for the material quality, decreases from 0.15 at 120 °C to 0.06 at 180 °C, as mainly Si-H₂ bonds are reduced, evident from the decrease in FTIR absorption at 2090 cm⁻¹. This implies a reduction of voids in the material when the deposition temperature is raised [232].

Regarding electrical properties shown in Tab. 4.1, the dark conductivity decreases slightly and the photo conductivity increases from $(2.2\pm1.0)\times10^{-6}\,\mathrm{S/cm}$ to $(9.0\pm3.0)\times10^{-6}\,\mathrm{S/cm}$ by raising the temperature from 120 °C to 180 °C. This leads to an increase in photo response by one order of magnitude from around 10^5 to 10^6 . Similar to the case of p-type a-Si:H layers, the optical gap E_{04} slightly decreases with increasing temperature from $1.92\,\mathrm{eV}$ to $1.89\,\mathrm{eV}$. The error bar for the E_{04} gap was determined from measurements

Table 4.1.: Electrical and optical properties of intrinsic a-Si:H layers deposited at substrate temperatures $T_{\rm s}$ of 120 °C and 180 °C: dark conductivity $\sigma_{\rm d}$, photo conductivity $\sigma_{\rm ph}$, E_{04} gap, defect absorption $\alpha_{1.2{\rm eV}}$ as well as hydrogen content $c_{\rm H}$.

| $T_{\rm s}~[^{\circ}{\rm C}]$ | $\sigma_{\rm d}~{\rm [S/cm]}$ | $\sigma_{\rm ph}~[{\rm S/cm}]$ | $E_{04} [eV]$ | $\alpha_{1.2eV} [cm^{-1}]$ | $c_{\rm H} \ [\%]$ |
|-------------------------------|-------------------------------|--|---------------|--------------------------------|----------------------------|
| 180 120 | | $(9.0\pm3.0)\times10^{-6}$ $(2.2\pm1.0)\times10^{-6}$ | | 1.2 ± 0.7 9.6 ± 1.3 | 7.8 ± 2.0 9.5 ± 2.0 |

on samples from various deposition runs but similar parameters and was smaller $(0.02\,\mathrm{eV})$ compared to that from p-type layers $(0.05\,\mathrm{eV})$. Simultaneously, the defect density, which is estimated by the sub-gap absorption $\alpha_{1.2\mathrm{eV}}$, decreases from 9.6 to $1.2\,\mathrm{cm}^{-1}$ when the substrate temperature is raised from $120\,^{\circ}\mathrm{C}$ to $180\,^{\circ}\mathrm{C}$ (see Table 4.1).

Effect of Silane Concentration It is well known and has been shown in [51] that the material quality of intrinsic a-Si:H layers deposited at low temperatures can be improved by reduction in silane concentration SC during deposition. A series was therefore conducted for the intrinsic absorber layer at a substrate temperature of 120 °C where the silane concentration was varied between 4.2 % and 25 %. An SC of 16.7 % corresponds to the high temperature reference layer in [223]. From Fig. 4.9(a), a significant increase in photo response by nearly two orders of magnitude is evident by reduction in silane concentration from 25 % to 8.3 %. At the same time, the optical E_{04} gap (Fig. 4.9(b)) slightly increases from 1.90 to 1.96 eV. No systematic change in FTIR absorption peak around $2000 \,\mathrm{cm^{-1}}$ could be detected for the various silane concentrations (not shown). The scatter in photo response for the sample at $4.2 \,\%\,SC$ is very large, as the material is on the edge to the evolution of microcrystals and some of the samples show already a tiny crystalline volume fraction in Raman spectroscopy, while others are completely amorphous. No PDS measurement was possible for these samples as the layer peels off the substrate as soon as it gets in contact with CCl₄.

The sub-gap absorption $\alpha_{1.2\text{eV}}$ of the layers is evaluated from Constant Photocurrent Measurements (CPM) and is shown in Fig. 4.10. It is evident that $\alpha_{1.2\text{eV}}$ decreases from $14.0\pm2.5\,\text{cm}^{-1}$ at an SC of $25\,\%$ to $4.2\pm2.5\,\text{cm}^{-1}$ at $8.3\,\%$. When SC is further decreased, a slight increase occurs to $7.3\pm2.5\,\text{cm}^{-1}$ at $SC=4.2\,\%$.

Discussion The effects of temperature and silane concentration during deposition on the electrical and optical properties of intrinsic a-Si:H layers can be discussed as follows: with lower deposition temperature, that is needed for deposition on PET substrates, more hydrogen is incorporated into the films. Similar to the case of p-type layers, the increased hydrogen content observed here at lower substrate temperature is probably a result of reduced desorption of hydrogen during the deposition process. The additional hydrogen incorporated for the low temperature sample contributes mainly to the Si-H stretching mode at 2090 cm⁻¹, indicating a void-rich silicon network and thus poor material quality. This is in agreement with the estimation for the defect density measured in these films, as

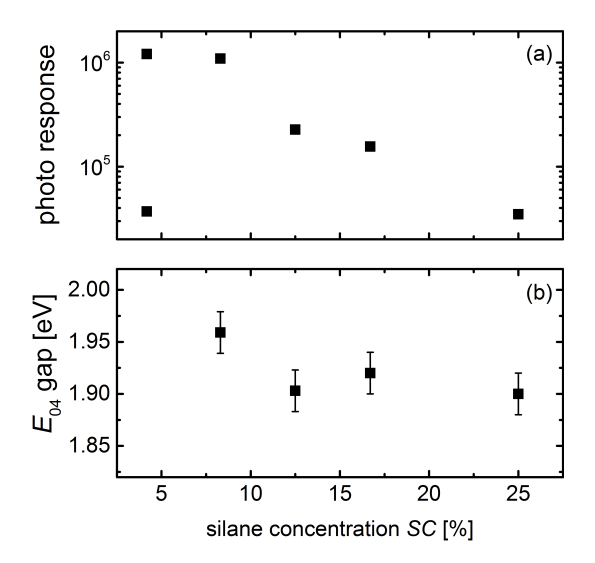


Figure 4.9.: (a) Photo response and (b) E_{04} gap of intrinsic a-Si:H layers deposited at 120 °C as a function of silane concentration SC during the deposition.

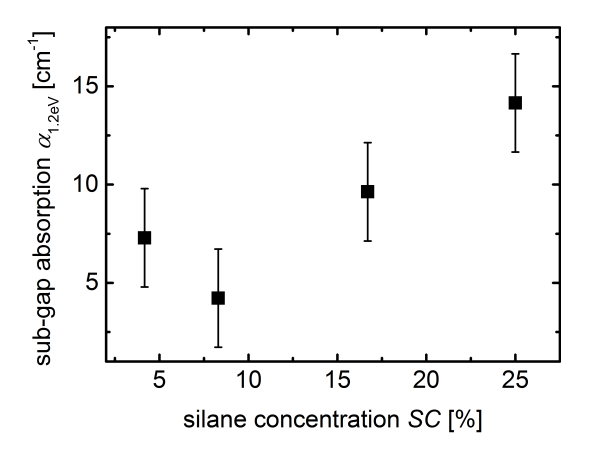


Figure 4.10.: Sub-gap absorption $\alpha_{1.2\text{eV}}$ of intrinsic a-Si:H layers deposited at 120 °C as a function of silane concentration SC during the deposition.

in a void-rich structure high defect densities are likely [28]. This in turn is reflected in the electrical properties of the films as the photo response is reduced for the low temperature film.

In this work, as well as in [51], no correlation between silane concentration during deposition and hydrogen content in the film was found for intrinsic a-Si:H layers. Still, the optical E_{04} gap increases slightly with decreasing SC (see Fig. 4.9(b)). A matter discussed in the literature is that the band gap in a-Si:H might not only be affected by the hydrogen content in the film, but additionally depends on the nanostructure, i.e. degree of structural disorder [233–237]. In a more ordered structure, the band tails would steepen thus virtually increasing the band gap. Structural order can be estimated by Raman scattering spectroscopy by evaluation of the TO peak position x_{TO} [205]. In Fig. 4.11, it can be seen that x_{TO} increases from 476 cm⁻¹ to 479 cm⁻¹ by reduction in SC from 25% to 8.3%, besides a large scatter for the sample at SC of 4.2% due to the partly microcrystalline volume fraction as discussed above. According to [205, 238] a

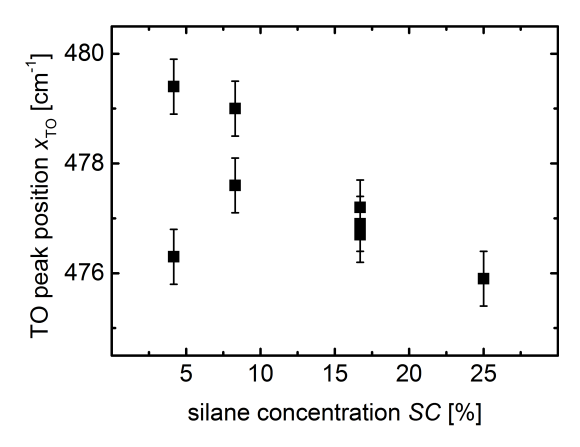


Figure 4.11.: Peak position of the transverse optical (TO) phonon mode x_{TO} evaluated from Raman scattering spectroscopy as a function of silane concentration SC for intrinsic a-Si:H layers deposited at 120 °C.

higher TO peak position can be related to higher degree of structural order, which would then increase the band gap.

An explanation, often discussed in the literature, is related to the etching effect of hydrogen: weak distorted Si-Si bonds are broken during PECVD at the surface by the increasing number of hydrogen atoms in the gas mixture at low silane concentrations and mainly strong Si-Si bonds remain. As a result, the network is more ordered and stable and tends to exhibit lower defect densities [39]. Another reason for better material quality can be related to the decreasing deposition rate when a low silane concentration is used and thus less silicon is available for deposition. In this case, SiH₃ radicals have more time for surface diffusion to find an energetically favorable place for film formation, and thus more ordered films are produced. This is in accordance with the defect absorption $\alpha_{1.2\text{eV}}$ as function of SC observed in Fig. 4.10. A lower defect density in turn increases the photo

conductivity, thereby explaining the trend of increasing photo response with decreasing SC.

4.1.3. Phosphorous-Doped a-Si:H Layers

For the n-type layer, similar to the case of p-type layers, conductivity is important to built up the electric field in the solar cell and thereby assure charge carrier collection. In contrast to the p-type window layer, the n-type layer is located at the back side of the solar cell, thus a large optical band gap is still but not so severely important as high energy photons are mainly absorbed in the front part of the solar cell. Measurements of FTIR were performed and the absorption peak of the Si-H stretching mode is shown in Fig. 4.12 for n-type a-Si:H layers deposited at $120\,^{\circ}$ C under various silane concentrations. The phosphine

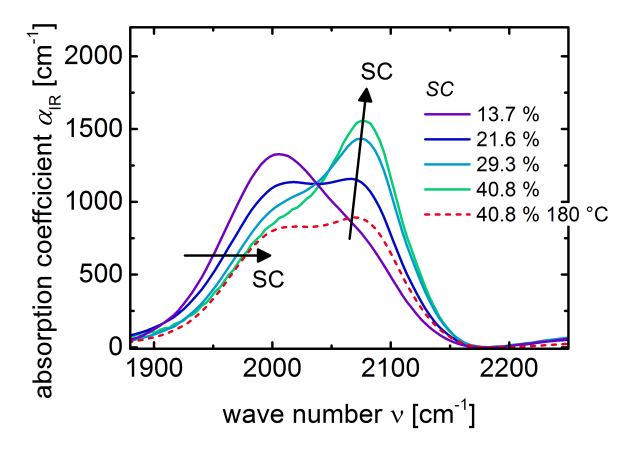


Figure 4.12.: Infrared absorption peak of the Si-H stretching mode for n-type a-Si:H deposited at 120 °C under various silane concentrations SC. Data for the high temperature reference n-type layer is shown for comparison (red dashed line).

concentration c_{PH3} was held constant at 2.0%. An n-type layer deposited at 180 °C is also shown for comparison (red dashed line). By reduction of the substrate temperature (compare red dashed and green solid line), the peak intensity increases, especially for the dihydride absorption band at 2090 cm⁻¹. This effect can be compensated by reduction of the silane concentration during deposition, where the stretching mode at 2000 cm⁻¹ grows at the expense of the stretching mode at 2090 cm⁻¹, meaning that dihydride bonds Si-H₂ are replaced by more favorable monohydride bonds Si-H.

The resulting hydrogen content is calculated from the Si-H stretching mode as described in Section 3.3.3 and is shown in Fig. 4.13(a). Similar to the case of intrinsic a-Si:H layers shown above and due to reasons already discussed, a reduction in substrate temperature leads to an increase in $c_{\rm H}$, as visible for the layers deposited at SC of 40.8%. In contrast to the intrinsic layers shown above however, a trend of decreasing hydrogen content with decreasing silane concentration can be found, from 15.9% at SC = 40.8% to

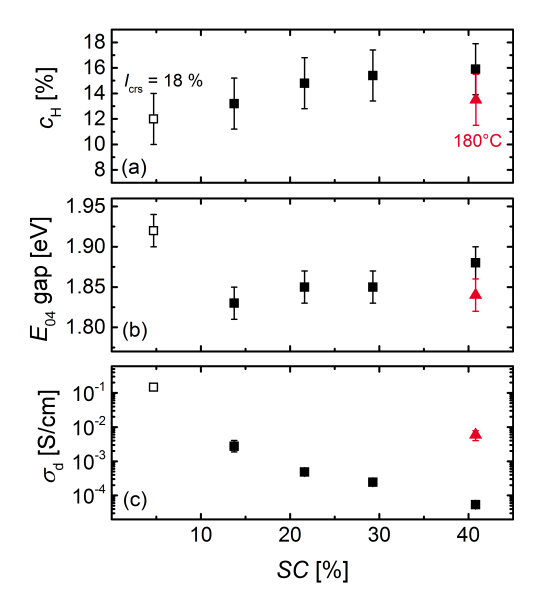


Figure 4.13.: (a) Hydrogen content $c_{\rm H}$, (b) E_{04} gap and (c) dark conductivity $\sigma_{\rm d}$ of n-type a-Si:H layers deposited at 120 °C as a function of silane concentration SC during deposition. The layer exhibiting a crystalline volume fraction of 18% is shown by an open square. The values for the reference n-type layer deposited at 180 °C are shown for comparison (red triangle).

 $12.0\,\%$ at $SC=4.7\,\%$. It should be noted here that the sample deposited under $SC=4.7\,\%$ (open square) already exhibits a crystalline volume fraction of 18 %, detected by Raman scattering measurements.

In Fig. 4.13(b) and (c), the optical E_{04} gap and dark conductivity $\sigma_{\rm d}$ of n-type layers deposited at 120 °C under various silane concentrations are shown, respectively. The values for the reference n-type layer, deposited at 180 °C with $SC=40.8\,\%$ is also shown for comparison (red triangle). Due to the dependence of the band gap on the hydrogen content, already discussed for p-type layers, E_{04} decreases slightly with decreasing SC from 1.88 eV at 40.8 % down to 1.83 eV at 13.6 %. Below 13.6 %, the optical gap increases sharply to a value of 1.92 eV. Regarding electrical properties of the n-type layer, a reduction in substrate temperature leads to a decrease in dark conductivity by more than two orders of magnitude from 5.9×10^{-3} to $5.4\times10^{-5}\,\mathrm{S/cm}$, as visible in Fig. 4.13(c) at $SC=40.8\,\%$. However, the dark conductivity for films deposited at low temperature can continuously be increased by reducing SC, up to a value of $2.8\times10^{-3}\,\mathrm{S/cm}$ for completely amorphous layers and 0.15 S/cm in case of n-type layer exhibiting crystalline volume fraction.

Discussion Similar to the case of intrinsic as well as p-type a-Si:H layers, a reduction in substrate temperature leads to an increase in hydrogen content and thus, due to reasons discussed above, an increase in band gap. The low temperature material has a more

void-rich structure, as visible from the Si-H stretching mode at 2090 cm⁻¹, which may induce a larger amount of defects acting as recombination centers and thus lower dark conductivities [27]. Another possible reason for the reduced dark conductivity might also be related to the increased band gap at low temperature, which may induce a shift of the Fermi level towards midgap.

The material quality at low temperature can significantly be improved by reducing the silane concentration during deposition. As visible from the Si-H stretching mode, hydrogen is mainly bonded as silicon monohydride bonds at lower SC, which tend to reduce the defect density [39]. As already discussed for the intrinsic absorber layer, a possible explanation is related to the etching effect of hydrogen that leads to a more ordered and stable structure and tends to produce material that exhibits lower defect densities [39]. The other possible reason for a reduced disorder in the films might also be related the lower deposition rate at low SC, as discussed above.

This higher structural order in the network at low SC gives rise to an increase in dark conductivity, which is even more enhanced when microcrystals, representing highly ordered material, evolve. Also in this case, another possible reason for the increasing dark conductivity with reduction of SC may be related to a change in Fermi level position relative to the conduction band due to the decrease in band gap. Several effects discussed above result in the increase in dark conductivity, demonstrating that an adjustment of deposition parameters can result in $\sigma_{\rm d}$ of $2.8\times10^{-3}\,{\rm S/cm}$ and an optical band gap E_{04} of $1.83\,{\rm eV}$ for an n-type a-Si:H layer deposited at $120\,{\rm ^{\circ}C}$, close to the values obtained at high substrate temperature.

4.1.4. Solar Cells

Improvement in the electrical properties of individual layers of a solar cell does not automatically result in an improved photovoltaic performance. This is because interfaces play an important role and on the other hand the conductivity of individual layers is measured in coplanar configuration, and thus perpendicular to the growth direction, while conduction inside the solar cell takes place in growth direction. Additionally, the solar cell performance can be limited by other factors like series or shunt resistances.

Therefore, a temperature series for the reference solar cell is conducted to see the influence of lower substrate temperature and thus deteriorated layer properties discussed above on the solar cell performance. Afterwards, the series of improved deposition parameters for the individual layers presented in the sections above are subsequently implemented in a solar cell in p-i-n configuration on glass substrate. Asahi-U type substrates are used for all solar cells investigated in this chapter as it is commercially available and provides excellent reproducibility.

It should be noted here, that during the experiments a strong post-deposition annealing effect in a-Si:H solar cells deposited at $120\,^{\circ}$ C was observed that will intensively be discussed in Chapter 5. The effect was as high as $34\,\%$ relative increase in efficiency for an annealing time of $120\,\mathrm{minutes}$ with the strongest effect within the first $30\,\mathrm{minutes}$. The

annealing times for the solar cells differ for various series studied here (between 30 and 240 minutes) and are indicated for each series. Unless stated differently, the annealing was carried out at 120 °C in air and the minimum annealing time for all cells was 30 minutes.

Effect of Substrate Temperature In order to investigate the influence of the substrate temperature on the performance of a-Si:H solar cells, the substrate temperature for a-Si:H layer deposition was varied from 120 to 180 °C, while other deposition parameters, including the deposition time of layers, were kept constant. The post-deposition annealing for this series was conducted at the respective deposition temperature of each solar cell but maximal at 160 °C. The effect of decreasing substrate temperature on the photovoltaic

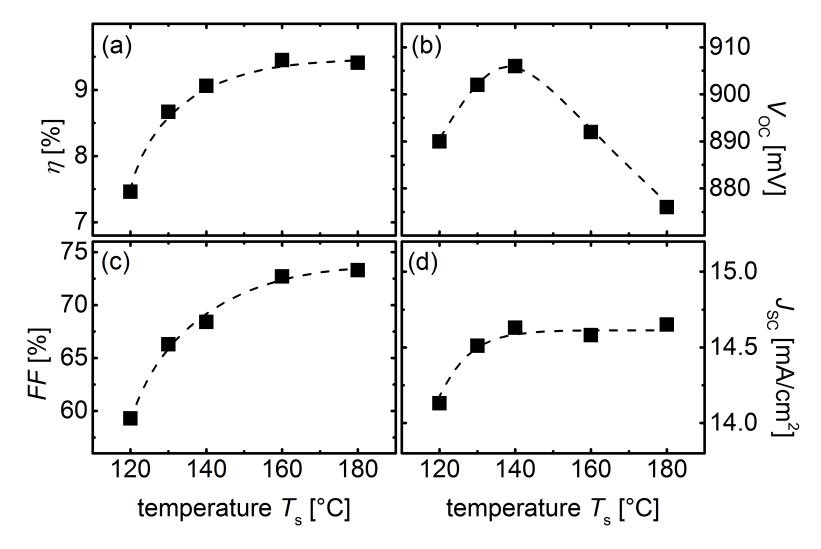


Figure 4.14.: Photovoltaic parameters of a-Si:H solar cells in p-i-n configuration as a function of substrate temperature T_s during deposition. Lines are guides to the eye.

parameters of the reference a-Si:H solar cell after 30 minutes annealing time is shown in Fig. 4.14. Corresponding J-V curves can be found in Fig. A.3 in the Appendix. The most significant effect is the decrease in fill factor FF with reduced temperature from 73.6% at $180\,^{\circ}\text{C}$ to $59.3\,\%$ at $120\,^{\circ}\text{C}$, as evident from Fig. 4.14(c). The short-circuit current density J_{SC} shown in (d) stays relatively constant down to a temperature of $140\,^{\circ}\text{C}$, but then decreases by $0.5\,\text{mA/cm}^2$. The open-circuit voltage V_{OC} presented in (b) first increases with increasing T_{s} from $875\,\text{mV}$ to $905\,\text{mV}$ at a temperature of $140\,^{\circ}\text{C}$, but then decreases down to a value of $890\,\text{mV}$ at $120\,^{\circ}\text{C}$. Overall, the effect of FF predominates, reducing the device efficiency by $21\,\%$ relative from $9.4\,\%$ to $7.5\,\%$. Corresponding external quantum efficiency EQE curves are presented in Fig. 4.15. A clear trend of increasing EQE with increasing temperature for wavelengths $>530\,\text{nm}$ can be seen. For light of shorter wavelength on the other hand, no distinct trend of EQE on temperature is observed.

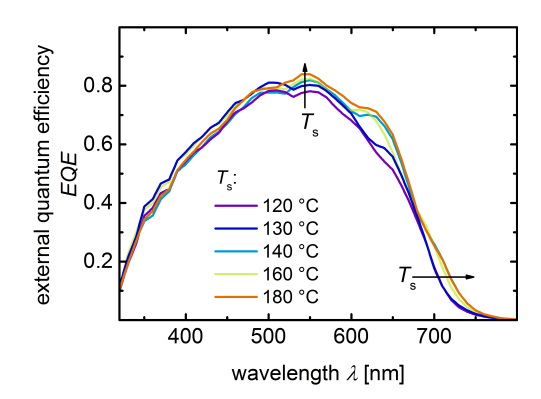


Figure 4.15.: External quantum efficiency EQE curves for solar cells deposited at various substrate temperatures T_s during deposition.

In such a series, where the deposition temperature of all layers is varied, many changes happen at once and effects due to variation in layer thickness, electrical as well as optical properties of the layers and also at interfaces can hardly be separated. Nevertheless, the results of solar cell performance as a function of substrate temperature shown here can broadly be associated with changes in the individual silicon layer properties with substrate temperature presented in Sections 4.1.1 to 4.1.3 as follows: The reduction in fill factor has several possible reasons. On one hand, it was shown in Tab. 4.1, that the defect density in the intrinsic a-Si:H layer increases by reduction of the substrate temperature, which usually decreases the lifetime of generated charge carriers and may lead to a deformation of the electrical field, thereby deteriorating the charge carrier collection and consequently the fill factor of the solar cell [239]. When less carriers are collected this can be visible in EQE curves (and also in J_{SC}) [239]. On the other hand, charge carrier collection depends on the built-in voltage of the device, which is mainly governed by the activation energy in p- and n-type layers in the device [227]. As the dark conductivity of both the p- and n-type layer decreases by around two orders of magnitude with decreasing $T_{\rm s}$ from 180 °C to 120 °C (see Figs. 4.3(a) and 4.13(c), respectively), a reduction in FFcould be expected.

Regarding the effect of substrate temperature on $J_{\rm SC}$, a higher EQE in the long wavelength range is expected for the solar cell deposited at higher temperature, due to the lower band gap of the intrinsic layer (see Tab. 4.1) and thus higher absorption coefficient for light of low energy [51]. Indeed, an increase in EQE for $\lambda > 650\,\mathrm{nm}$ is observed, although an additional effect might play a role in this range: as the deposition times were kept constant for all layers and the deposition rate of the intrinsic layer decreases with decreasing temperature (from 1.8 Å/s at 180 °C to 1.6 Å/s at 120 °C), the total thickness of the absorber layer is reduced with decreasing temperature. As a result, the light path through the absorber layer is reduced and less light of low energy can be absorbed. Regarding the short wavelength range below 500 nm, several effects resulting from variation in layer thickness and band gap of the p-type layer overlap and no distinct trend can be observed.

In contrast to $J_{\rm SC}$, $V_{\rm OC}$ increases with increasing band gap of the intrinsic absorber layer [28] as well as band gap of the p-type layer [227] and thus an increasing $V_{\rm OC}$ with decreasing temperature is expected (see Fig. 4.3 and Tab. 4.1). However, below a temperature of 140 °C, $V_{\rm OC}$ suddenly drops and possible reasons are a large number of defects in one of the doped layers and/or the intrinsic a-Si:H layer, as well as at the interfaces between.

P-Type Layer - Material Optimization Three types of p-type layers from Section 4.1.1 are implemented in the reference a-Si:H solar cell deposited at low temperature: (A) the reference p-type layer deposited at 120 °C (data from Fig. 4.14), (B) the optimized <p> a-SiC:H layer (with $c_{\rm TMB} = 2.5$ %, see Fig. 4.5) and (C) optimized <p> a-Si:H layer (with $c_{\rm TMB} = 2.5$ %, see Fig. 4.5). All solar cells of this series were annealed for 30 minutes. In Table 4.2, $\sigma_{\rm d}$ and $E_{\rm 04}$ of the various p-type layers are presented along with the photovoltaic parameters when they are implemented in a solar cell. A dependency of the fill factor

Table 4.2.: Dark conductivity σ_d and E_{04} gap of p-type a-Si(C):H layers deposited at 120 °C under various gas mixtures as well as photovoltaic parameters when implemented in an a-Si:H solar cell.

| p-type layer | $\sigma_{\rm d} \; [{\rm S/cm}]$ | $E_{04} [eV]$ | η [%] | <i>FF</i> [%] | $V_{\rm OC}~[{ m mV}]$ | $J_{\rm SC}~[{\rm mA/cm^2}]$ |
|-----------------|----------------------------------|---------------|------------|---------------|------------------------|------------------------------|
| A | $1.9{	imes}10^{-8}$ | 2.10 | 7.4 | 59.3 | 889 | 14.1 |
| В | 7.2×10^{-8} | 2.04 | 7.5 | 60.3 | 891 | 14.1 |
| $^{\mathrm{C}}$ | 9.0×10^{-7} | 2.11 | 8.0 | 64.3 | 896 | 13.8 |

and open-circuit voltage of the solar cells on the dark conductivity of the p-type layer is visible and both FF and $V_{\rm OC}$ increase with increasing $\sigma_{\rm d}$ from 59.3 to 64.3% and 889 to 896 mV, respectively. The effect can be related to an increase in built-in voltage $V_{\rm bi}$ when the activation energy in the p-type layer is reduced [28]. The short-circuit current density is lower for the cell with p-type a-Si:H layer. As no variation in E_{04} gap could be detected, an explanation may be related to differing p-type layer thicknesses. This is in agreement with calculated thickness values, evaluated from the deposition rates of 400 nm thick individual layers, which reveal that layer thickness in the solar cell is 11 nm and 14 nm for p-type layers (A) and (B), respectively, while the p-type layer (C) is calculated to be around 28 nm. As the solar cell with p-type layer (C) shows the highest efficiency, this layer is used for the following solar cells.

P-Type Layer - Thickness Series The thickness of the p-type layer has a significant influence on the photovoltaic parameters of the solar cell. The layer needs to be thick enough to ensure an appropriate built-in field and thus carrier collection, on the other hand it should be as thin as possible to reduce parasitic absorption [28]. The thickness of the p-type layer (C) was varied by adjusting the deposition time between 90 and 300 seconds and the corresponding photovoltaic parameters of the solar cells are shown in Fig. 4.16. All cells were annealed for 30 minutes. The data is plotted as a function of

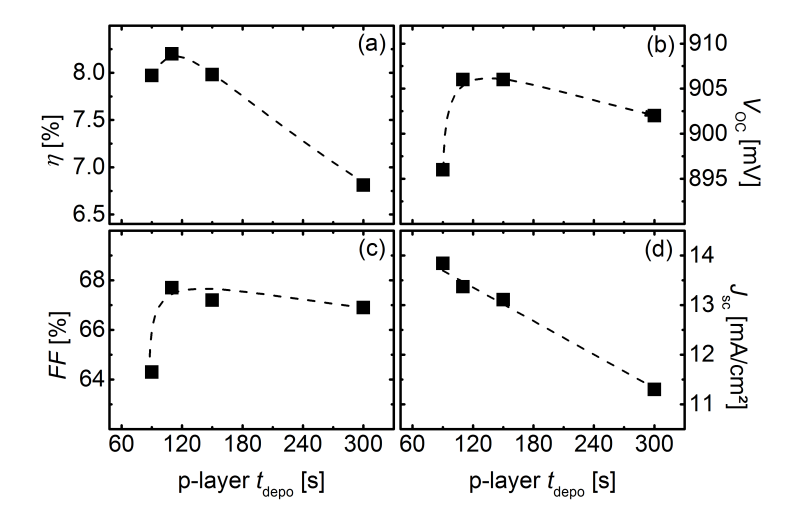


Figure 4.16.: Photovoltaic parameters as a function of p-type layer deposition time t_{depo} for a-Si:H solar cells deposited at 120 °C. Lines are guides to the eye.

a-Si:H p-type layer deposition time $t_{\rm depo}$, as the p-type layer thickness cannot easily be measured in a device. It can be seen that $J_{\rm SC}$ of the solar cell shown in (d) decreases linearly from 13.8 to $11.3\,{\rm mA/cm^2}$ with increasing deposition time from 90 to 300 s. From EQE curves in Fig. 4.17 it is evident that the reduction is due to increased parasitic absorption of light with $\lambda < 550\,{\rm nm}$. Open-circuit voltage and fill factor values, presented

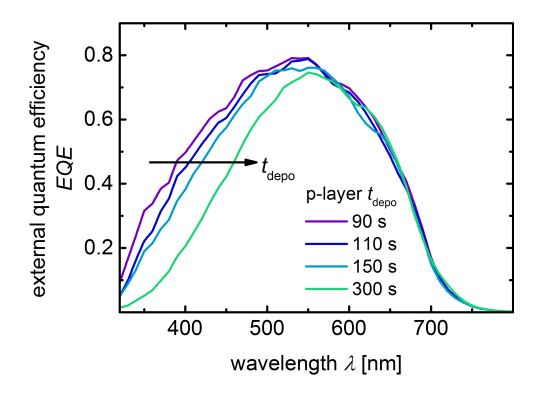


Figure 4.17.: External quantum efficiency EQE curves for a-Si:H solar cells deposited at 120 °C with various deposition times t_{depo} for the p-type a-Si:H layer.

in (b) and (c), are relatively constant at $904\pm2\,\mathrm{mV}$ and $67.3\pm0.4\,\%$, respectively, for $t_{\rm depo}>110\,\mathrm{s}$. Yet for shorter deposition times, both FF and $V_{\rm OC}$ decrease rapidly as the thickness is not sufficient to maintain an appropriate built-in field and losses in charge carrier collection occur. As a result, an optimal deposition time of 110 s was found where

the overall efficiency is 8.2%. This deposition time for the p-type layer will be applied for the following solar cells.

Intrinsic a-Si:H Layer - SC Series As evident from Section 4.1.2, the photo response of the intrinsic a-Si:H layer deposited at low temperature could be varied over one order of magnitude between 10^5 and 10^6 by varying the silane concentration during deposition. The respective layers are implemented in a solar cell and results are shown in Fig. 4.18. All cells in this study were annealed for 150 minutes. A slight increase in $V_{\rm OC}$ shown in (b)

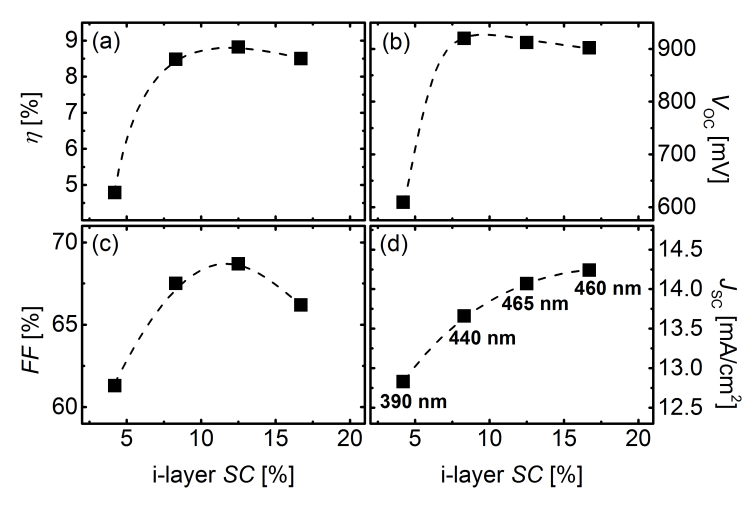


Figure 4.18.: Photovoltaic parameters as a function of silane concentration SC of the intrinsic a-Si:H layer for a-Si:H solar cells deposited at 120 °C. The overall thickness of the silicon layers is noted in (d). Lines are guides to the eye.

is visible when SC of the intrinsic layer is reduced from 16.7% to 8.3%, most likely due to the increasing E_{04} gap with decreasing SC (see Fig. 4.9(b)). Only a slight variation in FF presented in (c) is observed in the same SC range, nevertheless a small increase from 66.2% at SC=16.7% to 68.7% at SC=12.5% could be achieved. For even lower SC of 4.2%, FF and $V_{\rm OC}$ decrease dramatically. This is probably due to the evolution of a small microcrystalline volume fraction as some of the corresponding individual layers have exhibited $I_{\rm crs}$ of 2-4%.

With regards to the photocurrent, $J_{\rm SC}$ shown in (d) increases continuously with increasing SC in the investigated range. From EQE curves of the respective solar cells in Fig. 4.19, a shift of the EQE curve to longer wavelengths with increasing SC is visible which is probably related to the reduction in band gap (see Fig. 4.9(b)) [240]. It also reveals an enhanced absorption for $\lambda > 700$ nm for the layer with SC = 4.2%, due to the smaller band gap of microcrystalline silicon. With the evolution of microcrystals in the film, the deposition rate decreases significantly, resulting in a thinner intrinsic layer at 4.2% SC, which may account for the lower $J_{\rm SC}$. The highest solar cell performance is

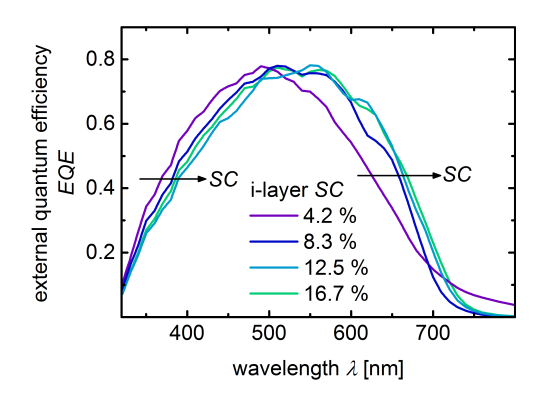


Figure 4.19.: External quantum efficiency EQE curves for a-Si:H solar cells deposited at 120 °C where the intrinsic absorber layer is deposited under varying silane concentrations SC.

found with an intrinsic a-Si:H layer deposited at $SC = 12.5 \,\%$, achieving an efficiency of 8.8 %.

Intrinsic a-Si:H Layer - Thickness Series and Back Contact Similar to the case of p-type layers, a trade-off exists between J_{SC} and FF when the thickness of the intrinsic absorber layer is varied. The built-in field $E_{\rm bi}$ in the device is determined by the built-in voltage $V_{\rm bi}$ and thickness d of the intrinsic layer by $E_{\rm bi} = V_{\rm bi}/d$ [28]. Consequently, the built-in field is stronger for thinner absorber layers and charge carrier collection is improved, which can result in higher FF values. On the contrary, with increased absorber layer thickness, more photons can be absorbed resulting in an increased $J_{\rm SC}$. The deposition time of the intrinsic a-Si:H layer with SC of 12.5% was varied to find the optimal absorber layer thickness. Furthermore, it is known that silver back contacts on rough surfaces, that were used for the solar cells investigated so far, are the cause for increased parasitic absorption at the n-type a-Si:H/Ag interface [107]. It is also known that a thin interlayer of ZnO:Al can be inserted between the n-type a-Si:H and silver layer, thus reducing plasmonic absorption and increasing $J_{\rm SC}$ of the solar cell [107]. The thickness series of the intrinsic absorber layer was therefore conducted with Ag as well as ZnO:Al/Ag back contacts. Corresponding photovoltaic parameters are shown in Fig. 4.20. All solar cells were annealed for 120 minutes.

For both types of back contacts, similar values for FF and $V_{\rm OC}$ are observed, which increase with decreasing layer thickness from around 67.0 to 72.6% and very slightly from 905 to 910 mV, respectively. As discussed above, this can be related to the improved built-in field with reduced layer thickness. Regarding $J_{\rm SC}$, a reduced i-layer thickness from 450 nm to 150 nm reduces the absorption of light and thus decreases $J_{\rm SC}$ by $3.0\,{\rm mA/cm^2}$ and $2.4\,{\rm mA/cm^2}$ for the solar cells with Ag and ZnO:Al/Ag back contact, respectively.

A difference between the two types of back contacts is visible and the insertion of thin ZnO:Al layer increases $J_{\rm SC}$ significantly by $1.3\,{\rm mA/cm^2}$ in the case of $d=450\,{\rm nm}$ and even $1.9\,{\rm mA/cm^2}$ in the case of $d=150\,{\rm nm}$. This is also visible in EQE curves exemplarily

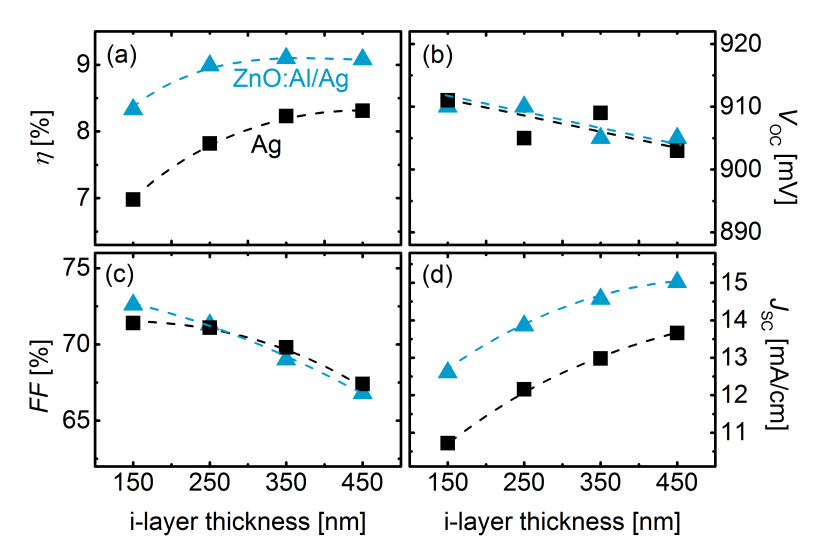


Figure 4.20.: Photovoltaic parameters of solar cells as a function of intrinsic absorber layer thickness with Ag (black squares) and ZnO:Al/Ag (blue triangles) back contact. Lines are guides to the eye.

shown in Fig. 4.21, where the ZnO:Al/Ag back contact significantly increases the EQE curve in the long wavelength range above 480 nm for a solar cell with d=150 nm (compare light blue and grey curve). Also the increase in absorber layer thickness is clearly visible by the shift of the EQE curve towards long wavelengths, exemplarily shown for the solar cell with ZnO:Al/Ag back contact in Fig. 4.21. The optimal thickness for the intrinsic absorber layer in this study is found to be 350 nm which results in an efficiency of 9.1 % when a ZnO:Al/Ag back contact is used.

N-Type Layer - SC Series Variation of SC during deposition of the n-type layer leads to a variation in $\sigma_{\rm d}$ by more than three orders of magnitude between $5.4\times10^{-5}\,{\rm S/cm}$ and $1.5\times10^{-1}\,{\rm S/cm}$ (see Fig. 4.13(c)). This series of layers is subsequently implemented in the a-Si:H solar cell with an absorber layer thickness of 450 nm and Ag back contact shown above. The annealing time for the solar cells in this series was 150 minutes. Photovoltaic parameters of the corresponding solar cells are presented in Fig. 4.22. With decreasing SC, a slight increase in FF shown in (c) from 68.7% at SC=40.8% to 70.6% at SC=13.7% is visible. $V_{\rm OC}$ presented in (b) increases from 912 to 918 mV in the same range. These changes are rather small, considering that $\sigma_{\rm d}$ varies over several orders of magnitude in this range, suggesting the n-type layer is not limiting the solar cell performance. Also the differences in $J_{\rm SC}$ are small with a maximum deviation of $0.4\,{\rm mA/cm^2}$ within this series. These variations might result from a superposition of increasing band gap with decreasing SC and subtly different thicknesses of the n-type layers. The n-type layer deposited at SC=4.7% is slightly microcrystalline but seems to work equally well. The

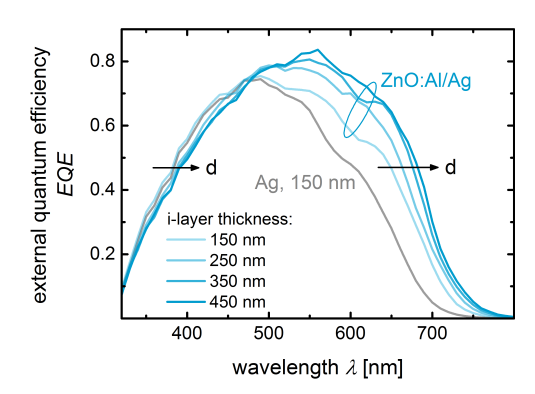


Figure 4.21.: External quantum efficiency EQE curves for a-Si:H solar cells deposited at 120 °C with various absorber layer thicknesses and ZnO:Al/Ag back contact. The EQE curve for the solar cell with 150 nm i-layer thickness and Ag back contact (grey) is shown for comparison.

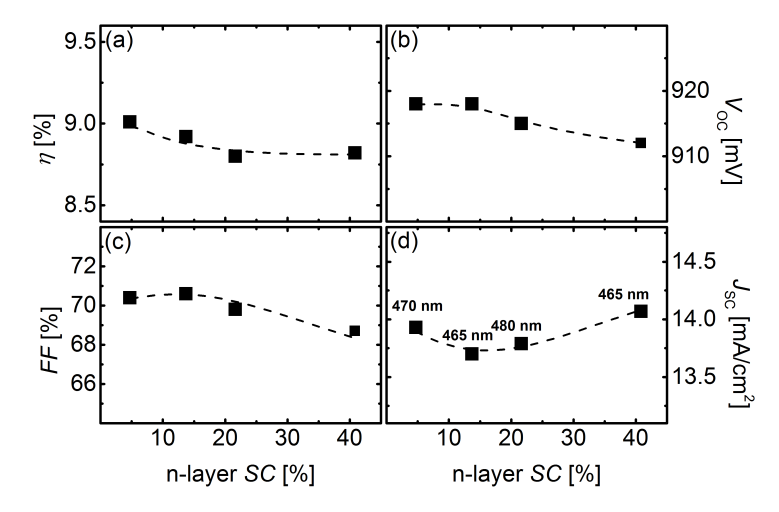


Figure 4.22.: Photovoltaic parameters for a-Si:H solar cells deposited at $120\,^{\circ}\text{C}$ as a function of silane concentration SC during the n-type layer deposition. Lines are guides to the eye.

efficiency could slightly be increased from 8.8% to 8.9% by using an SC of 13.7% during n-type layer deposition when a simple silver back contact is used.

N-Type Layer - Thickness Series Similar to the case of p-type layers, a certain thickness is essential to obtain an appropriate built-in field but simultaneously an increased thickness leads to parasitic absorption of light. In order to find the optimal thickness, the deposition time for the n-type layer is varied between 60 s and 140 s. All cells of this series were annealed for 120 minutes. Photovoltaic parameters of the solar cells are shown in Fig. 4.23. The data is plotted as a function of a-Si:H n-type layer deposition time $t_{\rm depo}$, as the n-type

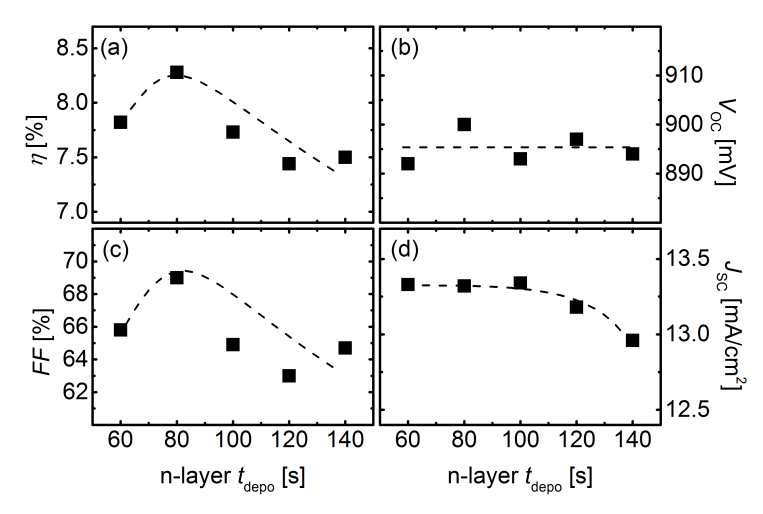


Figure 4.23.: Photovoltaic parameters of a-Si:H solar cells deposited at 120 °C as a function of n-type layer deposition time $t_{\rm depo}$. Lines are guides to the eye.

layer thickness cannot easily be measured in a device. It should be mentioned that this series was conducted one year after the results presented above. Due to changing system conditions, FF as well as $V_{\rm OC}$ are reduced from 70.6% to 64.7% and 918 mV to 894 mV, respectively, for similar deposition conditions used in the SC series for the n-type layer. For $V_{\rm OC}$ values presented in (b), no distinct trend is observed with varied deposition time of the n-type layer. The short-circuit current densities shown in (d) are constant up to a deposition time of 100 s, then decreases by $0.4\,\mathrm{mA/cm^2}$ for $t_{\rm depo} = 140\,\mathrm{s}$. This can be related to higher parasitic absorption losses in the long wavelength range, as also visible from EQE curves presented in Fig. 4.24. The fill factor first increases with increasing $t_{\rm depo}$ from 60 s to 80 s, then decreases again. The first increase may be related to an increase in built-in field with increasing layer thickness. The reduction in FF with further increasing thickness might possibly be due to an increased series resistance when the n-type layer becomes thicker. The optimal deposition time for the n-type layer was found to be 80 s, at which an absolute increase in FF and η of 4.3% and 0.8%, respectively, was observed compared to the 140 s deposition time that was used before.

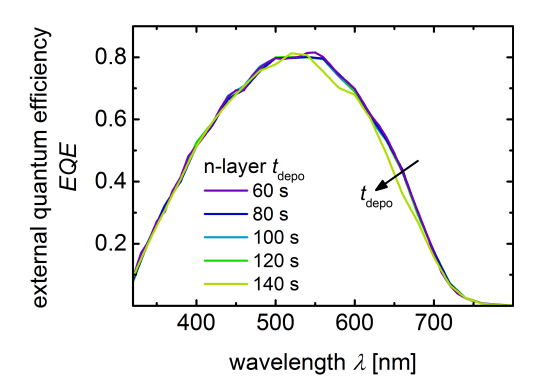


Figure 4.24.: External quantum efficiency EQE curves for a-Si:H solar cells deposited at 120 °C with various deposition times t_{depo} of the n-type layer.

4.1.5. Conclusion

The effects of a reduced substrate temperature, that is necessary for the application on PET substrates, on the electrical and optical properties of individual a-Si:H layers as well as on the performance of solar cells in p-i-n deposition sequence was investigated in this chapter. For all types of individual a-Si:H layers, a reduction in temperature during deposition leads to an increase in hydrogen content in the films, which in turn results in a slight increase in optical E_{04} gap. The electrical properties on the other hand are deteriorated when the temperature is reduced from 180 °C to 120 °C: by around two orders of magnitude in dark conductivity in case of p- and n-type layers and one order of magnitude in photo response for the intrinsic absorber layer. As a result, the fill factor of the solar cell deposited at low temperature decreases considerably from 73.6 % at 180 °C to 59.3 % at 120 °C. Down to a temperature of 140 °C, a drop in efficiency can be attenuated by an increase in $V_{\rm OC}$ due to the larger band gap of the absorber layer at lower temperature. But for $T_{\rm s} < 140$ °C, the influence of defects in low temperature a-Si:H layers overbalance and the efficiency drops by 21 % relative from 9.4 % at 180 °C down to 7.5 % at 120 °C.

In order to improve the device performance at low temperature, gas flow mixtures were adjusted for all individual layers. In case of p-type layers, the TMB and $\mathrm{CH_4}$ concentration was varied, revealing that the dark conductivity increases by more than one order of magnitude when no methane is added to the deposition gas mixture. The results obtained from FTIR measurements demonstrated that carbon is incorporated into the films not only from methane but also from TMB gas, which leads to a large carbon content in the case of <p> a-SiC:H layer. This in turn is known to induce defects in the film and would therefore result in a reduction of dark conductivity. In addition to this, due to the low temperature and incorporation of carbon from TMB gas, the band gap of the <p> a-Si:H layer is large enough for the application as window layer in a solar cell. Overall, the reduction in conductivity resulting from the low deposition temperature

could be almost compensated to the level of the high temperature reference layer, while the optical gap was even slightly increased from $2.0\,\mathrm{eV}$ to $2.1\,\mathrm{eV}$.

Regarding the n-type a-Si:H layer, the void-rich structure resulting from the low deposition temperature could be significantly improved by reduction in silane concentration during deposition. The corresponding increase in dark conductivity is as high as two orders of magnitude by reducing SC from 40.8% to 13.7%, almost up to the level of the high temperature reference. With further reduction in SC, the materials starts to grow microcrystalline, which increases the dark conductivity up to a level of 0.15 S/cm. In Fig. 4.25, the dark conductivity of the p- as well as n-type layers (circles and squares, respectively) investigated in this work are plotted as a function of E_{04} gap. Layers deposited at 180 °C are displayed in red color. The a-Si:H p-type layer requires a large band gap due

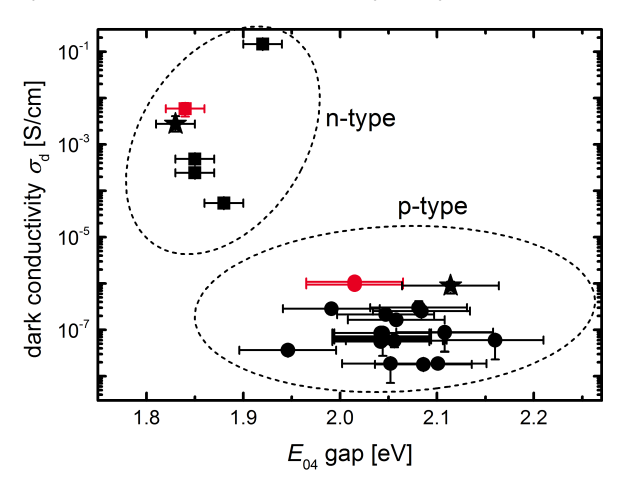


Figure 4.25.: Dark conductivity σ_d versus E_{04} gap for p-type (circles) as well as n-type (squares) silicon layers investigated in this work. The data for high temperature layers are shown in red color. Layers resulting in the best a-Si:H solar cell performance are displayed as stars.

to implementation as window layer in the solar cell. This however involves a relatively low conductivity as visible from the figure. Although the deposition gas mixture was varied in several ways, the dark conductivity varies only within two orders of magnitude with a maximum conductivity of $9\times10^{-7}\,\mathrm{S/cm}$ for a p-type layer deposited at $120\,^{\circ}\mathrm{C}$ (displayed as star in Fig. 4.25). As a consequence, FF and V_{OC} of the solar cell are improved from $59.3\,\%$ and $889\,\mathrm{mV}$ to $63.9\,\%$ and $896\,\mathrm{mV}$, respectively, when the optimized p-type layer is used as window layer instead of the reference p-type layer deposited at $120\,^{\circ}\mathrm{C}$. On the other hand, parasitic absorption in the n-type layer is less critical for the solar cell performance and lower band gaps can be tolerated. The result is a higher conductivity, which is relatively easy to vary over more than three orders of magnitude, just by varying the silane concentration during deposition. However, when implemented in a solar cell, this significant improvement only marginally affects the photovoltaic parameters, resulting in a small increase in efficiency from $8.8\,\%$ to $8.9\,\%$. This indicates that in this case other factors than n-type layer conductivity are limiting the solar cell performance.

In case of the intrinsic absorber layer, a reduction in silane concentration results in a higher structural order in the network, probably due to enhanced hydrogen etching during deposition and/or lower deposition rate. As a result, the defect density in the film (evaluated by $\alpha_{1.2\text{eV}}$) is reduced and the photo response could be improved to 10^6 at an SC of 8.3% for the low temperature layer. Simultaneously, the band gap slightly increases with lower SC. When the silane concentration is as low as 4.2%, the evolution of microcrystals in the film begins and a large scatter in the data could be observed. For the amorphous films, the slight increase in band gap results in an increasing $V_{\rm OC}$ and decreasing $J_{\rm SC}$, when implemented in a solar cell. Due to the improved material quality at lower SC, the fill factor is enhanced compared to the low temperature reference layer at SC=16.7%. The optimum silane concentration was found at 12.5%, resulting in an efficiency of 8.8%.

Besides variation of the deposition gas mixtures of individual layers at low temperature, layer thicknesses of each individual layer as well as the back contact was optimized. As a result, the efficiency could be increased from $7.5\,\%$ to $9.1\,\%$ for a solar cell deposited entirely at $120\,^{\circ}\mathrm{C}$ on Asahi-U substrates.

4.2. Microcrystalline Silicon and Tandem Solar Cells

The combination of absorber layers exhibiting different band gaps stacked on top of each other in tandem solar cells provide a potential to outperform the theoretical efficiency described by the Shockley-Queisser limit due to a more efficient photon utilization. Thereby thermalization losses may be reduced when high energy photons are absorbed in a large band gap material in the top cell, while low energy photons are mainly transmitted through and are absorbed in the bottom cell, whose absorber layer exhibits a smaller band gap. A widely investigated approach is the application of an amorphous silicon top cell with large band gap of $1.7-1.9\,\mathrm{eV}$ and a microcrystalline silicon bottom cell with a small band gap of $1.1\,\mathrm{eV}$. In order to fabricate this type of tandem solar cell at low temperature, the suitability of microcrystalline silicon layers deposited at $120\,\mathrm{^{\circ}C}$ for application in a single-junction solar cells is investigated first. Afterwards, the best amorphous solar cell from Section 4.1.4 as well as the microcrystalline solar cell with the highest efficiency are combined to an a-Si:H/ μ c-Si:H tandem device deposited at low substrate temperature.

It should be noted here that the following experiments were conducted at the end of this work and that only a limited number of microcrystalline layers and solar cells as well as tandem devices could be prepared within the remaining time frame. Accordingly, the results in this section represent only a first attempt for the development of low temperature a-Si:H/ μ c-Si:H tandem solar cells and further optimization need to be conducted in the future.

4.2.1. Microcrystalline Silicon

Individual layers are deposited on Corning glass substrates and the crystalline volume fraction $I_{\rm crs}$, which can serve as a measure for material composition, is estimated by Raman scattering measurements (see Section 3.3.3). The crystalline volume fraction in microcrystalline silicon layers can be adjusted by varying the silane concentration SC during deposition, and optimal solar cell efficiencies are usually observed for absorber layers with $I_{\rm crs}$ between 40 % to 70 % [241]. Therefore, a silane concentration series was conducted for intrinsic absorber layers deposited at $T_{\rm s} = 120\,^{\circ}{\rm C}$. The films (around 500 nm thick) tend to peel off the substrate after deposition, which is why the conductivity has not been measured. Raman scattering measurements were undertaken on the peeled-off layers.

In Fig. 4.26, resulting $I_{\rm crs}$ values are plotted as a function of silane concentration. Data for a silane concentration series for intrinsic layers deposited at 180 °C is taken from [180] and presented in the inset of the figure. A transition from amorphous ($I_{\rm crs} = 0\%$)

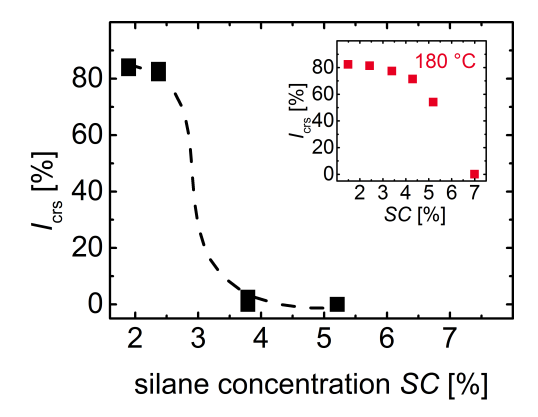


Figure 4.26.: Raman crystallinity I_{crs} as function of silane concentration SC for intrinsic absorber layers. The line is a guide to the eye. The inset shows data for intrinsic absorber layers deposited at 180 °C (taken from [180]).

to highly crystalline volume fraction of 84.0% is observed when the silane concentration is reduced from 5.2% to 1.9%. The transition occurs within a significantly narrower SC range between 3.8% and 2.4%, compared to the data for layers deposited at high deposition temperature in the inset, which is in agreement with literature [242]. This may result in a relatively difficult process control for obtaining optimal crystalline volume fractions between 40% to 70%.

It was shown that the crystallinity of microcrystalline films depends sensitively on the underlying substrate and layers [243–245], therefore the final optimization of silane concentration for the absorber layer deposition was directly performed in a p-i-n solar cell. The p-type layer should have sufficient crystalline fraction to serve as a nucleation layer for the development of microcrystals in the intrinsic absorber layer [246]. The reference ptype layer deposited at low temperature exhibits satisfactory properties with $I_{\rm crs}=43.8\,\%$ and dark conductivity of 0.1 S/cm (measured on a 100 nm thick film) and was therefore in the first instance not further optimized. As n-type layer, the optimized a-Si:H layer with SC of 13.7 % shown in Section 4.1.4 was used. Similar to the case of a-Si:H solar cells, a significant annealing effect was found for μ c-Si:H solar cells that will be discussed later in Section 5.6. The measurements on the solar cells shown in this chapter were conducted after post-deposition annealing for 30 minutes. A ZnO:Al/Ag back contact was used and $J_{\rm SC}$ was calculated from EQE curves to avoid the effect of additional charge carriers collected from regions outside the solar cell area due to the highly conductive p-type layer. The absorber layer thickness was around 1 μ m for all solar cells presented here. Due to reduction effects in SnO₂:F substrates under conditions with a high flux of atomic hydrogen at low silane concentrations, resulting in reduced transmission of light, ZnO:Al was used as TCO layer. Corning Eagle XG glass substrates were covered with a ZnO:Al layer deposited at high temperature of 300 °C and texture-etched in HCl for 40 s [118].

In Fig. 4.27, the photovoltaic parameters of the μ c-Si:H solar cells are shown as a function of $I_{\rm crs}$ of the intrinsic absorber layer resulting from various silane concentrations during deposition. The data for a reference cell deposited at 180 °C is shown for comparison (red circle). The reference device has an absorber layer thickness of 1.8 μ m and uses a ZnO:Al/Ag back contact as well. Typical trends (see [37]) for the dependence of photo-

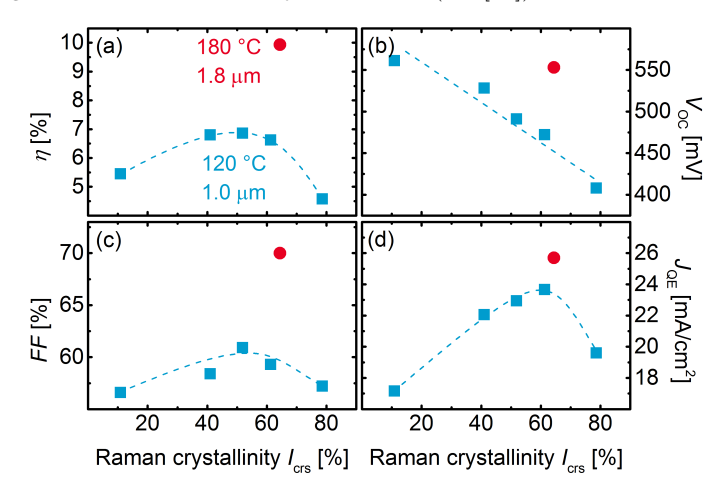


Figure 4.27.: Photovoltaic parameters of μ c-Si:H solar cells deposited at 120 °C as function of $I_{\rm crs}$ of the intrinsic absorber layer. The total thickness of silicon layers is around 1 μ m. The data for a reference cell deposited at 180 °C and with an absorber layer thickness of 1.8 μ m is shown for comparison (red circle). Lines are guides to the eye.

voltaic parameters on silane concentration or corresponding crystalline volume fractions are evident for the low temperature μ c-Si:H solar cells from Fig. 4.27 (blue squares). The open-circuit voltage shown in (b) decreases with increasing crystallinity of the absorber layer. This can be attributed to a reduction in the "effective" band gap, when a higher crystalline volume fraction exhibiting a small band gap of 1.1 eV is present in the layer.

Both FF and J_{QE} presented in (c) and (d), respectively, first increase when a larger crystalline volume fraction is present in the absorber layer, reach a maximum at around $I_{\rm crs}$ of 50-60% and decrease again with further increase in $I_{\rm crs}$. From EQE curves in Fig. 4.28 it is evident that charge carrier collection is hindered for $\lambda > 400$ nm at large $I_{\rm crs}$ of 78.6%. Vetterl et al. hypothesized that the deteriorated charge carrier collection may

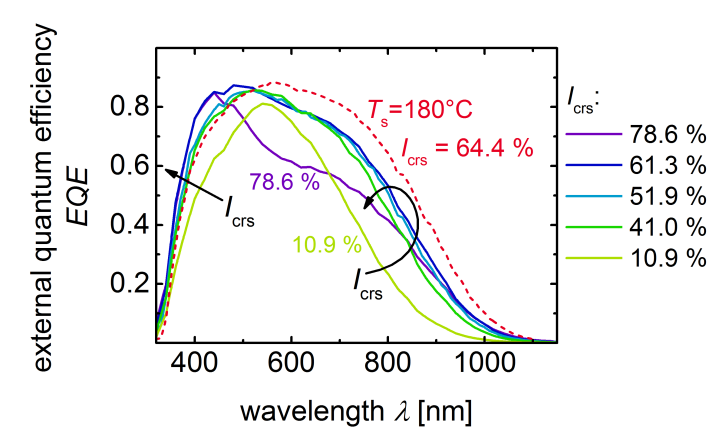


Figure 4.28.: External quantum efficiency EQE curves for μ c-Si:H solar cells deposited at 120 °C having an absorber layers thickness of 1 μ m and exhibiting various crystalline volume fractions $I_{\rm crs}$. The EQE curve for the reference μ c-Si:H solar cell deposited at 180 °C and with an absorber layer thickness of 1.8 μ m is shown for comparison (red dashed line).

result from possible breakdowns in the electrical field, recombination losses or interface effects between doped and intrinsic layers [37]. At high crystalline volume fractions the passivation of grain boundaries and/or crystalline columns may be insufficient, resulting in a large number of defects and thus poor charge carrier collection. Another possible reason for the drop in FF at high $I_{\rm crs}$ might be related to ohmic shunts in the microcrystalline solar cell, when a pronounced columnar growth of crystallites leads to cracks within the intrinsic layer [28]. This is in agreement with measured shunt resistance $R_{\rm sh}$ values, evaluated from dark J-V curves, shown in Fig. 4.29. Here, a decreased $R_{\rm sh}$ with increasing $I_{\rm crs}$ can be observed. In the case of low $I_{\rm crs}$ values, the drop in FF and $J_{\rm SC}$ might be related to losses in charge carrier collection losses due to a low electron mobility in microcrystalline silicon material with a large amorphous volume fraction, as suggested by Reynolds et al. [247]. Overall, the highest efficiency for a μ c-Si:H solar cell deposited at low temperature on glass substrate in this work was 6.9% at a crystallinity of 52%, with $V_{\rm OC}$ = 491 mV, FF = 60.9% and J_{QE} = 22.9 mA/cm².

Comparison to the high temperature solar cell reveals that, similar to a-Si:H solar cells, a high deposition temperature is beneficial for all photovoltaic parameters of the μ c-Si:H solar cell (see Fig. 4.27). Especially the fill factor is significantly higher around 70%. Possible reasons might be related to an increased number of cracks in the intrinsic layer at low substrate temperatures [248], limited activation of doped layers [249] or higher defect densities at crystalline grain boundaries [250]. Similar reasons might also affect

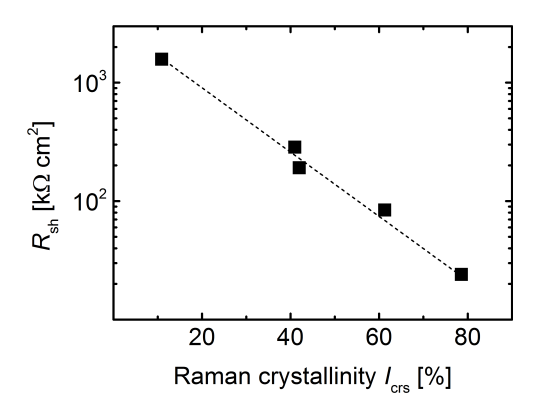


Figure 4.29.: Shunt resistance $R_{sc,dark}$ evaluated from dark J-V measurements as a function of Raman crystallinity I_{crs} . The line is a guide to the eye.

 $V_{\rm OC}$. However, it should be noted that the Raman crystallinity was measured with a laser wavelength of 488 nm in case of the high temperature solar cell which means that the probed thickness is less than in the case of the low temperature device which was measured with a laser wavelength of 532 nm. Since the intrinsic absorber layer usually gets more crystalline in growth direction [251] and the measurement was performed through the n-type layer of the device, the $I_{\rm crs}$ value for the high temperature solar cell might be overestimated. The higher J_{QE} may at least partly be related to the thicker absorber layer (1.8 μ m for the high temperature and 1.0 μ m for the low temperature solar cell, respectively), since the increase is mainly visible in the long wavelength range above 500 nm, as evident from Fig. 4.28.

4.2.2. Tandem Solar Cells

Efficiencies of 9.1% and 6.9% for a-Si:H and μ c-Si:H single junction solar cells deposited at 120 °C were achieved in this work and these solar cells were then stacked to tandem solar cells. The a-Si:H top cell is deposited first, allowing the use of SnO₂:F covered substrates. In this case, Asahi-VU type glass substrates were used. Microcrystalline n-and p-type layers are used for the tunnel recombination junction between the sub cells to ensure a low series resistance. The reference μ c-Si:H n-type layer deposited at 120 °C exhibits satisfactory properties with $I_{\rm crs}$ =67.6% and dark conductivity of 0.05 S/cm and was therefore in the first instance not further optimized. The resulting layer stack is as follows: a-Si:H / <i> a-Si:H / <n> μ c-Si:H / μ c-Si:H / <i> a-Si:H / <n> a-Si:H (see also Fig. 3.7(c) in Section 3.2.4). The post-deposition annealing was conducted for 5 hours. Similar to the case of μ c-Si:H single junction solar cells, the back contact consists of a ZnO:Al/Ag layer stack. The thickness of the top and bottom cell were 350 nm and 1000 nm, respectively.

Resulting photovoltaic parameters are presented in Table 4.3. In the case of a high

Table 4.3.: Photovoltaic parameters of the a-Si:H/µc-Si:H tandem solar cell deposited at 120 °C.

| η [%] | FF~[%] | $V_{\rm OC}~[{\rm mV}]$ | $J_{\rm SC}~[{\rm mA/cm^2}]$ |
|------------|--------|-------------------------|------------------------------|
| 9.8 | 70.2 | 1370 | 10.2 |

quality tunnel recombination junction, the $V_{\rm OC}$ value of the tandem device should roughly correspond to the sum of the $V_{\rm OC}$ values of the corresponding a-Si:H and μ c-Si:H single junction solar cells. The $V_{\rm OC}$ of the μ c-Si:H single junction cell is measured under red light (OG590 filter) in such a case to simulate the situation in the tandem cell, where the light of short wavelength is filtered by the top cell. The $V_{\rm OC}$ of the tandem solar cell attains nearly the sum of $V_{\rm OC}$ from single junction cells with 1370 mV, when the corresponding cells exhibit 900 mV (a-Si:H) and 477 mV (μ c-Si:H, under red light). This, and also an appropriate fill factor of 70.2%, indicate that the combination of sub cells was successful and the tunnel recombination junction works appropriately [252], although no distinct optimization of the doped microcrystalline silicon layers at low temperature was conducted.

An important point in the development of tandem solar cells is the current matching, as the top and bottom cell are connected in series and the sub cell providing the lowest current will limit the cell performance. From EQE curves in Fig. 4.30 it is evident that the bottom cell exhibits a lower current density and thus limits the overall J_{SC} of the device. The mismatched state of this tandem solar cell can also be the reason for the relatively

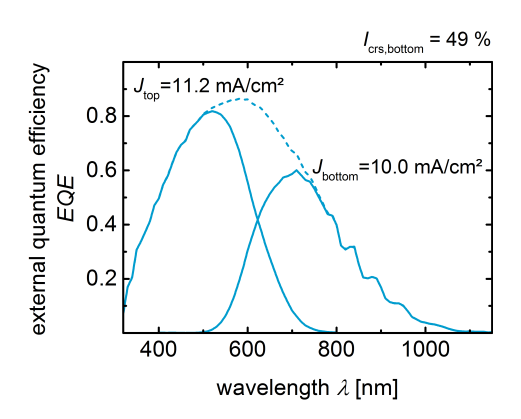


Figure 4.30.: External quantum efficiency EQE curve for the a-Si:H/ μ c-Si:H tandem solar cell with I_{crs} of the bottom cell of 49%, top and bottom cell thickness of 350 nm and 1000 nm, respectively.

high fill factor, which exceeds the ones from the single junction solar cells (68.9 % and 60.9 % in the case of a-Si:H and μ c-Si:H, respectively) [253, 254]. Nevertheless, in this unmatched state the tandem solar cell deposited at low temperature already achieves an efficiency of 9.8 %, thereby outperforming the single junction solar cells presented above.

4.2.3. Conclusion and Outlook

In the sections above, the development of μ c-Si:H and a-Si:H/ μ c-Si:H solar cells at low temperature of 120 °C was presented. Regarding the microcrystalline silicon doped layers and in contrast to the case of a-Si:H layers, satisfactory electrical properties were obtained for reference layers deposited at 120 °C. For this reason, deposition parameters were not adjusted so far. In terms of intrinsic μ c-Si:H, it was possible to obtain layers deposited at low temperatures with crystalline volume fractions of up to 82 %, yet the silane concentration range for optimal intrinsic absorber layers with $I_{\rm crs}$ between 40 % to 70 % is considerably smaller than for μ c-Si:H layers deposited at high temperature, which may result in a more difficult process control.

When these absorber layers are implemented in a p-i-n solar cell, similar trends as in series of varied silane concentration or respective crystallinity conducted at 180 °C were observed. At low $I_{\rm crs}$, the performance is limited by $J_{\rm SC}$ due to high fraction of amorphous material exhibiting a large band gap as well as a low electron mobility leading to additional reductions in FF. At high $I_{\rm crs}$ on the other hand, a reduction in shunt resistance was found, hindering the collection of charge carriers and thereby deteriorating FF and $J_{\rm SC}$. An efficiency of 6.9% was achieved when the intrinsic layer shows a crystalline volume fraction of 52%. Compared to the reference cell, deposited at higher substrate temperature but with increased absorber layer thickness of 1.8 μ m, reductions in all photovoltaic parameters were found. The largest difference was observed in FF, with an absolute reduction of 9% when the substrate temperature is lowered to 120 °C at similar values of $I_{\rm crs}$.

The μ c-Si:H solar cell with the highest efficiency at low temperature was combined with the low temperature a-Si:H solar cell exhibiting the highest efficiency of 9.1% in a tandem solar cell. As a result, an efficiency of 9.8% was achieved. The sub cells of the device are not matched in terms of current density, providing a great potential for further optimization. Efficiencies exceeding 10% should be feasible for a tandem solar cell fabricated at 120 °C by adjusting the sub cell current densities, for instance by reducing the top cell thickness or increasing the bottom cell thickness. Further potential for improvement in FF and $V_{\rm OC}$ is related to the material optimization of p- and n-type microcrystalline silicon layers deposited at low temperature, possibly even by use of microcrystalline silicon oxide layers that potentially improve $J_{\rm SC}$ [69]. In order to find the optimal trade-off between parasitic absorption and electrical properties, also the thickness of the μ c-Si:H doped layers, that constitute the tunnel recombination junction between the two sub cells, should be adjusted. In addition, profiling of the silane concentration during deposition as well as a-Si:H buffer layers between p-/i- or i-/n-interfaces have been shown to improve the $V_{\rm OC}$ in microcrystalline solar cells [63, 255].

5. Annealing Effects in Thin-Film Silicon Solar Cells

5.1. Introduction

Amorphous silicon solar cells deposited at low temperature can be sensitive to post-deposition annealing [75, 76]. In this work, a significant improvement in all photovoltaic parameters of a-Si:H solar cells (presented in Chapter 4) upon post-deposition annealing at $120\,^{\circ}$ C is observed. An example for typical changes in photovoltaic parameters with annealing time is shown in Fig. 5.1, for the case of an a-Si:H solar cell deposited at $120\,^{\circ}$ C on glass substrate (black squares). For the purpose of comparison, the effect of annealing on the standard (high temperature) solar cell deposited at $180\,^{\circ}$ C is shown (red triangles). The corresponding J-V curves for the low temperature solar cell are presented

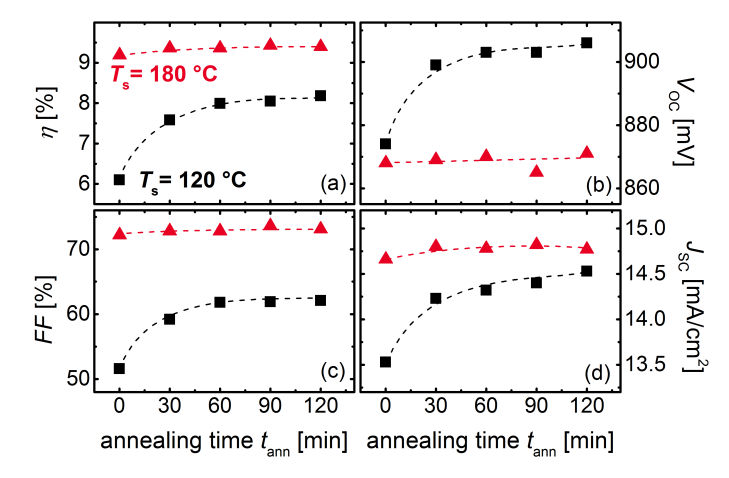


Figure 5.1.: Photovoltaic parameters for the reference a-Si:H solar cell deposited at $120\,^{\circ}$ C (black squares) and $180\,^{\circ}$ C (red triangles) as a function of post-deposition annealing time $t_{\rm ann}$ at $120\,^{\circ}$ C in air. Lines are guides to the eye.

in Fig. 5.2 for various annealing times. It can be seen that for the case of low deposition temperature, a significant improvement upon post-deposition annealing is observed in all photovoltaic parameters. The largest effect is visible in FF, increasing from 51.6 % to 62.1 % after 120 minutes annealing time, corresponding to a relative improvement of 20 %. Simultaneously, $V_{\rm OC}$ increases by 4 % from 874 mV to 906 mV and $J_{\rm SC}$ by 7 % from 13.5 to

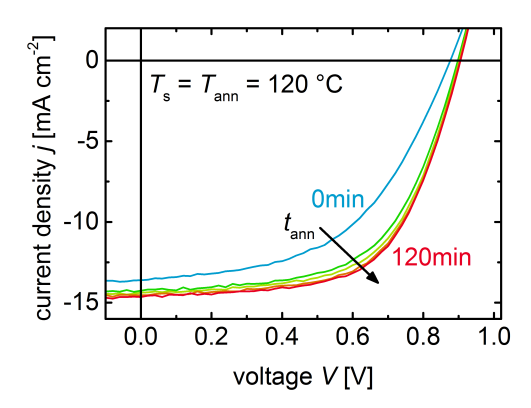


Figure 5.2.: Current density-voltage (J-V) curves for various annealing times $t_{\rm ann}$ for an a-Si:H solar cell deposited at 120 °C.

 $14.5\,\mathrm{mA/cm^2}$. This results in a relative efficiency η increase of $34\,\%$, from $6.1\,\%$ in the asdeposited state to $8.2\,\%$ after $120\,\mathrm{minutes}$ annealing. On the other hand, for the solar cell deposited at $180\,^\circ\mathrm{C}$ the efficiency increases by merely $3\,\%$ relative upon post-deposition annealing at $120\,^\circ\mathrm{C}$.

An improvement in solar cell efficiency upon annealing described above can be a result of improved properties in the individual layers and/or interfaces present in the solar cell. Here, the solar cell is a multilayer device consisting of TCO layers, various silicon thin films and metal (Ag) layer (see also Fig. 3.7 in Section 3.2.4). Therefore, a possible contribution from each particular layer in the observed annealing effects should be discussed:

- (i) Ag contacts (Ag/silicon interface): effects resulting from the Ag/n-type a-Si:H back contact can be excluded as similar improvements upon annealing were found for annealing procedures carried out before as well as after silver evaporation. Furthermore, the annealing effect is similar for application of Ag as well as ZnO:Al/Ag as back contact.
- (ii) TCO layer (TCO/p-contact): regarding the influence of the Asahi-U type substrate, no variation in optical or electrical properties upon annealing could be detected. As improvements upon annealing were found for various types of TCOs, like SnO₂:F, ZnO:Al, ITO and hydrogen-doped indium oxide (IO:H), also the TCO/p-contact is unlikely the cause.

Therefore, the contribution from the silver contact and TCO layer to the observed changes in the solar cell performance upon annealing can be excluded.

(iii) Another possibility to be discussed is related to the presence of ambient air during annealing of the solar cells. Since ambient air is a mixture of nitrogen, oxygen, carbon dioxide and other gases, a possible incorporation of these impurities into silicon layers upon annealing has to be studied. Secondary Ion Mass Spectrometry (SIMS) analysis was therefore performed on a-Si:H solar cells in the as-deposited state as well as after

annealing for 30 and 120 minutes. The corresponding depth profiles of hydrogen, phosphorus, oxygen, carbon and nitrogen (probed by secondary ions of ¹H⁻, ³¹P⁻, ¹⁶O⁻, ¹²C⁻ and ²⁸Si¹⁴N⁻, respectively) are shown in Fig. 5.3. It can be seen that the depth

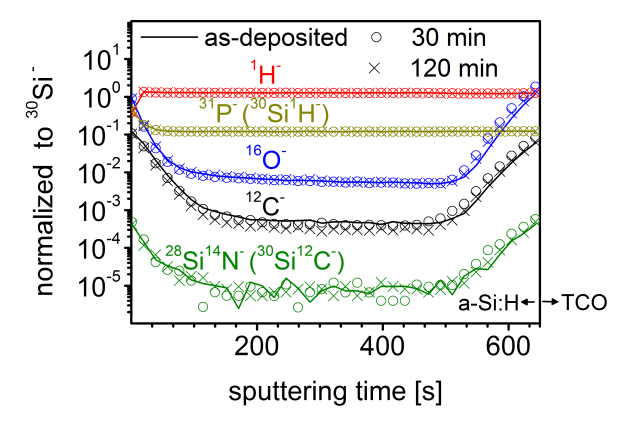


Figure 5.3.: Secondary Ion Mass Spectrometry (SIMS) profiles of an a-Si:H solar cell in the as-deposited state (line), after annealing for $30 \,\mathrm{minutes}$ (open circles) as well as $120 \,\mathrm{minutes}$ (crosses). Please note that the signal for $^{31}\mathrm{P}^-$ and $^{28}\mathrm{Si}^{14}\mathrm{N}^-$ ions are superimposed by signals from $^{30}\mathrm{Si}^{14}\mathrm{H}^-$ and $^{30}\mathrm{Si}^{12}\mathrm{C}^-$ ions, respectively.

profiles of the investigated secondary ion signals are similar to the as-deposited state for both annealing times, indicating no diffusion of air related impurities into the films upon annealing, probably due to the encapsulation of the silicon layers by the glass substrate and silver back contact. Additionally, it should be noted that no long-range diffusion of e.g. phosphorus atoms is observed.

Overall, our results indicate that changes in the photovoltaic parameters of a-Si:H solar cells upon annealing are related to changes in the amorphous silicon layers and/or interfaces. In the following sections, the origin of the annealing effect observed in the solar cells is investigated by examining individual a-Si:H layers and various cell configurations subject to post-deposition annealing. In the discussion (Section 5.4), a link between the properties of individual silicon layers and the solar cell performance upon annealing is addressed.

Unless noted differently, the samples shown in this chapter were all prepared on glass substrates. A remark about the annealing effect of solar cells on flexible substrates will be given in Section 5.5. Parts of the results shown in this chapter have previously been published in [256].

5.2. Annealing of Individual Silicon Layers

In the literature, the annealing effects observed in a-Si:H solar cells are frequently related to changes in the properties of individual silicon layers upon annealing (cf. Section 2.4). This includes changes in the electrical and optical properties of the layers, monitored by e.g. dark and photo conductivity and absorption coefficient spectra [86, 89]. Changes in the bonding configuration, especially related to hydrogen movement upon annealing, are analyzed by FTIR measurements [86, 89].

In this section, the electrical and optical properties as well as the bonding structure of the low temperature intrinsic, p- and n-type a-Si:H layer are investigated as a function of annealing time $t_{\rm ann}$. In order to investigate the Si-H bonding configuration, the FTIR spectrum in the range from 1900 to $2200\,{\rm cm}^{-1}$ is investigated, where the vibrational frequency of the Si-H stretching mode is present. The layers investigated in this section are the reference layers deposited under conditions specified in Table E.1 in Appendix E but at a substrate temperature of $120\,{}^{\circ}{\rm C}$. In all experiments presented in this section the annealing temperature was kept constant at $120\,{}^{\circ}{\rm C}$.

5.2.1. Annealing of P-Type a-Si:H Layers

Fourier transform infrared spectroscopy measurements were conducted on the p-type a-Si:H layer after various times of post-deposition annealing to investigate the influence of annealing on the structural bonding configuration of hydrogen in the film. The spectrum between 1900 and 2200 cm⁻¹, where the Si-H stretching vibration mode is present, is shown in Fig. 5.4 for various annealing times. For further details on the interpretation

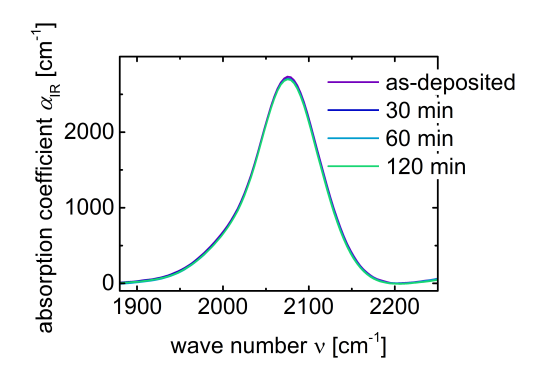


Figure 5.4.: Infrared absorption peak of the Si-H stretching mode of the p-type a-Si:H layer deposited at $120\,^{\circ}$ C after various post-deposition annealing times between 0 (as-deposited) and $120\,\text{minutes}$.

of FTIR spectra, see Sections 3.3.3 and 4.1.1. It is evident that no change in the Si-H stretching mode can be observed upon annealing up to 120 minutes, indicating that no significant change in the Si-H bonding configuration occurs.

The effect of post-deposition annealing on the electrical properties was probed by measurements of dark conductivity σ_d and results are shown as a function of annealing time in Fig. 5.5. It is evident that the dark conductivity increases with increasing anneal-

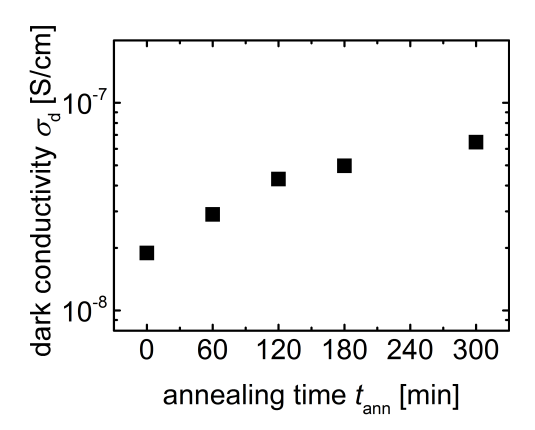


Figure 5.5.: Dark conductivity σ_d of the p-type a-Si:H layer deposited at 120 °C as function of post-deposition annealing time t_{ann} .

ing time from 1.9×10^{-8} S/cm in the as-deposited state (0 minutes) to 6.5×10^{-8} S/cm after 5 hours (300 minutes) annealing. After 120 minutes, which is the time where an increase in solar cell efficiency of 34% was found, the dark conductivity has increased by a factor of 2.3. A possible explanation is related to the activation of dopants by breaking boron-hydrogen complexes that keep the boron atoms in a non-active three-fold coordination [101, 102].

5.2.2. Annealing of N-Type a-Si:H Layers

Similar to the case of p-type layers, FTIR measurements were conducted after various annealing times and the corresponding FTIR absorption peaks of the Si-H stretching mode are shown in Fig. 5.6. It can be seen that no considerable change in the FTIR absorption peak between 1900 and 2200 cm⁻¹ occurs, implying that the number of Si-H bonds and thus hydrogen content is not affected by post-deposition annealing at 120 °C in air. The similarity of the curves also indicates that no transfer from dihydride bonds (Si-H₂) to monohydride bonds (Si-H) or vice versa has occurred.

Regarding optical properties, PDS measurements were performed after various times of annealing. From these measurements, the optical gap E_{04} and sub-gap absorption $\alpha_{1.2\text{eV}}$, which serves as a measure for the defect density, were evaluated. The results are shown in Fig. 5.7(a). A slight decrease in the E_{04} gap is visible with increasing annealing time. At the same time, the sub-gap absorption increases from 725 cm⁻¹ in the as-deposited state to 890 cm⁻¹ after 60 minutes annealing, implying that the defect density increases upon annealing. In Fig. 5.7(b) the dark conductivity is plotted as a function of

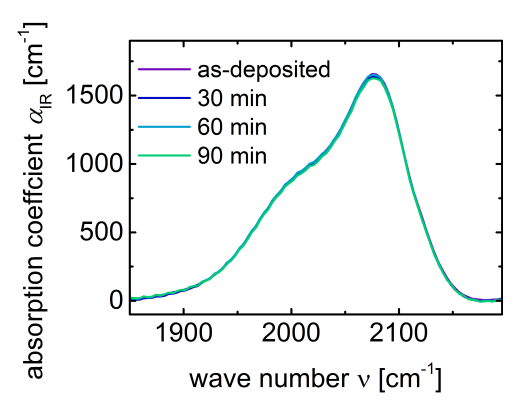


Figure 5.6.: Infrared absorption peak of Si-H stretching mode of the n-type a-Si:H layer deposited at $120\,^{\circ}\text{C}$ for various post-deposition annealing times between 0 and 90 minutes.

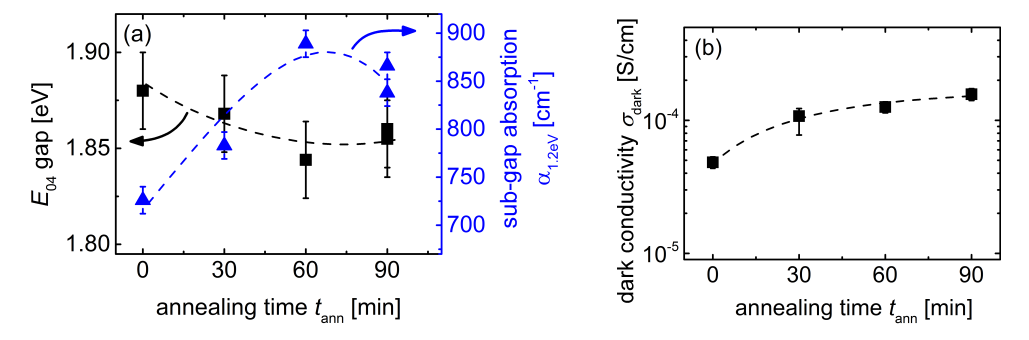


Figure 5.7.: (a) Sub-gap absorption $\alpha_{1.2\text{eV}}$ (blue triangles, right axis) and E_{04} gap (black squares, left axis) as well as (b) dark conductivity σ_{d} of the n-type a-Si:H layer deposited at $120\,^{\circ}\text{C}$ as a function of post-deposition annealing time t_{ann} . Lines are guides to the eye.

annealing time and similar to the case of p-type layers, an increase with annealing time can be observed. More precisely, $\sigma_{\rm d}$ increases from the as-deposited value of $4.8\times10^{-5}\,{\rm S/cm}$ by a factor of 3.1 to $1.5\times10^{-4}\,{\rm S/cm}$ after 90 minutes annealing.

The concurrent increase in sub-gap absorption and dark conductivity may indicate an activation of dopant atoms in the material, that is usually accompanied by an increase in defect density [27]. Furthermore, the slight reduction in band gap may change the Fermi level position and thus activation energy in the film, in agreement with increasing dark conductivity upon annealing.

5.2.3. Annealing of Intrinsic a-Si:H Layers

The device performance of an a-Si:H solar cell largely depends on the material properties of the intrinsic absorber layer. Incoming photons are absorbed in this layer and generated charge carriers need to pass through to be collected at the contacts. Variations in the intrinsic layer properties upon annealing may therefore significantly influence the device performance and are thus investigated in this section.

Similar to the case of doped layers, the FTIR absorption peak of the Si-H stretching vibration after various annealing times is shown in Fig. 5.8. Again, no change in the

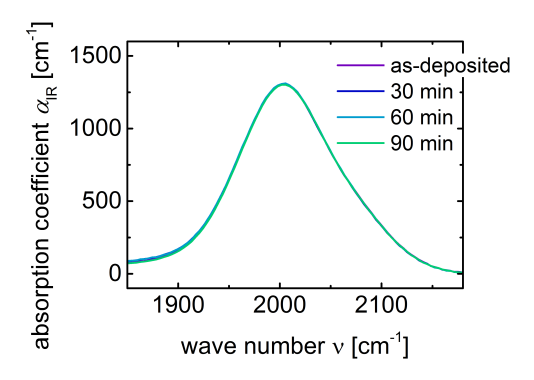


Figure 5.8.: Infrared absorption peak of the Si-H stretching mode of the intrinsic a-Si:H layer deposited at 120 °C for various annealing times between 0 and 90 minutes.

Si-H bonding configuration or number of Si-H bonds can be detected by FTIR, thereby suggesting that the annealing has no detectable effect on the hydrogen content in the film. As visible from Fig. 5.9, also no distinct trend can be observed in the E_{04} gap and sub-gap absorption $\alpha_{1.2\text{eV}}$ with annealing time, as evaluated from PDS measurements. Regarding the electrical properties, photo σ_{ph} and dark σ_{d} conductivity were measured after several annealing steps. The results are shown as a function of annealing time in Fig. 5.10(a). The photo conductivity increases within the first annealing step of 30 minutes by a factor of 3.3 from $3.0 \times 10^{-7} \,\text{S/cm}$ to $1.0 \times 10^{-6} \,\text{S/cm}$ and stays relatively constant with further annealing steps. The dark conductivity increases as well within the first annealing step from $7.1 \times 10^{-12} \,\text{S/cm}$ to $2.8 \times 10^{-11} \,\text{S/cm}$, but then slightly decreases again

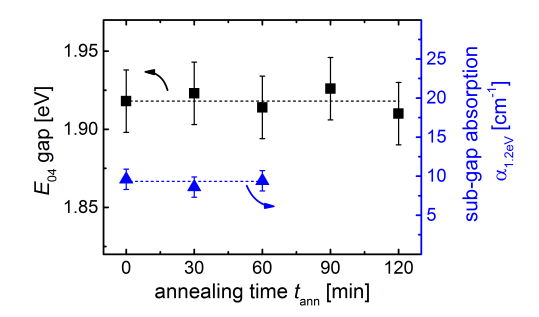


Figure 5.9.: Sub-gap absorption $\alpha_{1.2\text{eV}}$ (blue triangles, right axis) and E_{04} gap (black squares, left axis) of the intrinsic a-Si:H layer deposited at 120 °C as a function of annealing time t_{ann} . Lines are guides to the eye.

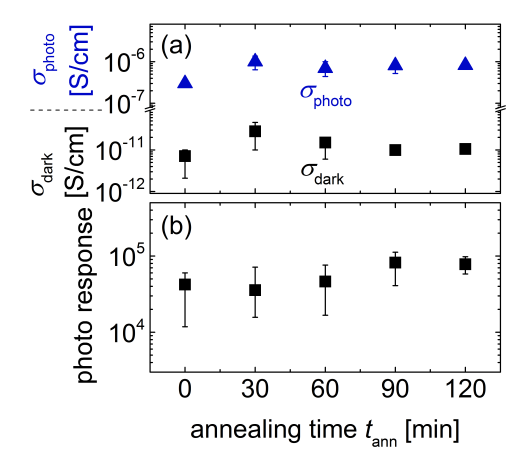
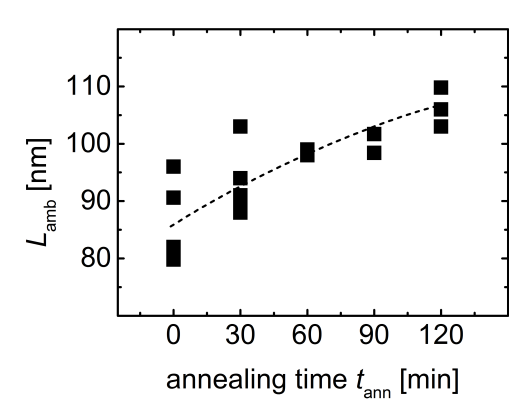


Figure 5.10.: (a) Dark $\sigma_{\rm d}$ (black squares) and photo $\sigma_{\rm ph}$ (blue triangles) conductivity as well as (b) photo response of the intrinsic a-Si:H layer deposited at 120 °C as function of annealing time $t_{\rm ann}$.

to 1.0×10^{-11} S/cm. As a result, the photo response shown in Fig. 5.10(b) increases slightly with annealing time.

In nominally undoped a-Si:H, electrons are majority carriers and measurements of photo conductivity are thus dominated by electron transport [210, 257]. Possible changes in the hole transport properties upon annealing would not be detectable from photocurrent measurements. In a solar cell however, the charge carriers with the lowest drift length may limit the cell performance. Steady-state photocarrier grating (SSPG) measurements were therefore performed to investigate the effect of post-deposition annealing on the hole transport properties in the intrinsic a-Si:H layer. The measurements were conducted by M. Güneş at the Mugla University, Turkey. From SSPG measurements, the ambipolar diffusion length $L_{\rm amb}$ is evaluated, which is dominated by minority carrier transport properties and thus serves as a measure for the latter. $L_{\rm amb}$ is plotted as a function of annealing



time $t_{\rm ann}$ in Fig. 5.11. Besides some scatter in the data, which results from various samples

Figure 5.11.: Ambipolar diffusion length $L_{\rm amb}$ evaluated from SSPG measurements of the intrinsic a-Si:H layer deposited at 120 °C as function of annealing time $t_{\rm ann}$. The dashed line is a guide to the eye.

as well as evaluation techniques [211], a clear trend of increasing $L_{\rm amb}$ from $88\pm8\,\rm nm$ to $106\pm4\,\rm nm$ with increasing annealing time up to 120 minutes is evident from the graph. This indicates an improvement in the transport properties of minority carriers in the film upon annealing at 120 °C. Comparison to the intrinsic layer deposited at 180 °C, $L_{\rm amb}$ is still significantly lower, as the high temperature layer exhibits a diffusion length of $198\pm15\,\rm nm$, without a detectable change upon annealing (not shown).

Discussion

The increase in dark conductivity of the intrinsic layer indicates a reduced activation energy and thus a shift of the Fermi level $E_{\rm F}$ towards conduction band upon annealing. Following Eq. 2.6, a maximum change in Fermi level position is estimated to be 0.034 eV. It is well known that a shift in Fermi level also influences the $\mu\tau$ -product of the charge carriers [210, 257, 258]. Upon a shift of the Fermi level towards the conduction band an increased number of defect states is negatively charged. As a result, the defects become less attractive for electron capture and the lifetime and thus $(\mu\tau)_{\rm e}$ -product of electrons increases. This in turn directly increases the photo conductivity as evident in Fig. 5.10. Beyer and Hoheisel [232] proposed that conductivities for all undoped or slightly doped a-Si:H films "deposited under optimized conditions" fall on one curve, which is indicated by the blue dash-dotted line in Fig. 5.12. It was suggested [232] that shifts along this curve, as it is the case for the layers in this work after prolonged annealing times up to 7 hours (see Fig. 5.12), result mainly from a change in Fermi level position rather than material quality, i.e. defect density. On the other hand, more negatively charged recombination centers, appearing with the shift in Fermi level towards conduction band, imply a higher probability for holes to recombine, thereby reducing their lifetime τ_h [232]. However, the ambipolar diffusion length $L_{\rm amb}$, which is proportional to the $(\mu\tau)_{\rm h}$ -product of minority

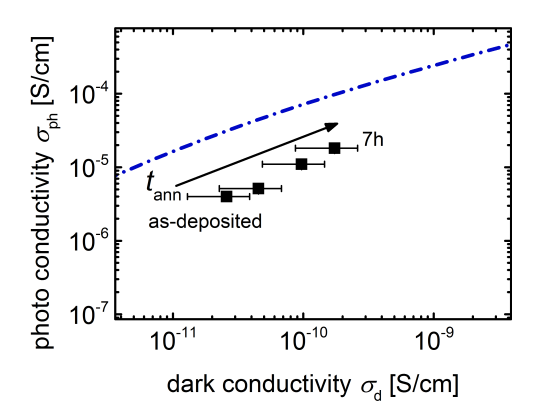


Figure 5.12.: Photo conductivity $\sigma_{\rm ph}$ as a function of dark conductivity $\sigma_{\rm d}$ for the intrinsic a-Si:H absorber layer deposited at 120 °C for various post-deposition annealing times $t_{\rm ann}$ between 0 and 120 minutes. The blue dash-dotted line indicates the curve on which films grown under optimized conditions fall, as suggested by Beyer and Hoheisel [232].

carriers, considerably increases upon annealing. This clearly indicates either a reduction in the total defect density (therefore an increase in τ_h) and/or an increase in μ_h upon annealing. The sub-gap absorption measured by CPM showed no change upon annealing, thereby suggesting a constant defect density. However, the measured photocurrent is dominated by the $(\mu\tau)_e$ -product of majority carriers [259] and a variation in τ_h would not be accessible in this measurement.

5.2.4. Summary

The results of post-deposition annealing of individual layers can be summarized as follows:

- In all three types of layers (p, n, i) no detectable change in hydrogen bonding configuration of the films could be observed.
- The dark conductivity of both p- and n-type layers increases with increasing annealing time, up to a factor of 2.3 and 3.3 (after 120 min/90 min annealing), respectively.
- Regarding the intrinsic a-Si:H layer, no change in sub-gap absorption or E_{04} gap upon annealing could be detected by CPM and PDS measurements.
- The Fermi level in the intrinsic a-Si:H layer is slightly shifted towards the conduction band upon annealing (maximum shift of 0.034 eV), leading to an increase in both dark conductivity and (μτ)_e-product of electrons as majority carriers.
- The ambipolar diffusion length $L_{\rm amb}$, related to the $(\mu\tau)_{\rm h}$ -product of holes as minority carriers increases upon annealing, as detected from the results of SSPG measurements.

5.3. Annealing of a-Si:H Solar Cells

After the investigation of individual layers, in this section the focus will be on the influence of annealing on the a-Si:H solar cell performance. Selected layers in the solar cell were replaced by layers exhibiting different material properties in order to investigate their influence on the annealing behavior of the solar cell. Variable Intensity Measurements (VIM) were performed to distinguish between the effects of charge carrier collection, series and shunt resistance in the device upon annealing. In order to learn more about charge carrier collection, external quantum efficiency measurements were conducted on solar cells of various absorber layer thicknesses and illumination sides (p- and n-side illuminated).

5.3.1. Effect of Individual Layers on the Annealing Behavior of Solar Cells

From the results in Section 5.2, improvements in the material properties of individual silicon layers were observed upon post-deposition annealing. In order to estimate the effect on the solar cell performance resulting from this improvement, silicon layers were systematically replaced by layers exhibiting various electronic properties. An attempt is made to determine to what extent each silicon layer contributes to the improvement in solar cell performance. For this purpose, the silicon layers are systematically replaced by high temperature layers (weakly sensitive to annealing at 120 °C) in order to eliminate a contribution of the respective layers to the annealing behavior of the solar cell. For simplicity, only the annealing behavior of the fill factor in the solar cell is presented in this section, as it shows the largest improvement upon annealing for all of the investigated a-Si:H solar cells.

Effect of Layer Temperature on the Annealing Behavior

Selected low temperature silicon layers were consecutively substituted by high temperature deposited layers. The layers deposited at 180 °C are expected to be only weakly sensitive to post-deposition annealing at 120 °C. This allows to assign the observed improvement in cell performance upon annealing to a specific low temperature component of the solar cell. In Fig. 5.13 fill factor values $FF_{\rm annealed}$ normalized to the as-deposited state $FF_{\rm as-deposited}$ are shown as a function of annealing time for solar cells in which specific low temperature layers are substituted by high temperature layers. The solar cell deposited entirely at 120 °C (black squares) and with only the p-type layer deposited at 180 °C (blue triangles) exhibit only a slight difference in the annealing characteristics of the fill factor, which may be considered to be within the error bar. Though their absolute values differ (62.1 % and 69.8 % after 120 min annealing, respectively), probably due to the higher dark conductivity of the p-type layer deposited at 180 °C (cf. Fig. 4.3(a) in Section 4.1.1), the improvement upon annealing is 21.6 ± 1.3 % relative (corresponding to a ratio of 1.216 in the figure) after 120 minutes annealing.

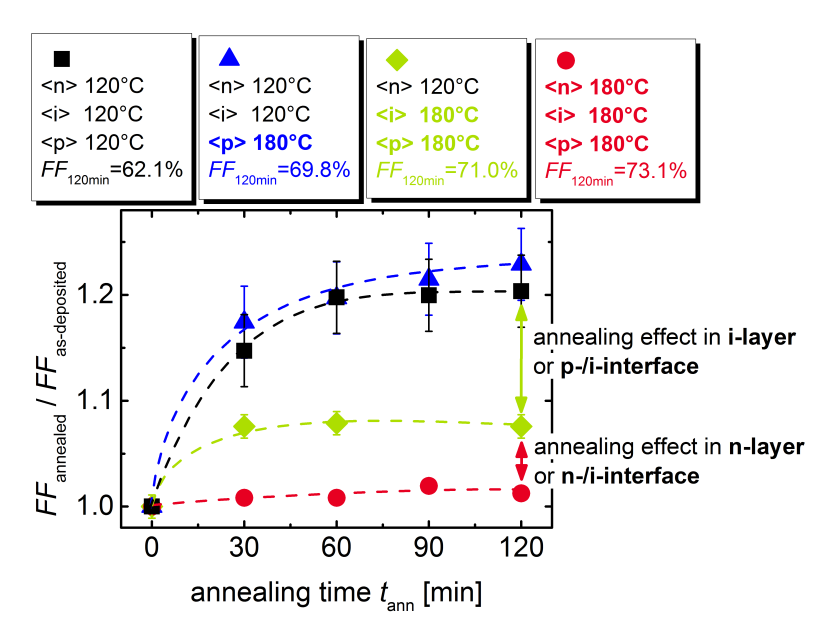


Figure 5.13.: Fill factor in the annealed state $FF_{\rm annealed}$ normalized to the as-deposited value $FF_{\rm as-deposited}$ as function of post-deposition annealing time $t_{\rm ann}$ for solar cells in which selected layers were deposited at 180 °C. The substrate temperatures used for the deposition of each layer are noted at the top for each of the presented solar cells along with absolute FF values after 120 minutes annealing time. Lines are guides to the eye.

The fill factor of the solar cell in which the p-type as well as intrinsic absorber layer were deposited at $T_s = 180\,^{\circ}\text{C}$ are presented as green diamonds. It can be seen that the improvement upon annealing is considerably reduced when the intrinsic absorber layer is deposited at high temperature of $180\,^{\circ}\text{C}$ and thus assumed to be only marginally sensitive to annealing at $120\,^{\circ}\text{C}$. The increase in FF is reduced to $7.4\,\%$ relative after $120\,\text{minutes}$ annealing time. When additionally the n-type layer is deposited at $180\,^{\circ}\text{C}$, resulting in a solar cell deposited entirely at high temperature (red circles), a mere relative improvement of $1.2\,\%$ in the fill factor is visible after $120\,\text{minutes}$ post-deposition annealing at $120\,^{\circ}\text{C}$.

For the following discussion it will be assumed that layers deposited at high temperature of 180 °C are not sensitive to post-deposition annealing at 120 °C. The p-type layers deposited at 120 °C and 180 °C exhibit quite different material properties, with higher dark conductivity (by two orders of magnitude) and lower E_{04} gap in the case of high deposition temperature (see also Fig. 4.3(a) in Section 4.1.1). However, the implementation of these p-type layers (exhibiting different dark conductivities and deposition temperatures) has only little effect on the annealing characteristic of the fill factor. This suggests that changes in the p-type layer properties upon annealing, as shown in Section 5.2.1, have no major contribution to the remarkable improvement in the a-Si:H solar cell performance. Moreover, similar improvement upon annealing for solar cells with these p-type layers also indicates a low level of relevance of the TCO/p-type layer interface for the annealing process. It should be noted that the low temperature p-type layer may also already be annealed during subsequent intrinsic and n-type layer deposition, thereby partially explaining the insensitivity of the p-type to post-deposition annealing.

In order to investigate the relevance of the intrinsic absorber for the annealing effect in solar cells, the low temperature intrinsic layer in the solar cell was substituted by one deposited at 180 °C (blue triangles compared to green diamonds, respectively). The annealing effect is significantly less pronounced when a high temperature intrinsic absorber layer is implemented. From the 21.6 % increase in fill factor after 120 minutes annealing when a low temperature i-layer is used, only an increase of 7.4 % remains when the i-layer is not sensitive to annealing due to the high deposition temperature. This suggests that the intrinsic absorber layer deposited at low temperature plays a main role (14.2 % of a total of 21.6 %) in the improvement upon annealing. Still from these results it can not be distinguished if the improvement upon annealing is a bulk effect in the intrinsic absorber layer or an interface effect at the p(180 °C)/i(120 °C)-interface, which would also be affected by changes in $T_{\rm s}$ of the intrinsic layer.

When additionally the n-type layer is deposited at 180 °C, meaning that all silicon layers are deposited at high temperature, the improvement in fill factor upon post-deposition annealing becomes negligible with an increase of merely 1.2 % after 120 minutes annealing. Accordingly, also the low temperature n-type layer, or i-/n-interface respectively, contributes to the improvement upon annealing, albeit to a smaller extent.

In summary, the results suggest that the considerable improvement upon annealing can mainly be attributed to the intrinsic absorber layer and/or the p-/i-interface, but also to the n-type layer and/or n-/i-interface. In the following, the influence of the material

properties of the intrinsic and n-type layer on the annealing behavior of the solar cell will thus further be investigated.

Effect of Material Properties on the Annealing Behavior

In this section, the effect of the intrinsic and n-type layer material properties on the annealing behavior of the solar cell is investigated. For this purpose, the annealing effects in solar cells having different intrinsic and n-type layers are examined. First, the magnitude of fill factor improvement after 150 minutes annealing time $FF_{150\text{min}}/FF_{\text{as-deposited}}$ is plotted as a function of photo response (measured on individual layers) of the respective intrinsic absorber layer used in the cell, which serves as a measure for the material quality. The results are shown in Fig. 5.14. The different values in the photo response for

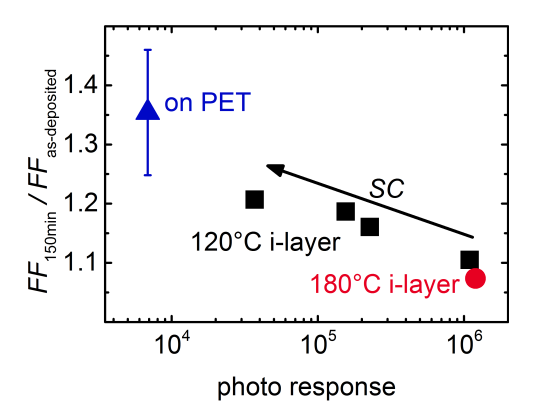


Figure 5.14.: Fill factor after 150 minutes annealing time $FF_{150\text{min}}$ normalized to the asdeposited value $FF_{\text{as-deposited}}$ of a-Si:H solar cells deposited at various silane concentrations SC of the intrinsic absorber layer as function its photo response (black squares). Solar cells/layers on PET (blue triangle) and deposited at 180 °C (red circle) are shown for comparison.

the solar cell with 120 °C intrinsic layer (black squares) are obtained by varying the silane concentration during deposition (for effects on solar cell performance see Section 4.1.4). For comparison, the data points for intrinsic layers and corresponding solar cells deposited at 180 °C (red circle) and on PET substrate (blue triangle) are shown as well. A general trend of reduced improvement upon annealing with increasing photo response (thus material quality) of the intrinsic absorber layer is visible. The intrinsic a-Si:H layer deposited on PET substrate exhibits a rather poor photo response of less than 10^4 , and simultaneously the solar cell using this layer shows a strong annealing effect with a relative improvement in fill factor of $35\pm10\,\%$. On the contrary, the intrinsic absorber layer deposited at $180\,^{\circ}$ C shows a high photo response of 10^6 and post-deposition annealing at $120\,^{\circ}$ C has only minor effect on the fill factor.

Similar to the case of the intrinsic absorber layers, the effects of n-type layers exhibiting various material properties are investigated. The relative improvement in fill

factor after 120 minutes $FF_{120\text{min}}/FF_{\text{as-deposited}}$ of solar cells with n-type layers exhibiting various dark conductivities $\sigma_{\text{d.n-layer}}$ is presented in Fig. 5.15. The different values $\sigma_{\text{d.n-layer}}$

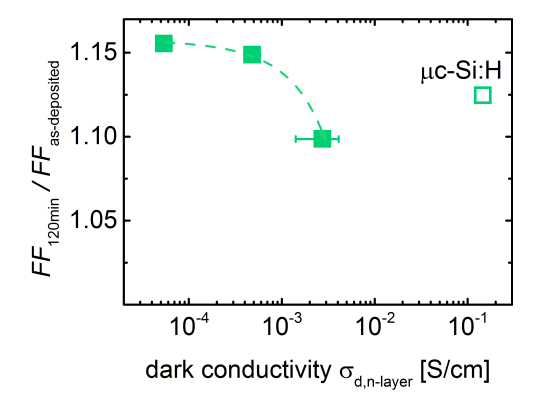


Figure 5.15.: Fill factor after 120 minutes annealing time $FF_{120\text{min}}$ normalized to the as-deposited value $FF_{\text{as-deposited}}$ of a-Si:H solar cells as a function of dark conductivity $\sigma_{\text{d,n-layer}}$ of the n-type layer. The n-type layer with $\sigma_{\text{d}} > 0.1 \,\text{S/cm}$ is microcrystalline with an I_{crs} of 18% (open symbol).

are obtained by varying the silane concentration during deposition (see Section 4.1.3). The intrinsic absorber layer in these solar cells was deposited at SC = 12.5%. It is evident that the relative improvement in fill factor after 120 minutes annealing decreases with increasing dark conductivity of the a-Si:H n-type layer, from 15.5% at 5.6×10^{-5} S/cm to 9.9% at 2.9×10^{-3} S/cm. The n-type layer with $\sigma_d>0.1$ S/cm is neglected for this investigation as it exhibits a crystalline volume fraction of 18% which in turn shows a different annealing behavior. The effect of post-deposition annealing on microcrystalline silicon will be shown and discussed later in Section 5.6. A possible explanation for the observed correlation may be related to an enhanced built-in field in the device with increasing dark conductivity of the n-type layer. The built-in field is constituted by the p- and n-type layer, and the lower activation energy of the n-type layer (evident from an increased dark conductivity) is expected to result in a higher built-in voltage and thus built-in field in the solar cell. As a result, the magnitude of the annealing effect is reduced, when the built-in field is already stronger in the as-deposited state. Further investigation of the effect of the built-in field in the solar cell on the annealing behavior will be given in the next section.

Effect of Built-In Field on the Annealing Behavior

In order to investigate the influence of the built-in field $E_{\rm bi}$ in the device on the annealing characteristics of the a-Si:H solar cell, the built-in field was varied by variation in absorber and n-type layer thickness. The built-in field within the intrinsic absorber layer is defined by the built-in voltage divided by the absorber layer thickness $E_{\rm bi} = V_{\rm bi}/d$. As result, a reduction in d increases $E_{\rm bi}$. On the other hand, the built-in field also depends on the

thickness of the doped layers and a certain thickness is required to support a stronger electric field for a given built-in voltage [28]. In the case of thicker doped layers, more space-charge is available to build up the electrical field within the intrinsic layer. The relative improvement in the fill factor after 120 minutes $FF_{120\mathrm{min}}/FF_{\mathrm{as-deposited}}$ of solar cells with various thicknesses of the absorber and n-type layer are shown in Fig. 5.16(a) and (b), respectively. In Fig. 5.16(a), the values are shown for two different photo responses

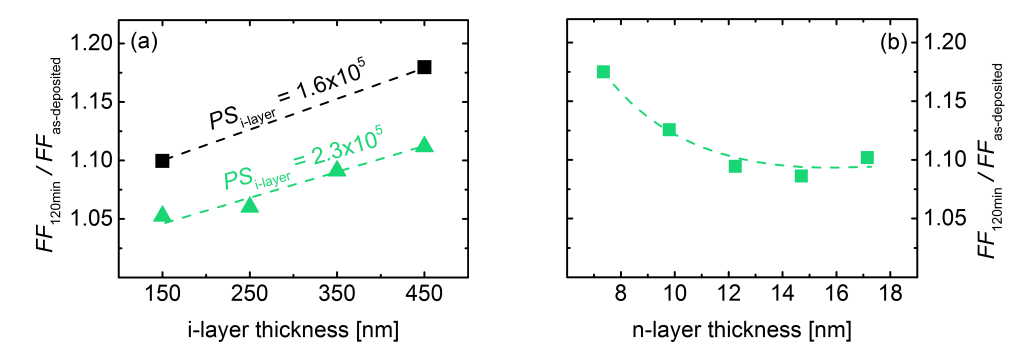


Figure 5.16.: (a) Fill factor of a-Si:H solar cells after 120 minutes annealing time $FF_{120 \text{min}}$ normalized to the as-deposited value $FF_{\text{as-deposited}}$ as a function of layer thickness of (a) the intrinsic absorber layer and (b) n-type layer. Data for two different photo responses PS of the intrinsic absorber layer are shown in (a). Lines are guides to the eye.

 $PS_{\text{i-layer}}$ of the intrinsic absorber layer, which have been shown in Fig. 5.14. It is evident that the magnitude of the annealing effect in the fill factor decreases with increasing built-in field in the device, i.e. with thinner intrinsic and thicker n-type layer. The FF improvement is reduced from 11% down to 5% and from 18% to 10% for the intrinsic absorber layer with PS of 2.3×10^5 and 1.6×10^5 , respectively, when the i-layer thickness is reduced from 450 nm to 150 nm. On the other hand, the FF improvement is reduced from 17% to 9% when the n-type layer thickness is increased from nominal 7 nm to 15 nm.

Summary

The results obtained from the consecutive replacement of silicon layers by high temperature layers suggest that though the n-type layer or n-/i-interface also contributes to some extent, the considerable improvement upon annealing can mainly be attributed to the intrinsic absorber layer and/or the p-/i-interface. No difference in the annealing behavior could be detected when the p-type layer was replaced by a high temperature layer, suggesting that changes in p-type layer properties are unlikely to contribute to the observed changes in solar cells upon annealing. Furthermore, it was found that the magnitude of the annealing effect considerably depends on the material quality in terms of photo response of the intrinsic absorber layer. A reduction in the magnitude of the annealing effect was also found for an enhanced built-in field in the device, due to higher dark conductivity or increased thickness of the n-type layer as well as reduced absorber layer thickness.

5.3.2. Variable Intensity Measurements

As shown in Section 5.1, the largest improvement upon post-deposition annealing is present in the fill factor of the solar cell, being enhanced by more than 20% relative, following 120 minutes of annealing. The fill factor in an a-Si:H solar cell is influenced by several effects, such as the series and shunt resistance of the device as well as the collection efficiency of generated charge carriers. The latter in turn depends on the quality of the interfaces between the doped and intrinsic layers as well as on the material quality of the intrinsic absorber layer itself [28]. The bulk material properties were shown to improve upon annealing by an increase in photo response in Section 5.2.3 and the improvement in fill factor upon annealing has actually been shown to decrease with an enhanced photo response of the intrinsic absorber layer in the section above.

Variable Intensity Measurement (VIM) is an effective tool to distinguish between the effects of series resistance $R_{\rm s}$, shunt resistance $R_{\rm sh}$ and collection efficiency [218]. The collection efficiency is estimated by the collection voltage $V_{\rm coll}$, which is described by Eq. 5.1 (see also Eq. 3.27):

$$V_{\text{coll}} = \frac{(\mu \tau)_{\text{eff}} V_{\text{bi}}^2}{\Psi d^2} \tag{5.1}$$

where $(\mu\tau)_{\rm eff}$ is the the effective mobility-lifetime product of charge carriers in the intrinsic absorber layer, $V_{\rm bi}$ the built-in voltage, Ψ a factor describing the electrical field deformation and d the absorber layer thickness. Variable intensity measurements were performed on a solar cell deposited at 120 °C (cell B in Table 4.2, see Section 4.1.4) after several annealing steps ranging from 0 hours (as-deposited state) to 3 hours.

In Fig. 5.17, the fill factor FF as well as $R_{\rm s}$, $V_{\rm coll}$ and $R_{\rm sh}$ are presented as a function of annealing time in (a), (b), (c) and (d), respectively. Further details about the evaluation of the quantities from VIM can be found in Section 3.4.3. The series resistance was evaluated from the inverse slope of the J-V curve at $V = V_{\rm OC}$ measured at 1 sun. The fill factor presented in (a) increases significantly within the first annealing step of 0.5 hours, namely from 41.9% in the as-deposited state to 48.2%. With increasing annealing time, FF continuously increases up to a value of 51.7% after 3 hours. At the same time, $R_{\rm s}$ shown in (b) decreases from $40.3\,\Omega{\rm cm^2}$ to $33.8\,\Omega{\rm cm^2}$. Regarding $V_{\rm coll}$ shown in (c), a significant increase from 6.5 V in the as-deposited state up to 14.8 V is observed with increasing annealing time up to 3 hours, corresponding to an increase by a factor of 2.3. From (d) it is evident that $R_{\rm sh}$ is constant over the investigated range of annealing times and thus not affected by post-deposition annealing, when the outlier after 1 hour annealing time is neglected. Comparison to the values obtained for the solar cell deposited at high temperature (red circles) shows that similar collection voltages of $14.7\pm1.0\,\mathrm{V}$ are obtained after sufficient annealing of the low temperature solar cell (see (c)). The shunt resistance shown in (d) is even larger in case of the low temperature solar cell and thus the results suggest that the loss in fill factor by more than 30 % absolute (see (a)) mainly results from a significantly increased series resistance in the case of the low temperature solar cell.

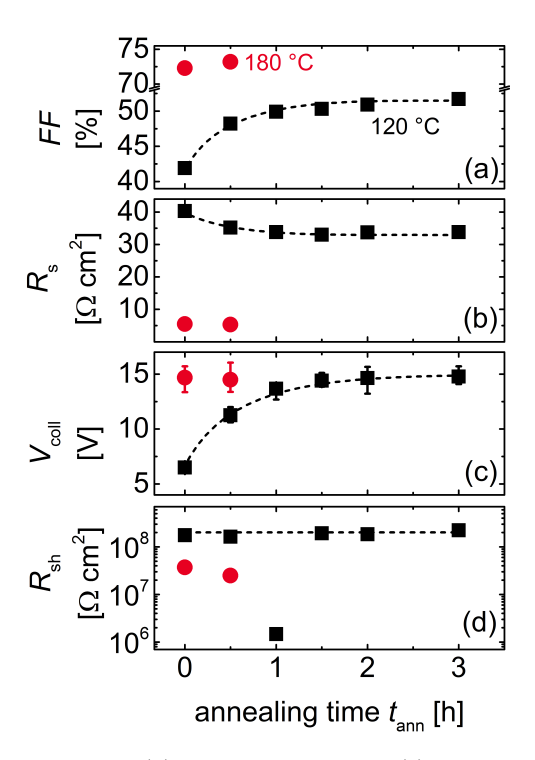


Figure 5.17.: (a) Fill factor FF, (b) series resistance $R_{\rm s}$, (c) collection voltage $V_{\rm coll}$ and (d) shunt resistance $R_{\rm sh}$ of an a-Si:H solar cell deposited at 120 °C as function of annealing time $t_{\rm ann}$ (black squares). The values of a solar cell deposited at 180 °C are shown for comparison (red circles). Lines are guides to the eye.

Discussion

The conclusions that can be drawn from the results obtained from VIM are discussed in the following. Although the fill factor varies significantly upon annealing, the shunt resistance is constant with only slight variations over the entire timescale of post-deposition annealing studied here (up to 3 hours). Accordingly, it is most unlikely that a reduction of ohmic shunts is the reason for the increased fill factor upon annealing. The increase in fill factor upon annealing can be ascribed to an improvement in charge carrier collection, measured by $V_{\rm coll}$, and a reduction in series resistance of the device. Regarding the series resistance, a possible reduction may be related to the observed increase in dark conductivities of pand n-type a-Si:H layers (see Section 5.2). However, the results obtained in Section 5.3.1 showed that the conductivity of the p-type layer has only slight influence on the annealing behavior. Also the Asahi-U substrate showed no evidence for a change in sheet resistance even after prolonged annealing for 20 hours, and can thus be excluded to be the origin for the annealing effect. Regarding the collection voltage, the pronounced increase clearly indicates a considerably enhanced charge carrier collection from the device. According to Equation 3.27, the increase in V_{coll} upon annealing may on one hand be attributed to an increase in the effective mobility-lifetime product $(\mu\tau)_{\text{eff}}$ of charge carriers in the intrinsic absorber layer. The charge carrier collection is most likely limited by a given carrier type (electrons or holes), however it is not possible to make unambiguous conclusions from these measurements in the case of p-side illuminated solar cells [260]. On the other hand, $V_{\rm coll}$ may be increased by an increased built-in voltage $V_{\rm bi}$ and/or reduced correction factor Ψ , that represents the deformation of the electrical field within the intrinsic absorber layer of the device due to charged defects or ionized contaminations within [261].

Summary

The influence of annealing on the fill factor of the a-Si:H solar cell, as deduced from VIM, can be summarized as follows:

- A contribution from the shunt resistance to the improvement in fill factor values upon annealing can be excluded.
- The fill factor increases upon annealing due to an increase in collection voltage V_{coll}
 and reduction in series resistance.
- The reduced series resistance may result from the increase in dark conductivity of the n-type layer.
- Upon annealing, the charge carrier collection is significantly enhanced. This maybe attributed to (i) an increased effective $(\mu\tau)_{\rm eff}$ -product of charge carriers in the intrinsic absorber layer and/or (ii) an enhanced built-in field in the device.

5.3.3. External Quantum Efficiencies

A convenient tool to further investigate charge carrier collection is the measurement of external quantum efficiency EQE curves. In order to investigate the effect of post-deposition annealing on the charge carrier collection, EQE curves were measured for an a-Si:H solar cell deposited at 120 °C (cell C in Table 4.2, see Section 4.1.4) after various annealing times, ranging from 0 minutes (as-deposited state) to 120 minutes. The wavelength resolved measurement also allows to probe different spatial regions of the device, as will be discussed later. External quantum efficiency curves after various annealing times are presented in Fig. 5.18(a), where an increase in EQE curve with annealing time $t_{\rm ann}$ over the entire investigated wavelength range can be observed. In order to have a closer look at relative variations in the charge carrier collection efficiency over wavelength, the EQE curves measured in each annealed state $EQE_{\rm annealed}$ were normalized to the initial $EQE_{\rm as-deposited}$ curve and are shown in Fig. 5.18(b). In more detail, the improvement

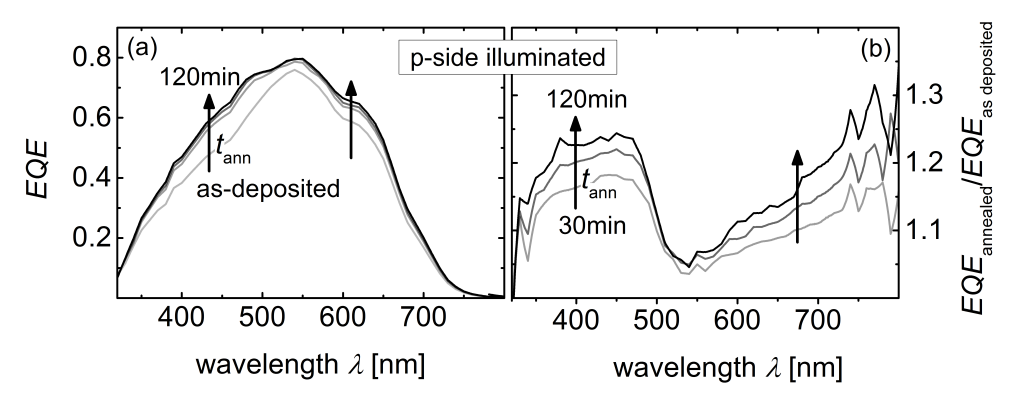


Figure 5.18.: External quantum efficiency curves as (a) absolute EQE and (b) normalized $EQE_{\rm annealed}/EQE_{\rm as-deposited}$ curves for various annealing times $t_{\rm ann}$ (as-deposited, 30 min, 60 min, 120 min) for an a-Si:H solar cell deposited at 120 °C.

in EQE upon annealing is not equally distributed over the wavelength λ , but is more pronounced at wavelengths below 500 nm and above 600 nm than in the middle of the spectrum. The maximum improvement is 30 % and 25 % (corresponding to a ratio of 1.3 and 1.25 in the figure) in the region of longer and shorter wavelength after 120 minutes annealing time, respectively. The noise in the EQE curve for $\lambda > 730$ nm results from the low absorption coefficient of a-Si:H in this region, thus leading to a poor spectral response and a correspondingly low signal-to-noise ratio.

Additional information on the charge carrier collection can be gained by comparison of p- and n-side illuminated solar cells. Such an approach has been previously used to study the effects of electronic defects [239, 262] or oxygen content [240] in the absorber layer on the performance of a-Si:H and μ c-Si:H solar cells. In order to enable illumination from the n-side, a solar cell with identical silicon layers but ITO/Ag grid was prepared (see Fig. 5.19). Additionally, the glass side was covered with a silver layer to form a

back reflector. The absolute EQE and normalized $EQE_{\text{annealed}}/EQE_{\text{as-deposited}}$ curves for

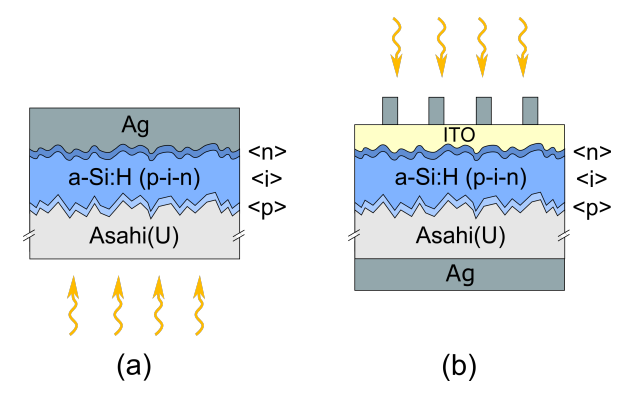


Figure 5.19.: Schematic layer stack of an a-Si:H solar cell deposited at 120 °C for the case of illumination through (a) the p-type layer (p-side illuminated) and (b) the n-type layer (n-side illuminated).

various annealing times of the n-side illuminated solar cell are shown in Fig. 5.20(a) and (b), respectively. Similar to the case of the p-side illuminated solar cell, an increase in

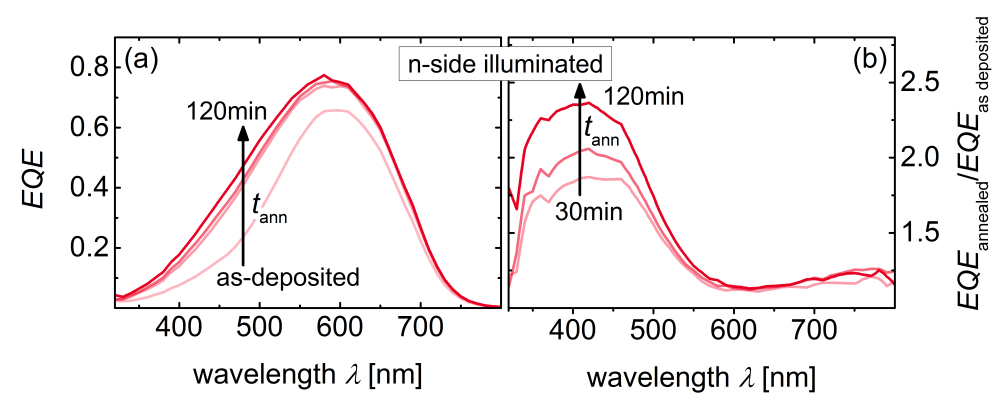


Figure 5.20.: External quantum efficiency curves as (a) absolute EQE and (b) normalized $EQE_{\text{annealed}}/EQE_{\text{as-deposited}}$ curves for various annealing times t_{ann} (as-deposited, 30 min, 60 min, 120 min) for the n-side illuminated a-Si:H solar cell deposited at 120 °C.

EQE curve over the entire investigated wavelength range upon post-deposition annealing is visible for the n-side illuminated solar cell, shown in (a). It can already be seen that the improvement is stronger for short wavelengths below 600 nm. The relative improvement is more clearly presented in Fig. 5.20(b). Obviously, the relative improvement for the wavelength range between 320-550 nm is significantly larger compared to the p-side illuminated solar cell with a maximum factor of 2.3 after 120 minutes annealing. For the improvement in EQE in the long wavelength range above 650 nm, a maximum improvement of 25%

(ratio of 1.25) after 120 minutes annealing, similar to that for the p-side illuminated solar cell, can be observed.

The drift length and thus collection of charge carriers also sensitively depends on the electrical field within the intrinsic absorber layer. This can be probed by applying a negative bias voltage during the spectral response measurement or by reducing the absorber layer thickness in the device. In Fig. 5.21, the ratio of the EQE curve measured under a bias voltage of -0.5 V to the EQE curve measured without additionally applied voltage $EQE_{-0.5\mathrm{V}}/EQE_{0\mathrm{V}}$ is shown for the p-side illuminated solar cell for various post-deposition annealing times. For the EQE curve in the as-deposited state (light grey curve), an in-

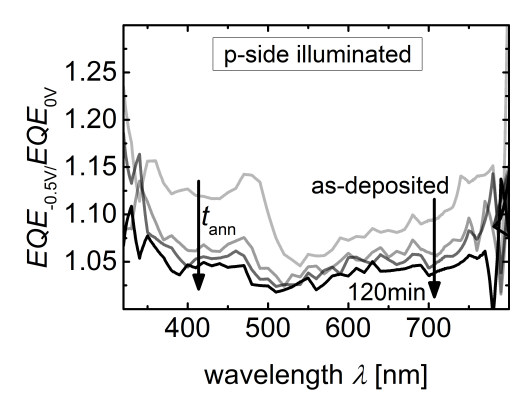


Figure 5.21.: Ratio of EQE curves with and without bias voltage of -0.5 V $EQE_{-0.5\text{V}}/EQE_{0\text{V}}$ for various annealing times t_{ann} of the p-side illuminated solar cell.

crease over the entire wavelength range could be achieved by applying a negative bias voltage of -0.5 V, indicating that not all charge carriers are collected under short-circuit operating conditions. Interestingly, the shape of the $EQE_{-0.5\mathrm{V}}/EQE_{0\mathrm{V}}$ curve resembles the $EQE_{\mathrm{annealed}}/EQE_{\mathrm{as-deposited}}$ curve in Fig. 5.18(b) with the lowest improvement in the middle of spectrum around 550 nm. The improvement in EQE due to the applied bias voltage is $14\pm2\,\%$ in the wavelength range $330 < \lambda < 500\,\mathrm{nm}$. With increasing annealing time t_{ann} , the effect of the bias voltage gradually decreases until $EQE_{-0.5\mathrm{V}}/EQE_{0\mathrm{V}}$ is below 5% for most of the wavelength after 120 minutes annealing.

Another way to increase the electrical field in the device is to reduce the thickness of the intrinsic absorber layer. Therefore a solar cell, similar to the p-side illuminated one in Fig. 5.18, but with an absorber layer thickness of only 150 nm, was fabricated (the p- and n-side illuminated devices had a thickness of 450 nm). The resulting normalized $EQE_{\rm annealed}/EQE_{\rm as-deposited}$ curves for various times of post-deposition annealing are shown in Fig. 5.22(a). In contrast to Fig. 5.18(b), the ratio $EQE_{\rm annealed}/EQE_{\rm as-deposited}$ in the short wavelength range below 500 nm is hardly affected by post-deposition annealing and is below 5%, meaning that the effect of annealing on the EQE curve is minor in this range. In the long wavelength range, the ratio increases with $t_{\rm ann}$ for $\lambda > 600$ nm up to 15% after 120 minutes annealing time, indicating an improvement in EQE. Similar to the case of the 450 nm thick p-side illuminated solar cell, the effect of a negative bias

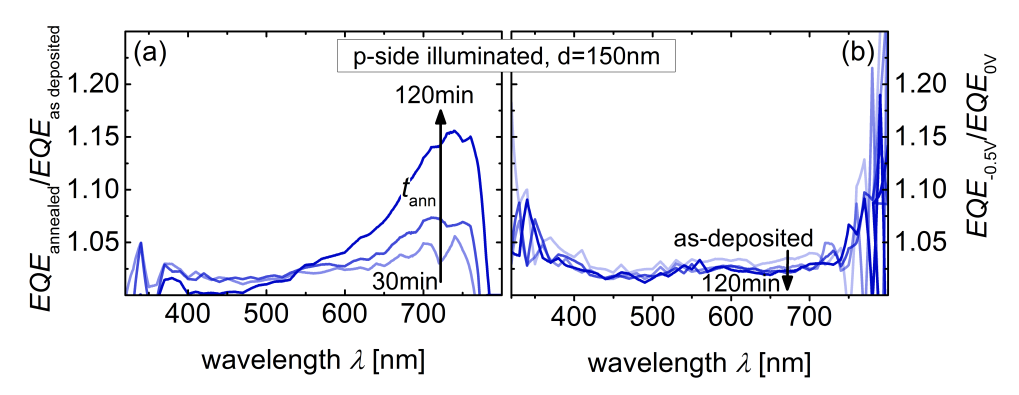


Figure 5.22.: Normalized external quantum efficiency curves for various annealing times $t_{\rm ann}$ (as-deposited, 30 min, 60 min, 120 min) for the p-side illuminated solar cell deposited at 120 °C with an absorber layer thickness d of 150 nm: (a) EQE curve in each annealed state normalized to the as-deposited state $EQE_{\rm annealed}/EQE_{\rm as-deposited}$ and (b) ratio of EQE with and without bias voltage of -0.5 V $EQE_{-0.5\text{V}}/EQE_{0\text{V}}$.

voltage on the EQE before and after annealing is investigated and $EQE_{-0.5V}/EQE_{0V}$ curves are presented in Fig. 5.22(b). The increase in EQE due to the applied negative bias voltage in the as-deposited state is below 5% for most of the wavelengths and only a slight reduction can be seen upon annealing.

Discussion

From comparison of p- and n-side illuminated solar cells the effects of minority and majority carriers on the charge carrier collection may be separated [260]. The carrier collection efficiency is mainly governed by the drift length $L_{\rm d,e}$ and $L_{\rm d,h}$ of electrons and holes, respectively, which can be described by

$$L_{\rm d,e/h} = \mu_{\rm e/h} \, \tau_{\rm e/h} \, E \tag{5.2}$$

where $\mu_{e/h}$ and $\tau_{e/h}$ are the mobility and lifetime of electrons and holes, respectively, and E is the electric field within the intrinsic absorber layer. As electrons and holes need to be collected in pairs to ensure charge neutrality, the charge carrier exhibiting the lowest drift length, and thus higher probability to be captured in deep defects, limits the solar cell performance. The normalized EQE curves in various annealed states presented in Fig. 5.18(b) can be discussed as follows: for light of short wavelength (320-500 nm), a great extent of photons is absorbed, and thus charge carriers are generated, in the front part of the solar cell. As the solar cell is illuminated through the p-type layer, holes are easily collected due to the short distance between the site of charge carrier generation and p-type contact layer. The electrons on the other hand have to drift towards the n-type back contact through the i-layer, thereby increasing the probability for recombination. The collection efficiency is in this case limited by the collection of electrons. As a consequence, an improvement in EQE for this wavelength range ($\lambda < 500 \, \mathrm{nm}$) upon annealing

suggests that the drift length of electrons $L_{\rm d,e}$ is increased. Vice versa, light of longer wavelength (600-800 nm), that is nearly homogeneously absorbed in the intrinsic layer, will be limited by the hole drift length $L_{\rm d,h}$, as the ($\mu\tau$)_h-product of minority carriers is known to be smaller than that of electrons as majority carriers [210, 257]. As a result, the improvement in EQE upon annealing for the wavelength range above 600 nm can probably be ascribed to an increase in $L_{\rm d,h}$. The minimum in the middle of the spectrum can be related to relatively high EQE values of more than 0.7 in the as-deposited state for 510 nm $< \lambda < 570$ nm, providing not as much potential for improvement upon annealing than in the remaining wavelength range. Recapitulating, the increase in EQE for short as well as long wavelengths suggests that both the electron and hole drift length may be increased upon annealing.

Comparison to the results of the n-side illuminated solar cell in Fig. 5.20(b) reveals a considerably increased ratio of $EQE_{\rm annealed}/EQE_{\rm as-deposited}$ in the short wavelength range. This results from an "inverse" carrier generation profile in the case of n-side illumination [260]. In this case, illumination with light of short wavelength leads predominantly to charge carrier generation near the n-type layer and $L_{\rm d,h}$ is limiting the charge carrier collection. The significant improvement in this range confirms a rise in hole drift length $L_{\rm d,h}$ upon annealing.

Investigating the results of the EQE measurements under negative bias voltage shown in Fig. 5.21, the shape of the $EQE_{-0.5\text{V}}/EQE_{0\text{V}}$ curve in the as-deposited state attracts attention. The larger improvement for $\lambda < 500\,\mathrm{nm}$ and $\lambda > 600\,\mathrm{nm}$ with the reduction in the middle of the spectrum resembles the $EQE_{\mathrm{annealed}}/EQE_{\mathrm{as-deposited}}$ curves in Fig. 5.18(b). This suggests that qualitatively similar effects can be induced by either an increase in the electrical field in the absorber layer or by post-deposition annealing. Indeed, about the same EQE increase can be achieved by applying a bias voltage of -0.5 V or annealing for 30 minutes (compare Figs. 5.21 and 5.18(b)). As the electrical field E directly influences the drift length (see Eq. 5.2), the results support the view that the drift length is the parameter sensitive to annealing.

Another way to increase the electrical field in the device is to reduce the absorber layer thickness. In case of the 150 nm p-side illuminated solar cell shown in Fig. 5.22(a), no significant improvement in EQE in the short wavelength range can be observed with $t_{\rm ann}$. As discussed above, for light of short wavelength the electron drift length is limiting the carrier collection and thus the EQE curve in the case of illumination through the p-type layer. The facts that no visible improvement upon annealing takes place and also an applied negative bias voltage does not lead to a significantly enhanced carrier collection suggest that $L_{\rm d,e}$ already exceeds the i-layer thickness of 150 nm and most of the electrons are already collected in the as-deposited state without negative bias voltage. Regarding the collection of holes, the increasing ratio $EQE_{\rm annealed}/EQE_{\rm as-deposited}$ in the long wavelength range above 600 nm implies that $L_{\rm d,h}$ is still limiting the charge carrier collection and is improved upon annealing.

Summary

External quantum efficiency measurements were conducted in the as-deposited state and after various annealing times up to 120 minutes on p-side illuminated solar cells with absorber layer thickness of 150 nm and 450 nm, an n-side illuminated solar cell as well as with applied bias voltage. The conclusions are listed in the following.

- Upon annealing, the drift length of electrons and especially holes increases thus enhancing charge carrier collection.
- About the same EQE increase can be achieved by applying a negative bias voltage of $0.5\,\mathrm{V}$ or $30\,\mathrm{minutes}$ annealing at $120\,^{\circ}\mathrm{C}$. This confirms the drift length to be the quantity enhanced upon annealing.
- In the case of 150 nm thick solar cells, the drift length of electrons $L_{\rm d,e}$ exceeds the absorber layer thickness, while an improvement in $L_{\rm d,h}$ is still visible upon annealing.

5.3.4. Summary

From the results shown above it can be concluded that the major contribution to the annealing effect results from changes in the intrinsic absorber layer, though a small contribution from the n-type layer should not be neglected. The magnitude of the annealing effect was shown to be reduced by improved material properties of the intrinsic absorber layer as well as by an enhanced built-in field in the device. It could be seen that the fill factor improvement is related to a reduction in series resistance in the device, as well as an increase in charge carrier collection, i.e. drift length of charge carriers, as probed by the collection voltage. This is in agreement with the results of EQE measurements. From these results, it could be concluded that both the drift length of electrons and holes increases upon annealing. This implies that during annealing either the $\mu\tau$ -product of charge carriers, the built-in voltage and/or the distribution of the electrical field in the device is enhanced upon post-deposition annealing. A more detailed discussion and possible mechanisms that lead to these enhancements are presented in the following.

5.4. Discussion

As derived from the results presented above, besides a slight reduction in the series resistance the major contribution to the annealing effect is most probably related to an increase in the drift length $L_{\rm d}$ of charge carriers. This in turn may be increased by (i) an enhanced built-in field in the device and/or (ii) an enhanced $\mu\tau$ -product of charge carriers in the intrinsic absorber layer. The discussion is structured as follows: First, possible effects improving the built-in field in the device are discussed. Afterwards, possible mechanisms increasing the mobility μ as well as lifetime τ of electrons and holes are considered. Finally, possible structural processes that may occur in the intrinsic a-Si:H layer upon post-deposition annealing are discussed.

5.4.1. Built-In Field

The drift length of charge carriers sensitively depends on the strength and distribution of the electrical field E within the intrinsic absorber layer. An enhanced built-in field in the intrinsic absorber layer may be caused by:

i) a reduction in absorber layer thickness d

In the case of solar cell annealing, changes in the layer thickness are unlikely and can therefore be excluded in the discussion of changes in the built-in field.

ii) an improved built-in voltage $V_{\rm bi}$

This may be caused by a reduction in activation energy of the doped layers [227]. This is in agreement with the observed increase in dark conductivity of the n-type layer upon annealing (see Fig. 5.7(b)). Furthermore, this would account for the increased $V_{\rm OC}$ upon annealing (cf. Fig. 5.1), as an improvement in charge carrier collection is correlated mainly to an increase in FF as well as $J_{\rm SC}$ [28].

iii) a reduction of field deformation Ψ

The electrical field is strongly influenced by deformation within the intrinsic absorber layer due to charged defects or impurities [28]. A change in Fermi level position, as indicated in Section 5.2.3, or number of defects might therefore have an influence on the drift length via the electrical field, in addition to the direct influence via $\mu\tau$ -product. Furthermore, it was shown that a low mobility of minority carriers may also induce additional space charge, leading to deformations in the electrical field [263]. This suggests that a possible improvement in $\mu\tau$ -products of electrons and holes upon annealing (that will be discussed below) have an additional value to the drift length by concomitantly reducing the electrical field deformation.

5.4.2. Mobility-Lifetime Product

It was shown in Section 5.2.3 that the $\mu\tau$ -products of both electrons and holes increase upon annealing, as probed by measurements of photo conductivity and ambipolar diffusion length. This implicates directly a likely origin for the increase in drift length of charge carriers and thus improvement in solar cell performance upon annealing. In the following, possible changes in the intrinsic absorber layer, that might influence the lifetime and mobility of charge carriers, are separately discussed. However, different types of $\mu\tau$ -products as well as their relevance for the solar cell performance need to be discussed in advance: The band mobility of charge carriers is related to the transport of free carriers in the extended states, i.e. conduction band in the case of electrons and valence band in the case of holes. It can not unambiguously be accessed experimentally as all measurement techniques, such as the time-of-flight method, measure the average motion of carriers over a longer time, thus trapping events are included [27]. Accordingly, the so-called effective mobility or drift mobility is evaluated, which corresponds to the band mobility reduced by the time a carrier stays in localized traps. The measurements performed in this work on individual layers (photo conductivity and SSPG measurements) provide measures of

 $\sigma_{\rm ph}$ and $L_{\rm amb}$ that are related to some kind of "effective" $\mu\tau$ -product of electrons and holes, respectively. On the other hand, the equations from which $V_{\rm coll}$ is deduced, involve a $\mu\tau$ -product that includes band mobilities of electrons and holes [221]. Disunity remains whether band or drift mobility is the important parameter for the charge carrier transport in an a-Si:H solar cell under steady-state operation [27, 260]. In this work, relative changes occurring upon annealing are under investigation and therefore the following discussion will address effects that in general may influence the mobility and lifetime of electrons and holes.

Regarding the relevance of electron and/or hole transport for the device performance, the situation is also not conclusive. Since electrons are majority carriers in undoped a-Si:H and $(\mu\tau)_e$ is usually considerably higher as $(\mu\tau)_h$, photocurrent measurements on an individual layer will be dominated by electron transport. Hole transport properties are accessible by e.g. measurements of ambipolar diffusion length by means of SSPG. In a solar cell on the other hand, the charge carrier collection and thus device performance will be limited by a given carrier type (electrons or holes) and only an enhanced $\mu\tau$ of the limiting carrier type will improve the solar cell performance. Hack and Shur have shown that for uniformly absorbed light in an a-Si:H solar cell hole transport will mainly determine the device performance as its $(\mu\tau)_h$ -product is significantly smaller [260]. In the case of AM1.5 illumination however, most of the light is absorbed in the front part of the device. For n-side illuminated solar cells, where the majority of photogenerated charge carriers is near the n-type layer, holes will be the limiting charge carrier since they have to travel through the entire absorber layer to be collected at the p-type contact (see also Section 5.3.3). But the situation is more complex for the case of p-side illuminated solar cells. Here, the device performance is limited by a trade-off between slow holes that have to travel a shorter distance toward the p-type layer, and faster electrons traveling a longer distance toward the n-type layer. As a result, it can not be firmly concluded which carrier transport is limiting the carrier collection and thus V_{coll} , FF and J_{SC} of the p-side illuminated solar cells investigated in this work. Especially as it was shown by the results of EQE measurements that both the electron and hole transport is improved upon annealing, both carrier types are conceivable to be responsible for an increased device performance upon annealing. More general remarks will therefore be given on what may influence the $\mu\tau$ -product of charge carriers.

Lifetime In literature, most of the changes in the $\mu\tau$ -product of charge carriers are related to changes in the recombination lifetime τ [219, 258, 264–266]. This was shown to be closely linked to the number of recombination centers available, i.e. number of dangling bonds in the midgap [267]. On the other hand, also the charge state of the dangling bond defect is of relevance, as e.g. negatively charged dangling bonds do not provide a recombination center for electrons. The charge state in turn is governed by the position of the Fermi level $E_{\rm F}$ in individual layers and thus also by the distribution of the internal electrical field in a solar cell [28, 258]. In Section 5.2.3 it was shown that $E_{\rm F}$ shifts slightly toward the conduction band upon annealing thus increasing the $(\mu\tau)_{\rm e}$ -product of electrons. The concurrent increase in $(\mu\tau)_{\rm h}$ may however indicate that

the number of recombination centers for holes is reduced, due to a reduced total defect density [210]. No indication of such effect could be observed from the results of subgap absorption measurements by CPM on individual layers (cf. Fig. 5.9), which however measures the photocurrent and thus mainly electron transport [259]. An indication results from the fact that similar improvements in EQE for p- as well as n-side illuminated solar cells are obtained if defects are reduced by annealing following degradation by electron bombardment [239]. This suggests that a reduced number of defects can lead to carrier collection profiles such as observed in this work.

Mobility In order to investigate the effect of hole and electron mobility on EQE curves, computer simulations were carried out by Shuo Wang [268] using wxAMPS software [269, 270]. These simulations, though using a simplified model (no glass/TCO substrate, no light trapping), show that the ratios of EQE curves presented in Section 5.3.3 may also be qualitatively reproduced by increasing the band mobility of electrons and holes (μ_e and μ_h , respectively). The simulations were carried out for absorber layer thicknesses of 150 nm and 450 nm as well as p- and n-side illuminated solar cells, similar to the experimental results presented in Section 5.3.3. The results are shown in Fig. 5.23.

Comparison with measured results as a function on annealing time in Section 5.3.3 shows that the general trends are similar, i.e. a pronounced minimum in EQE improvement between 500 nm and 600 nm (compare Fig. 5.23(a) with Fig. 5.18(b)), an increased improvement in the short wavelength range for the n-side illuminated solar cell (compare Fig. 5.23(b) with Fig. 5.20(b)) and a vanishing improvement in the short wavelength range for the thin p-side illuminated solar cell (compare Fig. 5.23(c) with Fig. 5.22(a)). A minor difference to the experimental results for $\lambda < 350$ nm results from the missing glass/TCO substrate in the simulation, which leads to parasitic absorption and thus diminished EQE improvement in the case of experimental results. Mobility values for electrons and holes were also varied separately and the correlation to the discussed wavelength ranges are confirmed (not shown). These simulations show that the improvement in EQE upon annealing may well be reproduced by increasing the band mobilities of both electrons and holes. However, more detailed simulations, using a more sophisticated model, are needed to investigate possible influences from other parameters, such as variation in band tail or dangling bond states.

5.4.3. Structural Processes

In this section, possible structural processes that might lead to a change in defect density or mobility of charge carriers upon annealing are discussed. Furthermore, the driving force of these processes is considered in terms of equilibrium models and the thermal activation of the device improvement is discussed.

Structural Processes The defect states located in the middle of the mobility gap, whose number greatly influences the lifetime τ of charge carriers in a-Si:H, can be ascribed to

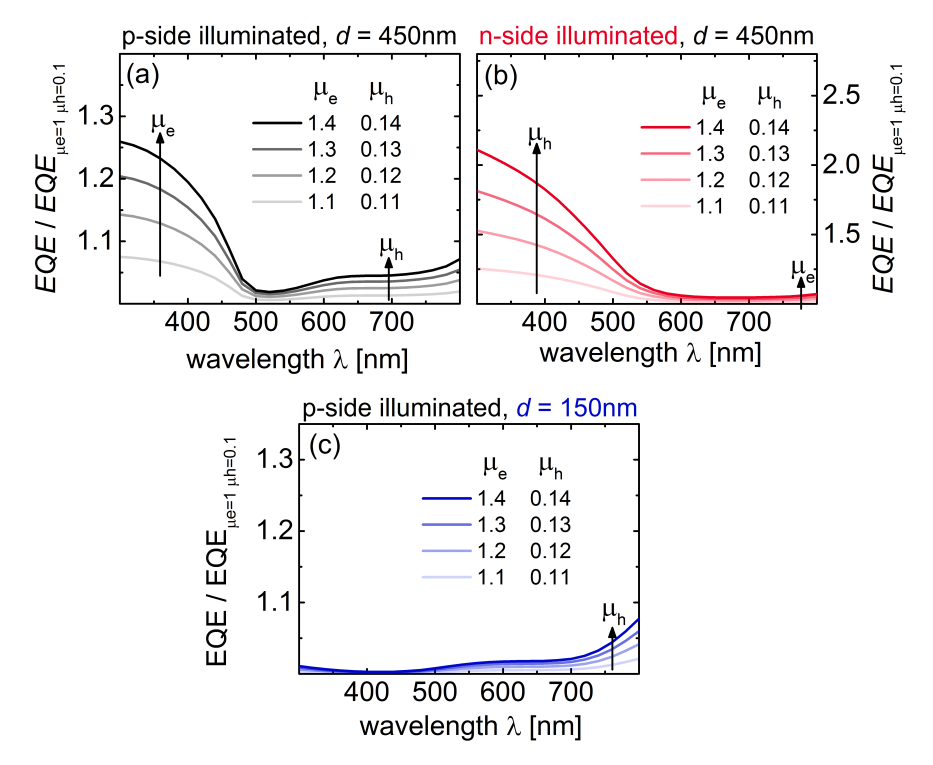


Figure 5.23.: External quantum efficiency EQE curves normalized the EQE curve for $\mu_{\rm e} = 1~{\rm cm}^2/{\rm Vs}$ and $\mu_{\rm h} = 0.1~{\rm cm}^2/{\rm Vs}$ for various values of $\mu_{\rm e}$ and $\mu_{\rm h}$ in (a) a p-side illuminated solar cell with an absorber layer thickness of 450 nm, (b) an n-side illuminated solar cell with an absorber layer thickness of 450 nm and (c) a p-side illuminated solar cell with an absorber layer thickness of 150 nm. The ratio $\mu_{\rm e}/\mu_{\rm h} = 10$ is kept constant.

unsaturated silicon bonds, so-called dangling bonds. On the other hand, due to dispersive trapping in the band tails, the effective mobility of a charge carrier depends on the fraction of time that the carrier is trapped in the localized band tail states. The mobility will therefore be determined by the number of trap states and thus the density of states in the band tails [27].

One possible explanation for the reduced number of deep defects upon annealing is related to the saturation of a dangling bond by a hydrogen atom, that was previously not bonded [78]. Another reason, which may also give an explanation for an enhanced mobility, is related to the weak-bond model [27]. This model describes that weak Si-Si bonds, that built up states in the valence and conduction band tail, can be broken under the formation of two dangling bonds, and that this reaction is in equilibrium. The defect creation can be mediated by hydrogen diffusion, which binds to one of the Si atoms. Street and Winer have illustrated this reaction, as shown in Fig. 5.24 [271]. In that case, hydrogen is released from an Si-H bond and breaks a weak Si-Si bond by

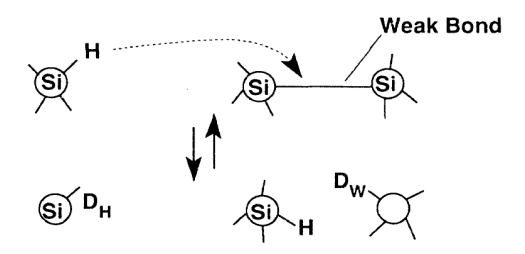


Figure 5.24.: Illustration of the hydrogen-mediated weak bond model [271].

attaching to one of the silicon atoms. The equilibration of this process suggests that by reducing the number of weak bonds, and thus steepen the band tail slope, also the number of dangling bonds is reduced. The number of weak bonds is usually reduced by using optimal deposition conditions but may also be reduced due to restructuring upon post-deposition annealing [27]. It was actually proposed [27] that in the case of low deposition temperatures (< 200 °C), the diffusion coefficient of growth precursors on the substrate surface is too low to allow structural equlibration during the deposition and broad band tails resulting from a large number of weak bonds leads to the often observed higher defect density. Upon post-deposition annealing, some relaxation of the band tail disorder takes place steepening the band tails and thus reducing the defect density [27]. A possible explanation for the changes in the structure upon annealing might therefore be related to the equilibrium state. At low substrate temperatures during deposition, the amorphous silicon material is incapable of reaching its equilibrium state regarding e.g. the distribution of weak bonds. During post-deposition annealing, the structure may relax and draw a bit nearer towards the equilibrium state, thereby steepen the band tails and accordingly reducing the defect density. This in turn would increase the lifetime as well as the mobility of charge carriers. It may also account for the shift in Fermi level of the conduction band observed in the individual intrinsic a-Si:H layer upon annealing, as a changing density of band tail states and a reduced number of defects will most probably affect the Fermi level position. Furthermore, due to the reduced number of defects and enhanced mobility of charge carriers, a possible deformation of the electrical field within the intrinsic absorber layer would be reduced.

Equilibrium temperatures for p-type, n-type and intrinsic a-Si:H layers are 80, 130 and 200 °C, respectively [84, 104, 105]. This would account for the low level of relevance of the p-type layer for the observed annealing effect of solar cells (see Section 5.3.1), since for a substrate temperature of 120 °C, the p-type layer would already be in equilibrium after deposition.

A fact that might query the discussion is that no significant change in the band tail width and sub-gap absorption is experimentally observed upon annealing, as shown in Fig. 5.25. Here, the question to what extent the applied experimental methods are ca-

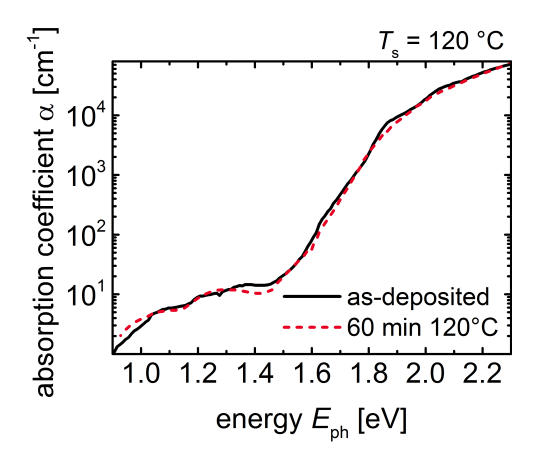


Figure 5.25.: Absorption coefficient α as a function of photon energy $E_{\rm ph}$ measured by Constant Photocurrent Method (CPM) on intrinsic a-Si:H layers deposited at $T_{\rm s} = 120\,^{\circ}{\rm C}$ in the as-deposited state (black solid line) as well as after 60 minutes annealing at 120 °C (red dashed line).

pable to resolve small changes in the material properties still remains open. Comparison with data of various thin-film silicon materials summarized by Schiff [272] suggests that a change in hole mobility within $30\,\%$ (as in the case of simulations shown in Fig. 5.23) can be a result of a minor change in the valence band tail width of maximum 1-2 meV. Furthermore, it should be considered that absorption coefficient data measured on individual layers can not be directly compared to data obtained from solar cells. Amongst other reasons [83], this is due to a difference in spatial electric field distribution in a film compared to a absorber layer of a solar cell, leading to e.g. a variation in charge states of defects.

Thermal Activation In order to analyze if the processes that occur upon post-deposition annealing are thermally activated, low temperature a-Si:H solar cells were deposited on

Asahi-U substrates in several deposition runs and annealed at various temperatures $T_{\rm ann}$ between room temperature and 200 °C. The fill factor of every annealed state $FF_{\rm annealed}$ is normalized to the as-deposited value $FF_{\rm as-deposited}$ and the results are shown in Fig. 5.26. An improvement in fill factor is visible for all annealing temperatures in the investigated

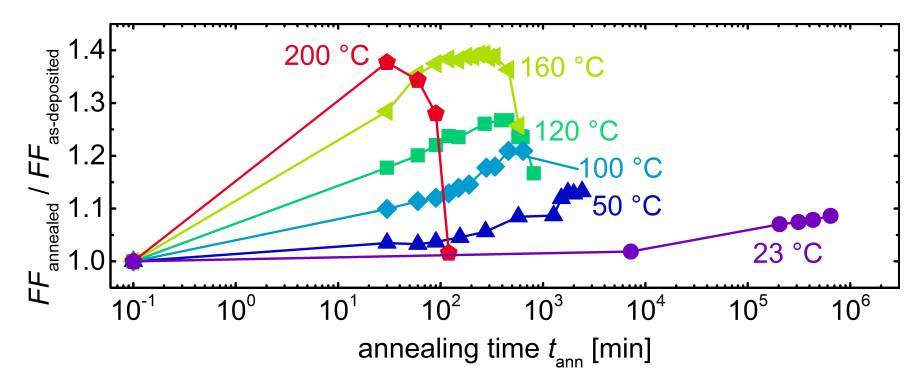


Figure 5.26.: Fill factor in the annealed state FF_{annealed} normalized to the as-deposited value $FF_{\text{as-deposited}}$ as function of annealing time t_{ann} for various annealing temperatures T_{ann} .

range, even for a solar cell kept at room temperature in the dark, albeit only slight. The fill factor can significantly be improved (37% relative) by a rapid annealing step (few minutes only) by using an annealing temperature of 200 °C. In general, the improvement tends to saturate after a certain temperature-dependent time. After prolonged annealing, the fill factor starts to decrease again. The collection voltage and shunt resistance remain constant though (not shown), indicating that an increased series resistance in the device is the reason for the deterioration upon prolonged annealing. For an annealing temperature of 200 °C (red pentagons), the highest achieved value might already be in the declining part of the curve and shorter annealing times less than 30 minutes are needed to find the maximum $FF_{\text{annealed}}/FF_{\text{as-deposited}}$ value. In the cases of 50 °C and 100 °C (dark blue triangles and light blue diamonds, respectively), saturation seems to be just reached in the investigated time frame. For the solar cell stored at room temperature, the saturation could not be reached within the remaining time frame of this work. According to the equilibrium models introduced by Smith et al. [106] and Street et al. [104, 105], the equilibration process follows a stretched-exponential behavior, typical for glass-like materials. Stretched exponential functions might be fitted to the curves in Fig. 5.26, however more data points are needed for short time scales to result in an accurate fit.

Activation energies may still be estimated by defining a characteristic relaxation time $\tau_{\rm R}$ as the time needed for a certain quantity to reach 63% (1- e^{-1}) of its saturation level [86]. The resulting Arrhenius plot for the normalized fill factor values annealed at various $T_{\rm ann}$ is shown in Fig. 5.27. The data for 200 °C was not evaluated as the saturation level is not known. From this plot an activation energy of $0.57\pm0.17\,\rm eV$ is estimated. However, this value should be interpreted with caution. First, an empirical characteristic as the fill factor includes several effects, such as charge carrier collection as well as changes in series resistance as shown in Section 5.3.2. Second, even if only charge carrier collection

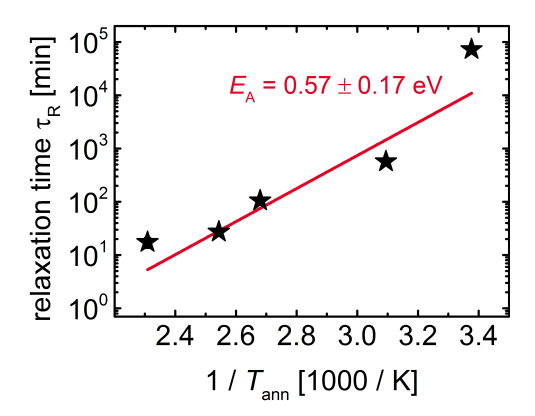


Figure 5.27.: Relaxation time $\tau_{\rm R}$, defined as the time needed for the fill factor to reach 63 % of its saturation level, as a function of inverse annealing temperature $1/T_{\rm ann}$. The red line corresponds to a linear fit of the data, suggesting an activation energy $E_{\rm A}$ of $0.57\pm0.17\,{\rm eV}$.

is considered, it was shown that several effects can overlap, such as the increasing $\mu\tau$ -product in the intrinsic a-Si:H layer and increase in dark conductivity of the n-type layer. This means that the activation energy, evaluated from the fill factor improvement, can most probably not be related to a single process occurring in the intrinsic absorber layer upon annealing.

In conclusion, the evaluation of the collection voltage and external quantum efficiencies provide evidence that an enhanced charge carrier collection plays an essential role in the improvement of a-Si:H solar cells upon post-deposition annealing. The results demonstrate that the collection of both types of carriers (electrons and holes) is improved. Here, an increase in the $\mu\tau$ -product of charge carriers in the intrinsic absorber layer and/or the built-in field in the device could be responsible for the observed improvement in the charge carrier collection upon annealing. One could speculate that these effects may be a result of structural changes in the material upon annealing, namely the equilibration of the frozen-in density of states resulting from the low substrate temperatures during deposition.

5.5. Annealing of Flexible Solar Cells

An improvement upon annealing was also found in a-Si:H solar cells on flexible PET substrates and the corresponding photovoltaic parameters are shown in Fig. 5.28. A detailed investigation of solar cells on PET substrates will be given in Chapter 6. Qualitatively, all photovoltaic parameters of the solar cell on PET substrate change in a similar way but significantly stronger compared to the solar cell on glass substrate. Overall, a relative improvement in efficiency by 71% after 150 minutes annealing can be observed. It was shown previously that poorer material properties result in a stronger annealing effect in

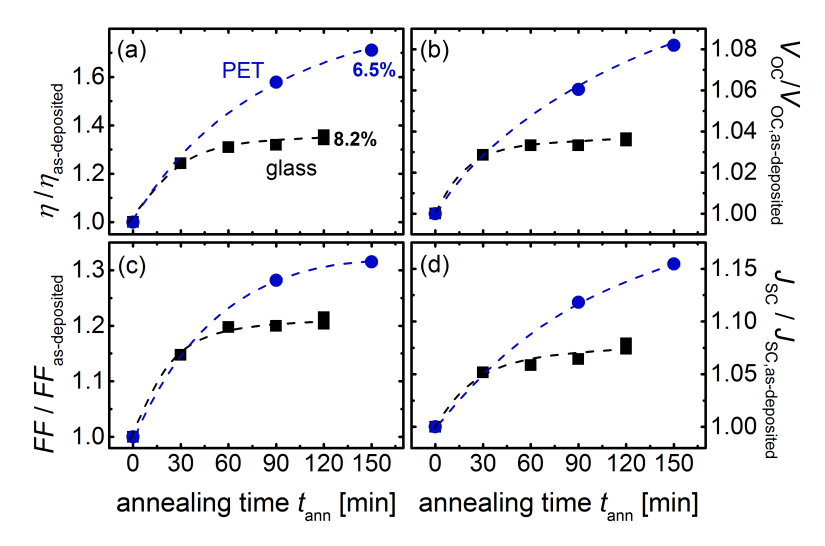


Figure 5.28.: Photovoltaic parameters normalized to the as-deposited value as a function of post-deposition annealing time $t_{\rm ann}$ for solar cells deposited at a substrate temperature $T_{\rm s}$ of 120 °C (black squares) on glass as well as on PET substrate (blue circles). The numbers on the right hand side of (a) indicate the absolute efficiency values after 120 minutes and 150 minutes annealing of the solar cell on glass and PET substrate, respectively. Lines are guides to the eye.

the case of a-Si:H solar cells on glass substrate (see Section 5.3.1). Accordingly, the pronounced annealing effect observed here is most likely related to the difference in properties of silicon layers prepared on PET and glass substrate. This point will be addressed in Section 6.1, indicating a general trend of reduction in the material quality for the case of PET substrates.

5.6. Annealing of μc -Si:H Solar Cells

The low temperature microcrystalline solar cells, developed in Section 4.2, were annealed after deposition according to the same procedure as the amorphous silicon solar cells. The resulting photovoltaic parameters are shown in Fig. 5.29. The data for a typical low temperature amorphous silicon solar cell is shown for comparison. It can be seen that also for the case of microcrystalline silicon solar cells, a significant improvement in the device performance upon post-deposition annealing at 120 °C is found. However, the improvements in each of the photovoltaic parameters are quite different from that observed in the case of a-Si:H solar cells. In contrast to the a-Si:H solar cell, the improvement in fill factor is only minor with up to 6 % relative after 8.5 hours annealing. On the other hand, both $J_{\rm SC}$ and $V_{\rm OC}$ increase stronger in the case of the μ c-Si:H solar cell, by 22 % and 8.5 % after 8.5 hours of annealing, respectively. In particular, both values do not tend to saturate even after this long time of annealing. No change in $I_{\rm crs}$, as estimated from

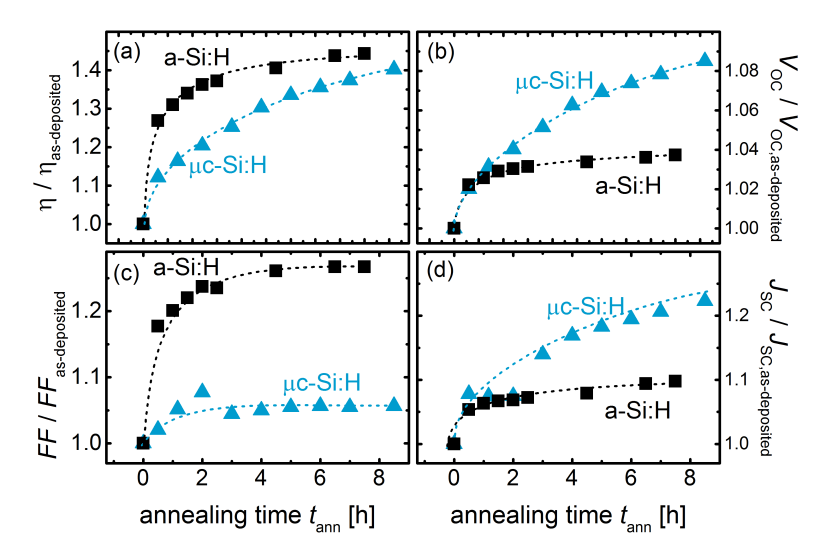


Figure 5.29.: Photovoltaic parameters normalized to the as-deposited value as a function of annealing time $t_{\rm ann}$ for a-Si:H (black squares) and μ c-Si:H (red triangles) solar cells deposited at 120 °C.

the results of Raman scattering measurements on individual layers as well as solar cells, could be detected upon annealing (not shown). Similar to the case of a-Si:H solar cells in Section 5.3.3, EQE curves were measured before and after post-deposition annealing for both p- and n-side illuminated solar cells. Information on the preparation of the n-side illuminated solar cells can be found in Section 5.3.3. The results are shown in Fig. 5.30 (a) and (b) for the p-side and n-side illuminated solar cell, respectively. In the case of illumination through the p-type layer in (a), the improvement in EQE upon annealing is only visible in the wavelength range above 500 nm, while in the case of n-side illumination in (b) the improvement is observed over the entire wavelength range.

Remarkably, similar changes in EQE curves for p- and n-side illuminated microcrystalline silicon solar cells upon annealing of irradiation induced deep defects were previously observed [262]. Computer simulations performed in [262] suggested that such an asymmetry in performance could result from a Fermi level motion in the microcrystalline silicon absorber layer towards the conduction band (by as much as $0.2\,\mathrm{eV}$) with reduction in the defect density upon annealing. One could speculate that changes in the performance of p- and n-side illuminated microcrystalline silicon solar cells observed here can be due to a similar mechanism, e.g. reduction in the density of defects upon annealing, accompanied by shift in the Fermi level towards conduction band. However, further investigations are needed to develop a more detailed model of the effects of post-deposition annealing on the performance of μ c-Si:H solar cells.

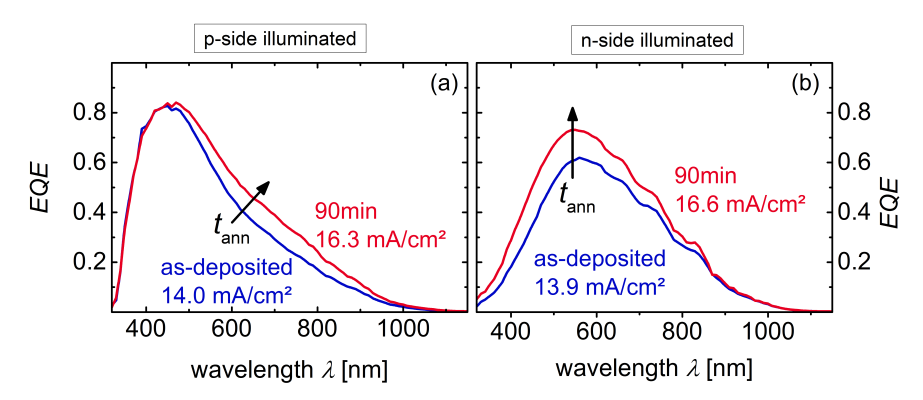


Figure 5.30.: External quantum efficiency EQE curves in the as-deposited state (blue) and after 90 minutes annealing time $t_{\rm ann}$ (red) for (a) a p-side and (b) an n-side illuminated μ c-Si:H solar cell.

5.7. Conclusion and Outlook

In this chapter the effects of post-deposition annealing on low temperature thin-film silicon solar cells were investigated. A strong improvement in the performance of both a-Si:H and μ c-Si:H solar cells was found. A detailed study of amorphous silicon layers and solar cells revealed that the main influence of the post-deposition annealing is on the intrinsic a-Si:H absorber layer. It was shown that the strongest effect is visible in the fill factor of the solar cell, which could be attributed to a reduced series resistance as well as improved charge carrier collection.

The charge carrier collection upon annealing was further investigated and it was shown that both the collection of electrons and holes is considerably improved. Possible reasons were related to (i) improved $\mu\tau$ -products of charge carriers in the intrinsic absorber layer and (ii) an enhanced built-in field in the device, either due to an increase in built-in voltage or a reduced deformation of the electrical field upon annealing. The experimentally observed increase in photo conductivity and ambipolar diffusion length measured on individual intrinsic a-Si:H layers provide evidence that the $\mu\tau$ -product of both electrons and holes is improved upon annealing. Possible reasons were related to a reduced number of defects resulting in an enhanced lifetime for both types of carriers. Furthermore, computer simulations utilizing a simplified solar cell model revealed that the increase in EQE curves upon annealing (for solar cells with different absorber layer thicknesses as well as both p- and n-side illuminated solar cells) can well be reproduced assuming an increase in both electron and hole mobility. Regarding the built-in field in solar cells, an observed increase in dark conductivity of the n-type layer upon annealing may improve the built-in voltage and thus the drift length of both electrons and holes. This in turn would also account for the observed increase in $V_{\rm OC}$ of the a-Si:H solar cell upon annealing. On the other hand, possible deformations of the electrical field within the intrinsic absorber layer would be reduced by an improvement in the $\mu\tau$ -product of charge carriers upon annealing, thus additionally improving the charge carrier collection.

The annealing effect was shown to be thermally activated and corresponding possible structural processes may be related to a frozen-in density of states due to the low deposition temperatures. It was hypothesized that upon annealing the film structure equilibrates by reducing the number of weak bonds. This would simultaneously lead to an increase in charge carrier mobility due to steeper band tails and a reduced number of defect states.

In order to make quantitative statements about the changes in the properties of layers and solar cells upon annealing, more sophisticated computer simulations need to be conducted that take into account light trapping and glass/TCO front interfaces. In that case, changes in e.g. charge carrier mobilities, density of band tail states, defect densities, etc. may be directly correlated to changes in photovoltaic parameters of the solar cells upon annealing. From the results of varying annealing temperatures it can be seen that for temperatures above the deposition temperature larger improvements in the device performance can be achieved in shorter time. It would be interesting to extend these studies towards very high temperatures and significantly shorter times, for example achieved by laser annealing.

An even stronger improvement in photovoltaic parameters is found for a-Si:H solar cells deposited on PET substrates. A possible explanation might be related to poorer material quality for silicon films grown on PET substrate, as will also be discussed in the following chapter. Regarding the influence of annealing on low temperature microcrystalline silicon solar cells, a distinct difference in the annealing behavior of photovoltaic parameters compared to a-Si:H solar cells was observed. Comparison to literature suggests that an improvement in cell performance upon annealing might be due to a reduction in the defect density in the intrinsic absorber layer, accompanied by shift in the Fermi level towards conduction band. However, more detailed studies - e.g. evaluation of the defect density in the absorber layer upon annealing - need to be undertaken to develop a more comprehensive model on the effects of post-deposition annealing on a-Si:H solar cells on PET substrates as well as on low temperature μ c-Si:H solar cells on glass substrates.

6. Solar Cells on Flexible Substrates

6.1. Silicon Films Grown on PET Substrate

In order to study the properties of silicon layers deposited on flexible substrates, individual p-type, n-type and intrinsic a-Si:H as well as p-type μ c-Si:H layers were deposited on bare PET substrate. Comparison to similar layers deposited on glass substrates was undertaken and the resulting electrical properties are presented in Table 6.1. In the case of microcrystalline p-type layers, the crystalline volume fraction $I_{\rm crs}$, evaluated from Raman scattering measurements, is shown as well. In the case of the doped layers, a reduction

Table 6.1.: Dark conductivity $\sigma_{\rm d}$ of p-type, n-type and intrinsic a-Si:H layers deposited at $T_{\rm s} = 120\,^{\circ}{\rm C}$ on glass and PET substrate. Additionally, in the case of intrinsic and microcrystalline layers, photo conductivity $\sigma_{\rm ph}$ and Raman crystallinity $I_{\rm crs}$ are presented, respectively.

| layer | substrate | $I_{\rm crs}~[\%]$ | $\sigma_{\rm d} \; [{ m S/cm}]$ | $\sigma_{\rm ph}~[{\rm S/cm}]$ |
|---------------------|-----------|--------------------|---------------------------------|--------------------------------|
| p-type a-Si:H | glass | - | 9.0×10^{-7} | - |
| p-type a-Si:H | PET | - | 5.4×10^{-8} | _ |
| p-type μ c-Si:H | glass | 45 ± 3 | 0.1 | - |
| p-type μ c-Si:H | PET | 28 ± 10 | 5×10^{-5} | - |
| n-type a-Si:H | glass | - | $8.7{	imes}10^{-4}$ | - |
| n-type a-Si:H | PET | - | 5.7×10^{-4} | |
| intrinsic a-Si:H | glass | - | 1.8×10^{-11} | 2.8×10^{-6} |
| intrinsic a-Si:H | PET | - | 3.4×10^{-10} | 2.3×10^{-6} |

in dark conductivity of all layers on PET compared to glass substrate is visible. The reduction is especially critical for the microcrystalline p-type layer, where a difference by nearly four orders of magnitude can be observed. This is probably due to a lower crystalline volume fraction of the film grown on PET substrate, which exhibits an $I_{\rm crs}$ of $28\pm10\,\%$ compared to $45\pm3\,\%$ on glass substrate. In the case of intrinsic a-Si:H layers, a considerably increased dark conductivity and a slightly lower photo conductivity leads to a reduced photo response for the film grown on PET substrate. In Fig. 6.1, the absorption coefficient α spectrum evaluated from the Constant Photocurrent Method (CPM) is presented for the intrinsic a-Si:H layer on glass (black line) as well as PET (blue dashed line) substrate. It is clearly visible that the sub-gap absorption at $1.2\,\mathrm{eV}$ is increased from $9.3\,\mathrm{cm}^{-1}$ in the case of the layer deposited on glass to $20.0\,\mathrm{cm}^{-1}$ in the

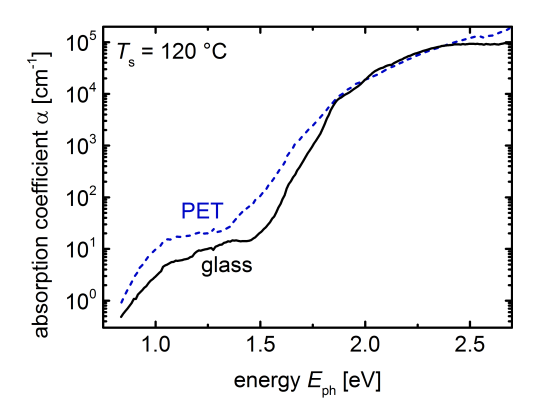


Figure 6.1.: Absorption coefficient α evaluated from CPM measurements as a function of photon energy $E_{\rm ph}$ for intrinsic a-Si:H layers deposited at $T_{\rm s}$ of 120 °C on glass (black line) and PET (blue dashed line) substrate.

case of deposition on PET substrate, respectively. Additionally, also the absorption in the region $1.3\,\mathrm{eV} < E_\mathrm{ph} < 1.8\,\mathrm{eV}$, which is related the transition between band tail states and extended states (i.e. conduction band tail \rightarrow valence band and/or valence band \rightarrow conduction band-tail), is significantly shifted to lower energies in case of the layer on PET substrate. This is usually attributed to an increased disorder in the films [28].

For the deposition of silicon layers on PET substrates, several reasons might lead to a possible variation in growth conditions. First, the actual temperature of the PET substrate during deposition might be lower than that of the glass substrate, due to the reduced contact area between heater and flexible substrate holder (see Section 3.1.3). This can lead to lower dark conductivities of doped a-Si:H layers, as shown in Chapter 4. Additionally, the microcrystalline growth is temperature dependent and a lower crystallinity is expected with decreasing temperature [248], thereby explaining the difference in $I_{\rm crs}$ values of the μ c-Si:H p-type layer on glass and PET substrate. The lower crystalline volume fraction in turn reduces the dark conductivity of the p-type μ c-Si:H layer.

Furthermore, although the deposition times for the layers on glass and PET substrate were similar, it was not possible to determine the actual layer thickness of the films grown on the PET substrate by simple profilometer measurements. Only in the case of the intrinsic a-Si:H layer on PET, the layer thickness was estimated from the interference fringes in transmittance measurements (see Section 3.3.1). The results show that for a deposition time of 53 minutes, the resulting layer thickness on glass and PET substrate is around 500 nm and 340 nm, respectively. However, a difference in substrate temperature of a few tens of degrees can not solely account for such a large difference in layer thickness, meaning that other effects but temperature influence the deposition rate. The layer thickness enters the calculation for the conductivity (see Section 3.3.3), and the assumption of similar layer thicknesses in the case of doped layers may therefore underestimate actual dark conductivity values. Furthermore, the crystalline volume fraction is thickness dependent [245] and it might therefore be possible that the reduced I_{crs} evaluated from Raman

measurements in case of the film on PET substrate is partly the result of a reduced layer thickness. In addition to the effect of thickness and temperature, the structural evolution of microcrystallites sensitively depends on the underlying substrate [243–245], and might thus also contribute to the observed differences in $I_{\rm crs}$ for the p-type μ c-Si:H layer on glass and PET substrate.

Additional contribution to the observed differences could be related to possible desorption and/or diffusion of atmospheric species (for example oxygen and/or carbon) and subsequent incorporation of these impurities in the silicon layers during growth. If that would be the case, additional defects and an increased structural disorder for the intrinsic a-Si:H layer on PET film, accompanied by an increase in dark conductivity, would be expected [273, 274]. This is in agreement with the experimental results shown above. In the following, to prevent possible desorption from and/or diffusion through the PET substrate, the solar cells were prepared on PET substrates covered with a barrier layer of zinc tin oxide (ZnSnO_x) or silicon oxynitride (SiO_xN_y) [275]. Furthermore, a TCO layer is deposited on top of the PET substrate in the case of solar cells, thereby leading to different growth conditions of the subsequently deposited silicon layers, compared to the results shown in this section.

6.2. Light Management on PET Substrate

6.2.1. Introduction

The term light management comprises the effects of light incoupling and light trapping. The first describes to what extent the incoming light reaches the absorber layer and is not reflected at or absorbed inside the front window layers or substrate. The latter describes trapping of the light inside the solar cell layers by repeated scattering and reflection, thereby prolonging the light path inside the absorber layer. There are several ways to optimize light management in a thin-film silicon solar cell, all of which utilize texturing of surfaces or interfaces to scatter or diffract the light. Considering techniques where texturing is implemented at the front side of a solar cell in superstrate configuration, one can texture the substrate itself and/or the TCO layer on top. The front TCO layer can be textured either using TCO materials that evolve an as-grown texture during the deposition like atmospheric-pressure (AP) CVD SnO₂:F [276] or zinc oxide materials fabricated by low-pressure CVD (LPCVD-ZnO) [25]. Alternatively, texturing can be undertaken by post-deposition treatments of the TCO like e.g. wet-chemical etching of ZnO:Al [116]. However, LPCVD-ZnO is not well compatible to PET substrates due to the substantial layer thickness of 2-3 μ m, which easily leads to stress-induced cracks in the zinc oxide layer on the flexible film due to differing thermal expansion coefficients [137]. Typical deposition temperatures for optimized device-grade material are around 300 °C for doped zinc oxide [118] and between 350-550 °C for APCVD SnO₂:F [18], which is too high for temperature-sensitive plastic substrates like PET with a limited process temperature range below 150 °C. Yet, some authors have shown that these materials can

also be prepared at lower temperatures [118, 277]. On the other hand, substrate texturing techniques include etching of the substrate [112], hot-embossing of polymer films [111, 278, 279] or nanoimprint lithography, where a resist layer on top of the substrate is textured [134, 135]. All of these three techniques are suitable for application on plastic substrates.

In this chapter two light management concepts, namely etching of ZnO:Al and nanoimprint lithography, are investigated and compared regarding their suitability for application in flexible solar cells on PET substrate. First, the ZnO:Al deposition process will be developed on glass substrates for low temperature deposition to be suitable for PET substrates. Then, results of each approach are described separately (Section 6.2.2 and 6.2.3, respectively) and comparison between deposition on glass and PET substrates are made. In the last section, both concepts applied on PET substrates are compared and discussed.

It can be shown that insertion of a thin barrier layer between the PET substrate and the front contact influences the growth of the ZnO:Al layer and leads to an improvement in solar cell performance in all photovoltaic parameters as well as EQE curve over the entire wavelength range (see Appendix D). Therefore all investigated layers and solar cells in the following sections are prepared on PET substrate covered with a thin layer of silicon oxynitride (SiO_xN_y) or zinc tin oxide (ZnSnO_x).

6.2.2. Texture-Etching of ZnO:Al Layers

Wet-chemical etching of ZnO:Al in HCl solution to obtain textured surfaces for application in thin-film silicon solar cells was early developed by Löffl et al. in 1997 [121] and has been intensively investigated since then [118, 119, 280, 281]. Rath et al. have applied this approach on PET as well as PEN substrates, yet the solar cells using these substrates were deposited in substrate configuration, where the transparency of the substrate does not need to be considered. In that work, an additional step of embossing of the polymer films was necessary to prevent stress and cracking of the ZnO:Al films.

In this section, the ZnO:Al deposition process will be developed on glass substrates for low temperature deposition to be suitable for PET substrates. Then, ZnO:Al layers deposited at a substrate temperature of 135 °C were deposited on glass and PET substrates and investigated regarding their electrical and optical properties before and after wetchemical etching in HCl. Afterwards, the effect on the performance of a-Si:H solar cells deposited on top of these substrates is examined. It is noteworthy that no change in e.g. optical properties of the PET substrate could be detected after the wet-chemical etching treatment in HCl solution. Parts of the results on etching of low temperature ZnO:Al have previously been published in [282].

ZnO:Al at Low Temperature

Electrical and optical properties of sputter-deposited ZnO:Al films, as well as the surface texture upon etching, depend greatly on the deposition conditions such as sputter pressure, substrate temperature and aluminum dopant concentration [118, 119]. A tradeoff is usually found especially between electrical and optical properties, and deposition conditions for optimal material depend on the type of solar cell and the layer position within (front or back contact). State-of-the-art ZnO:Al front contacts for thin-film silicon solar cells are usually deposited at temperatures around 300 °C with an aluminum dopant concentration of 1% [118]. In general, a dopant concentration of 2% provides better electrical properties at low deposition temperatures resulting from a larger carrier concentration [118]. However, free carrier absorption strongly limits the transparency in the wavelength range above 800 nm and would thus lead to losses in the short-circuit current density of a-Si:H/ μ c-Si:H tandem solar cells. Therefore, a sputter target with aluminum dopant concentration of 1% is chosen in this work. The influence of the substrate temperature on the electrical and optical properties of ZnO:Al layers on glass substrates is investigated and PET compatible deposition temperatures below 150 °C are considered. Afterwards, electrical and optical properties of thick (800 nm) ZnO: Al layers deposited on glass and PET substrates are compared and discussed.

In Fig. 6.2(a)-(c), electrical properties of ZnO:Al films having a thickness of $300 \,\mathrm{nm}$ are shown as a function of substrate temperature T_{s} . When the substrate temperature

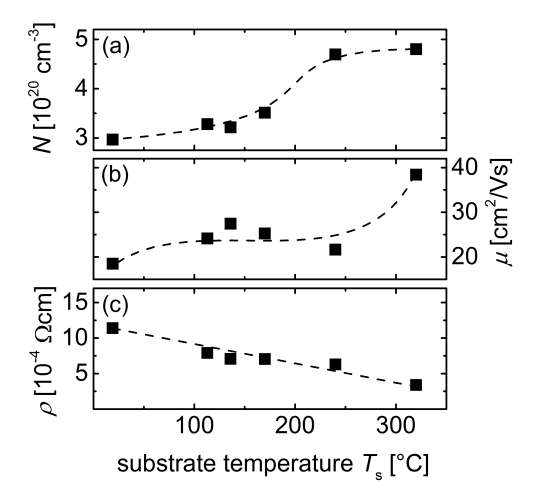


Figure 6.2.: Hall characteristics as a function of substrate temperature $T_{\rm s}$ for ZnO:Al prepared on glass substrates: (a) carrier density N, (b) carrier mobility μ and (c) resistivity ρ . Lines are guides to the eye.

is reduced from 320 °C to room temperature, a significant decrease can be seen in both carrier density N (Fig. 6.2(a)) and carrier mobility μ (Fig. 6.2(b)): from 4.8×10^{20} to 3.0×10^{20} cm⁻³ and 38 to $18 \, \mathrm{cm^2/Vs}$, respectively. This in turn leads to an increasing resistivity

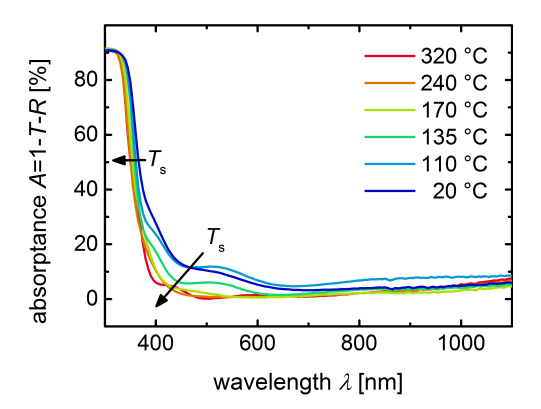


Figure 6.3.: Absorptance curves A=1-T-R of ZnO:Al layers prepared on glass substrates at various substrate temperatures T_s . Interference fringes result from different positions for transmittance T and reflectance R measurements on the substrate and thus slightly different layer thickness.

from 3.5×10^{-4} to $11.4\times10^{-4}\,\Omega$ cm (Fig. 6.2(c)). In Fig. 6.3, absorption curves A=1-T-R are plotted for various substrate temperatures. The absorptance of the ZnO:Al layer continuously decreases with increasing substrate temperature in the visible wavelength range. The results confirm that high deposition temperatures are beneficial for both conductivity and transparency of the ZnO:Al material in the investigated range. In order to be suitable for application in solar cells on PET substrates, a substrate temperature of 135 °C was chosen, which is close but still sufficiently below the maximum process temperature of the PET substrate to allow tolerance for temperature fluctuations (e.g. due to heating upon ion bombardment).

In the following, ZnO:Al layers deposited at $135\,^{\circ}\mathrm{C}$ on glass and PET substrates are compared to a highly optimized reference ZnO:Al on glass, fabricated at high temperature of $300\,^{\circ}\mathrm{C}$. The layer thickness was $800\,\mathrm{nm}$ for all three films. Hall characteristics of the as-deposited films for all three types of ZnO:Al are presented in Table 6.2. Please note

Table 6.2.: Resistivity ρ , carrier density n and mobility μ of as-deposited ZnO:Al layers with a thickness of 800 nm on glass and PET substrate.

| substrate | $T_{\rm s}$ [°C] | $\rho \ [10^{-4} \ \Omega \mathrm{cm}]$ | $n \ [10^{20} \mathrm{cm}^{-3}]$ | $\mu \ [\mathrm{cm^2/Vs}]$ |
|-------------------|------------------|---|-----------------------------------|----------------------------|
| glass (reference) | 300 | 3.0 ± 0.2 | 5.0 ± 0.5 | 45 ± 2 |
| glass | 135 | 4.8 ± 0.7 | 3.8 ± 0.4 | 34 ± 2 |
| PET | 135 | $6.4 \!\pm\! 0.7$ | $3.4 \!\pm\! 0.4$ | 28 ± 2 |

the difference in the values for low temperature ZnO:Al on glass to that in Fig. 6.2(a)-(c), which is due to the increased layer thickness (800 nm) that is needed to provide enough material for texturing by chemical etching. It has been shown that especially the

carrier mobility is thickness dependent due to an increased grain size in thicker films, thus reducing grain boundary scattering of carriers [283].

For a substrate temperature of 135 °C, ZnO:Al deposited on glass substrate shows a higher mobility (34 cm²/Vs) compared to that on PET substrate (28 cm²/Vs), while variations in carrier density are within the error bar. A possible explanation might be related to lower actual substrate temperatures when PET substrates are used, as in the case of PECVD deposition discussed above (see Section 6.1). Yet, considering that the substrate in the sputter chamber is not in contact with the heater, no significant difference in temperature would be expected (see also Section 3.1.3). Furthermore, the mobility does not change significantly down to a temperature of 110 °C as shown in Fig. 6.2(b). The carrier mobility is mainly affected by grain boundary scattering, lattice defects and impurity scattering introduced by Al dopants [188]. A more likely explanation might therefore be related to growth conditions of the ZnO:Al on the PET substrate, where smaller grain size and/or more defective material would lower the mobility. Similar explanations can be related to the higher mobility and carrier density of the reference ZnO:Al, in this case resulting from the higher deposition temperature, as shown above.

Texture-Etched ZnO:Al Layers

In the following, results for electrical, optical and structural properties of the low temperature ($T_s = 135\,^{\circ}$ C) ZnO:Al layer on both glass and PET substrate are presented before and after wet-chemical etching in 0.5 % HCl solution for 10, 20 and 30 s. The PET substrate for this study was covered with a thin (20 nm) barrier layer of ZnSnO_x. The results are compared to the standard reference of state-of-the-art ZnO:Al on glass with highly optimized electrical and optical properties, which is deposited at 300 °C in another deposition system and etched for 40 s (named reference in the following) [118]. The layer thickness before etching was around 800 nm for all investigated films to provide enough material for etching over the investigated timescale of etching steps. It is noteworthy that no cracks were visible by eye or optical microscope before and after wet-chemical etching for all ZnO:Al layers. The discussion of the results will be presented at the end of this section.

Electrical Properties The sheet resistance R_{\square} for low temperature ZnO:Al on both glass and PET substrate, as well as for the high temperature reference, is shown in Fig. 6.4 as a function of etching time $t_{\rm etch}$. The values at 0 s correspond to the layers presented in Table 6.2. Before etching (0 s), the sheet resistance of all three ZnO:Al layers is below 10 Ω. With increasing etching time, the sheet resistance increases with different rates for the three materials: in case of the high temperature reference (black circles), the sheet resistance stays very low, below 10 Ω even after 40 s etching. For the low temperature ZnO:Al on glass substrate (red squares), the sheet resistance increases faster with etching time, up to 27 Ω after 30 s etching. In the case of ZnO:Al on PET substrate (blue triangles), the sheet resistance increases even faster, reaching 28 Ω after 20 s and approaching 50 Ω after 30 s etching time with a large error bar of ±15 Ω.

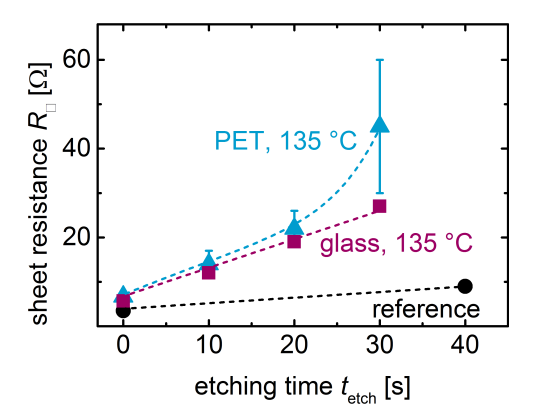


Figure 6.4.: Sheet resistance R_{\Box} as function of etching time $t_{\rm etch}$ for ZnO:Al layers deposited at $T_{\rm s}\!=\!300\,^{\circ}{\rm C}$ (black circles) and $T_{\rm s}\!=\!135\,^{\circ}{\rm C}$ (red squares) on glass substrate as well as on PET substrate (blue triangles).

Optical Properties Concerning the optical properties of the ZnO:Al layers before and after etching, transmittance T and reflectance R curves are shown for the etching series of low temperature ZnO:Al on glass and PET substrate in Fig. 6.5(a) and (b), respectively. In (a), the data for the reference ZnO:Al after 40 s etching is also shown for comparison

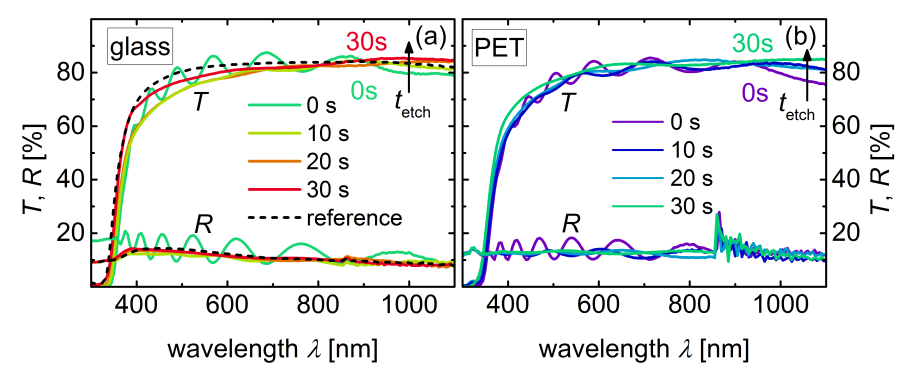


Figure 6.5.: Transmittance T and reflectance R curves for ZnO:Al deposited at $T_s = 135$ °C on (a) glass and (b) PET substrate after various etching times $t_{\rm etch}$ from 0 s to 30 s. Reference ZnO:Al after 40 s etching time is shown for comparison in (a) (black dashed line).

(black dashed line). Evaluation of the position of the interference fringes in transmittance and reflectance data of ZnO:Al before etching on both glass (green line in Fig. 6.5(a)) and PET substrate (purple line in Fig. 6.5(b)), according to Eq. 3.1, indicates that the ZnO:Al layer thickness is similar (837 \pm 52 nm) on both types of substrates, assuming that the refractive index of the ZnO:Al is 2.1 and does not change considerably in the range between 430 nm and 685 nm. This also suggests a similar substrate temperature, as the deposition rate is sensitive to the deposition temperature. In general, trends and values

for T and R with etching time do not significantly differ for both types of substrates. The reflectance of the ZnO:Al covered substrate is reduced for most of the wavelengths after the first etching step of 10 s (light green line in (a), dark blue line in (b)). Evaluation of the corresponding average reflectance in the wavelength range between 300 nm and 1200 nm shows a slight reduction from 12.6 % to 10.2 %. This is due to the evolving texture upon etching, and light scattering can already be seen by naked eye as the surface of the ZnO:Al becomes milky. Consequently, interference fringes are diminished. However, at the same time the transmittance decreases for $\lambda < 900$ nm as light scattering prolongs the light path inside the ZnO:Al layer thus increasing the absorptance. With further etching, the reflectance is constant whereas the transmittance continuously increases over the entire wavelength range due to the reduction in layer thickness of the ZnO:Al. After 30 s etching time, the transmittance and reflectance curves are roughly similar to that of the reference ZnO:Al (black dashed line).

Texture upon Etching In order to investigate the evolving surface texture of the ZnO:Al layers, SEM images were taken and selected images are shown in Fig. 6.6. In (a), a typical

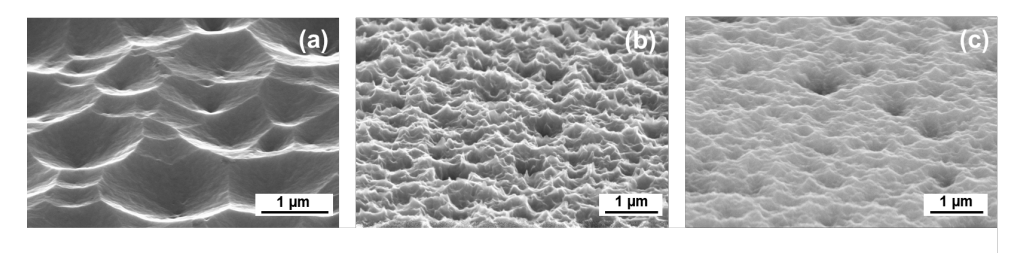


Figure 6.6.: SEM images for ZnO:Al deposited at (a) $T_s = 300$ °C on glass (reference), (b) $T_s = 135$ °C on glass and (c) $T_s = 135$ °C on PET substrate, after 40 s, 20 s and 20 s etching time, respectively.

crater-like structure after 40 s etching of the optimized high temperature reference is visible [118]. The size of the craters is typically 1-2 μ m. The SEM image of the 20 s etched low temperature ZnO:Al on glass substrate in (b) shows significantly smaller features with steeper edges and lateral sizes of about 300 nm that are regularly distributed over the substrate. The etched ZnO:Al on PET substrate (c) has similar feature sizes but shows a smoother surface compared to the layer on glass substrate.

Light Scattering Properties Light scattering properties of ZnO:Al films for application in thin-film silicon solar cells are evaluated by measurements of haze in transmission $H_{\rm T}$ and angle resolved scattering ARS. The haze value describes the amount of light that is diffusely transmitted, while the angular intensity distribution AID, evaluated from ARS measurements, resolves the angles the light is scattered into. Though direct relations between $H_{\rm T}$, AID of ZnO:Al films and short-circuit current densities in solar cells can not be derived, as a general rule $H_{\rm T}$ should be as high as possible and the light should preferably be scattered into large angles above the angle of total internal reflection θ_c

to increase light trapping [284, 285]. Assuming refractive indexes of 2.1 and 3.5 for the ZnO:Al and a-Si:H layer, the value for θ_c is around 37°. Haze and AID curves for the low temperature ZnO:Al layers after various etching times can be found in Fig. 6.7 and 6.8, respectively. The results on glass and PET substrates are shown in (a) and (b), respectively. As expected, the non-etched samples (0 s, green line in (a) and purple line

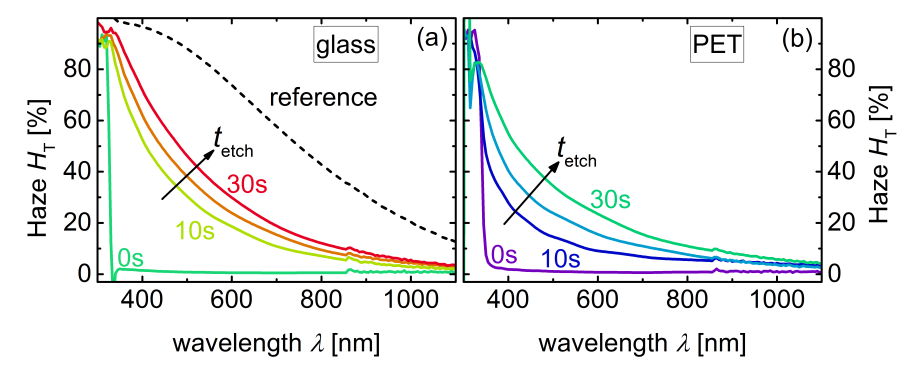


Figure 6.7.: Haze in transmission $H_{\rm T}$ curves for ZnO:Al deposited at $T_{\rm s} = 135\,^{\circ}{\rm C}$ on (a) glass and (b) PET substrate after various etching times $t_{\rm etch}$ from 0 s to 30 s. Reference ZnO:Al after 40 s etching time is shown for comparison in (a) (black dashed line).

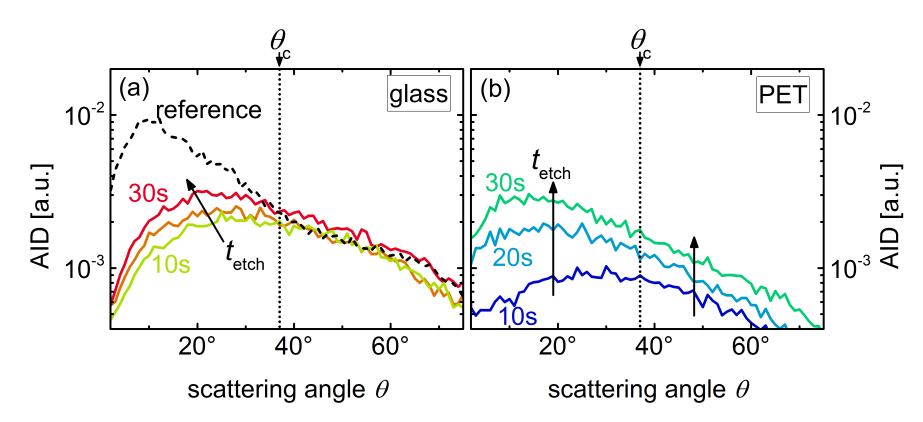


Figure 6.8.: Angular intensity distribution AID for ZnO:Al deposited at $T_s = 135$ °C on (a) glass and (b) PET substrate after various etching times t_{etch} from 0 s to 30 s. Reference ZnO:Al after 40 s etching time is shown for comparison in (a) (black dashed line).

in (b)) show hardly any light scattering and the haze value is close to zero for most of the wavelengths. After the first etching step of $10\,\mathrm{s}$, H_T significantly increases up to $11\,\%$ and $7\,\%$ at $700\,\mathrm{nm}$ for the samples on glass and PET substrate, respectively. The AID shows a broad distribution of scattering angles θ , which peak at around 20° in both cases. With further etching, H_T continues increasing up to $19\,\%$ and $16\,\%$ at $700\,\mathrm{nm}$ after $30\,\mathrm{s}$ etching, respectively, and the additionally scattered light is mainly coupled into angles below 37°

in both cases. In the case of ZnO:Al on PET substrate, also a considerable increase of scattering into large angles with continued etching is visible. Comparison to the reference (black dashed line in (a)) shows that the optimized high temperature ZnO:Al exhibits a considerably larger haze, with values of 58% at 700 nm. Though due to the large feature size, the additionally scattered light is mainly scattered to small angles below 37°, thus below the angle of total internal reflection. Concerning scattering of light into large angles above 37°, the low temperature ZnO:Al shows similar performance as the reference.

Discussion The results presented above indicate that the growth conditions of the ZnO:Al layer critically depend on the deposition temperature as well as substrate material. It was shown in this section that the electrical properties, evaluated from Hall effect measurements, as well as the evolution of the sheet resistance with etching time differ for the three types of ZnO:Al layers investigated. In general, the sheet resistance is expected to increase upon etching due to the continuous erosion of material resulting in a reduced layer thickness. The stronger increase for the low temperature ZnO:Al on glass substrate can thus partly be related to different etching rates, exhibiting a layer thickness of 410 nm after 30 s etching, while the reference has a thickness of around 600 nm after 40s etching time. However, the thickness values obtained from textured surfaces must be treated with care, as the tip of the profilometer may not be able to penetrate small features, thus overestimating the layer thickness [280]. Another contribution may be related to a thickness-dependent grain size and/or grain boundary quality as evident by comparison of layers with thicknesses of 300 nm and 800 nm. This may result in changing material quality when the outer (higher quality) material is removed. The different trends in sheet resistance therefore indicate a difference in the evolution of material quality with increasing thickness for the three types of ZnO:Al material.

Regarding transmittance and reflectance of the ZnO:Al layers on glass and PET substrates, similar trends are observed with etching time. The change in transmittance with etching time results from a combination of increased absorption in the ZnO:Al layer due to light scattering and a reduction in layer thickness. A direct correlation of transmittance measurements in air to parasitic absorption in a solar cell can not be established from these results, as light trapping in the ZnO:Al layer will change when silicon layers are deposited on top of the ZnO:Al layer [286]. A possibility to improve the compatibility between transmittance measurements and parasitic absorption in a device would be the use of an index-matching liquid during transmittance measurements [118].

It was shown in literature that the surface topography of ZnO:Al layers after post-deposition wet-chemical treatment in HCl is highly affected by the material quality (especially compactness) and thus growth conditions of the ZnO:Al layer, such as deposition pressure, temperature and Al-dopant concentration [118, 119]. This is in agreement with the observed deviation of the texture for the ZnO:Al deposited at 135 °C visible in Fig. 6.6(b) compared to the optimized high temperature texture (Fig. 6.6(a)). The evolving texture shows significantly smaller feature sizes with steep edges regularly distributed over the substrate area. According to Owen, the steepness of craters may be related to the etch potential and size of grain boundaries [20]. Assuming that etching conditions

(etchant concentration and temperature) are similar, a possible explanation for steeper edges on the surface of the low temperature ZnO:Al film after etching might be related to a larger lateral expansion of grain boundaries compared to the ZnO:Al deposited at high temperature. Etching molecules may thus penetrate into a larger number and deeper into grain boundaries resulting in steeper opening angles of the craters [20]. The influence of the substrate material on the material structure is also visible from comparison of the low temperature ZnO:Al grown on glass and PET substrate (Fig. 6.6(b) and (c), respectively). The feature size is similar to that on glass substrate, however the edges are smoother.

Concerning light scattering properties, $H_{\rm T}$ for low temperature ZnO:Al on glass substrate and the reference are different, nevertheless, equal amount of light is scattered to large angles $\theta > \theta_{\rm c}$ for all three types of substrates. Larger surface features lead to scattering into preferably small angles [115], thus the reference shows superior scattering in this range compared to the low temperature ZnO:Al on glass. Regarding light trapping however, scattering into large angles is most effective, as the light is to a large amount trapped inside the solar cell for angles above the angle of total internal reflection [285]. In the case of ZnO:Al on PET, a more pronounced increase in $H_{\rm T}$ as well as AID is visible with increased etching time from 10 s to 30 s. Nevertheless, light scattering properties for the low temperature ZnO:Al on glass after 30 s and on PET substrate after 20 s, which were used for the solar cell deposition, can be considered as similar. It should be noted here that the AID for etched ZnO:Al layers may be different when the layers are implemented in a solar cell, i.e. the ZnO:Al is in contact with silicon layers instead of air [285].

In this study, different growth conditions and consequently material quality of the ZnO:Al layers are the consequence of the difference in substrate temperature, as obviously present by comparison of ZnO:Al layers deposited at 300 °C (reference) and 150 °C on glass substrates. In the case of PET substrates, growth conditions may be affected by different nucleation on the (ZnSnO_x-covered) PET substrate compared to glass, presence of stress due to a large mismatch in thermal expansion coefficients of PET and ZnO:Al, as well as possible impurities originating from the PET substrate. Possible consequences due to these effects are variations in grain size as well as more defective material and/or grain boundaries.

In the following section, the influence of the different electrical and optical properties discussed above on the performance of an a-Si:H solar cell will be investigated.

Solar Cells on Etched ZnO:Al Layers

Solar cells were deposited on top of the low temperature ZnO:Al layers on glass substrates etched for various times between 10 s and 30 s. Comparisons were made between the solar cell on 30 s etched low temperature ZnO:Al and on the reference ZnO:Al, as well as on ZnO:Al on PET substrate after etching for 20 s. Though the ZnO:Al on PET substrate etched for 30 s exhibits higher transparency than that etched for 20 s (see Fig. 6.5(b)), the sheet resistance and homogeneity are rather poor after 30 s etching, making it unattractive for application in solar cells. Again, a thin $(20\,\mathrm{nm})$ layer of ZnSnO_x was used as

barrier layer on top of the PET substrate. An additional microcrystalline p-type layer was inserted between the ZnO:Al and p-type a-Si:H layer which has proved to be beneficial for the performance of solar cells on glass substrates due to improvement of the ZnO:Al/p-interface [287, 288]. Furthermore, the double p-type layer provided a higher optical transparency compared to the single p-type a-Si:H layer (not shown). The solar cells were annealed until the improvement in photovoltaic parameters saturated, which was in this case 3.5 hours for the solar cells on glass and 6 hours for the solar cell on PET substrate. The solar cells are investigated by measurements of J-V and EQE curves and the results are discussed at the end of this section.

In Fig. 6.9(a), external quantum efficiency EQE curves and cell absorptance 1-R are shown for solar cells on low temperature ZnO:Al layers etched for various times $t_{\rm etch}$. Corresponding $J_{\rm SC}$ values are presented in Fig. 6.10(a). The solar cell with the smooth,

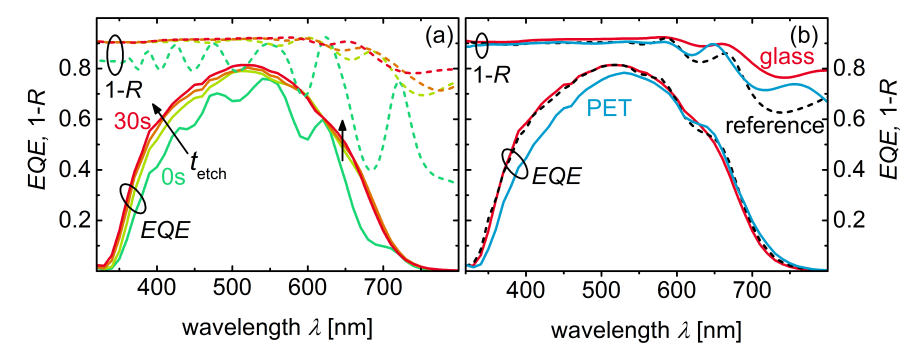


Figure 6.9.: External quantum efficiency EQE curves and cell absorptance 1-R for solar cells using ZnO:Al as front contact: (a) on glass substrate with $T_{\rm s}({\rm ZnO:Al}) = 135\,^{\circ}{\rm C}$ after various etching times $t_{\rm etch}$ of the ZnO:Al from 0 s to 30 s, (b) comparison of the solar cells with various ZnO:Al layers on glass and PET substrate: $T_{\rm s}({\rm ZnO:Al}) = 135\,^{\circ}{\rm C}$ on glass after 30 s etching (red solid line), $T_{\rm s}({\rm ZnO:Al}) = 300\,^{\circ}{\rm C}$ on glass after 40 s etching (reference, black dashed line) and $T_{\rm s}({\rm ZnO:Al}) = 135\,^{\circ}{\rm C}$ on PET after 20 s etching (blue solid line).

non-etched (0 s) ZnO:Al layer as front contact (green line) shows a poor EQE curve with interference fringes, as light passes specularly without significant scattering of the light (green line), resulting in a $J_{\rm SC}$ of $11.3\,{\rm mA/cm^2}$. By introduction of a texture after the first etching step of 10 s (light green line), the EQE curve is significantly improved over the entire wavelength range compared to the smooth substrate, which results from an enhanced cell absorptance. The short-circuit current density is thus significantly increased up to a value of $13.2\,{\rm mA/cm^2}$. With continued etching, the EQE further increases, especially for $\lambda < 580\,{\rm nm}$, while no considerable change in cell reflectance can be observed. The solar cell on $30\,{\rm s}$ etched ZnO:Al achieves therefore the highest short-circuit current density of $13.9\,{\rm mA/cm^2}$. Comparison of this solar cell (red line) with the solar cell on reference ZnO:Al (black dashed line) in Fig. 6.9(b) shows similar EQE curves, despite a difference in cell absorptance for $\lambda > 600\,{\rm nm}$. Similar EQE curves in the long wavelength range above $550\,{\rm nm}$ can also be observed for the solar cell on PET substrate (blue line),

yet a significant reduction in EQE is detected for $\lambda < 550 \,\mathrm{nm}$. This results in a J_{SC} of $13.3 \,\mathrm{mA/cm^2}$ for the solar cell on PET substrate.

In Fig. 6.10, corresponding photovoltaic parameters of the solar cells are presented as a function of etching time t_{etch} . With increasing etching time of the low temperature

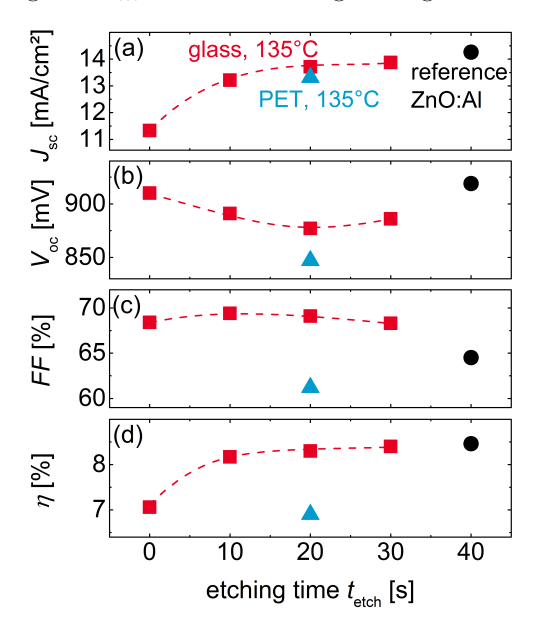


Figure 6.10.: Photovoltaic parameters of solar cells using various types of ZnO:Al as front contact as a function of ZnO:Al etching time $t_{\rm etch}$: $T_{\rm s}({\rm ZnO:Al}) = 135\,^{\circ}{\rm C}$ on glass (red squares), $T_{\rm s}({\rm ZnO:Al}) = 300\,^{\circ}{\rm C}$ on glass (reference, black circle) and $T_{\rm s}({\rm ZnO:Al}) = 135\,^{\circ}{\rm C}$ on PET (blue triangles). Lines are guides to the eye.

ZnO:Al on glass substrate (red squares), the open-circuit voltage $V_{\rm OC}$ decreases by 20 mV when a texture is introduced after 10 s etching and stays relatively constant around 884±7 mV with further etching time. In contrast, $V_{\rm OC}$ for the solar cell on the reference ZnO:Al is significantly higher, attaining a value of nearly 920 mV. The fill factor is only slightly affected by an increasing etching time and is $68.8\pm0.5\%$. Surprisingly, the solar cell on reference ZnO:Al exhibits a low fill factor of 64.8%, although it shows the lowest sheet resistance (see Fig. 6.4). Overall, the solar cell on etched low temperature ZnO:Al achieves an efficiency of 8.4%, similar to that on the reference ZnO:Al (8.5%). The solar cell on PET substrate shows lower $V_{\rm OC}$ by $42\,\rm mV$ as well as a reduction in fill factor by 9.1% absolute, leading to an efficiency of 6.9%.

Discussion Implementing the low temperature ZnO:Al front contact in an amorphous silicon solar cell, it was found that introduction of a texture by etching of ZnO:Al leads to a significant increase in external quantum efficiency over the entire wavelength range. This can be related to two effects: improved *trapping* of the light, as visible in the long

wavelength range above 600 nm, which results in multiple passes through the absorber layer in the case of weakly absorbed light. Light of short wavelength on the other hand is mainly absorbed within the front part of the solar cell and the effect of light trapping is negligible in the wavelength range below 500 nm. The increase in EQE due to an increased cell absorptance for these wavelengths is therefore probably due to enhanced light incoupling into the solar cell. This results from rough surfaces at the front side of the solar cell that act as refractive index grading [107]. The resulting current increase due to a short etching time of 10 s is as high as $1.7 \,\mathrm{mA/cm^2}$. The continuously increasing EQE curve in the short wavelength range with further etching is probably simply due to thinning of the ZnO:Al layer and thereby reduced parasitic absorption as no change could be detected in cell absorptance 1-R of the solar cell. Indications for this are also given by the increasing transmittance in the short wavelength range with etching time of ZnO:Al layers (see Fig. 6.5(a)), though the trend is not as clear due to overlapping light trapping effects in single layers, as discussed above.

Although having different surface textures, all three types of ZnO:Al covered substrates lead to similar effective light trapping when implemented in a-Si:H solar cells. This is evident from EQE curves in the long wavelength range above 550 nm were no remarkable difference between the three curves can be observed. This may possibly be related to similar AIDs in the large angle range for all three types of substrates (Fig. 6.8). Light incoupling and parasitic absorption in the low temperature ZnO:Al and reference are also similar, which is mainly visible in the short wavelength range below 550 nm (Fig. 6.9(b)). As a result, similar $J_{\rm SC}$ of $13.9\,{\rm mA/cm^2}$ and $14.2\,{\rm mA/cm^2}$ are achieved (Fig. 6.10 (a)), thus confirming that the light scattering properties of the etched low temperature ZnO:Al are adequate for use in amorphous silicon solar cells.

The solar cell on etched ZnO:Al on PET substrate shows considerably lower EQEvalues for $320 \,\mathrm{nm} < \lambda < 550 \,\mathrm{nm}$, for which there are two likely causes. First, the transmittance for the 20s etched ZnO:Al on PET is slightly lower compared to the 30s etched ZnO:Al on glass due to the shorter etching time, which would cause increased parasitic absorption in the solar cell. However, when substrates with identical transmittance on glass and PET substrate are compared as in [282], the EQE curve of the solar cell on PET substrate is still lower. Differences in light incoupling are also improbable, as this would be visible in the cell absorptance, where there is only marginal variation for the solar cells on both types of substrates. Instead, another possible explanation is related to the growth conditions of the μ c-Si:H p-type layer, where the nucleation properties and/or the actual temperature of the PET substrate may be different from glass substrates. As already shown and discussed in Section 6.1, the crystallinity of the p-type μ c-Si:H layer on PET is considerably lower with $I_{\rm crs}$ of 28±10 % compared to 45±3 % on glass substrate (see Table 6.1). This in turn leads to additional parasitic absorption in the discussed wavelength range [289]. Additionally, the structural evolution of the microcrystalline silicon layer with thickness could be different, which may contribute to the observed differences in I_{crs} and would particularly be important in thinner (around 20 nm) layers used in solar cells.

Regarding photovoltaic parameters in Fig. 6.10, the low fill factor of 64.6% for the solar cell on reference ZnO:Al despite its low sheet resistance is surprising. Furthermore, fill factor values of the etched low temperature ZnO:Al are nearly constant for a sheet resistance range from 12Ω to 27Ω (after etching for 10 s to 30 s, respectively, Fig. 6.4). This suggests that the ZnO:Al sheet resistance in this range is not limiting the fill factor in this kind of low temperature amorphous silicon solar cell, but a low shunt resistance or other series resistances in the device structure, such as non-optimal interfaces (e.g. TCO/p-contact) [290] or the material quality of the low temperature a-Si:H absorber layer. The difference in $V_{\rm OC}$ between the solar cell on low temperature ZnO:Al and reference ZnO:Al on glass substrate may partly be related to the varying surface areas of the ZnO:Al covered substrate. Comparing $V_{\rm OC}$ values to the normalized surface area $A_{\rm norm}$ of the various ZnO:Al textures evaluated from AFM measurements (see Table 6.3), it seems likely that a larger surface area of the TCO/p-type layer interface in case of the etched low temperature ZnO:Al leads to enhanced surface recombination between electrons and holes, which in turn causes losses in $V_{\rm OC}$ [291]. However, the low $V_{\rm OC}$ in

Table 6.3.: Normalized surface area A_{norm} , evaluated from AFM measurements, for ZnO:Al layers deposited at various substrate temperatures T_{s} on glass and PET substrate.

| substrate | $T_{\rm s}$ [°C] | $\mathbf{A}_{\mathrm{norm}}$ |
|-----------|------------------|------------------------------|
| reference | 300 | 1.10 |
| glass | 135 | 1.36 |
| PET | 135 | 1.22 |

case of the solar cell on PET can not be related to the surface area though, as $A_{\rm norm}$ is between that of the reference and low temperature ZnO:Al on glass substrate. The result may therefore be related to an inferior material quality of silicon layers, especially reduced dark conductivity of the p-type layer when grown on PET substrates (more than one order magnitude lower than on glass substrate, see Table 6.1). According to Wang et al., a reduction in the p-type layer conductivity can reduce the built-in potential in solar cells which consequently leads to a reduction in $V_{\rm OC}$ [227]. Furthermore, a possibly poorer material quality of the microcrystalline p-type layer on PET substrate would also give an explanation for the low fill factor of 61.2% for the solar cell on PET substrate.

In Fig. 6.9, a varying cell absorptance for $\lambda > 600\,\mathrm{nm}$ for solar cells on the three types of investigated substrates was found: average values for 1-R between 600 nm < $\lambda < 800\,\mathrm{nm}$ are 74% on reference ZnO:Al, 78% on PET and 83% for low temperature ZnO:Al on glass, respectively. This is likely to be related to plasmonic absorption losses at the n-type a-Si:H/Ag interface. Palanchoke et al. have shown that absorption losses due to surface plasmon resonance at the a-Si:H/metallic back contact interface are more severe for textures exhibiting smaller features [292], such as present in the etched low temperature ZnO:Al. This implicates that a high cell absorptance in this case is only due to an increased parasitic absorption which does not lead to generation of charge carriers. The trend among the three substrates is in agreement with the feature sizes of the corresponding substrates. Plasmonic absorption losses can be reduced by insertion of a thin ZnO:Al layer between



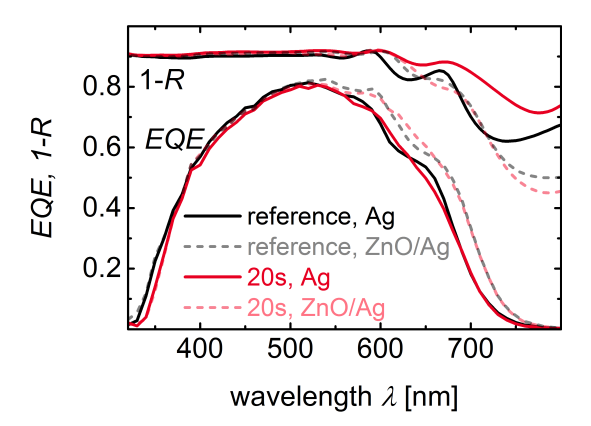


Figure 6.11.: External quantum efficiency EQE curves and cell absorptance 1-R for solar cells on glass substrates with various front and back contacts: $T_s(\text{front ZnO:Al}) = 135\,^{\circ}\text{C}$ after 20 s etching time with Ag and ZnO/Ag back contact (red solid and red dashed line, respectively), $T_s(\text{front ZnO:Al}) = 300\,^{\circ}\text{C}$ after 40 s etching time (reference) with Ag and ZnO/Ag back contact (black solid and black dashed line, respectively).

increases for $\lambda > 500\,\mathrm{nm}$ (dashed lines). At the same time, the cell absorptance 1-R decreases, as due to reduced parasitic absorption, non-absorbed light is reflected back. In the case of diminished plasmonic absorption, 1-R is identical for both types of surface textures with small and large feature sizes, in agreement with the hypothesis of Palanchoke et al. In general, it is important to bear in mind that thin amorphous silicon absorber layers, due to its quasi-direct band gap and thus relatively steep absorption edge might be less sensitive to varying texture types. The investigated textures will have different effects when applied in a solar cell with a typical microcrystalline silicon absorber layer.

6.2.3. Nanoimprint Lithography

Several reports have shown that nanoimprint lithography, where a UV sensitive photo resist layer is spin-coated and textured on top of a substrate, is an appropriate technique to introduce rough surfaces at the front or back side of the solar cell for efficient light management [134, 135, 139]. Previous studies have implemented nanoimprint lithography in solar cells on polymer films [150, 155, 294, 295], though these devices were all deposited in substrate configuration, so losses in substrate transparency were not taken into account. In the present work, the effects of nanoimprint lithography on the transparency of the PET substrates were investigated for a flexible solar cell in superstrate configuration, where the light enters through the substrate. In that case, one needs to take care of the possible impact on the transparency of the flexible substrate resulting from the imprint process.

It should be noted here that the deposition temperature for ZnO:Al layers used as TCO for the results presented in this section was intended to be nominally 135 °C, yet was estimated to be up to 180 °C, which was only noticed after the results for this study were obtained. The impact on the long-term stability of the substrates when temperatures higher than the nominal upper process temperature are used is not predictable. Furthermore, stress present in the films, resulting from the difference in thermal expansions coefficient, increases with a rise in deposition temperature, which will especially be critical for the deposition of thicker films. Such high process temperatures should therefore be avoided in future.

Results on properties of ZnO:Al layers deposited on non-imprinted and imprint-textured glass and PET substrates are presented first, followed by characteristics of a-Si:H solar cells deposited on top of these substrates. A comprehensive discussion will be given at the end of this section. Parts of the results shown here have previously been published in [296] and [297].

Properties of ZnO:Al Covered Substrates

In this section, the effect of texturing by nanoimprint lithography on the characteristics of the TCO covered substrates is investigated. The process flow and types of substrates investigated are shown in Fig. 6.12. All PET and glass substrates were covered with a photo resist layer which was imprint-textured in (a), while no treatment was conducted in (b), resulting in a smooth layer. Subsequently, the films were covered with a 240 nm ZnO:Al layer and characterized regarding their electrical, optical and structural properties. This particular thickness was chosen as it has been shown that reflection losses are relatively low at a ZnO:Al window layer thickness of 240 nm, while providing an acceptable sheet resistance [298]. Additionally, a-Si:H solar cells were deposited directly without vacuum break on top of the ZnO:Al layer.

First, the reproduction quality of the texture by nanoimprint lithography is estimated via SEM images, shown in Fig. 6.13. In (a) and (b), smooth glass and PET substrates covered with the non-imprinted resist and ZnO:Al is presented, which are named nG and nP in the following, respectively. Both images show a nearly identical homogeneous surface where the grains resulting from the columnar growth of the ZnO:Al are visible. The original morphology of the highly optimized reference ZnO:Al film deposited at 300 °C is presented in (c). The crater-like surface presents a morphology optimized for advanced light management in μ c-Si:H solar cells [118] and was therefore used as master texture for the imprint. The SEM images of imprint-textured glass and PET substrates are shown in Figs. 6.13(d) and (e) and are named tG and tP hereafter, respectively. It appears that the crater-like structure is well replicated on both glass and PET substrate. A slight variation from the master texture is obtained by the superimposed grain-structure resulting from the deposition of ZnO:Al on top of the imprint-textured resist.

Optical properties of the substrates covered with ZnO:Al are evaluated by measurements of transmittance T, reflectance R as well as haze in transmission H_T to investigate

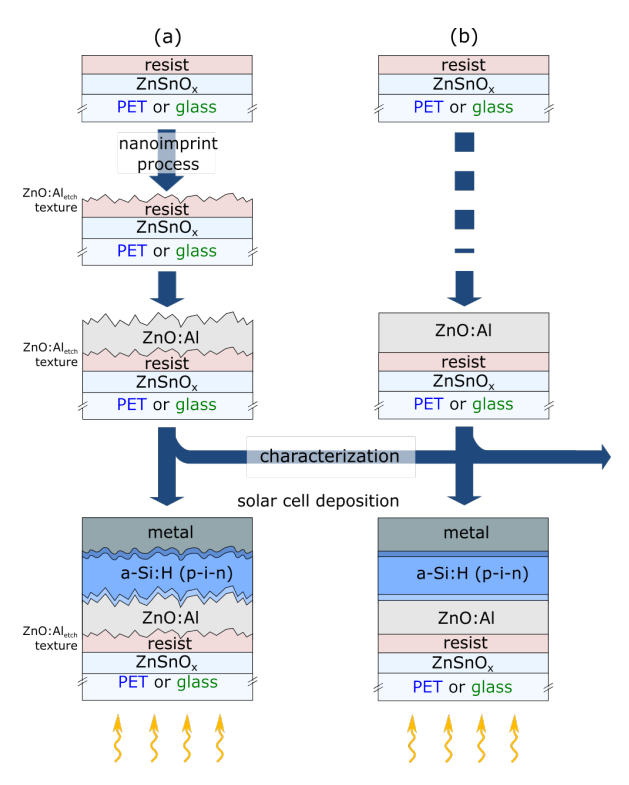


Figure 6.12.: Fabrication process flow of the substrates and solar cells on (a) imprint-textured and (b) non-imprinted glass or PET substrates.

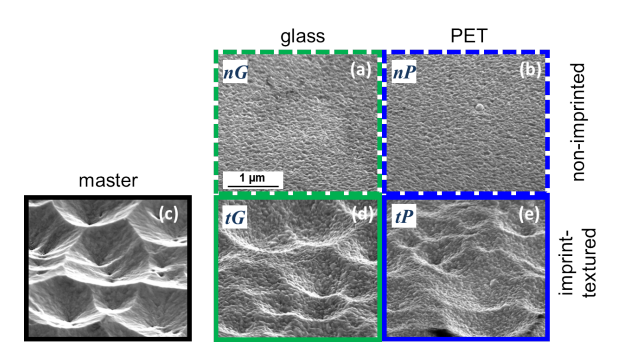


Figure 6.13.: Scanning electron microscopy (SEM) images of various substrates covered with ZnO:Al. (a) non-imprinted glass nG, (b) non-imprinted PET nP, (c) master texture of reference ZnO:Al deposited at 300 °C and etched for 40 s, (d) imprint-textured glass tG and (e) imprint-textured PET tP.

the light scattering properties. The results are shown in Fig. 6.14(a), (b) and (c), respectively. Comparison of ZnO:Al on PET substrate with and without imprinted texture (tP

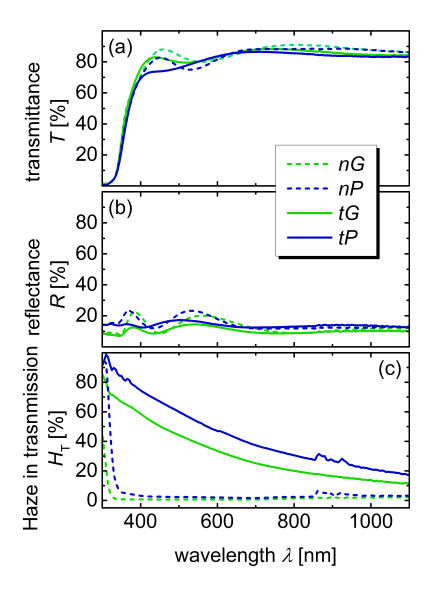


Figure 6.14.: (a) total transmittance T, (b) reflectance R and (c) haze in transmission H_T for the different types of substrates, covered with ZnO:Al: non-imprinted glass nG (green-dashed line), non-imprinted PET nP (blue-dashed line), imprint-textured glass tG (green solid line) and imprint-textured PET tP (blue solid line).

and nP, respectively) shows that there is only a slight difference (within 4% absolute) in transmittance for most of the wavelength range. Only in the range between 400 and 500 nm, due to constructive interferences in the non-textured layer stack, the transmittance is around 10% higher. However, interferences depend on the particular layer stack and will change when silicon layers are deposited on the top of the substrate. Thus it cannot be directly related to the substrate transparency when implemented in a solar cell [286]. The transmittance exceeds 74 % for $\lambda > 430 \,\mathrm{nm}$ in both cases. Furthermore, the reflectance is reduced due to the nanoimprinted texture. Results for the comparison of non-imprinted and imprint-textured glass substrates covered with ZnO:Al (nG and tG, respectively) are qualitatively similar to that of PET/ZnO:Al substrates just described. Principally, PET/ZnO:Al substrates exhibit a slightly higher reflectance compared to glass/ZnO:Al substrates. Regarding light scattering properties, evaluated by $H_{\rm T}$, shown in Fig. 6.14(c), for ZnO:Al on both PET and glass substrates the haze values could be significantly increased by imprint-texturing of the substrate; from basically 0% for the non-imprinted substrates nG and nP to 25% and 37% at 700 nm in the case of samples tG and tP, respectively.

Regarding the electrical properties of the ZnO:Al layer deposited on top of the four different substrates, the sheet resistance R_{\square} was measured and is presented in Table 6.4. No difference could be detected between ZnO:Al on non-imprinted and imprint-textured

13.1

0.5

| 0 | on top of theses substrates. | | | | | | |
|---|------------------------------|------------------------|------------|--------|------------------------|-------------------------------|---------------|
| | substrate | $R_{\square} [\Omega]$ | η [%] | FF~[%] | $V_{\rm OC}~[{ m mV}]$ | $J_{QE} \ [\mathrm{mA/cm^2}]$ | area $[cm^2]$ |
| | nG glass | 32 ± 2 | 5.7 | 57.7 | 905 | 11.0 | 0.4 |
| | nP PET | 46 ± 3 | 4.8 | 54.3 | 855 | 10.4 | 0.5 |
| | tG glass $+$ imprint | 32 ± 2 | 7.0 | 60.6 | 905 | 12.7 | 0.4 |
| | tP PET + imprint | 46 ± 3 | 6.9 | 61.8 | 870 | 12.9 | 0.1 |

68.6

905

Table 6.4.: Sheet resistance R_{\square} of ZnO:Al covered non-imprinted and imprint-textured glass and PET substrates, as well as photovoltaic parameters and active area of solar cells deposited on top of theses substrates.

substrates, for both glass and PET substrate, implying that the ZnO:Al growth is unimpaired by the substrate texturing. This is in agreement with literature, where the crater-like structure was shown to provide suitable growth conditions for ZnO:Al layers [299]. Yet the sheet resistance values of the ZnO:Al layer on PET substrate are higher compared to that on glass substrate. In general, the sheet resistance is rather high compared to state-of-the-art commercially available substrates, like e.g. Asahi U-type substrates, which usually provide a sheet resistance of around $10\,\Omega$.

Solar Cells on Imprint-Textured Substrates

 9 ± 2

8.1

Asahi-U

In order to evaluate the effect of imprint-texturing on the device performance, a-Si:H solar cells were deposited on top of the ZnO:Al covered glass and PET substrates discussed above. In contrast to the solar cells presented in Section 6.2.2, no μ c-Si:H p-type layer was used between the ZnO:Al and p-type a-Si:H layer. Three different cell areas were used for the various types of solar cells (0.1, 0.4 and 0.5 cm²). It was found that the difference in FF for these cell areas is negligible for the same substrate in most cases. Yet in this section, the short-circuit current densities J_{QE} were calculated from EQE measurements. Each solar cell was annealed until the improvement in photovoltaic parameters had saturated (see Chapter 5 for further information).

In Fig. 6.15(a) and (b), external quantum efficiencies EQE and cell absorptance 1-R curves of these solar cells are shown, respectively. In both cases of glass and PET substrates, the cell absorptance is significantly increased due to the nanoimprinted texture for most of the wavelength range (solid lines compared to dashed lines). This in turn leads to a significantly increased EQE over nearly the entire wavelength range and confirms excellent light scattering properties of the imprint-textured substrates. The increase is especially strong for wavelengths > 600 nm. Comparison of the solar cells on substrates tG and tP, a slightly lower cell absorptance (and correspondingly higher reflectance) can be observed for the solar cell on PET substrate. Still, similar EQE curves were achieved for solar cells on both glass and PET substrate for most of the wavelength range.

Photovoltaic parameters of the solar cells on the four types of substrates are presented in Table 6.4. Corresponding J-V curves can be found in Fig. B.1 in the Appendix.

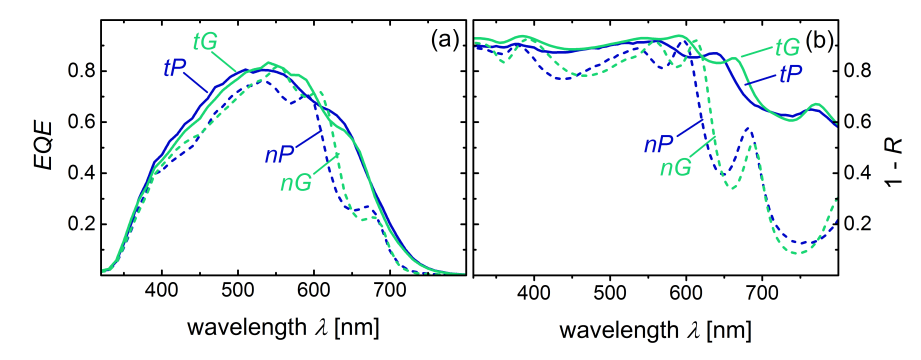


Figure 6.15.: (a) External quantum efficiency EQE and (b) cell absorptance 1-R for the solar cells on various substrates: non-imprinted glass nG (green-dashed line), non-imprinted PET nP (blue-dashed line), imprint-textured glass tG (green solid line), and imprint-textured PET tP (blue solid line).

The characteristics of a reference cell on Asahi-U substrate is shown for comparison. As already visible from EQE curves, nanoimprint texturing significantly improves J_{QE} by 1.7 and 2.5 mA/cm² in case of glass and PET substrate, respectively. Thereby, a J_{QE} of 12.9 mA/cm² is achieved on substrate tP, only slightly lower compared to that on an optimized commercial Asahi-U glass substrate (13.1 mA/cm²). In addition, the fill factor and open-circuit voltage of the solar cell on PET substrate is improved by 7.5 % and 15 mV, respectively, by imprint-texturing of the substrate. However, $V_{\rm OC}$ is still considerably lower for the solar cell on PET substrate (870 mV) compared to that on glass substrate (905 mV). Overall, the a-Si:H solar cell on substrate tP achieves similar efficiency (6.9 %) to that on tG (7.0 %). The reduction in efficiency of these cells compared to the solar cell on Asahi-U substrate (8.0 %) is mainly caused by a reduction in fill factor by absolute 6.4 ± 0.6 %.

Discussion

The outcome of these studies demonstrated that the nanoimprint process significantly improves the light scattering properties of the PET substrate, while a high overall transmittance is maintained and no deterioration in electrical conductance could be detected. This is also the case for glass substrates. The higher sheet resistance of the ZnO:Al layer grown on PET substrate (46 Ω), compared to that on glass substrate (32 Ω), can be related to different growth conditions and thus structural evolution of the ZnO:Al material on PET substrate (see Section 6.2.2).

Reflectance measurements on ZnO:Al layers (Fig. 6.14(b)) as well as solar cells (Fig. 6.15(b)) reveal a slightly higher reflectance for the layers and solar cells on PET substrate. This can partly be related to the difference in refractive index (1.6 for PET and 1.5 for glass at a wavelength of $500\,\mathrm{nm}$), which causes increased reflectance at the air/PET interface

according to Fresnel equations: 4% for the glass and 5.3% for the PET substrate in the case of normal incidence of the light.

Another finding was that introduction of a texture by nanoimprint lithography leads to a significant increase in external quantum efficiency over the entire wavelength range. Similar to the case of the texture evolving upon etching (Section 6.2.2) this can be related to improved trapping as well as incoupling of the light, as visible in the long and short wavelength range, respectively.

Regarding the photovoltaic parameters of the solar cells on PET substrate (nP and tP), both FF and $V_{\rm OC}$ were significantly improved by imprint-texturing of the substrate, by 7.5 % and 15 mV, respectively. A possible explanation for this might be that the texture may act as stress reliever and reduces the compressive stress that results from varying thermal expansion coefficients of PET and solar cell layers, as suggested by de Jong [179]. Speculating, this might cause an improved microstructure of the ZnO:Al and/or silicon layers containing less voids or cracks, thereby improving electrical properties of the layers, which would increase both FF and $V_{\rm OC}$. This higher level of stress on PET substrate might also account for the generally lower $V_{\rm OC}$ of the solar cells on PET substrate compared to those on glass substrate. Another possible explanation might be related to lower dark conductivities of the doped layers, in particular the p-type layer, when grown on PET instead of glass substrate (see Table 6.1) as pointed out in [227] and already discussed in Section 6.2.2. The low fill factor of $61.2\pm0.6\%$ of the solar cells on glass and PET substrate compared to 67.6% on Asahi-U substrate is likely caused by two reasons. On the one hand, the solar cell on Asahi-U substrate benefits from its significantly lower sheet resistance (see Table 6.4), which usually promotes an increase in fill factor [28]. On the other hand, it is well known that p-type a-Si(C):H layers in contact with ZnO:Al might develop a contact barrier at the TCO/p-interface that reduces the fill factor of the solar cell [288]. This can be improved by using a p-type μ c-Si:H/a-Si:H double window layer, which would then likely increase the fill factor for the solar cell on ZnO:Al covered substrates [287, 288, 300]. In contrast to Section 6.2.2, this double window layer should be optimized for application on PET substrates regarding e.g. crystalline volume fraction.

6.2.4. Comparison and Discussion of Light Management Approaches

The results presented above (Sections 6.2.2 and 6.2.3) were obtained over one year time, thus an accurate comparison between various devices is interfered by drifts in the deposition system and use of different deposition conditions. Therefore, in order to enable an accurate comparison between the two light management approaches, selected solar cells were re-deposited under similar conditions. Parts of the results shown in this section have previously been published in [282].

A scheme of the layer stacks for both types of solar cells using different light management approaches on PET substrates is shown in Fig. 6.16. This time, a thin $(70 \,\mathrm{nm})$ film of $\mathrm{SiO_xN_y}$ was used as barrier layer on the PET substrate. For the nanoimprint approach (a), the texture of high temperature reference ZnO:Al was used, while the low

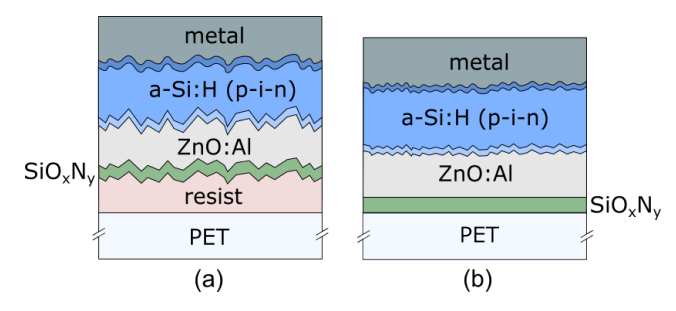


Figure 6.16.: Layer stacks of the solar cells on PET substrate where rough surfaces for light management are produced by (a) imprint-texturing of the PET substrate and (b) etching of low temperature $\rm ZnO:Al$ for $\rm 20\,s.~SiO_xN_y$ was used as barrier layer on the PET substrate in this case.

temperature ZnO:Al (b) exhibits the texture with small feature size (SEM images (a) and (b) in Fig. 6.6, respectively).

In Fig. 6.17, EQE curves of the solar cells on PET substrate using nanoimprint lithography (blue solid line) and etching of ZnO:Al (green dash-dotted line) are shown and compared to a flat reference without any texture (gray dashed line). Photovoltaic parameters are shown in Table 6.5. Corresponding J-V curves can be found in Fig. B.2 in the Appendix. Equally efficient light incoupling and trapping, as visible from similar

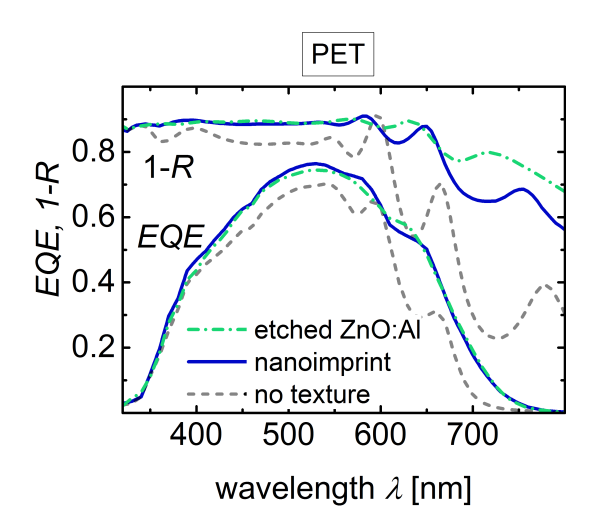


Figure 6.17.: External quantum efficiencies EQE curves and cell absorptance 1-R for a-Si:H solar cells on PET substrate, where nanoimprint (blue solid line) and etching of ZnO:Al (green dash-dotted line) are used as light management approaches. A solar cell on smooth PET substrate is shown for comparison (gray dashed line).

EQE curves, are obtained for both types of light management approaches, achieving

Table 6.5.: Photovoltaic parameters of solar cells on PET substrate using various light scattering techniques.

| light scattering by | η [%] | <i>FF</i> [%] | $V_{\rm OC}~[{ m mV}]$ | $J_{\rm SC}~[{\rm mA/cm^2}]$ |
|---------------------|------------|---------------|------------------------|------------------------------|
| - | 5.1 | 54.2 | 865 | 10.8 |
| nanoimprint | 6.4 | 57.8 | 860 | 12.7 |
| etching of ZnO:Al | 6.2 | 60.0 | 835 | 12.4 |

a $J_{\rm SC}$ of 12.7 mA/cm² in case of nanoimprint lithography and 12.4 mA/cm² in case of etched ZnO:Al, respectively. This depicts a significant increase by $1.8\pm0.2\,\mathrm{mA/cm^2}$ in $J_{\rm SC}$ compared to the flat reference, as already discussed in Section 6.2.3. Besides, an increased cell absorptance is observed for most of the wavelengths above 600 nm in the case of low temperature etched ZnO:Al compared to the nanoimprinted sample. This difference is qualitatively similar to that observed in Fig. 6.11 for the comparison between solar cells on etched low temperature ZnO:Al and reference ZnO:Al. An explanation is therefore probably be related to plasmonic absorption losses and their dependence on the feature size of surface textures (see also end of Section 6.2.2).

The fill factor is again increased by introduction of a texture in both cases, which might be related to the already discussed reason of reduced stress in case of a textured substrate (see Section 6.2.3). The lower $V_{\rm OC}$ in case of the solar cell on low temperature etched ZnO:Al emerges again, which further supports the interpretation of increased surface recombination between holes and electrons due to a larger surface area (see Section 6.2.2). Overall, similar efficiencies of $6.3\pm0.1\%$ are achieved for both types of light management approaches, inferring that nanoimprint lithography as well as etching of ZnO:Al are well suited to maintain advanced light management in a-Si:H solar cells on transparent flexible PET substrates. As mentioned earlier, the situation may be different for solar cells with a microcrystalline absorber layer or a-Si:H/ μ c-Si:H tandem solar cells, where a higher sensitivity to light management textures might be present.

Pros and cons of the two investigated light management approaches are discussed in the following. A great advantage of the nanoimprint lithography approach is the possibility to decouple the surface texture from the electrical and optical properties of the TCO material, meaning that a virtually unlimited range of textures can be used like e.g. periodic nanostructures [135, 301] or textures that can only be obtained under conditions incompatible with PET substrates, e.g. at high temperatures [296]. Furthermore, TCO materials can be optimized with respect to high electrical conductance and transparency, without consideration of and limitation by scattering properties. Particularly, also nontexturable TCOs like e.g. indium-doped tin oxide (ITO) can be used, which have shown superior electrical and optical properties at low deposition temperatures compared to ZnO:Al [302]. Also the critical TCO/p-contact tends to be improved when ITO is used instead of ZnO:Al [303]. In order to underline this point, a brief comparison of ITO, hydrogen-doped indium oxide (IO:H) and ZnO:Al layers prepared at low temperatures on glass substrates is presented in Appendix C.

Technologically, both nanoimprint lithography and chemical etching are non-vacuum processes and compatible with roll-to-roll deposition [279, 304, 305]. However, in the case of ZnO:Al etching, a vacuum break is needed after the sputter deposition of ZnO:Al, while nanoimprint processing occurs as first step prior to vacuum depositions. This vacuum break leads to retardation of the roll-to-roll fabrication by additional venting and pumping time. On the other hand, wet-chemical etching of ZnO:Al has the advantage of simplicity (especially on a laboratory scale), requiring only a solution of hydrochloric acid in addition to the TCO deposition system. Regarding process reproducibility, the wet-chemical etching of ZnO:Al depends on precise sputtering conditions, solution concentration, etching time, etc. and can thus be challenging to control [306]. On the contrary, once a nanoimprint stamp is manufactured, it may be used several times, replicating the same texture with high precision [134].

Another aspect that needs to be considered in the case of polymer substrates is the mechanical stress that evolves because of the different thermal expansion coefficients of the substrate and subsequently deposited layers [307]. Accordingly, thin layers are preferred to reduce stress in the films. In the case of texturing by chemical etching of ZnO:Al, initially relatively thick layers (around 800 nm) are needed to provide enough material for the etching step. This in turn may induce crack initiation in the ZnO:Al layer and thereby deteriorate electrical properties of the layers and device performance.

6.3. Performance under Bending

Flexible solar cells and modules can, in contrast to rigid devices, be operated in a bent state. Bending and effects of variable angles of incidence are thus an important part of device development and performance evaluation. The influence of incident angles on the performance has been investigated for solar cells on rigid glass substrates, especially with a focus on the effects of periodic light-trapping structures, or on the influence of varied incident angles and spectra during the day [301, 308–311]. However, in the case of flexible solar cells addressed here, varied angles of incidence might simultaneously be present under operation due to the flexibility of the device. In this chapter, the influence of various angles of incidence on the flexible solar cell performance is evaluated and a model is presented to evaluate the effects of operation in a bent state and corresponding changes in the device performance. Parts of the results presented in this chapter have previously been published in [297].

6.3.1. Angular Dependence

The dependence of the incident angle of the light on the solar cell performance has been investigated for various types of solar cells on rigid glass substrates, including organic solar cells [312], crystalline silicon solar cells and modules [309] and thin-film silicon solar cells [301, 308, 309]. The influence of an increased angle of incidence γ of the light was found to be caused by three effects, depicted in Fig. 6.18:

- (i) an increase in illumination area F decreasing the density of incident photons following the cosine law [313]
- (ii) increased reflection losses at front surfaces and/or interfaces
- (iii) prolongation of the light path inside the device.

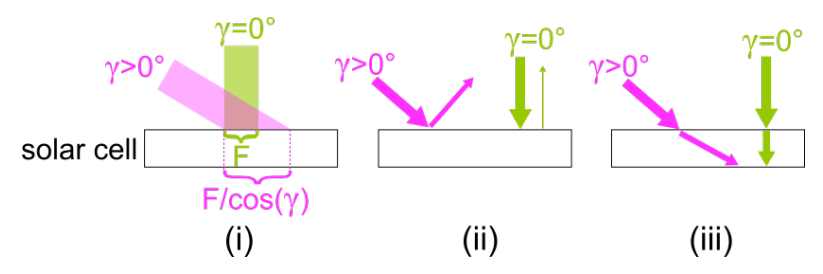


Figure 6.18.: Schematic drawing to depict the effects of an increased light incident angle γ : (i) increased illuminated area due to cosine law and thus reduced density of photons, (ii) increased reflection losses at front surfaces/interfaces and (iii) prolongation of the light path inside the device. Green and magenta color corresponds to normal (γ =0°) and increased (γ >0°, tilted state) angle of incidence, respectively.

External quantum efficiency EQE measurements under various incident angles γ from 0° (normal incidence) to 60° were carried out on the solar cells on imprint-textured and non-imprinted PET substrates presented in Section 6.2.3, and the results are shown in Fig. 6.19(a) and (b), respectively. Please note that for these measurements, the illu-

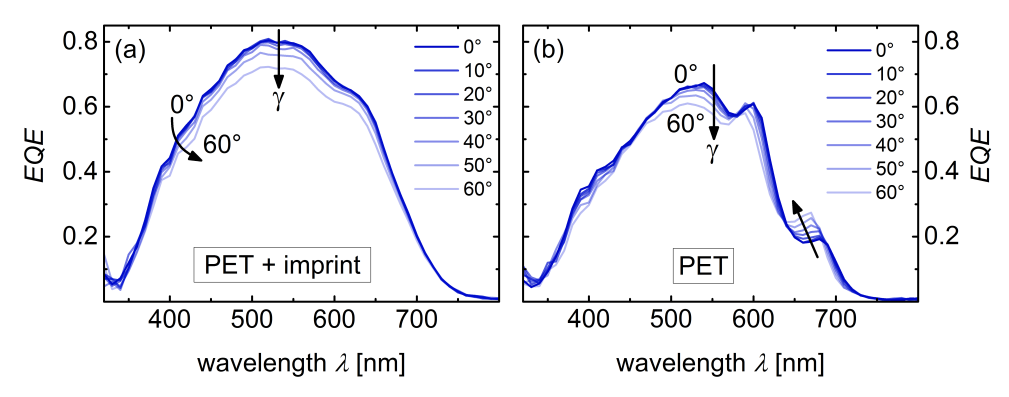


Figure 6.19.: External quantum efficiencies EQE curves of flexible solar cells for various incident angles γ of the light. (a) Imprint-textured PET and (b) non-imprinted PET substrate. An angle of 0° corresponds to normal incidence.

mination spot is considerably smaller than the area of the solar cell, meaning that the number of incident photons is identical for all incident angles (see Fig. 6.20(a)). As a consequence, the cosine law (i) does not affect the results. For a better visualization, EQE curves normalized to the EQE at $\gamma=0^{\circ}$, are plotted in Fig. 6.21(a) and (b) for the solar cells on imprint-textured and non-imprinted PET substrate, respectively.

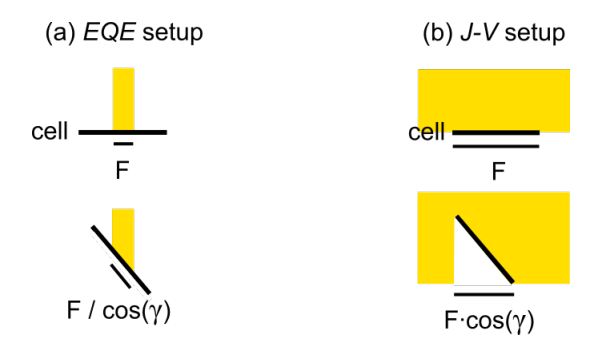


Figure 6.20.: Schematic drawing to depict illumination conditions in the different measurement setups. In the EQE setup (a), the illumination spot is considerably smaller than the solar cell area, thereby the number of incident photons is constant for all incident angles. In the J-V setup (b) on the other hand, the illumination spot is larger than the solar cell area and with increasing incident angle the number of incident photons is reduced due to a reduction in effective solar cell area.

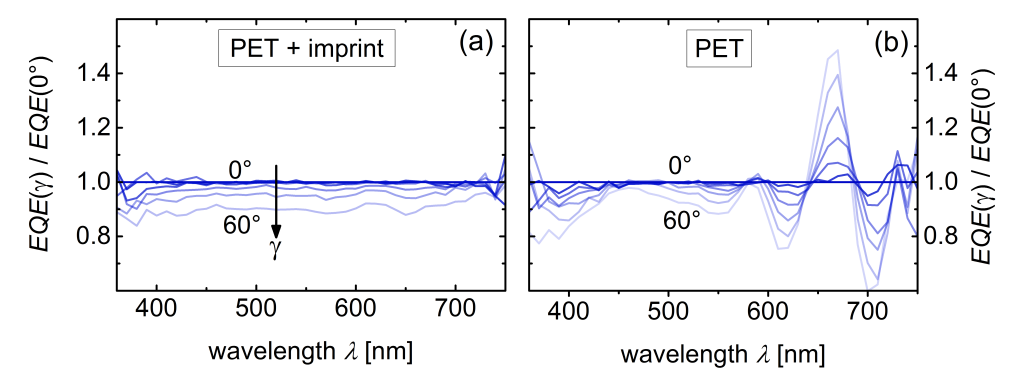


Figure 6.21.: External quantum efficiencies for each incident angle $EQE(\gamma)$ normalized to the $EQE(0^{\circ})$ at normal incidence for the solar cell on (a) imprint-textured PET and (b) non-imprinted PET substrate.

For the solar cell on imprint-textured PET substrate in (a), a decrease in EQE curve with increasing angle of incidence over the entire wavelength range can be observed. The effects (ii) and (iii), described above, show different wavelength dependencies: (ii) depends indirectly on the wavelength via the refractive index of the front window layers (according to Fresnel equations), which usually varies only slightly in the investigated wavelength range. On the other hand, (iii) can have opposite effects for different wavelengths: Prolonging the path of short wavelength light leads mainly to increased parasitic absorption in the front TCO layer with increasing γ , thereby leading to a reduction in EQE. For long wavelength light on the other hand, the light path is mainly prolonged inside the intrinsic absorber layer, leading to an enhanced EQE. As the reduction in the EQE curve with increasing γ is nearly constant for all wavelengths (see Fig. 6.21(a)), it seems likely that the reduction can be ascribed to enhanced reflections at front interfaces with increasing γ . This is in agreement with the calculated reflection increase at the air/PET interface with increasing incident angle, as calculated from Fresnel formula and shown in Fig. 6.22. Here, the relative reflection increase at $\lambda = 500 \, \text{nm}$ according to

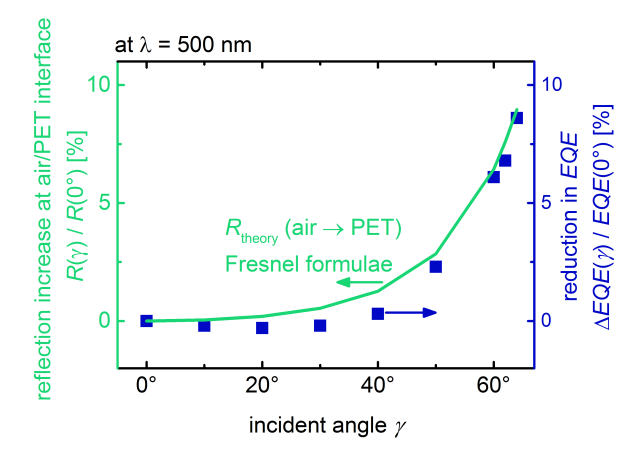


Figure 6.22.: Relative increase in reflection at the air/PET interface at a wavelength λ of 500 nm with increasing angle of incidence γ according to Fresnel equations (green line), as well as relative reduction in $EQE(\gamma)$ at 500 nm compared to the $EQE(0^{\circ})$ at normal incidence (blue squares).

Fresnel equations (green line) is similar to the relative reduction in the EQE curve at $\lambda = 500 \,\mathrm{nm}$ (blue squares), thereby confirming that these reflections are the main reason for the reduction in EQE curve.

For the solar cell on non-imprinted PET substrate, the EQE curve is also reduced for most of the wavelengths (see Fig. 6.19(b)). However, effects resulting from constructive and destructive interference of light that is reflected at the flat interfaces lead to additional features: the interference fringes located at 680 nm and 600 nm for normal incidence of the light ($\gamma = 0^{\circ}$) are blue-shifted by 10 nm to 670 nm and 590 nm for $\gamma = 60^{\circ}$, respectively, due to prolongation of the light path in the absorber layer with increasing incident angle. As

the absorption coefficient, evaluated from PDS measurements, of the amorphous silicon absorber layer increases from $4100\,\mathrm{cm^{-1}}$ at $680\,\mathrm{nm}$ to $5500\,\mathrm{cm^{-1}}$ at $670\,\mathrm{nm}$, the blue-shift leads to an increase in EQE with increasing incident angle in the corresponding wavelength range. The constant EQE for all investigated angles of incidence at a wavelength of $450\,\mathrm{nm}$ (see Fig. $6.21(\mathrm{b})$) cannot be related to interference effects inside the absorber layer, as most of the light of this wavelength is absorbed within the first part of the solar cell. In this case, an interplay between interference effects in the front TCO layer and/or reflection changes at the air/PET interface might be a possible reason.

From EQE curves, integrated short-circuit current densities J_{SC} can be evaluated, as described in Section 3.4.2, using the AM1.5 spectrum in the wavelength range between 320 and 800 nm. Absolute and normalized J_{SC} values as a function of incident angle γ are shown in Fig. 6.23(a) and (b), respectively. It should be noted that the absolute

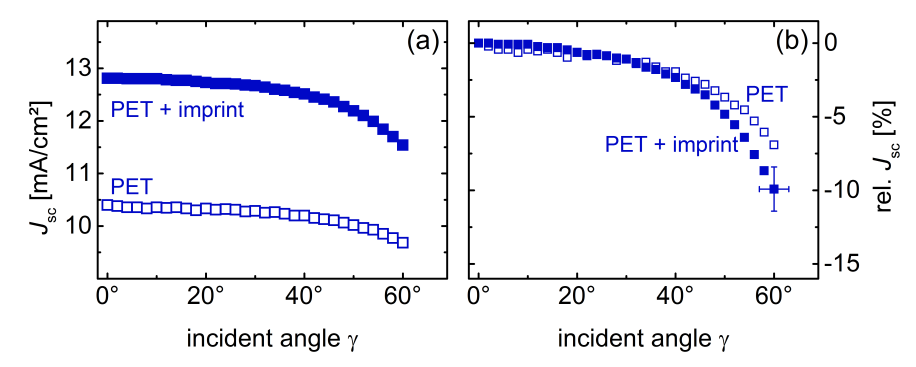


Figure 6.23.: Short-circuit current density $J_{\rm SC}$, calculated from EQE curves, as a function of incident angle γ for the cells on various types of substrates: non-imprinted PET (blue open squares) and imprint-textured PET substrate (blue full squares). (a) Absolute values and (b) normalized to the value at normal incidence. Error bars are exemplarily shown for the imprint-textured sample.

values of the solar cell on the non-imprinted PET substrate were slightly lower than shown in Table 6.4. In order to enable a more accurate comparison of the angular effects in both types of solar cells, in this case $J_{\rm SC}$ values were normalized to the $J_{\rm SC}$ value of $10.4\,\mathrm{mA/cm^2}$ at 0° incident angle. Up to an incident angle of 40°, the relative reduction in $J_{\rm SC}$ is only minor within 2.4% for the solar cells on both imprint-textured (filled squares) and non-imprinted (open squares) PET substrates. Even at an incident angle of 60°, the relative reduction in $J_{\rm SC}$ is less than 10%. The reduction in $J_{\rm SC}$ is less pronounced for the solar cell on non-imprinted PET substrate, which can be related to the blue-shift of the interference fringe at 680 nm with increasing incident angle and the resulting increase in EQE. However, considering the error bar of the measurement, only minor difference can be observed between textured and non-textured substrates.

In addition to EQE measurements, J-V curves of the solar cell on imprint-textured PET substrate were measured under various angles of incidence under AM1.5 illumination. It should be noted that the illumination spot in this setup is considerably larger than the

cell area (see Fig. 6.20(b)). This implies that the number of incident photons on the solar cell is reduced with increasing incident angle due to a reduction in the effective solar cell area. The measured values were therefore normalized to the effective solar cell area $F\cos(\gamma)$ using the cosine law, thus allowing to focus on the optical properties of the device. The relative changes in J_{SC} , FF, V_{OC} and η as a function of incident angle γ are shown in Fig. 6.24(a), (b), (c) and (d), respectively. For comparison, relative changes in

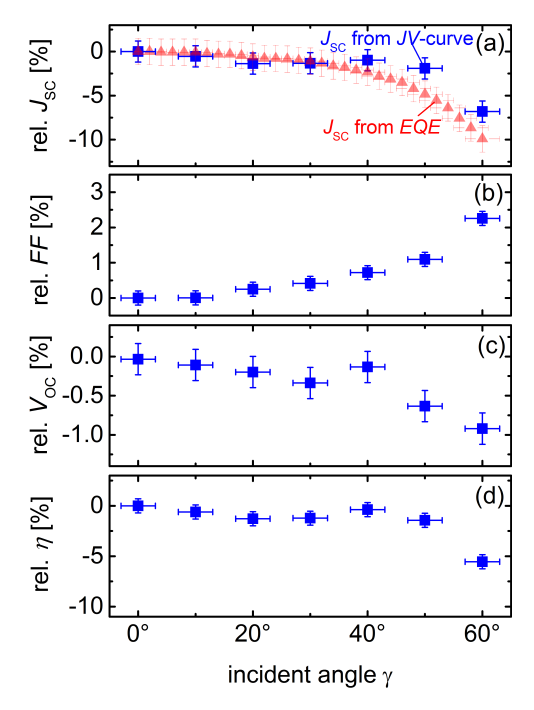


Figure 6.24.: Current-voltage (J-V) parameters as a function of incident angle γ for the solar cell on imprint-textured PET substrate. (a) Short-circuit current density $J_{\rm SC}$, (b) fill factor FF, (c) open-circuit voltage $V_{\rm OC}$ and (d) efficiency η , normalized to the value at normal incidence. In (a), $J_{\rm SC}$ values calculated from EQE curves are shown for comparison (red triangles).

 $J_{\rm SC}$ values evaluated from EQE measurements, as shown in Fig. 6.23(b), are also shown in Fig. 6.24(a) (red triangles).

The results from EQE and J-V measurements are in good agreement, considering that the measurements were performed using different measurement setups. It can be seen from Figs. 6.24(b) and (c), that FF increases slightly with increasing γ up to a value of 2.2% at $\gamma = 60^{\circ}$, while V_{OC} simultaneously decreases by 1%. Both effects can be related to the reduced light intensity (number of incident photons), when the effective solar cell area decreases with increasing incident angle. The open-circuit voltage depends directly on the generated photocurrent which is reduced with decreasing light intensity [28]. The fill factor on the other hand was shown to decrease with increasing light intensity, caused by photogenerated space charge trapped to a greater extent in the band-tail states of the

absorber layer at higher illumination levels [263]. However, one has to consider that the fill factor depends also on the shunt and series resistance of the device, which influence the fill factor mainly at low and high illumination levels, respectively. With decreasing light intensity, the influence of the series resistance is weakened, meaning that an increase in fill factor may also be related to a high series resistance in the device whose influence is attenuated with decreasing light intensity. Still the effects of $V_{\rm OC}$ (-1%) and FF (+2%) with increasing γ are rather small compared to the changes in $J_{\rm SC}$ (-7%), so that the efficiency follows mainly $J_{\rm SC}$, down to a relative reduction of 6% at an incident angle of 60°.

6.3.2. Bent Solar Cell Performance

As mentioned earlier, flexible solar cells can operate in a bent state, implying that various incident angles are simultaneously present. In order to investigate the current loss that is induced by the bending, a simple model is developed to calculate the short-circuit current density as well as the overall performance of a solar cell in bent state, on the basis of the results presented in Section 6.3.1.

For the calculations, semicircular bending is assumed and defined, in general case, by the ratio between length of the solar cell L and bending radius r, as shown in Fig. 6.25. The ratio L/r is varied between $0 < L/r < \pi$, where 0 and π correspond to the extreme

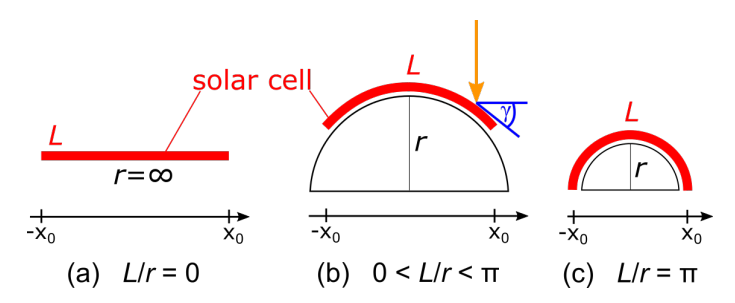


Figure 6.25.: Schematic figure of the bent states considered in the model. For a solar cell length L to bending radius r ratio of $L/r = \pi$, the solar cell builds up a complete semicircle.

cases of infinite radius (non-bent state) in (a) and semicircle in (c), respectively. The angle of incidence γ at each position x of the solar cell can then be deduced from the semicircle function f(x) (Eq. 6.1):

$$\gamma(x) = \left| \tan^{-1} \left(f'(x) \right) \right| = \left| \tan^{-1} \left(-\frac{x}{\sqrt{r^2 + x^2}} \right) \right|$$
 (6.1)

where r is the bending radius of the semicircle. An exponential function is fitted to the angle-dependent short-circuit current density shown in Fig. 6.23(a), assuming $J_{\rm SC} = 0 \, {\rm mA/cm^2}$ at $\gamma = 90^{\circ}$, thus no photocurrent generation at parallel incidence of the light. The resulting fit and function $J_{\rm SC}(\gamma)$ are shown in Fig. 6.26.

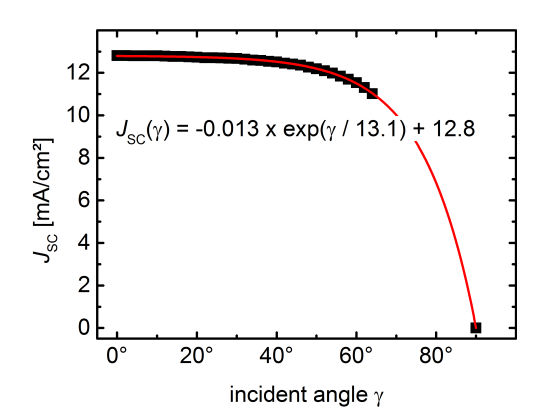


Figure 6.26.: Short-circuit current density J_{SC} , calculated from EQE, as a function of incident angle γ for the solar cell on imprint-textured PET substrate: Experimental data (black points) and fitting curve $J_{SC}(\gamma)$ (red line).

Short-circuit current densities of the entire device in bent state can then be calculated by integration of $J(\gamma(x))$ over x. Two different cases are investigated in the following; (I) without and (II) with consideration of the reduction in effective solar cell area. In the first case, the integral is divided by $2x_0$ (see Fig. 6.25(b)), which corresponds to the effective solar area thus eliminating the effect of reduced number of photons impinging the solar cell in the bent state. This helps understanding the effect of device optics on the solar cell performance in a bent state. In case (II) on the other hand, the integral is divided by the solar cell length L, thereby taking into account the fabricated solar cell area and the potential number of photons that could be absorbed by the solar cell.

In case (I), the overall short-circuit current density in the bent state $J_{SC,bent}$ of the solar cell can be calculated as follows (Eq. 6.2):

$$J_{\text{SC,bent}} = \frac{1}{2x_0} \int_{-x_0}^{x_0} J_{\text{SC}}(\gamma(x)) dx$$
(6.2)

The resulting $J_{\text{sc,bent}}$ values are plotted as a function of L/r in Fig. 6.27(a) for the solar cell on both imprint-textured (filled squares) and non-imprinted (open squares) PET substrates. In addition, values normalized to the non-bent state (L/r=0) are shown in (b). The value L/r=0 on the x-axis corresponds to the non-bent state and L/r increases with decreasing bending radius r. It can be seen, that for both types of solar cells the reduction due to the bent state is rather small: 0.4 and $0.7\,\text{mA/cm}^2$ for the solar cell on non-imprinted and imprint-textured PET substrate, respectively, when the solar cell is bent in a semicircle. This corresponds to a relative reduction in $J_{\text{SC,bent}}$ of maximum 5.3%. The solar cell on non-imprinted PET substrate shows a weaker dependence on the L/r ratio, which results from the interference-shift effect, as discussed in Section 6.3.1. For the calculation of the overall efficiency of the solar cell in bent state, angle-dependent FF and V_{OC} values from Fig. 6.24 are taken into account as well. Please consider that

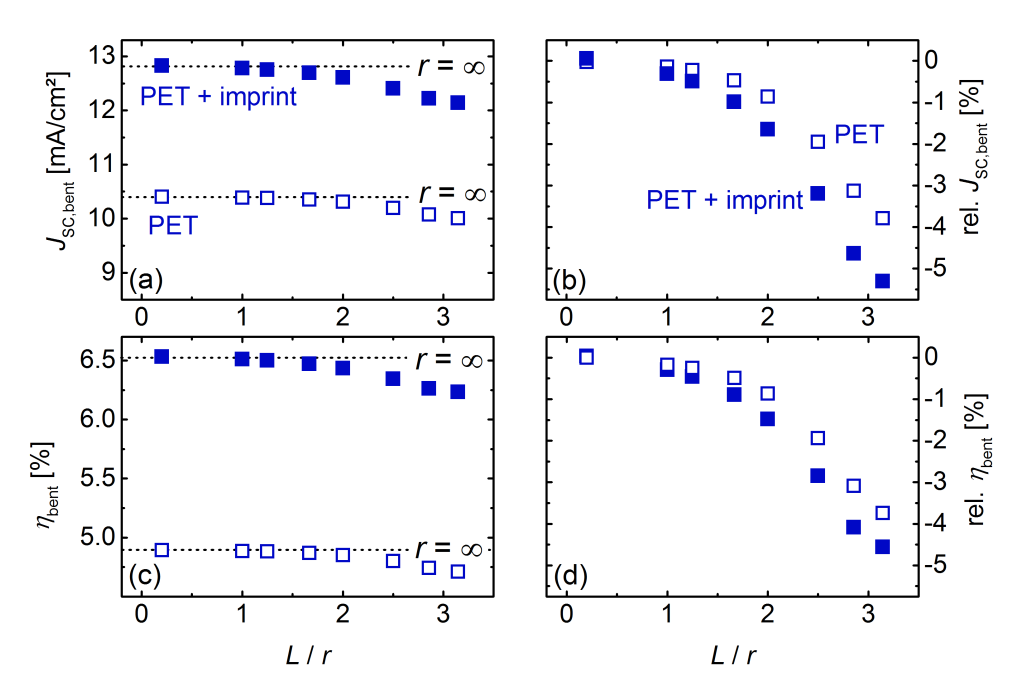


Figure 6.27.: Calculated short-circuit current densities $J_{\text{SC,bent}}$ and efficiency η_{bent} of flexible solar cells in bent state for various ratios L/r of solar cell length L to bending radius r, when the reduction in effective solar cell area is neglected. (a) Absolute values of $J_{\text{SC,bent}}$, (b) $J_{\text{SC,bent}}$ normalized to the non-bent state, (c) absolute values of η_{bent} and (d) η_{bent} normalized to the non-bent state. Open symbols: solar cell on non-imprinted PET substrate; full symbols: solar cell on imprint-textured PET substrate.

these values are affected by reduction in effective solar cell area (as noted earlier), but are negligible compared to changes in $J_{\rm SC}$. Absolute efficiency values $\eta_{\rm bent}$ as well as efficiency values normalized to the non-bent state for the solar cells on both types of substrates are shown in Fig. 6.27(c) and (d), respectively. As expected, the change in efficiency follows mainly the variation in $J_{\rm sc,bent}$ and the relative reduction remains below 5% when the solar cell is bent in semicircle state. It is worth noting that imprint-texturing of the PET substrate improves both $J_{\rm SC}$ and η of the solar cell for all investigated incident angles and bending states L/r, compared to the solar cell on non-imprinted substrate.

In case (II), the fabricated area of the solar cell is considered (cf. Fig. 6.25) and the overall short-circuit current density in bent state can be calculated by the following equation:

$$J_{\text{SC,bent}} = \frac{1}{L} \int_{-x_0}^{x_0} J_{\text{SC}}(x) dx$$
 (6.3)

with L being the length of the solar cell. In this case, the reduction in effective solar cell area and thus loss in the number of incident photons is considered in the calculation. The effect can clearly be seen in Fig. 6.28(a) and (b), where the absolute values of $J_{\text{sc,bent}}$ and η_{bent} are shown, respectively. With reduction in effective solar cell area upon bending,

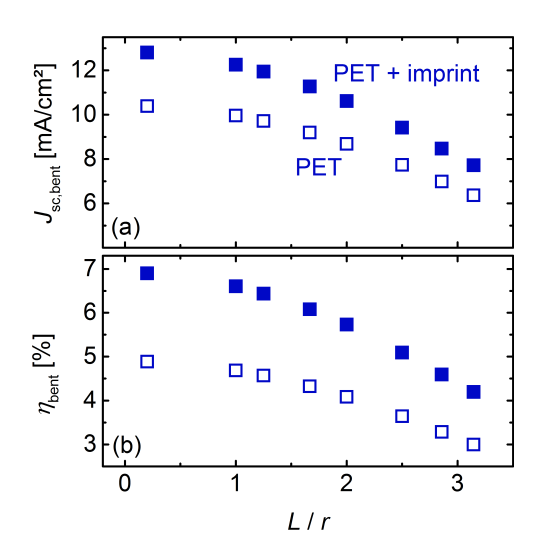


Figure 6.28.: (a) Calculated short-circuit current densities $J_{\text{SC,bent}}$ and (b) efficiencies η_{bent} of flexible solar cells in bent state for various ratios L/r of solar cell length L to bending radius r, taking into account the reduction in effective area due to the bending. Open symbols: solar cell on non-imprinted PET substrate; full symbols: solar cell on imprint-textured PET substrate.

 $J_{\rm SC,bent}$ dramatically decreases with increasing bending ratio L/r by 5.1 and 4.1 mA/cm² in the investigated range, and results in a corresponding drop in absolute efficiency from 6.9 to 4.2 % and 4.9 to 3.0 % for the solar cell on imprint-textured and non-imprinted PET substrate, respectively.

6.3.3. Discussion and Outlook

The results presented above show clearly that significant losses occur when the solar cell operates in a bent state, mainly due to a reduced number of collected photons as the effective area of the solar cell is reduced. This implies that for a given application in flexible form, the power output per fabricated area must be recalculated. The model proposed in this chapter allows to calculate the power loss for solar cells operating in bent state for various non-planar shapes, like e.g. wavy rooftops, roof tiles, tents, etc. compared to operation in non-bent state. The model also allows to easily calculate the effects of various spectra (e.g. for different times of the day or year) on the bent solar cell performance by substituting the AM1.5 spectrum used for the calculation of $J_{SC}(\gamma)$. Though no severe effects resulting from different spectra are expected for the type of solar cell presented here, as it was shown in Fig. 6.21(a) that the reduction in EQE is wavelength-independent, it may be a major effect in other types of solar cells or in flat devices, as shown in Fig. 6.21(b).

An important factor is also the orientation of a module that consists of multiple solar cells connected in series. Much research has been conducted about the issue of partial shading conditions of conventional PV modules due to dust coverage or shadows of surrounding objects or clouds, which lead to significant losses in output power and possible damages of the module (see [314] and references herein). Additional bypass diodes are employed by module manufacturers and complex maximum power point (MPP) tracking systems are necessary due to the development of several local MPPs. Likewise, one has to consider that in the case of flexible PV modules, this effect will be intensified when the solar cell is installed in a bent state and individual cells within the module provide a low current due to an increased light incident angle accompanied with a reduction of incident photons [315].

7. Conclusion

Transparent polymer films are required for the fabrication of flexible solar cells in superstrate configuration, as well as for flexible (semi-)transparent BIPV products. These types of substrates however also limit the temperature range for fabrication processes. This work therefore investigated the effects of low deposition temperatures on the material properties of silicon and TCO layers, and on the performance of entire photovoltaic devices. Post-deposition annealing effects have been found to have a significant impact of the performance of low temperature a-Si:H and μ c-Si:H solar cells on glass and PET substrates. Extensive studies have been carried out to understand the underlying physical processes upon annealing in individual layers and entire devices. Light management approaches with low process temperatures, compatible with PET substrates, have been developed and the influence on the properties of TCO covered substrates as well as on the solar cell performance was investigated. Finally, the dependence of the photovoltaic parameters on the angle of incident light was studied for a-Si:H solar cells on PET substrates. From these results, calculations were performed to investigate the solar cell performance in various bent states.

First, the influence of low deposition temperatures on the material properties of ptype, n-type and intrinsic a-Si:H layers on glass substrates was investigated in Chapter 4. As expected from literature, lowering the substrate temperature leads to a significant drop in electrical properties of all types of a-Si:H layers, and consequently in a deteriorated performance of a-Si:H solar cells. It was shown that adjustment of gas flow mixtures during deposition can compensate for the reduction in deposition temperature. Doped and intrinsic a-Si:H layers with appropriate material properties could be fabricated by leaving out methane during the p-type layer deposition and reducing the silane concentration for intrinsic and n-type layer deposition. When these low temperature layers were implemented in an a-Si:H solar cell in p-i-n configuration on glass substrate, a best efficiency of 9.1% was achieved after device optimization in terms of variations in layer thickness and back contact design.

Doped microcrystalline silicon layers on the other hand showed less sensitivity to low deposition temperatures and exhibited satisfactory electrical properties at a substrate temperature of 120 °C without additional tuning. In the case of intrinsic μ c-Si:H layers, optimal crystalline volume fractions of 40-70% could be achieved at 120 °C by varying the silane concentration, yet the parameter range was shown to be considerably smaller compared to high substrate temperatures. This may suggest a requirement for more sophisticated process control for the fabrication of a-Si:H/ μ c-Si:H solar cells and modules at low temperature. Overall, an efficiency of 6.9% for μ c-Si:H single junction solar cells

exhibiting a crystalline volume fraction of 52% and an absorber layer thickness of 1 μ m have been achieved at 120 °C on glass substrates. There is probably considerable potential for efficiency enhancement by improvement of the doped μ c-Si:H layers, for example by implementation of microcrystalline silicon oxide layers that potentially improve J_{SC} .

The best a-Si:H and μ c-Si:H solar cells were combined in a prototype tandem device, leading to an efficiency of 9.8%. Great potential for future improvement in device performance is visible, once accurate matching of the sub cell current densities is realized. Further steps may include the insertion of buffer layers or silane concentration profiling of intrinsic layers, and implementation of silicon oxide intermediate reflecting layers. This clearly indicates that high efficiencies of thin-film silicon solar cells are achievable even at deposition temperatures as low as 120 °C, and thus suitable for transparent PET substrates.

Low temperature a-Si:H solar cells on glass substrates exhibit a strong improvement in all photovoltaic parameters, particularly in the fill factor, after post-deposition annealing for more than two hours at temperatures similar to the deposition temperature. Extensive studies were carried out and presented in Chapter 5 to identify the layers sensitive to annealing and to understand the underlying physical processes relating layer properties and device performance. The main contribution to the annealing effect could be ascribed to changes in the intrinsic a-Si:H absorber layer and/or the p-/i-interface upon annealing. The charge carrier collection efficiency of the device was the parameter identified to be sensitive to post-deposition annealing, due to improvements in both electron and hole drift length. Possible reasons were related to an increased $\mu\tau$ -product of both electrons and holes in the intrinsic a-Si:H absorber layer, which could be confirmed by the results of measurements of photo conductivity and steady-state photocarrier grating technique on individual layers, respectively. Using a simplified model, simulations showed that improvements in external quantum efficiencies of solar cells upon annealing could well be reproduced by increasing the mobility of both electrons and holes. Furthermore, an enhanced built-in field may also contribute to the improvement in charge carrier collection and thus solar cell performance upon annealing. Supporting evidence was given by an increasing dark conductivity of the n-type a-Si:H layer upon annealing, likely raising the built-in voltage of the device. Moreover, an increased $\mu\tau$ -product in the intrinsic layer, resulting in less trapped charges, may also reduce deformations of the built-in field. More sophisticated simulations are needed in future to further analyze possible origins for the improvement in device performance upon annealing.

It was shown that the annealing effect is thermally activated and possible structural processes upon post-deposition annealing might be related to a non-equilibrium density of states after deposition due to the low deposition temperature. A significant rise in solar cell efficiency could also be achieved in a rapid annealing step (few minutes only) by using temperatures above the deposition temperature and future investigations may aim at the reduction of annealing times by using laser irradiation.

When fabricated on PET substrates, the annealing effect was shown to be even more pronounced and a link between lower material quality of individual layers and stronger annealing effects in the solar cell were presented. Also μ c-Si:H solar cells deposited at low temperature exhibited a pronounced improvement upon annealing, in this case with the strongest effect in the short-circuit current density. Measurements of external quantum efficiencies of p- and n-side illuminated solar cells showed remarkable similarities to a study in which solar solar cells were annealed after inducing deep defects by irradiation, suggesting a relation between defect density in the films and post-deposition annealing.

In Chapter 6, light management approaches procured at temperatures below 150 °C, and thus suitable for application on PET substrates, were investigated. Textured interfaces were inserted in the layer stack of a-Si:H single junction solar cells by wet-chemical etching of ZnO: Al layers in HCl solution as well as nanoimprint lithography. In the case of wet-chemically etched ZnO:Al films, layer properties on glass and PET substrates were investigated as a function of etching time. Similar optical properties were found for etched ZnO:Al layers on both types of substrates, while the sheet resistance in the case of the PET substrate proved to deteriorate slightly faster upon prolonged etching. Evolving textures and light scattering properties were probed by SEM imaging and measurements of angle-resolved scattering as well as haze in transmission, respectively. Though textures visible from SEM images appear differently, similar light scattering properties were found for etched ZnO:Al layers on both types of substrates. The adaption of the nanoimprint lithography approach showed that a master texture can well be reproduced on glass as well as PET substrates, without impairing the substrate transparency or the material properties of ZnO:Al layers grown on top of the imprinted resist. Light scattering properties of TCO covered substrates were evaluated by haze measurements and could be significantly enhanced. Similar results could be achieved on PET and glass substrates.

A-Si:H solar cells deposited on top of these textured substrates show significantly enhanced external quantum efficiencies compared to a flat reference for both types of light management schemes. This could be attributed to (i) reduced reflections at front interfaces due to the refractive index grading, and (ii) trapping of light in the absorber layer. The short-circuit current density could significantly be improved in addition to an enhancement in fill factor, compared to the flat reference. Overall, similar efficiencies are obtained for both light management approaches for flexible a-Si:H solar cells entirely fabricated at temperatures below 150 °C on transparent PET film. On the example of the nanoimprint lithography approach, it was shown that similar efficiencies of 7.0 % and 6.9 % for low temperature a-Si:H solar cells can be achieved on glass and flexible PET substrates, respectively. Further progress should focus on the deposition of tandem solar cells on PET substrates. Development is needed especially with regards to microcrystalline silicon layers grown on PET substrates, which revealed to exhibit lower crystalline volume fractions compared to that on glass substrates.

Pros and cons of both approaches were discussed, with nanoimprint lithography being favorable due to its high flexibility regarding the choice of texture and TCO material, though etching of ZnO:Al requires only simple laboratory equipment.

In conclusion, the results presented here reveal that deposition of thin-film silicon solar cells at low temperature of $120\,^{\circ}\mathrm{C}$ may achieve nearly $10\,\%$ efficiency. Moreover,

similar photovoltaic performance for solar cells on flexible PET substrates as on glass substrates is achievable by adopting light management concepts for low temperature processing.

In the last chapter, issues regarding the flexibility of solar cells were more closely evaluated. Current density-voltage curves of a-Si:H solar cells on non-imprinted and imprint-textured PET substrates were measured under various angles of light incidence. The largest effect was found in a reduction of the short-circuit current density due to increased reflections at the front interfaces. Losses were shown to be minor up to angles of 40° and were still below $10\,\%$ relative at incident angles of 60° . The fill factor and open-circuit voltage have been shown to increase and decrease slightly with increasing incident angle.

Calculations of device performance in bent state were performed based on these results. On the example of semicircular bending, integration over present incident angles resulted in overall photovoltaic parameters in the bent state. When only the losses due to increased incident angles and thus higher reflections are taken into account, only minor relative losses in efficiency of less than 5%, in the case of semicircular bending, occur. However, if one considers the reduction in effective solar cell area due to the bending and thus a reduced number of collected photons, the loss in efficiency increases considerably and is as high as 39% (relative) in the case of the a-Si:H solar cell on the imprint-textured PET substrate. Accordingly, the power output per fabricated area must be adjusted regarding the shape of application. The proposed model allows to calculate power losses for solar cells operating in bent state compared to non-bent state and may be extended for various non-planar shapes like wavy rooftops, roof tiles, tents, etc., as well as different spectra of light. It also reveals that for flexible photovoltaic modules conditions similar to "partial shading conditions" in conventional PV modules must be considered, meaning that bent parts of the module may limit the power output of a flexible solar module.

A. Appendix to Chapter 4

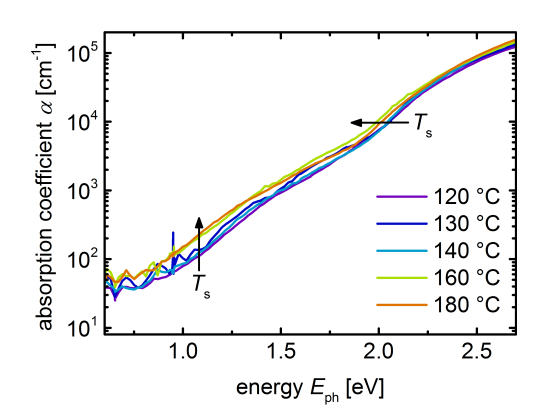


Figure A.1.: Absorption coefficient α as a function of photon energy $E_{\rm ph}$ measured by Photothermal Deflection Spectroscopy (PDS) on p-type a-SiC:H layers deposited at various substrate temperatures $T_{\rm s}$.

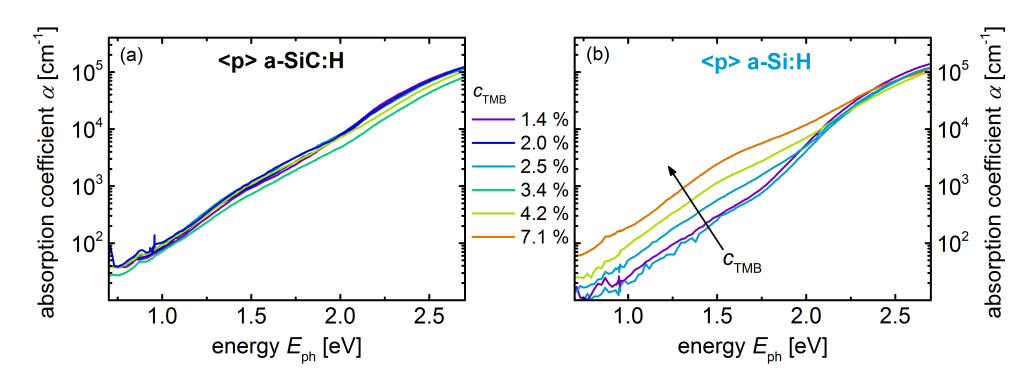


Figure A.2.: Absorption coefficient α as a function of photon energy $E_{\rm ph}$ measured by Photothermal Deflection Spectroscopy (PDS) on (a) a-SiC:H and (b) a-Si:H layers deposited deposited at 120 °C at various TMB concentrations $c_{\rm TMB}$.

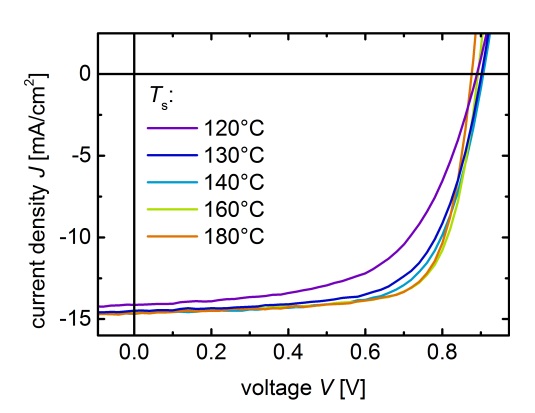


Figure A.3.: Current density-voltage (J-V) curves for a-Si:H solar cells deposited at various substrate temperatures $T_{\rm s}$ during deposition.

B. Appendix to Chapter 6

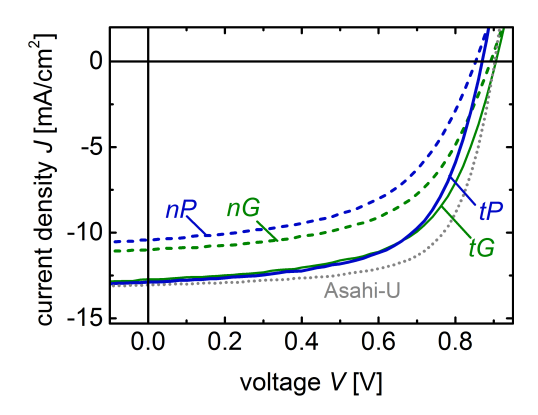


Figure B.1.: Current density-voltage (J-V) curves for a-Si:H solar cells on various substrates: non-imprinted glass nG (green dashed line), non-imprinted PET nP (blue dashed line), imprint-textured glass tG (green solid line), imprint-textured PET tP (blue solid line), and Asahi-U. The current density J is normalized so that the short-circuit current corresponds to $J_{\rm QE}$ obtained from EQE measurements.

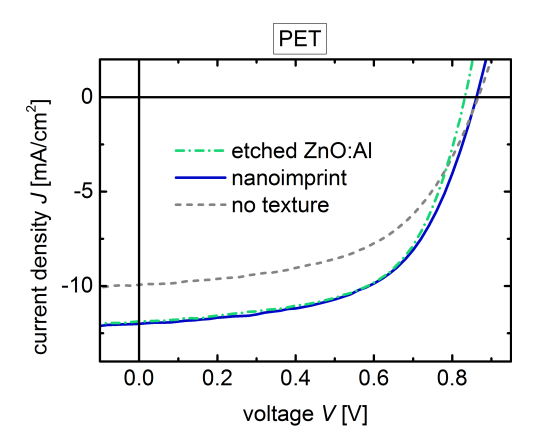


Figure B.2.: Current density-voltage (J-V) curves for a-Si:H solar cells on PET substrate, where nanoimprint (blue solid line) and etching of ZnO:Al (green dash-dotted line) are used as light management approaches. A solar cell on smooth PET substrate is shown for comparison (gray dashed line).

C. Solar Cells with ITO and IO:H Layers

In Chapter 6 it was indicated that indium containing TCO layers such as indium-doped tin oxide (ITO) and hydrogen-doped indium oxide (IO:H) might have superior electrical and optical properties compared to ZnO:Al layers. Therefore, electrical and optical properties of various TCO layers and prototype devices are presented in the following. The nominal substrate temperatures for IO:H, ITO and ZnO:Al layers are around 20 °C, 125 °C and 135 °C, respectively. The absorptance A = 1-T-R curves of the layers deposited on Corning Eagle XG glass substrates with a thickness of 230-240 nm are shown in Fig. C.1. It can

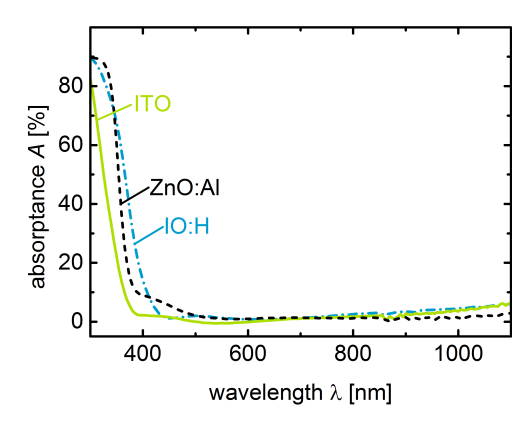


Figure C.1.: Absorptance A curves for layers of ZnO:Al (black dashed line), ITO (green solid line) and IO:H (blue dash-dotted line) deposited on Corning Eagle XG glass substrates. The layer thickness is 230-240 nm.

be seen that the absorption edge varies for the three types of TCO layers, with ITO providing the lowest absorptance in the range below $500\,\mathrm{nm}$. In the wavelength range $500\,\mathrm{nm} < \lambda < 1100\,\mathrm{nm}$, no significant difference in the absorptance can be detected. The electrical properties of the three types of layers are presented in Table C.1. In comparison to ZnO:Al, the indium containing TCOs provide a significantly higher charge carrier mobility as well as charge carrier density resulting in a lower resistivity and thus sheet resistance. The electrical properties of ITO and IO:H are roughly similar.

The resistance of the ITO and IO:H layers against reduction resulting from plasma containing a high hydrogen flux, as present for silicon layers deposited under low silane concentrations, was simulated by exposing the layers to a pure hydrogen plasma for

Table C.1.: Layer thickness d and Hall characteristics for the three TCO materials: sheet resistance R_{\square} , resistivity ρ , carrier density n and carrier mobility μ .

| TCO material | d [nm] | $R_{\square} [\Omega]$ | $\rho~[10^{-4}\Omega\mathrm{cm}]$ | $n \ [10^{20} \mathrm{cm}^{-3}]$ | $\mu \ [\mathrm{cm^2/Vs}]$ |
|--------------|--------|------------------------|-----------------------------------|-----------------------------------|----------------------------|
| ZnO:Al | 230 | 29 | 6.6 | 3.5 | 27 |
| ITO | 240 | 11 | 2.7 | 4.7 | 49 |
| IO:H | 240 | 14 | 3.3 | 4.0 | 48 |

5 minutes. The resulting absorptance curves are presented in Fig. C.2 An increase in

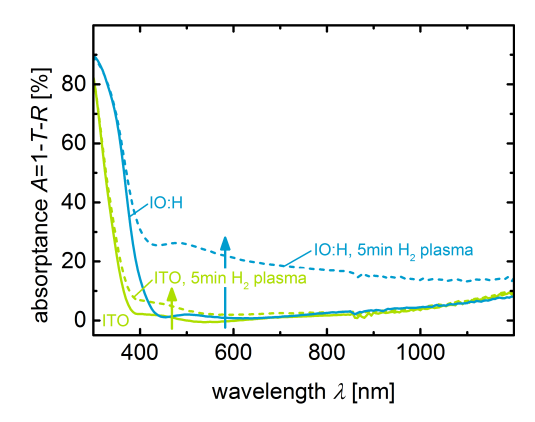


Figure C.2.: Absorptance A curves for ITO (green) and IO:H (blue) layers deposited on Corning Eagle XG glass substrates in the as-deposited state (solid lines) and after exposure to a hydrogen plasma for 5 minutes (dashed lines). The arrows indicate the increase in absorptance due to the hydrogen plasma treatment.

absorptance can be observed for both ITO and IO:H layers: up to 4% in the wavelength range $350\,\mathrm{nm} < \lambda < 800\,\mathrm{nm}$ in the case of ITO and even up to 25% in the wavelength range $350\,\mathrm{nm} < \lambda < 1200\,\mathrm{nm}$ in the case of IO:H layers. A possible explanation might be related to the reduction of metallic indium and/or tin in the TCO layer [316]. The ZnO:Al layer on the other hand showed no change in optical properties after exposure to the hydrogen plasma (not shown).

The three types of layers were implemented in a-Si:H single junction solar cells on glass substrates. In order to prevent exposure to the plasma, some ITO and IO:H layers were covered with a thin (15 nm) capping layer of ZnO:Al, that is known to be stable to hydrogen plasma. Since no light management concept was applied in all cases, strong differences in the reflectance of the solar cells are obtained due to the varying refractive indexes of the TCO layers. Therefore, internal quantum efficiencies are evaluated and the results after 150 minutes annealing are shown in Fig. C.3. In the case of no additional capping layer (Fig. C.3(a)), the IQE curves for the solar cells on the ITO and IO:H covered glass substrates are significantly reduced in the wavelength range $380 \,\mathrm{nm} < \lambda < 700 \,\mathrm{nm}$ compared to that using ZnO:Al as TCO, probably due to the increased absorptance in

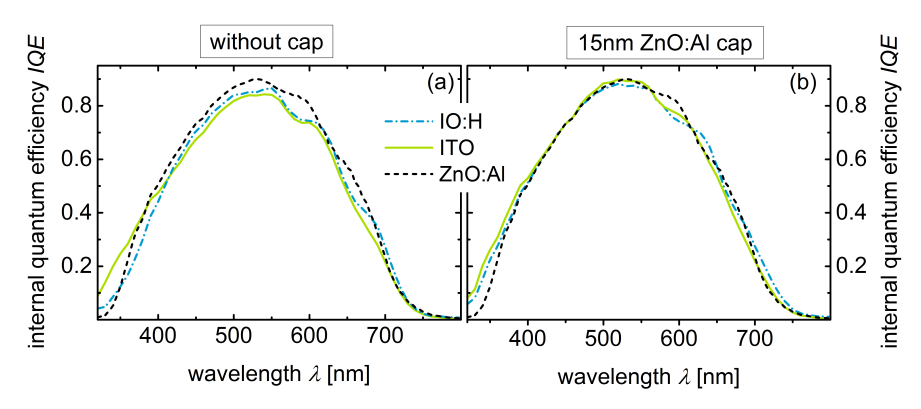


Figure C.3.: Internal quantum efficiency IQE for non-textured solar cells using ZnO:Al (black dashed line), ITO (green solid line) and IO:H (blue dash-dotted line) as TCO. (a) without capping layer, (b) with 15 nm ZnO:Al capping layer on top of ITO and IO:H.

the layers resulting from the plasma exposure upon the deposition of silicon layers. When a thin ZnO:Al capping layer is deposited on top of the ITO and IO:H layer before solar cell deposition (Fig. C.3(b)), similar IQE curves are obtained for all three types of TCOs for $\lambda > 400\,\mathrm{nm}$. In the wavelength range below $400\,\mathrm{nm}$, the IQE is enhanced for the case of ITO and IO:H as TCO, compared to the solar cell on ZnO:Al. The corresponding photovoltaic parameters are shown in Table C.2. Due to the difference in cell areas, the

Table C.2.: Photovoltaic parameters and cell areas of a-Si:H solar cells on glass substrates using various TCO materials with and without a thin (15 nm) ZnO:Al capping layer.

| TCO material | capping layer | cell area $[{\rm cm}^2]$ | $\eta~[\%]$ | FF~[%] | $V_{\rm OC}~[{\rm mV}]$ | $J_{\rm SC}~[{\rm mA/cm^2}]$ |
|--------------|---------------|--------------------------|-------------|--------|-------------------------|------------------------------|
| ZnO:Al | - | 0.36 | 5.1 | 57.1 | 890 | 10.7 |
| ITO | no | 1.0 | 5.6 | 62.4 | 910 | 9.8 |
| ITO | yes | 1.0 | 6.3 | 61.4 | 920 | 10.4 |
| IO:H | no | 1.0 | 5.5 | 61.0 | 910 | 9.9 |
| IO:H | yes | 1.0 | 6.1 | 59.4 | 920 | 10.4 |

short-circuit current density is evaluated from EQE curves, as described in Section 3.4.2. For the solar cells using ITO and IO:H as TCO, an increase J_{SC} due to the ZnO:Al capping layer can be detected. The solar cells on ITO and IO:H covered glass substrates exhibit a higher FF and V_{OC} compared to that on ZnO:Al, independent of the application of a capping layer.

D. Effects of Barrier Layers on PET Substrates

The influence of thin barrier layers of $ZnSnO_x$ and SiO_xN_y deposited on top of PET substrates on the properties of ZnO:Al layers after wet-chemical etching as well as on the performance of solar cells is investigated in the following. In Fig. D.1, SEM images of ZnO:Al layers deposited on PET substrates (a) with and (b) without $ZnSnO_x$ layer after etching for $20 \, s$ in HCl solution are shown, respectively. In the case of PET substrates

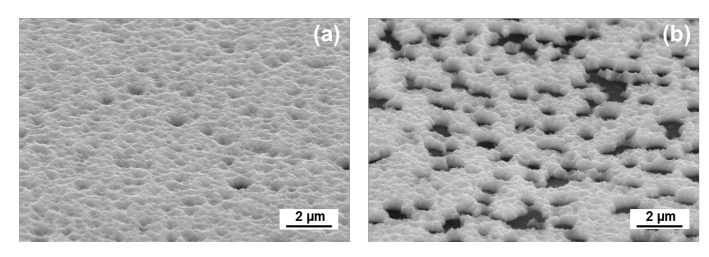


Figure D.1.: Scanning electron microscopy (SEM) image of ZnO:Al layers deposited on PET substrates (a) with and (b) without a thin $(20\,\mathrm{nm})$ barrier layer of ZnSnO_x after $20\,\mathrm{s}$ etching in HCl.

without barrier layer, the wet-chemical etching of ZnO:Al leads to partial over-etching of the ZnO:Al layer down to the substrate. Similar initial ZnO:Al layer thicknesses were estimated from interference fringes in transmittance and reflectance curves in the asdeposited state (not shown).

Transmittance and reflectance curves of the etched ZnO:Al layer on top of the bare PET substrate (without barrier) are shown in Fig. D.2. Similar to the case of ZnO:Al layers on PET substrate with barrier layer (cf. Fig. 6.5), interference fringes are diminished due to the evolving texture after the first etching step. Interestingly however, the reflectance of the etched ZnO:Al layer on bare PET substrate shown here continuously increases with etching time, thereby reducing the transmittance of the ZnO:Al covered substrate. An interesting feature is also the step-like absorption edge visible in the range below 350 nm, which is magnified in Fig. D.3. The step-like transmittance curve in this range probably results from a superposition of the transmittance of areas where only PET (ZnO:Al etched down to the substrate) and where PET/ZnO:Al are present. Indeed, by weighted superposition of the transmittance curves of bare PET substrate (grey line) and thick ZnO:Al on top of PET (purple line) shown in Fig. D.3, the transmittance spectrum after etching can well be reproduced (dashed lines). The result implicates a percentage of

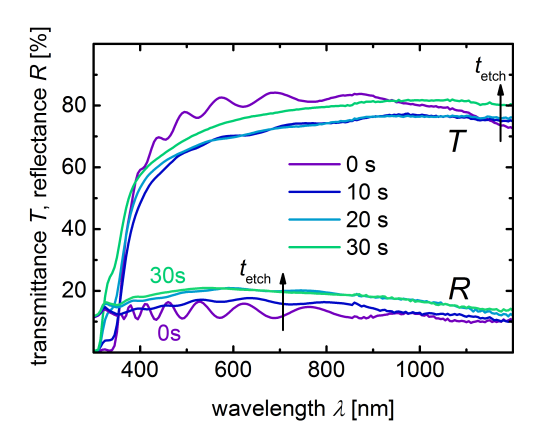


Figure D.2.: Transmittance T and reflectance R curves for ZnO:Al layers deposited on PET substrate without barrier layer after various etching times t_{etch} from 0 s to 30 s in HCl solution.

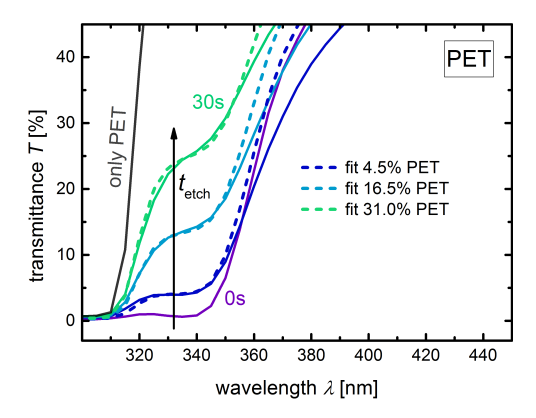


Figure D.3.: Transmittance T curves for ZnO:Al layers deposited on PET substrate without barrier layer after various etching times $t_{\rm etch}$ from 0 s to 30 s in HCl solution. The transmittance curve for bare PET substrate without ZnO:Al is shown for comparison (grey line). The dashed lines indicate the fit for weighted superposition of bare PET substrate (grey line) and non-etched PET/ZnO:Al substrate (purple line).

holes (which corresponds to the share of bare PET substrate) of 5%, 17% and 31% after of $10 \, \text{s}$, $20 \, \text{s}$ and $30 \, \text{s}$ etching time, respectively.

The sheet resistance was measured as a function of etching time and the result is shown in Fig. D.4. The sheet resistance increases quickly with etching time, up to a value

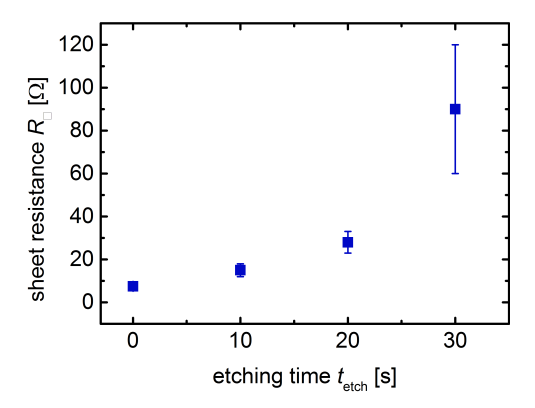


Figure D.4.: Sheet resistance R_{\square} of ZnO:Al layers deposited on PET substrate without barrier layer as a function of etching time t_{etch} in HCl solution.

of $90\pm30\,\Omega$ after 30 s etching.

Subsequently, a-Si:H solar cells were deposited on top of the different substrates: $PET/ZnSnO_x(20nm)/ZnO:Al(20s etched)$, $PET/SiO_xN_y(70nm)/ZnO:Al(20s etched)$ and PET/ZnO:Al(20s etched). The resulting external quantum efficiency EQE and cell absorptance 1-R curves are shown in Fig. D.5. Similar EQE curves for solar cells on PET

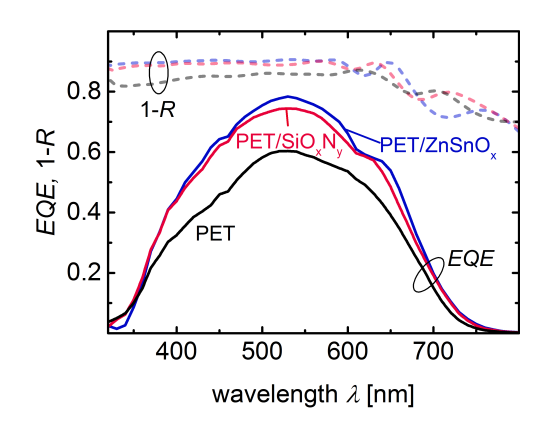


Figure D.5.: External quantum efficiency EQE (solid lines) and cell absorptance 1-R (dashed lines) curves for a-Si:H solar cells on different types of substrates: $PET/ZnSnO_x(20nm)/ZnO:Al$ (blue), $PET/SiO_xN_y(70nm)/ZnO:Al$ (red) and PET/ZnO:Al (black). The ZnO:Al was etched for 20 s in all cases.

substrates covered with SiO_xN_y and $ZnSnO_x$ are observed. The solar cell on PET substrate without barrier layer exhibits a significantly reduced EQE over the entire wavelength range. This can partly be related to a reduced cell absorptance, however the difference is still significant in IQE curves (not shown).

Corresponding J-V curves are shown in Fig. D.6. A significantly lower J_{SC}, V_{OC}

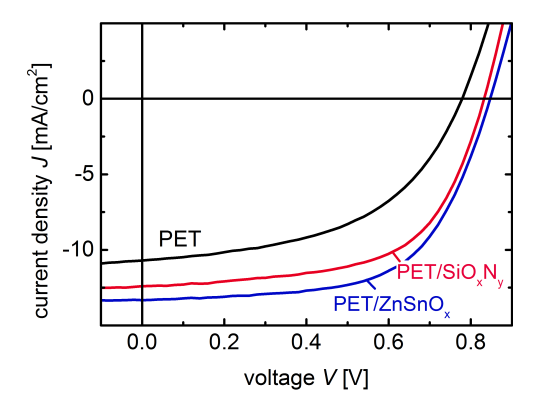


Figure D.6.: Current density-voltage J-V curves for a-Si:H solar cells on different types of substrates: $PET/ZnSnO_x(20nm)/ZnO:Al$ (blue), $PET/SiO_xN_y(70nm)/ZnO:Al$ (red) and PET/ZnO:Al (black). The ZnO:Al was etched for 20 s in all cases.

and FF for the solar cell on PET substrate without barrier is evident. Comparison of the two types of barrier layers, a slightly lower J_{SC} and V_{OC} for the solar cell on PET/SiO_xN_y substrate can be observed.

E. Deposition Parameters for Individual Layers and Solar Cells

Reference Layers

Table E.1.: Parameters for the deposition of reference silicon layers for solar cells developed in [223] and applied in Chapter 4: power P, excitation frequency f, electrode distance $d_{\rm el}$, deposition pressure p, nominal substrate temperature $T_{\rm s}$, process gas flows and deposition time $t_{\rm depo}$. Dopant gas flow corresponds to TMB and PH₃ in the case of p-type and n-type layers, respectively. The flows are given as absolute values including dilution gases (2.54% TMB in helium and 5% PH₃ in silane, respectively).

| Layer | P [W] | f [MHz] | $d_{ m el}$ [mm] | p [mbar] | $T_{\rm s}$ [°C] | SiH_4 flow [sccm] | H_2 flow [sccm] | $ \begin{array}{c} \mathrm{CH_4} \\ \mathrm{flow} \\ [\mathrm{sccm}] \end{array} $ | dopant flow [sccm] | $t_{ m depo}$ h:mm:ss |
|-------------------------|----------|---------|------------------|----------|------------------|---------------------|-------------------|--|--------------------------|-----------------------|
| a-Si:H solar cell | | | | | | | | | | _ |
| p-type a-Si:H | 4 | 13.56 | 12 | 1.6 | 180 | 9 | 90 | 5 | 5 | 0:01:40 |
| intrinsic a-Si:H | 4 | 13.56 | 12 | 1.6 | 180 | 20 | 100 | - | _ | 0:45:00 |
| n-type a-Si:H | 4 | 13.56 | 12 | 1.6 | 180 | 50 | 100 | _ | 20 | 0:01:40 |
| μ c-Si:H solar cell | | | | | | | | | | |
| p-type μ c-Si:H | 30 | 81.36 | 22 | 1.0 | 180 | 1.5 | 200 | _ | 1.2 | 0:04:20 |
| intrinsic μ c-Si:H | 20 | 81.36 | 11 | 1.0 | 180 | 11 | 200 | _ | _ | 1:30:00 |
| n-type a-Si:H | 4 | 13.56 | 12 | 1.6 | 180 | 50 | 100 | - | 20 | 0:01:40 |

Series of Individual Layers

Table E.2.: Parameters for the deposition of individual silicon layers for the different types of series presented in Chapter 4: power P, excitation frequency f, electrode distance $d_{\rm el}$, deposition pressure p, nominal substrate temperature $T_{\rm s}$ and process gas flows. Dopant gas flow corresponds to TMB and PH₃ in the case of p-type and n-type layers, respectively. The flows are given as absolute values including dilution gases (2.54% TMB in helium and 5% PH₃ in silane, respectively).

| series | P | f | $d_{ m el}$ | p | $T_{ m s}$ | SiH_4 flow | $_{\rm flow}^{\rm H_2}$ | CH_4 flow | dopant flow |
|-------------------------------|-----|-------|-------------|--------|---------------|--------------|-------------------------|----------------------|----------------|
| | [W] | [MHz] | [mm] | [mbar] | $[^{\circ}C]$ | [sccm] | [sccm] | [sccm] | [sccm] |
| p-type a-Si:H layers | | | | | | | | | |
| T series | 4 | 13.56 | 12 | 1.6 | 120-180 | 9 | 90 | 5 | 5 |
| $c_{\rm TMB}$ series | 4 | 13.56 | 12 | 1.6 | 120 | 9 | 90 | 0, 5 | 5-25 |
| on PET | 4 | 13.56 | 14 | 1.6 | 120 | 9 | 90 | 0 | 9 |
| intrinsic a-Si:H layers | | | | | | | | | |
| T series | 4 | 13.56 | 12 | 1.6 | 120, 180 | 20 | 100 | _ | _ |
| SC series | 4 | 13.56 | 12 | 1.6 | 120 | 5-30 | 90-115 | - | _ |
| $c_{\rm CH4}~{\rm series}^1$ | 4 | 13.56 | 12 | 1.6 | 120 | 9 | 90 | 0-10 | _ |
| on PET | 4 | 13.56 | 14 | 1.6 | 120 | 15 | 105 | _ | _ |
| n-type a-Si:H layers | | | | | | | | | |
| T series | 4 | 13.56 | 12 | 1.6 | 120, 180 | 50 | 100 | _ | 20 |
| SC series | 4 | 13.56 | 12 | 1.6 | 120 | 5-50 | 100-140 | _ | 2-20 |
| on PET | 4 | 13.56 | 14 | 1.6 | 120 | 15 | 130 | _ | 6 |
| intrinsic μ c-Si:H layers | | | | | | | | | |
| SC series | 20 | 81.36 | 11 | 1.0 | 120 | 4-11 | 200-207 | _ | _ |
| | | | | | | | | | |

¹for comparison purposes with p-type layers in Section 4.1.1

Tandem Solar Cell

Table E.3.: Parameters for the deposition of silicon layers for the a-Si:H/ μ c-Si:H tandem solar cell presented in Chapter 4 (sample number 15P-557): power P, excitation frequency f, electrode distance $d_{\rm el}$, deposition pressure p, nominal substrate temperature $T_{\rm s}$, process gas flows and deposition time $t_{\rm depo}$. Dopant gas flow corresponds to TMB and PH₃ in the case of p-type and n-type layers, respectively. The flows are given as absolute values including dilution gases (2.54% TMB) in helium and $5\% \text{ PH}_3$ in silane, respectively).

| Layer | P [W] | f [MHz] | $d_{\rm el}$ [mm] | p [mbar] | $T_{\rm s}$ [°C] | $\begin{array}{c} {\rm SiH_4} \\ {\rm flow} \\ {\rm [sccm]} \end{array}$ | H_2 flow [sccm] | dopant flow [sccm] | $t_{\rm depo}$ h:mm:ss |
|------------------------|----------|------------|-------------------|----------|------------------|--|-------------------|--------------------------|------------------------|
| p-type a-Si:H | 4 | 13.56 | 12 | 1.6 | 120 | 9 | 90 | 9 | 0:01:50 |
| intrinsic a-Si:H | 4 | 13.56 | 12 | 1.6 | 120 | 15 | 105 | _ | 0:40:00 |
| n-type μ c-Si:H | 12 | 81.36 | 9.6 | 1.0 | 120 | 2.7 | 200 | 1.2 | 0:06:40 |
| p-type μc-Si:H | 30 | 81.36 | 22 | 1.0 | 120 | 1.5 | 200 | 1.2 | 0:04:20 |
| intrinsic μ c-Si:H | 20 | 81.36 | 11 | 1.0 | 120 | 6.5 | 205 | _ | 1:40:00 |
| n-type a-Si:H | 4 | 13.56 | 12 | 1.6 | 120 | 15 | 130 | 6 | 0:02:20 |

ZnO:Al Layers

Table E.4.: Parameters for the deposition of ZnO:Al layers presented in Chapter 6: power P, deposition pressure p, nominal substrate temperature $T_{\rm s}$ and Ar process gas flow.

| series | P [W] | $p \\ [\mu \mathrm{bar}]$ | $T_{\rm s}$ [°C] | Ar flow [sccm] |
|-------------------------|-------|---------------------------|------------------|----------------|
| T series | 100 | 4.7 | 20-320 | 30 |
| on imprinted substrates | 100 | 4.7 | 180 | 30 |
| etching series | 100 | 4.7 | 135 | 30 |

Bibliography

- [1] "Key World Energy Statistics 2015", International Energy Agency, 2015.
- [2] "World Energy Outlook Energy and Air Pollution", International Energy Agency, 2016.
- [3] R. E. Smalley, "Future Global Energy Prosperity: The Terawatt Challenge", MRS Bulletin, vol. 30, pp. 412–417, 2005.
- [4] "Next Generation Wind and Solar Power", International Energy Agency, 2016.
- [5] I. Clover, Masdar selected by DEWA to lead consortium on 800 MW solar PV project in Dubai, pv magazine, 27. June 2016, retrieved from http://www.pv-magazine.com/news/details/beitrag/masdar-selected-by-dewa-to-lead-consortium-on-800-mw-solar-pv-project-in-dubai_100025158.
- [6] "Technology Roadmap Solar Photovoltaic Energy", International Energy Agency, 2014.
- [7] M. A. Green, K. Emery, Y. Hishikawa, W. Warta, and E. D. Dunlop, "Solar cell efficiency tables (version 47)", Progress in Photovoltaics: Research and Applications, vol. 24, pp. 3–11, 2016.
- [8] "Technology Roadmap Solar Photovoltaic Energy", International Energy Agency, 2010.
- [9] A. Polman, M. Knight, E. C. Garnett, B. Ehrler, and W. C. Sinke, "Photovoltaic materials: Present efficiencies and future challenges", *Science*, vol. 352, pp. aad4424-1–aad4424-10, 2016.
- [10] E. Cuce, "Toward multi-functional PV glazing technologies in low/zero carbon buildings: Heat insulation solar glass – Latest developments and future prospects", Renewable and Sustainable Energy Reviews, vol. 60, pp. 1286–1301, 2016.
- [11] "Printed, Organic & Flexible Electronics: Forecasts, Players & Opportunities 2011-2021", IDTechEx, 2011.
- [12] C. W. Wessner, The Future of Photovoltaic Manufacturing in the United States. Washington, D.C.: The National Academies Press, 2011.
- [13] K. Wilken, V. Smirnov, and F. Finger, "Abschlussbericht für das Teilprojekt Entwicklung von Solarzellen auf flexiblen Substraten im Verbundprojekt Entwicklung und Untersuchung der Beschichtung von Folienbändern mit Kontakten, Barrieren und Solarzellen (FlexSol)", Technische Informationsbibliothek Hannover (TIB), 2016.

- [14] R. G. Gordon, "Criteria for choosing transparent conductors", MRS Bulletin, vol. 25, pp. 52–57, 2000.
- [15] M. Layani, A. Kamyshny, and S. Magdassi, "Transparent conductors composed of nanomaterials", *Nanoscale*, vol. 6, pp. 5581–5591, 2014.
- [16] K. Ellmer, "Past achievements and future challenges in the development of optically transparent electrodes", *Nature Photonics*, vol. 6, pp. 809–817, 2012.
- [17] W. Cao, J. Li, H. Chen, and J. Xue, "Transparent electrodes for organic optoelectronic devices: A review", Journal of Photonics for Energy, vol. 4, p. 040 990, 2014.
- [18] D. S. Ginley, Ed., *Handbook of Transparent Conductors*. Boston, MA: Springer US, 2011.
- [19] K. Ellmer, A. Klein, and B. Rech, Eds., *Transparent Conductive Zinc Oxide*. Springer Berlin Heidelberg, 2008.
- [20] J. I. Owen, "Growth, etching, and stability of sputtered ZnO:Al for thin-film silicon solar cells", PhD Thesis, RWTH Aachen University, 2011.
- [21] P. Drude, "Zur Elektronentheorie der Metalle", Annalen der Physik, vol. 306, pp. 566–613, 1900.
- [22] K. Ellmer, "Resistivity of polycrystalline zinc oxide films: current status and physical limit", *Journal of Physics D: Applied Physics*, vol. 34, pp. 3097–3108, 2001.
- [23] E. Burstein, "Anomalous optical absorption limit in InSb", Physical Review, vol. 93, pp. 632–633, 1954.
- [24] T. S. Moss, "The interpretation of the properties of indium antimonide", *Proceedings of the Physical Society. Section B*, vol. 67, pp. 775–782, 1954.
- [25] S. Faÿ, U. Kroll, C. Bucher, E. Vallat-Sauvain, and A. Shah, "Low pressure chemical vapour deposition of ZnO layers for thin-film solar cells: Temperature-induced morphological changes", Solar Energy Materials and Solar Cells, vol. 86, pp. 385–397, 2005.
- [26] A. Stadler, "Transparent conducting oxides—An up-to-date overview", *Materials*, vol. 5, pp. 661–683, 2012.
- [27] R. A. Street, *Hydrogenated amorphous silicon*. Cambridge University Press, 1991.
- [28]~ A. Shah, Ed., $\it Thin\mbox{-} \it Film$ $\it Silicon$ $\it Solar$ $\it Cells.$ Lausanne: EFPL Press, 2010.
- [29] A. Matsuda, "Thin-film silicon –Growth process and solar cell application—", Japanese Journal of Applied Physics, vol. 43, pp. 7909–7920, 2004.
- [30] A. Rockett, *The Materials Science of Semiconductors*. Boston, MA: Springer US, 2008.
- [31] M. H. Brodsky and R. S. Title, "Electron spin resonance in amorphous silicon, germanium, and silicon carbide", *Physical Review Letters*, vol. 23, pp. 581–585, 1969.

- [32] V. Smirnov, O. Astakhov, R. Carius, Y. Petrusenko, V. Borysenko, and F. Finger, "Variation in absorber layer defect density in amorphous and microcrystalline silicon thin film solar cells with 2 MeV electron bombardment", *Japanese Journal of Applied Physics*, vol. 51, p. 022 301, 2012.
- [33] W. E. Spear and P. G. LeComber, "Substitutional doping of amorphous silicon", Solid State Communications, vol. 17, pp. 1193–1196, 1975.
- [34] D. L. Staebler and C. R. Wronski, "Reversible conductivity changes in discharge-produced amorphous Si", *Applied Physics Letters*, vol. 31, pp. 292–294, 1977.
- [35] M. Stutzmann, W. B. Jackson, and C. C. Tsai, "Light-induced metastable defects in hydrogenated amorphous silicon: A systematic study", *Physical Review B*, vol. 32, pp. 23–47, 1985.
- [36] J. Stuke, "Problems in the understanding of electronic properties of amorphous silicon", *Journal of Non-Crystalline Solids*, vol. 97–98, pp. 1–14, 1987.
- [37] O. Vetterl, F. Finger, R. Carius, P. Hapke, L. Houben, O. Kluth, A. Lambertz, A. Mück, B. Rech, and H. Wagner, "Intrinsic microcrystalline silicon: A new material for photovoltaics", *Solar Energy Materials and Solar Cells*, vol. 62, pp. 97–108, 2000.
- [38] L. Houben, "Plasmaabscheidung von mikrokristallinem Silizium: Merkmale und Mikrostruktur und deren Deutung im Sinne von Wachstumsvorgängen", PhD Thesis, Universität Düsseldorf, 1999.
- [39] C. C. Tsai, Amorphous Silicon and Related Materials, H. Fritzsche, Ed. Singapore: World Scientific, 1988, pp. 123–147.
- [40] M. Vaněček, A. Poruba, Z. Remeš, N. Beck, and M. Nesládek, "Optical properties of microcrystalline materials", *Journal of Non-Crystalline Solids*, vol. 227-230, pp. 967–972, 1998.
- [41] F. Finger, R. Carius, T. Dylla, S. Klein, S. Okur, and M. Günes, "Stability of microcrystalline silicon for thin film solar cell applications", *IEE Proceedings Circuits, Devices and Systems*, vol. 150, p. 300, 2003.
- [42] Y. Wang, X. Geng, H. Stiebig, and F. Finger, "Stability of microcrystalline silicon solar cells with HWCVD buffer layer", *Thin Solid Films*, vol. 516, pp. 733–735, 2008.
- [43] T. Hogness, T. L. Wilson, and W. C. Johnson, "The thermal decomposition of silane", *Journal of the American Chemical Society*, vol. 58, pp. 108–112, 1936.
- [44] A. Matsuda, K. Nomoto, Y. Takeuchi, A. Suzuki, A. Yuuki, and J. Perrin, "Temperature dependence of the sticking and loss probabilities of silyl radicals on hydrogenated amorphous silicon", *Surface Science*, vol. 227, pp. 50–56, 1990.
- [45] Y. Toyoshima, K. Arai, A. Matsuda, and K. Tanaka, "In situ characterization of the growing a-Si:H surface by IR spectroscopy", *Journal of Non-Crystalline Solids*, vol. 137-138, pp. 765–770, 1991.

- [46] R. E. I. Schropp and M. Zeman, Amorphous and Microcrystalline Silicon Solar Cells: Modeling, Materials and Device Technology, Boston, MA: Springer US, 1998.
- [47] A. Matsuda, "Microcrystalline silicon. Growth and device application", *Journal of Non-Crystalline Solids*, vol. 338-340, pp. 1–12, 2004.
- [48] R. W. Collins and A. S. Ferlauto, "Advances in plasma-enhanced chemical vapor deposition of silicon films at low temperatures", *Current Opinion in Solid State and Materials Science*, vol. 6, pp. 425–437, 2002.
- [49] J. Robertson, "Growth mechanism of hydrogenated amorphous silicon", *Journal of Non-Crystalline Solids*, vol. 266-269, pp. 79–83, 2000.
- [50] P. Roca i Cabarrocas, Y. Bouizem, and M. L. Theye, "Defect density and hydrogen bonding in hydrogenated amorphous silicon as functions of substrate temperature and deposition rate", *Philosophical Magazine Part B*, vol. 65, pp. 1025–1040, 1992.
- [51] K. Wilken, "Tandem cells providing high open circuit voltages for photoelectrochemical water splitting", Diploma Thesis, Technical University Darmstadt, 2013.
- [52] J. C. Knights, G. Lucovsky, and R. J. Nemanich, "Defects in plasma-deposited a-Si:H", *Journal of Non-Crystalline Solids*, vol. 32, pp. 393–403, 1979.
- [53] R. A. Street and D. K. Biegelsen, "The spectroscopy of localized states", *Topics in Applied Physics: The Physics of Hydrogenated Amorphous Silicon II*, vol. 56, pp. 61–168, 1984.
- [54] W. M. M. Kessels, R. J. Severens, M. C. M. van de Sanden, and D. C. Schram, "Temperature and growth-rate effects on the hydrogen incorporation in a-Si:H", Journal of Non-Crystalline Solids, vol. 227-230, pp. 133-137, 1998.
- [55] A. Matsuda, M. Matsumura, S. Yamasaki, H. Yamamoto, T. Imura, H. Okushi, S. Iizima, and K. Tanaka, "Boron doping of hydrogenated silicon thin films", *Japanese Journal of Applied Physics*, vol. 20, pp. L183–L186, 1981.
- [56] R. C. Ross and J. Kaklik Jr, "Plasma polymerization and deposition of amorphous hydrogenated silicon from rf and dc silane plasmas", *Journal of Applied Physics*, vol. 55, pp. 3785–3794, 1984.
- [57] J. C. van den Heuvel, M. J. Geerts, and J. W. Metselaar, "The relation between the optical properties and the hydrogen concentration in a-Si:H", *Solar Energy Materials*, vol. 22, pp. 185–194, 1991.
- [58] A. J. M. Berntsen, W. F. van der Weg, P. A. Stolk, and F. W. Saris, "Separating the effects of hydrogen and bond-angle variation on the amorphous-silicon band gap", *Physical Review B*, vol. 48, pp. 14656–14658, 1993.
- [59] M. Yamaguchi and K. Morigaki, "Effect of hydrogen dilution on the optical properties of hydrogenated amorphous silicon prepared by plasma deposition", *Philosophical Magazine Part B*, vol. 79, pp. 387–405, 1999.

- [60] F. Urbain, K. Wilken, V. Smirnov, O. Astakhov, A. Lambertz, J.-P. Becker, U. Rau, J. Ziegler, B. Kaiser, W. Jaegermann, and F. Finger, "Development of thin film amorphous silicon tandem junction based photocathodes providing high open-circuit voltages for hydrogen production", *International Journal of Photoenergy*, vol. 2014, p. 249 317, 2014.
- [61] J. He, W. Li, R. Xu, K.-C. Qi, and Y.-D. Jiang, "Structure and electronic states in a-Si:H thin films", *Journal of Materials Science*, vol. 47, pp. 5121–5127, 2012.
- [62] J. Ni, J. Zhang, Y. Cao, X. Wang, X. Chen, X. Geng, and Y. Zhao, "Low temperature deposition of high open-circuit voltage (>1.0 V) p-i-n type amorphous silicon solar cells", Solar Energy Materials and Solar Cells, vol. 95, pp. 1922–1926, 2011.
- [63] F. Urbain, V. Smirnov, J.-P. Becker, U. Rau, F. Finger, J. Ziegler, B. Kaiser, and W. Jaegermann, "a-Si:H/μc-Si:H tandem junction based photocathodes with high open-circuit voltage for efficient hydrogen production", *Journal of Materials Research*, vol. 29, pp. 2605–2614, 2014.
- [64] W. Shockley and H. J. Queisser, "Detailed balance limit of efficiency of p-n junction solar cells", *Journal of Applied Physics*, vol. 32, pp. 510–519, 1961.
- [65] I. Tobías and A. Luque, "Ideal efficiency of monolithic, series-connected multijunction solar cells", Progress in Photovoltaics: Research and Applications, vol. 10, pp. 323–329, 2002.
- [66] J. Meier, E. Vallat-Sauvain, S. Dubail, U. Kroll, J. Dubail, S. Golay, L. Feitknecht, P. Torres, S. Faÿ, D. Fischer, and A. Shah, "Microcrystalline/micromorph silicon thin-film solar cells prepared by VHF-GD technique", Solar Energy Materials and Solar Cells, vol. 66, pp. 73–84, 2001.
- [67] B. Bills, X. Liao, D. W. Galipeau, and Q. H. Fan, "Effect of tunnel recombination junction on crossover between the dark and illuminated current-voltage curves of tandem solar cells", *IEEE Transactions on Electron Devices*, vol. 59, pp. 2327– 2330, 2012.
- [68] J. Kuendig, M. Goetz, A. Shah, L. Gerlach, and E. Fernandez, "Thin film silicon solar cells for space applications: Study of proton irradiation and thermal annealing effects on the characteristics of solar cells and individual layers", Solar Energy Materials and Solar Cells, vol. 79, pp. 425–438, 2003.
- [69] A. Lambertz, V. Smirnov, T. Merdzhanova, K. Ding, S. Haas, G. Jost, R. E. I. Schropp, F. Finger, and U. Rau, "Microcrystalline silicon—oxygen alloys for application in silicon solar cells and modules", *Solar Energy Materials and Solar Cells*, vol. 119, pp. 134–143, 2013.
- [70] M. Stuckelberger, Y. Riesen, M. Despeisse, J.-W. Schüttauf, F.-J. Haug, and C. Ballif, "Light-induced Voc increase and decrease in high-efficiency amorphous silicon solar cells", *Journal of Applied Physics*, vol. 116, p. 094503, 2014.
- [71] W. Beyer, "Diffusion and evolution of hydrogen in hydrogenated amorphous and microcrystalline silicon", Solar Energy Materials and Solar Cells, vol. 78, pp. 235– 267, 2003.

- [72] D. K. Biegelsen, R. A. Street, C. C. Tsai, and J. C. Knights, "Hydrogen evolution and defect creation in amorphous Si:H alloys", *Physical Review B*, vol. 20, pp. 4839– 4846, 1979.
- [73] W. Beyer and H. Wagner, "The role of hydrogen in a-Si:H results of evolution and annealing studies", *Journal of Non-Crystalline Solids*, vol. 59-60, pp. 161–168, 1983.
- [74] M. Stutzmann, "The defect density in amorphous silicon", *Philosophical Magazine Part B*, vol. 60, pp. 531–546, 1989.
- [75] M. Brinza, J. Rath, and R. E. I. Schropp, "Thin film silicon n-i-p solar cells deposited by VHF PECVD at 100°C substrate temperature", *Solar Energy Materials and Solar Cells*, vol. 93, pp. 680–683, 2009.
- [76] C. Koch, M. B. Schubert, and J. H. Werner, "Protocrystalline growth of silicon below 80°C", in *Proceedings of the 16th European Photovoltaic Solar Energy Conference*, vol. 609, London: James & James, 2000, pp. 401–404.
- [77] C. Koch, "Niedertemperaturabscheidung von Dünnschicht-Silicium für Solarzellen auf Kunststofffolien", PhD Thesis, Universität Stuttgart, 2003.
- [78] G. H. Wang, C. Y. Shi, L. Zhao, R. D. Hu, L. L. Li, G. H. Wang, J. W. Chen, H. W. Diao, and W. J. Wang, "Performance improvement of amorphous silicon germanium single junction solar cell modules by low temperature annealing", *Thin Solid Films*, vol. 552, pp. 180–183, 2014.
- [79] A. Mittal, M. Rennhofer, A. Dangel, B. Duman, and V. Schlosser, "Power change in amorphous silicon technology by low temperature annealing", *EPJ Photovoltaics*, vol. 6, p. 65304, 2015.
- [80] H. Fritzsche, "Development in understanding and controlling the Staebler-Wronski effect in a-Si:H", *Annual Review of Materials Research*, vol. 31, pp. 47–79, 2001.
- [81] M. S. Bennett, J. L. Newton, K. Rajan, and A. Rothwarf, "Kinetic studies of the annealing behavior of a-Si:H p-i-n solar cells", *Journal of Applied Physics*, vol. 62, pp. 3968–3975, 1987.
- [82] S. Y. Myong and K. S. Lim, "Modeling of annealing kinetics for hydrogenated-amorphous-silicon-based solar cells using two-component metastable defects", Applied Physics Letters, vol. 88, p. 243510, 2006.
- [83] J. Melskens, M. Schouten, R. Santbergen, M. Fischer, R. Vasudevan, D. van der Vlies, R. Quax, S. Heirman, K. Jäger, V. Demontis, M. Zeman, and A. Smets, "In situ manipulation of the sub gap states in hydrogenated amorphous silicon monitored by advanced application of Fourier transform photocurrent spectroscopy", Solar Energy Materials and Solar Cells, vol. 129, pp. 70–81, 2014.
- [84] T. J. McMahon and R. Tsu, "Equilibrium temperature and related defects in intrinsic glow discharge amorphous silicon", Applied Physics Letters, vol. 51, pp. 412– 414, 1987.

- [85] C. Lee, W. D. Ohlsen, and P. C. Taylor, "Metastable paramagnetism in hydrogenated amorphous-silicon Evidence for a new class of defects in tetrahedrally bonded amorphous-semiconductors", *Physical Review B*, vol. 36, pp. 2965–2968, 1987.
- [86] G. N. Parsons, C. Wang, M. J. Williams, and G. Lucovsky, "Post-deposition relaxation of electronic defects in hydrogenated amorphous silicon", Applied Physics Letters, vol. 56, pp. 1895–1897, 1990.
- [87] T. Seth, P. Dixit, C. Mukherjee, C. Anandan, and R. Bhattacharyya, "Hydrogenated amorphous silicon films prepared at low substrate temperature on a cathode of an asymmetric r.f. plasma CVD system", *Thin Solid Films*, vol. 264, pp. 11–17, 1995.
- [88] D. Roy, C. Longeaud, and O. Saadane, "Influence of light-soaking and annealing on the microstructure of a-Si:H deposited at 423 K", *Journal of Non-Crystalline Solids*, vol. 299-302, pp. 511–515, 2002.
- [89] O. S. Panwar, C. Mukherjee, and R. Bhattacharyya, "Effect of annealing on the electrical, optical and structural properties of hydrogenated amorphous silicon films deposited in an asymmetric R.F. plasma CVD system at room temperature", Solar Energy Materials and Solar Cells, vol. 57, pp. 373–391, 1999.
- [90] E. Srinivasan, "Dominant monohydride bonding in hydrogenated amorphous silicon thin films formed by plasma enhanced chemical vapor deposition at room temperature", Journal of Vacuum Science & Technology A: Vacuum, Surfaces, and Films, vol. 15, pp. 77–84, 1997.
- [91] G. N. Parsons, C. Wang, M. J. Williams, and G. Lucovsky, "Reduction of defects by high temperature annealing (150°C–240°C) in hydrogenated amorphous silicon films deposited at room temperature", *Journal of Non-Crystalline Solids*, vol. 114, pp. 178–180, 1989.
- [92] J. P. Conde, K. K. Chan, J. M. Blum, M. Arienzo, P. A. Monteiro, J. A. Ferreira, V. Chu, and N. Wyrsh, "Annealing kinetics of a-Si:H deposited by concentricelectrode rf glow discharge at room temperature", *Journal of Applied Physics*, vol. 73, pp. 1826–1831, 1993.
- [93] Y. Ziegler, H. Curtins, J. Baumann, and A. Shah, "VHF-GD a-Si:H films prepared at very low temperature", MRS Proceedings, vol. 149, pp. 81–86, 1989.
- [94] M. Kunst and H.-C. Neitzert, "The influence of deposition temperature and annealing temperature on the optoelectronic properties of hydrogenated amorphous silicon films", *Journal of Applied Physics*, vol. 69, pp. 8320–8328, 1991.
- [95] H. C. Neitzert, W. Hirsch, C. Swiatkowski, S. Schroetter, and M. Kunst, "Transient microwave detected photoconductivity as a tool for in-situ evaluation of intrinsic a-Si:H films deposited and annealed at different temperatures", *Journal of Non-Crystalline Solids*, vol. 137-138, pp. 487-490, 1991.

- [96] N. Hata and A. Matsuda, "Difference in light-induced annealing behavior of deposition- and light-induced defects in hydrogenated amorphous silicon", Applied Physics Letters, vol. 63, pp. 1948–1950, 1993.
- [97] J. P. Kleider, C. Longeaud, and P. Roca i Cabarrocas, "Experimental evidence for the annealing of surface defects in a-Si:H during deposition", *Journal of Applied Physics*, vol. 72, pp. 4727–4731, 1992.
- [98] M. K. Cheung and M. A. Petrich, "²⁹Si magnetic resonance study of amorphous hydrogenated silicon plasma deposited at 50°C", *Journal of Applied Physics*, vol. 73, pp. 3237–3241, 1993.
- [99] H. Y. Seba, R. Cherfi, F. Hamadache, and M. Aoucher, "Correlation between physicochemical and electrical properties of hydrogenated amorphous silicon doped with boron: Effect of thermal annealing", *Materials Science Forum*, vol. 609, pp. 129–132, 2009.
- [100] P. Roca i Cabarrocas, "Deposition of intrinsic, phosphorus-doped, and boron-doped hydrogenated amorphous silicon films at 50 °C", Applied Physics Letters, vol. 65, pp. 1674–1676, 1994.
- [101] J. I. Pankove, P. J. Zanzucchi, C. W. Magee, and G. Lucovsky, "Hydrogen localization near boron in silicon", *Applied Physics Letters*, vol. 46, pp. 421–423, 1985.
- [102] P. Alpuim, V. Chu, and J. P. Conde, "Electronic and structural properties of doped amorphous and nanocrystalline silicon deposited at low substrate temperatures by radio-frequency plasma-enhanced chemical vapor deposition", *Journal of Vacuum Science & Technology A: Vacuum, Surfaces, and Films*, vol. 21, pp. 1048–1054, 2003.
- [103] Z. E. Smith and S. Wagner, "Intrinsic dangling-bond density in hydrogenated amorphous silicon", *Physical Review B*, vol. 32, pp. 5510–5513, 1985.
- [104] R. Street, J. Kakalios, C. Tsai, and T. Hayes, "Thermal-equilibrium processes in amorphous silicon", *Physical Review B*, vol. 35, pp. 1316–1333, 1987.
- [105] R. A. Street, "The origin of metastable states in a-Si:H", Solar Cells, vol. 24, pp. 211–221, 1988.
- [106] Z. E. Smith, S. Aljishi, D. Slobodin, V. Chu, S. Wagner, P. M. Lenahan, R. R. Arya, and M. S. Bennett, "Thermal-equilibrium defect processes in hydrogenated amorphous silicon", *Physical Review Letters*, vol. 57, pp. 2450–2453, 1986.
- [107] J. Müller, B. Rech, J. Springer, and M. Vanecek, "TCO and light trapping in silicon thin film solar cells", *Solar Energy*, vol. 77, pp. 917–930, 2004.
- [108] K. Schwanitz, S. Klein, T. Stolley, M. Rohde, D. Severin, and R. Trassl, "Anti-reflective microcrystalline silicon oxide p-layer for thin-film silicon solar cells on ZnO", Solar Energy Materials and Solar Cells, vol. 105, pp. 187–191, 2012.
- [109] C. Ballif, J. Dicker, D. Borchert, and T. Hofmann, "Solar glass with industrial porous SiO₂ antireflection coating: measurements of photovoltaic module properties improvement and modelling of yearly energy yield gain", Solar Energy Materials and Solar Cells, vol. 82, pp. 331–344, 2004.

- [110] F.-J. Haug and C. Ballif, "Light management in thin film silicon solar cells", *Energy Environmental Science*, vol. 8, pp. 824–837, 2015.
- [111] M. M. de Jong, P. J. Sonneveld, J. Baggerman, C. J. M. van Rijn, J. K. Rath, and R. E. I. Schropp, "Utilization of geometric light trapping in thin film silicon solar cells: simulations and experiments", Progress in Photovoltaics: Research and Applications, vol. 22, pp. 540–547, 2014.
- [112] W. Zhang, E. Bunte, J. Worbs, H. Siekmann, J. Kirchhoff, A. Gordijn, and J. Hüpkes, "Rough glass by 3d texture transfer for silicon thin film solar cells", *Phys. Status Solidi C*, vol. 7, pp. 1120–1123, 2010.
- [113] B. P. Rand, J. Genoe, P. Heremans, and J. Poortmans, "Solar cells utilizing small molecular weight organic semiconductors", *Progress in Photovoltaics: Research and Applications*, vol. 15, pp. 659–676, 2007.
- [114] D. Dominé, F.-J. Haug, C. Battaglia, and C. Ballif, "Modeling of light scattering from micro- and nanotextured surfaces", *Journal of Applied Physics*, vol. 107, p. 044504, 2010.
- [115] K. Bittkau, M. Schulte, T. Beckers, and R. Carius, "Fourier analysis for the study of light scattering properties of randomly textured ZnO films", in *Proceedings of SPIE*, R. B. Wehrspohn and A. Gombert, Eds., vol. 7725, 2010, 77250N.
- [116] O. Kluth, B. Rech, L. Houben, S. Wieder, G. Schöpe, C. Beneking, H. Wagner, A. Löffl, and H. W. Schock, "Texture etched ZnO:Al coated glass substrates for silicon based thin film solar cells", *Thin Solid Films*, vol. 351, pp. 247–253, 1999.
- [117] J. Hüpkes, B. Rech, S. Calnan, O. Kluth, U. Zastrow, H. Siekmann, and M. Wuttig, "Material study on reactively sputtered zinc oxide for thin film silicon solar cells", *Thin Solid Films*, vol. 502, pp. 286–291, 2006.
- [118] M. Berginski, J. Hüpkes, M. Schulte, G. Schoöpe, H. Stiebig, B. Rech, and M. Wuttig, "The effect of front ZnO:Al surface texture and optical transparency on efficient light trapping in silicon thin-film solar cells", Journal of Applied Physics, vol. 101, p. 074 903, 2007.
- [119] O. Kluth, G. Schöpe, J. Hüpkes, C. Agashe, J. Müller, and B. Rech, "Modified Thornton model for magnetron sputtered zinc oxide: film structure and etching behaviour", *Thin Solid Films*, vol. 442, pp. 80–85, 2003.
- [120] J. A. Thornton, "Influence of apparatus geometry and deposition conditions on the structure and topography of thick sputtered coatings", *Journal of Vacuum Science* and Technology, vol. 11, pp. 666–670, 1974.
- [121] A. Löffl, S. Wieder, B. Rech, O. Kluth, C. Beneking, and H. Wagner, "Al-doped ZnO films for thin-film solar cells with very low sheet resistance and controlled texture", in 14th European Photovoltaic Solar Energy Conference, Barcelona, Spain, 1997, pp. 2089–2092.
- [122] S. Y. Chou, P. R. Krauss, and P. J. Renstrom, "Imprint lithography with 25nanometer resolution", Science, vol. 272, pp. 85–87, 1996.

- [123] F. Hua, Y. Sun, A. Gaur, M. A. Meitl, L. Bilhaut, L. Rotkina, J. Wang, P. Geil, M. Shim, J. A. Rogers, and A. Shim, "Polymer imprint lithography with molecular-scale resolution", *Nano Letters*, vol. 4, pp. 2467–2471, 2004.
- [124] N. Kooy, K. Mohamed, L. T. Pin, and O. S. Guan, "A review of roll-to-roll nanoim-print lithography.", *Nanoscale research letters*, vol. 9, p. 320, 2014.
- [125] M. D. Austin and S. Y. Chou, "Fabrication of 70 nm channel length polymer organic thin-film transistors using nanoimprint lithography", Applied Physics Letters, vol. 81, pp. 4431–4433, 2002.
- [126] M. C. McAlpine, R. S. Friedman, and C. M. Lieber, "Nanoimprint lithography for hybrid plastic electronics", *Nano Letters*, vol. 3, pp. 443–445, 2003.
- [127] S. Yoo, S. Chae, H. Jeong, C.-Y. Jang, and H.-H. Park, "Direct patterning of a SiO₂-based diffractive optical element on a lateral-type LED by using nano-imprint technology", *Journal of the Korean Physical Society*, vol. 63, pp. 1740–1745, 2013.
- [128] R. Bruck, P. Muellner, N. Kataeva, A. Koeck, S. Trassl, V. Rinnerbauer, K. Schmidegg, and R. Hainberger, "Flexible thin-film polymer waveguides fabricated in an industrial roll-to-roll process", *Applied Optics*, vol. 52, pp. 4510–4514, 2013.
- [129] S. H. Kim, K.-D. Lee, J.-Y. Kim, M.-K. Kwon, and S.-J. Park, "Fabrication of photonic crystal structures on light emitting diodes by nanoimprint lithography", *Nanotechnology*, vol. 18, p. 055 306, 2007.
- [130] C. Trompoukis, O. El Daif, V. Depauw, I. Gordon, and J. Poortmans, "Photonic assisted light trapping integrated in ultrathin crystalline silicon solar cells by nanoimprint lithography", *Applied Physics Letters*, vol. 101, p. 103 901, 2012.
- [131] C. Ross, "Patterned magnetic recording media", Annual Review of Materials Research, vol. 31, pp. 203–235, 2001.
- [132] H. Schift, "Nanoimprint lithography: An old story in modern times? A review", Journal of Vacuum Science & Technology B: Microelectronics and Nanometer Structures, vol. 26, pp. 458–480, 2008.
- [133] W. Zhou, G. Min, J. Zhang, Y. Liu, J. Wang, Y. Zhang, and F. Sun, "Nanoim-print lithography: A processing technique for nanofabrication advancement", Nano-Micro Letters, vol. 3, pp. 135–140, 2011.
- [134] M. Meier, U. W. Paetzold, M. Prömpers, T. Merdzhanova, R. Carius, and A. Gordijn, "UV nanoimprint for the replication of etched ZnO:Al textures applied in thin-film silicon solar cells", Progress in Photovoltaics: Research and Applications, vol. 22, pp. 1226–1236, 2014.
- [135] U. W. Paetzold, W. Zhang, M. Prömpers, J. Kirchhoff, T. Merdzhanova, S. Michard, R. Carius, A. Gordijn, and M. Meier, "Thin-film silicon solar cell development on imprint-textured glass substrates", *Materials Science and Engineering: B*, vol. 178, pp. 617–622, 2013.

- [136] C. Battaglia, J. Escarré, K. Söderström, L. Erni, L. Ding, G. Bugnon, A. Billet, M. Boccard, L. Barraud, S. De Wolf, F.-J. Haug, M. Despeisse, and C. Ballif, "Nanoimprint Lithography for High-Efficiency Thin-Film Silicon Solar Cells", Nano Letters, vol. 11, pp. 661–665, 2011.
- [137] K. Söderström, J. Escarré, O. Cubero, F.-J. Haug, S. Perregaux, and C. Ballif, "UV-nano-imprint lithography technique for the replication of back reflectors for n-i-p thin film silicon solar cells", *Progress in Photovoltaics: Research and Applications*, vol. 19, pp. 202–210, 2011.
- [138] A. Bessonov, Y. Cho, S.-J. Jung, E.-A. Park, E.-S. Hwang, J.-W. Lee, M. Shin, and S. Lee, "Nanoimprint patterning for tunable light trapping in large-area silicon solar cells", *Solar Energy Materials and Solar Cells*, vol. 95, pp. 2886–2892, 2011.
- [139] W. Soppe, M. Dörenkämper, J.-B. Notta, P. Pex, W. Schipper, and R. Wilde, "Nanoimprint lithography of textures for light trapping in thin film silicon solar cells", *Phys. Status Solidi A*, vol. 210, pp. 707–710, 2013.
- [140] M. Izu and T. Ellison, "Roll-to-roll manufacturing of amorphous silicon alloy solar cells with in situ cell performance diagnostics", Solar Energy Materials and Solar Cells, vol. 78, pp. 613–626, 2003.
- [141] IRENA, "Renewable Energy Cost Analysis Solar Photovoltaics", in *Reports and Papers*, 2012, p. 16.
- [142] M. Izu and S. R. Ovshinsky, "Roll-to-roll plasma deposition machine for the production of tandem amorphous silicon alloy solar cells", *Thin Solid Films*, vol. 119, pp. 55–58, 1984.
- [143] F. R. Jeffrey, G. D. Vernstrom, F. E. Aspen, and R. L. Jacobson, "Fabrication of amorphous silicon devices on plastic substrates", *Materials Research Society Symposium Proceedings*, vol. 49, pp. 41–46, 1985.
- [144] M. Yano, K. Suzuki, K. Nakatani, and H. Okaniwa, "Roll-to-roll preparation of a hydrogenated amorphous silicon solar cell on a polymer film substrate", *Thin Solid Films*, vol. 146, pp. 75–81, 1987.
- [145] G. D. Vernstrom, R. L. Jacobson, R. K. Westerberg, and F. R. Jeffrey, "Continuous-mode fabrication of amorphous silicon solar cells on polyimide substrates", Solar Cells, vol. 21, pp. 141–146, 1987.
- [146] Y. Kishi, H. Inoue, K. Murata, S. Kouzuma, M. Morizane, H. Shibuya, H. Nishiwaki, and Y. Kuwano, "A New Type of Ultralight Flexible a-Si Solar Cell", *Japanese Journal of Applied Physics*, vol. 31, pp. 12–17, 1992.
- [147] P. Pernet, R. Felder, M. Goetz, H. Keppner, D. Fischer, and A. Shah, "Optimization of amorphous silicon solar cells on polymer film substrates", in 14th EC Photovoltaic Solar Energy Conference, 1997, pp. 2339–2342.
- [148] Y. Ichikawa, T. Yoshida, T. Hama, H. Sakai, and K. Harashima, "Production technology for amorphous silicon-based flexible solar cells", Solar Energy Materials and Solar Cells, vol. 66, pp. 107–115, 2001.

- [149] K. Saito, M. Sano, H. Otoshi, A. Sakai, S. Okabe, and K. Ogawa, "High efficiency large area solar cells using microcrystalline silicon", in 3rd World Conference on Photovoltaic Energy Conversion, 2003, pp. 2793–2798.
- [150] A. Takano, M. Uno, M. Tanda, S. Iwasaki, H. Tanaka, J. Yasuda, and T. Kamoshita, "Highly Texturized Silver Electrode Deposition Using Roll-to-Roll Low-Temperature Sputtering Process", *Japanese Journal of Applied Physics*, vol. 43, pp. L277–L279, 2004.
- [151] A. Vijh, X. Yang, W. Du, and X. Deng, "Triple-junction amorphous silicon-based flexible solar minimodule with integrated interconnects", *Solar Energy Materials and Solar Cells*, vol. 90, pp. 2657–2664, 2006.
- [152] C.-H. Yang, C.-Y. Hsueh, D.-J. Yeh, C.-I. Ho, C.-M. Leu, Y.-H. Yeh, and S.-C. Lee, "Hydrogenated Amorphous Silicon Solar Cells on Textured Flexible Substrate Copied From a Textured Glass Substrate Template", *IEEE Electron Device Letters*, vol. 32, pp. 1254–1256, 2011.
- [153] S.-J. Kim, J. Yoo, J. H. Park, S. Ahn, K. Shin, K. H. Yoon, and J.-S. Cho, "Development of flexible silicon thin-film solar cells on nanotextured Ag/Al:Si bilayers", 2013 IEEE 39th Photovoltaic Specialists Conference (PVSC), pp. 0575–0579, 2013.
- [154] M. Foti, C. Tringali, A. Battaglia, N. Sparta, S. Lombardo, and C. Gerardi, "Efficient flexible thin film silicon module on plastics for indoor energy harvesting", Solar Energy Materials and Solar Cells, vol. 130, pp. 490–494, 2014.
- [155] E. Marins, M. Warzecha, S. Michard, J. Hotovy, W. Böttler, P. Alpuim, and F. Finger, "Flexible n-i-p thin film silicon solar cells on polyimide foils with textured ZnO:Ga back reflector", Thin Solid Films, vol. 571, pp. 9–12, 2014.
- [156] S.-F. Leung, L. Gu, Q. Zhang, K.-H. Tsui, J.-M. Shieh, C.-H. Shen, T.-H. Hsiao, C.-H. Hsu, L. Lu, D. Li, Q. Lin, and Z. Fan, "Roll-to-roll fabrication of large scale and regular arrays of three-dimensional nanospikes for high efficiency and flexible photovoltaics.", Scientific Reports, vol. 4, p. 4243, 2014.
- [157] H. Xiao, J. Wang, H. Huang, L. Lu, Q. Lin, Z. Fan, X. Chen, C. Jeong, X. Zhu, and D. Li, "Performance optimization of flexible a-Si:H solar cells with nanotextured plasmonic substrate by tuning the thickness of oxide spacer layer", *Nano Energy*, vol. 11, pp. 78–87, 2015.
- [158] B. Yan, G. Yue, L. Sivec, J. Yang, S. Guha, and C.-S. Jiang, "Innovative dual function nc-SiOx:H layer leading to a >16% efficient multi-junction thin-film silicon solar cell", *Applied Physics Letters*, vol. 99, p. 113512, 2011.
- [159] J. Ma, J. Ni, J. Zhang, Q. Liu, G. Hou, X. Chen, X. Zhang, X. Geng, and Y. Zhao, "The influence of perpendicular transport behavior on the properties of n-i-p type amorphous silicon solar cells", Solar Energy Materials and Solar Cells, vol. 120, pp. 635–641, 2014.
- [160] S. Y. Myong, L. S. Jeon, and S. W. Kwon, "Superstrate type flexible thin-film Si solar cells using flexible glass substrates", *Thin Solid Films*, vol. 550, pp. 705–709, 2014.

- [161] A. Vicente, H. Águas, T. Mateus, A. Araújo, A. Lyubchyk, S. Siitonen, E. Fortunato, and R. Martins, "Solar cells for self-sustainable intelligent packaging", *Journal of Materials Chemistry A*, vol. 3, pp. 13226–13236, 2015.
- [162] S. Fakirov, F. J. Balta Calleja, and M. Krumova, "On the relationship between microhardness and glass transition temperature of some amorphous polymers", Journal of Polymer Science Part B: Polymer Physics, vol. 37, pp. 1413–1419, 1999.
- [163] W. A. MacDonald, M. K. Looney, D. MacKerron, R. Eveson, R. Adam, K. Hashimoto, and K. Rakos, "Latest advances in substrates for flexible electronics", *Journal of the Society for Information Display*, vol. 15, pp. 1075–1083, 2007.
- [164] R. E. I. Schropp, H. Meiling, C. H. M. van der Werf, E. Middelman, E. van Andel, P. M. G. M. Peters, L. V. de Jonge-Meschaninova, J. Winkeler, R. J. Severens, G. J. Jongerden, M. Zeman, M. C. M. van de Sanden, A. Kuipers, C. I. M. A. Spechaninova, J. Winkeler, R. J. Severens, G. J. Jongerden, M. Zeman, and C. I. M. A. Spee, "Novel superstrate process for textured SnO2:F pin amorphous silicon solar cells suitable for roll-to-roll deposition", in 2nd World Conference and Exhibition on Photovoltaic Solar Energy Conversion, Vienna, Austria, 1998, p. 820.
- [165] M. van den Donker, A. Gordijn, H. Stiebig, F. Finger, B. Rech, B. Stannowski, R. Bartl, E. Hamers, R. Schlatmann, and G. Jongerden, "Flexible amorphous and microcrystalline silicon tandem solar modules in the temporary superstrate concept", Solar Energy Materials and Solar Cells, vol. 91, pp. 572–580, 2007.
- [166] J. K. Rath, M. Brinza, Y. Liu, A. Borreman, and R. E. I. Schropp, "Fabrication of thin film silicon solar cells on plastic substrate by very high frequency PECVD", Solar Energy Materials and Solar Cells, vol. 94, pp. 1534–1541, 2010.
- [167] H. Mase, M. Kondo, and A. Matsuda, "Microcrystalline silicon solar cells fabricated on polymer substrate", Solar Energy Materials and Solar Cells, vol. 74, pp. 547– 552, 2002.
- [168] J. K. Rath, Y. Liu, M. M. de Jong, J. de Wild, J. A. Schuttauf, M. Brinza, and R. E. I. Schropp, "Transparent conducting oxide layers for thin film silicon solar cells", *Thin Solid Films*, vol. 518, e129–e135, 2010.
- [169] W. J. Dong, C. J. Yoo, H. W. Cho, K.-B. Kim, M. Kim, and J.-L. Lee, "Flexible a-Si:H Solar Cells with Spontaneously Formed Parabolic Nanostructures on a Hexagonal-Pyramid Reflector", Small, vol. 11, pp. 1947–1953, 2015.
- [170] F.-J. Haug, T. Söderström, M. Python, V. Terrazzoni-Daudrix, X. Niquille, and C. Ballif, "Development of micromorph tandem solar cells on flexible low-cost plastic substrates", *Solar Energy Materials and Solar Cells*, vol. 93, pp. 884–887, 2009.
- [171] V. Terrazzoni-Daudrix, F.-J. Haug, T. Söderström, C. Ballif, D. Fischer, W. Soppe, J. Bertomeu, M. Fahland, H. Schlemm, M. Grimm, M. Topic, and M. Wutz, "Final results of the european project FLEXCELLENCE Roll-to-roll technology for the production of high efficiency low cost thin film solar cells", 24th European Photovoltaic Solar Energy Conference, pp. 2831–2834, 2009.

- [172] T. Söderström, F.-J. Haug, V. Terrazzoni-Daudrix, and C. Ballif, "Flexible micromorph tandem a-Si/ μ c-Si solar cells", *Journal of Applied Physics*, vol. 107, p. 014 507, 2010.
- [173] Y. Ishikawa and M. B. Schubert, "Flexible Protocrystalline Silicon Solar Cells with Amorphous Buffer Layer", *Japanese Journal of Applied Physics*, vol. 45, pp. 6812–6822, 2006.
- [174] A. Lambertz, C. Roß, H. Siekmann, G. Stollwerk, and F. Finger, "Thin film silicon solar cells on transparent and flexible plastic films", in *Proceedings of 21st European Photovoltaic Solar Energy Conference*, Dresden, 2006, pp. 1771–1774.
- [175] E. Fathi, "Thin Film Solar Cells on Transparent Plastic Foils", PhD Thesis, University of Waterloo, 2011.
- [176] E. S. M. V. Pinto, "Thin-film silicon solar cells and sensors deposited on flexible substrates", PhD Thesis, Universidade do Minho, 2014.
- [177] Y. Vygranenko, A. Khosropour, R. Yang, A. Sazonov, A. Kosarev, A. Abramov, and E. Terukov, "Lightweight amorphous silicon photovoltaic modules on flexible plastic substrate", *Canadian Journal of Physics*, vol. 92, pp. 871–874, 2014.
- [178] M. M. De Jong, J. K. Rath, R. E. I. Schropp, P. J. Sonneveld, G. L. A. M. Swinkels, H. J. Holterman, J. Baggerman, C. J. M. V. Rijn, and E. A. G. Hamers, "A novel structured plastic substrate for light con fi nement in thin fi lm silicon solar cells by a geometric optical effect", *Journal of Non-Crystalline Solids*, vol. 358, pp. 2308– 2312, 2012.
- [179] M. M. de Jong, "Light Trapping in Thin Film Silicon Solar Cells on Plastic Substrates", PhD Thesis, Utrecht University, 2013.
- [180] S. Y. Michard, "Entwicklung und Herstellung von Siliziumschichten und Schichtsystemen zur Applikation in Dünnfilm-Solarzellen durch Einsatz eines innovativen Clustertool Depositionssystems", Diploma Thesis, RWTH Aachen University, 2011.
- [181] S. Y. Michard, "Relation between growth rate, material quality, and device grade condition for intrinsic microcrystalline silicon", PhD Thesis, RWTH Aachen University, 2015.
- [182] B. Bayindirli, "In-situ temperature measurements in CVD processes for silicon thin-film solar cells", Master Thesis, Aachen University of Applied Sciences, 2013.
- [183] G. C. E. Jost, "Analyse der Lichtstreuung zur Textur-Optimierung von Zinkoxid-Frontkontakten für Silizium-Dünnschichtsolarzellen", PhD Thesis, RWTH Aachen University, 2013.
- [184] U. W. Paetzold, "Light Trapping with Plasmonic Back Contacts in Thin-Film Silicon Solar Cells", PhD thesis, RWTH Aachen University, 2013.
- [185] S. A. Jabarin and E. A. Lofgren, "Effects of water absorption on physical properties and degree of molecular orientation of poly(ethylene terephthalate)", *Polymer Engineering and Science*, vol. 26, pp. 620–625, 1986.

- [186] J. Löffler, A. Gordijn, R. L. Stolk, H. Li, J. K. Rath, and R. E. I. Schropp, "Amorphous and 'micromorph' silicon tandem cells with high open-circuit voltage", Solar Energy Materials and Solar Cells, vol. 87, pp. 251–259, 2005.
- [187] R. Swanepoel, "Determination of the thickness and optical constants of amorphous silicon", Journal of Physics E: Scientific Instruments, vol. 16, pp. 1214–1222, 1983.
- [188] H. L. Hartnagel, A. L. Dawar, A. K. Jain, and C. Jagdish, *Semiconducting Transparent Thin Films*. Bristol: Institute of Physics Publishing, 1995.
- [189] L. J. van der Pauw, "A method of measuring specific resistivity and Hall effect of discs of arbitrary shape", *Philips Research Reports*, vol. 13, pp. 1–9, 1958.
- [190] M. Berginski, "Lichtstreuende Oberflächen, Schichten und Schichtsysteme zur Verbesserung der Lichteinkopplung in Silizium Dünnschichtsolarzellen", PhD Thesis, RWTH Aachen University, 2007.
- [191] D. Nečas and P. Klapetek, "Gwyddion: an open-source software for SPM data analysis", Central European Journal of Physics, vol. 10, pp. 181–188, 1 2012.
- [192] L. Zanzig, "Einsatz alternativer Depositionmethoden zur Herstellung von Silizium-legierungen", PhD Thesis, Technische Universität Berlin, 1995.
- [193] M. H. Brodsky, M. Cardona, and J. J. Cuomo, "Infrared and Raman spectra of the silicon-hydrogen bonds in amorphous silicon prepared by glow discharge and sputtering", *Physical Review B*, vol. 16, pp. 3556–3571, 1977.
- [194] G. Lucovsky, R. J. Nemanich, and J. C. Knights, "Structural interpretation of the vibrational spectra of a-Si:H alloys", *Physical Review B*, vol. 19, pp. 2064–2073, 1979.
- [195] H. Wieder, M. Cardona, and C. R. Guarnieri, "Vibrational spectrum of hydrogenated amorphous Si-C films", *Phys. Status Solidi B*, vol. 92, pp. 99–112, 1979.
- [196] H. Wagner and W. Beyer, "Reinterpretation of the silicon-hydrogen stretch frequencies in amorphous silicon", Solid State Communications, vol. 48, pp. 585–587, 1983.
- [197] F. Demichelis, C. F. Pirri, E. Tresso, G. Della Mea, V. Rigato, and P. Rava, "Physical properties of undoped and doped hydrogenated amorphous silicon carbide", Semiconductor Science and Technology, vol. 6, pp. 1141–1146, 1991.
- [198] A. A. Langford, M. L. Fleet, B. P. Nelson, W. A. Lanford, and N. Maley, "Infrared absorption strength and hydrogen content of hydrogenated amorphous silicon", Physical Review B, vol. 45, pp. 13367–13377, 1992.
- [199] P. John, I. M. Odeh, M. J. K. Thomas, M. J. Tricker, and J. I. B. Wilson, "Studies of the Oscillator Strengths of Infrared Vibrational Modes in Glow-Discharge Hydrogenated Amorphous Silicon", *Phys. Status Solidi B*, vol. 104, pp. 607–612, 1981.
- [200] N. Maley, A. Myers, M. Pinarbasi, D. Leet, J. R. Abelson, and J. A. Thornton, "Infrared absorption and thermal evolution study of hydrogen bonding in a-SiH", Journal of Vacuum Science & Technology A: Vacuum, Surfaces, and Films, vol. 7, pp. 1267–1270, 1989.

- [201] W. Beyer and M. S. Abo Ghazala, "Absorption strengths of Si-H vibrational modes in hydrogenated silicon", vol. 507, 1998, pp. 601–606.
- [202] N. Maley and I. Szafranek, "Systematic Errors in the Analysis of the Infrared Transmission Data Of Hydrogenated Amorphous Silicon", MRS Proceedings, vol. 192, pp. 663–668, 1990.
- [203] K. F. Feenstra, R. E. I. Schropp, and W. F. van der Weg, "Deposition of amorphous silicon films by hot-wire chemical vapor deposition", *Journal of Applied Physics*, vol. 85, pp. 6843–6852, 1999.
- [204] L. Houben, "Plasmaabscheidung von mikrokristallinem Silizium: Merkmale und Mikrostruktur und deren Deutung im Sinne von Wachstumsvorgängen", PhD thesis, Heinrich-Heine-Universität Düsseldorf, 1998.
- [205] R. Tsu, J. Gonzalez-Hernandez, J. Doehler, and S. Ovshinsky, "Order parameters in a-Si systems", *Solid State Communications*, vol. 46, pp. 79–82, 1983.
- [206] S. Muthmann, F. Köhler, R. Carius, and A. Gordijn, "Structural order on different length scales in amorphous silicon investigated by Raman spectroscopy", *Phys. Status Solidi A*, vol. 207, pp. 544–547, 2010.
- [207] F. Köhler, "Zur Mikrostruktur siliziumbasierter Dünnschichten für die Photovoltaik", PhD Thesis, RWTH Aachen University, 2012.
- [208] V. Smirnov, S. Reynolds, F. Finger, R. Carius, and C. Main, "Metastable effects in silicon thin films: Atmospheric adsorption and light-induced degradation", *Journal* of Non-Crystalline Solids, vol. 352, pp. 1075–1078, 2006.
- [209] D. Ritter, E. Zeldov, and K. Weiser, "Steady-state photocarrier grating technique for diffusion length measurement in photoconductive insulators", Applied Physics Letters, vol. 49, pp. 791–793, 1986.
- [210] R. Brüggemann, "Steady-state photocarrier grating technique for the minority-carrier characterisation of thin-film semiconductors", *Journal of Physics: Conference Series*, vol. 253, p. 012 081, 2010.
- [211] M. Günes, H. Cansever, G. Yilmaz, M. H. Sagban, V. Smirnov, F. Finger, and R. Brüggemann, "Investigation of meta- and in-stability effects in hydrogenated microcrystalline silicon thin films by the steady-state measurement methods", Canadian Journal of Physics, vol. 92, pp. 763–767, 2014.
- [212] F. Einsele, "Amorphe Siliziumoxidschichten zur Oberflächenpassivierung und Kontaktierung von Heterostruktur-Solarzellen aus amorphem und kristallinem Silizium", PhD Thesis, Rheinisch-Westfälische Technische Hochschule Aachen, 2010.
- [213] J. S. M. Vaněček J. Kočka and A. Třiska, "Direct measurement of the gap states and band tail absorption by constant photocurrent method in amorphous-silicon", Solid State Communications, vol. 39, pp. 1199–1202, 1981.
- [214] N. Wyrsch, F. Finger, T. J. McMahon, and M. Vanecek, "How to reach more precise interpretation of subgap absorption spectra in terms of deep defect density in a-Si:H", *Journal of Non-Crystalline Solids*, vol. 137-138, pp. 347–350, 1991.

- [215] A. Luque and S. Hegedus, Eds., Handbook of photovoltaic science and engineering. Chichester, UK: John Wiley & Sons, Ltd, 2003.
- [216] W. Reetz, H. Stiebig, T. Brammer, B. Rech, and J. Fölsch, "Spectral responce of stacked solar cells based on a-Si:H", in *Proceedings of the 2nd ISEC-Europe Solar Congress*, 1999, V.1.5–1.
- [217] W. Reetz, T. Kirchartz, A. Lambertz, J. Hüpkes, and A. Gerber, "Current-Voltage and Spectral Response Based Characterization of Thin Film Silicon Solar Cells Investigation of Primary Error Sources", 24th European Photovoltaic Solar Energy Conference, pp. 2784–2788, 2009.
- [218] A. V. Shah, F. Sculati-Meillaud, Z. J. Bernyi, O. M. Ghahfarokhi, and R. Kumar, "Diagnostics of thin-film silicon solar cells and solar panels/modules with variable intensity measurements (VIM)", Solar Energy Materials and Solar Cells, vol. 95, pp. 398–403, 2011.
- [219] F. Sculati-Meillaud, "Microcrystalline silicon solar cells: Theory, diagnosis and stability", PhD Thesis, Université de Neuchâtel, 2006.
- [220] M. Stückelberger, A. Shah, J. Krc, M. Despeisse, F. Meillaud, and C. Ballif, "Internal electric field and fill factor of amorphous silicon solar cells", *Photovoltaic Specialists Conference (PVSC)*, 2010 35th IEEE, pp. 1569–1574, 2010.
- [221] J. Merten, J. M. Asensi, C. Voz, A. V. Shah, R. Platz, and J. Andreu, "Improved equivalent circuit and analytical model for amorphous silicon solar cells and modules", *IEEE Transactions on Electron Devices*, vol. 45, pp. 423–429, 1998.
- [222] P. van der Heide, Secondary Ion Mass Spectrometry: An Introduction to Principles and Practices. Hoboken, NJ: John Wiley & Sons, 2014.
- [223] V. Balmes, "Entwicklung und Herstellung von unter Einsatz eines PECVD-Cluster-tool-Depositionssystems", Diploma Thesis, RWTH Aachen University, 2013.
- [224] K. Wilken, V. Smirnov, O. Astakhov, and F. Finger, "Thin-film silicon solar cells fabricated at low temperature: A versatile technology for application on transparent flexible plastic substrates and in integrated photoelectrochemical water splitting modules", in 2014 IEEE 40th Photovoltaic Specialist Conference (PVSC), IEEE, 2014, pp. 3051–3054.
- [225] B. Yan, L. Zhao, B. Zhao, J. Chen, H. Diao, G. Wang, Y. Mao, and W. Wang, "Wide bandgap p-type window layer prepared by trimethylboron doping at high temperature for a-Si:H superstrate solar cell", *Journal of Non-Crystalline Solids*, vol. 358, pp. 3243–3247, 2012.
- [226] J. M. Essick, F. Pool, and Y. Shing, "Deposition temperature dependence of the deep defect density for a-Si:H films grown by electron cyclotron resonance microwave plasma", *Journal of Vacuum Science & Technology A: Vacuum, Surfaces, and Films*, vol. 10, pp. 521–524, 1992.
- [227] S. Wang, V. Smirnov, T. Chen, X. Zhang, S. Xiong, Y. Zhao, and F. Finger, "Tuning of the open-circuit voltage by wide band-gap absorber and doped layers in thin film silicon solar cells", *Phys. Status Solidi RRL*, vol. 9, pp. 453–456, 2015.

- [228] Y. Tawada, K. Tsuge, M. Kondo, H. Okamoto, and Y. Hamakawa, "Properties and structure of a-SiC:H for high-efficiency a-Si solar cell", *Journal of Applied Physics*, vol. 53, p. 5273, 1982.
- [229] A. Hadjadj, P. St'ahel, P. Roca i Cabarrocas, V. Paret, Y. Bounouh, and J. C. Martin, "Optimum doping level in a-Si:H and a-SiC:H materials", *Journal of Applied Physics*, vol. 83, pp. 830–836, 1998.
- [230] A. Lloret, Z. Y. Wu, M. L. Théye, I. El Zawawi, J. M. Siéfert, and B. Equer, "Hydrogenated amorphous silicon p-doping with diborane, trimethylboron and trimethylgallium", Applied Physics A, vol. 55, pp. 573–581, 1992.
- [231] F. Demichelis, F. Giorgis, and C. F. Pirri, "Effects of hydrogen dilution of silane/me-thane gas mixtures on growth and structure of a-Si_(1-x)C_(x):H alloys", Solid State Communications, vol. 96, pp. 17–21, 1995.
- [232] W. Beyer and B. Hoheisel, "Photoconductivity and dark conductivity of hydrogenated amorphous silicon", Solid State Communications, vol. 47, pp. 573–576, 1983.
- [233] G. D. Cody, T. Tiedje, B. Abeles, B. Brooks, and Y. Goldstein, "Disorder and the Optical-Absorption Edge of Hydrogenated Amorphous Silicon", *Physical Review Letters*, vol. 47, pp. 1480–1483, 1981.
- [234] N. Maley and J. S. Lannin, "Influence of hydrogen on vibrational and optical properties of a-Si_{1-x}H $_x$ alloys", *Physical Review B*, vol. 36, pp. 1146–1152, 1987.
- [235] A. H. Mahan, J. Carapella, B. P. Nelson, R. S. Crandall, and I. Balberg, "Deposition of device quality, low H content amorphous silicon", *Journal of Applied Physics*, vol. 69, pp. 6728–6730, 1991.
- [236] S. K. O'Leary, S. Zukotynski, and J. M. Perz, "Disorder and optical absorption in amorphous silicon and amorphous germanium", *Journal of Non-Crystalline Solids*, vol. 210, pp. 249–253, 1997.
- [237] A. H. M. Smets, M. A. Wank, B. Vet, M. Fischer, R. A. C. M. M. van Swaaij, M. Zeman, D. C. Bobela, C. R. Wronski, and M. C. M. van de Sanden, "The relation between the band gap and the anisotropic nature of hydrogenated amorphous silicon", *IEEE Journal of Photovoltaics*, vol. 2, pp. 94–98, 2012.
- [238] F. Köhler, T. Zimmermann, S. Muthmann, A. Gordijn, and R. Carius, "Structural Order and Staebler-Wronski Effect in Hydrogenated Amorphous Silicon Films and Solar Cells", *IEEE Journal of Photovoltaics*, vol. 4, pp. 4–9, 2014.
- [239] O. Astakhov, V. Smirnov, R. Carius, B. Pieters, Y. Petrusenko, V. Borysenko, and F. Finger, "Relationship between absorber layer defect density and performance of a-Si:H and μ c-Si:H solar cells studied over a wide range of defect densities generated by 2 MeV electron bombardment", Solar Energy Materials and Solar Cells, vol. 129, pp. 17–31, 2014.
- [240] S. Wang, V. Smirnov, T. Chen, B. Holländer, X. Zhang, S. Xiong, Y. Zhao, and F. Finger, "Effects of oxygen incorporation in solar cells with a-SiOx:H absorber layer", *Japanese Journal of Applied Physics*, vol. 54, p. 011 401, 2015.

- [241] Y. Mai, S. Klein, R. Carius, H. Stiebig, X. Geng, and F. Finger, "Open circuit voltage improvement of high-deposition-rate microcrystalline silicon solar cells by hot wire interface layers", *Applied Physics Letters*, vol. 87, p. 073 503, 2005.
- [242] J. K. Rath, "Low temperature polycrystalline silicon: a review on deposition, physical properties and solar cell applications", *Solar Energy Materials and Solar Cells*, vol. 76, pp. 431–487, 2003.
- [243] P. Roca i Cabarrocas, N. Layadi, T. Heitz, B. Drévillon, and I. Solomon, "Substrate selectivity in the formation of microcrystalline silicon: Mechanisms and technological consequences", *Applied Physics Letters*, vol. 66, pp. 3609–3611, 1995.
- [244] Y. Nasuno, M. Kondo, and A. Matsuda, "Effects of Substrate Surface Morphology on Microcrystalline Silicon Solar Cells", *Japanese Journal of Applied Physics*, vol. 40, pp. L303–L305, 2001.
- [245] O. Vetterl, M. Hülsbeck, J. Wolff, R. Carius, and F. Finger, "Preparation of microcrystalline silicon seed-layers with defined structural properties", *Thin Solid Films*, vol. 427, pp. 46–50, 2003.
- [246] T. Fujibayashi and M. Kondo, "Roles of microcrystalline silicon p layer as seed, window, and doping layers for microcrystalline silicon p-i-n solar cells", *Journal of Applied Physics*, vol. 99, p. 043703, 2006.
- [247] S. Reynolds, R. Carius, F. Finger, and V. Smirnov, "Correlation of structural and optoelectronic properties of thin film silicon prepared at the transition from microcrystalline to amorphous growth", *Thin Solid Films*, vol. 517, pp. 6392–6395, 2009.
- [248] M. Python, D. Dominé, T. Söderström, F. Meillaud, and C. Ballif, "Microcrystalline silicon solar cells: effect of substrate temperature on cracks and their role in postoxidation", Progress in Photovoltaics: Research and Applications, vol. 18, pp. 491– 499, 2010.
- [249] M. Kondo, Y. Nasuno, H. Mase, T. Wada, and A. Matsuda, "Low-temperature fabrication of microcrystalline silicon and its application to solar cells", *Journal of Non-Crystalline Solids*, vol. 299-302, pp. 108-112, 2002.
- [250] Y. Nasuno, M. Kondo, and A. Matsuda, "Microcrystalline silicon thin-film solar cells prepared at low temperature using RF-PECVD", in *Conference Records of the Twenty-Eighth IEEE Photovoltaic Specialists Conference*, IEEE, 2000, pp. 142–145.
- [251] T. Fink, S. Muthmann, and M. Meier, "Highly controlled microcrystalline silicon growth using in-situ Raman spectroscopy", in 2015 IEEE 42nd Photovoltaic Specialists Conference (PVSC), New Orleans, LA: IEEE, 2015, pp. 1–3.
- [252] L. Gui-Jun, H. Guo-Fu, H. Xiao-Yan, Y. Yu-Jie, W. Chang-Chun, S. Jian, Z. Yin, and G. Xin-Hua, "The study of a new n/p tunnel recombination junction and its application in a-Si:H/μc-Si:H tandem solar cells", Chinese Physics B, vol. 18, pp. 1674–1678, 2009.

- [253] C. Ulbrich, C. Zahren, A. Gerber, B. Blank, T. Merdzhanova, A. Gordijn, and U. Rau, "Matching of Silicon Thin-Film Tandem Solar Cells for Maximum Power Output", *International Journal of Photoenergy*, vol. 2013, pp. 1–7, 2013.
- [254] S. Reynolds and V. Smirnov, "Modelling Performance of Two- And Four-terminal Thin-film Silicon Tandem Solar Cells under Varying Spectral Conditions", *Energy Procedia*, vol. 84, pp. 251–260, 2015.
- [255] T. Fink, S. Muthmann, A. Mück, A. Gordijn, R. Carius, and M. Meier, "Interplay between crystallinity profiles and the performance of microcrystalline thin-film silicon solar cells studied by in-situ Raman spectroscopy", *Journal of Applied Physics*, vol. 118, p. 215 304, 2015.
- [256] K. Wilken, F. Finger, and V. Smirnov, "Annealing effects in low temperature amorphous silicon flexible solar cells", *Energy Procedia*, vol. 84, pp. 17–24, 2015.
- [257] J. Kočka, C. E. Nebel, and C. D. Abel, "Solution of the $\mu\tau$ problem in a-Si:H", Philosophical Magazine Part B, vol. 63, pp. 221–246, 1991.
- [258] E. Morgado, "Influence of light-soaking and annealing on electron and hole mobility-lifetime products in a-Si:H", *Journal of Non-Crystalline Solids*, vol. 338-340, pp. 386–389, 2004.
- [259] J. Kočka, M. Vaněček, and A. Tříska, "Energy and Density of Gap States in a-Si:H", in Amorphous silicon and related materials, H. Fritzsche, Ed., World Scientific Publishing Company, 1988, pp. 297–327.
- [260] M. Hack and M. Shur, "Physics of amorphous silicon alloy p-i-n solar cells", Journal of Applied Physics, vol. 58, pp. 997–1020, 1985.
- [261] F. Meillaud, E. Vallat-Sauvain, X. Niquille, M. Dubey, J. Bailat, A. Shah, and C. Ballif, "Light-induced degradation of thin film amorphous and microcrystalline silicon solar cells", in *Conference Record of the Thirty-first IEEE Photovoltaic Specialists Conference*, 2005., IEEE, 2005, pp. 1412–1415.
- [262] V. Smirnov, O. Astakhov, R. Carius, B. E. Pieters, Y. Petrusenko, V. Borysenko, and F. Finger, "Performance of p- and n-side illuminated microcrystalline silicon solar cells following 2 MeV electron bombardment", *Applied Physics Letters*, vol. 101, p. 143 903, 2012.
- [263] Q. Wang, "Fill factor related issues in hydrogenated amorphous Si solar cells", Solar Energy Materials and Solar Cells, vol. 129, pp. 64–69, 2014.
- [264] P. Štulík and J. Singh, "A simple method to simulate the influence of defects on the short circuit current in amorphous silicon solar cells", *Journal of Non-Crystalline* Solids, vol. 226, pp. 299–303, 1998.
- [265] J. D. Santos, S. Fernández, J. Cárabe, and J. J. Gandía, "Cause of the fill factor loss of a-Si:H p-i-n devices with ZnO:Al front electrode: Blocking contact vs. defect density", Thin Solid Films, vol. 548, pp. 617–622, 2013.
- [266] C. R. Wronski and X. Niu, "The Limited Relevance of SWE Dangling Bonds to Degradation in High-Quality a-Si:H Solar Cells", *IEEE Journal of Photovoltaics*, vol. 4, pp. 778–784, 2014.

- [267] O. Astakhov, R. Carius, F. Finger, Y. Petrusenko, V. Borysenko, and D. Barankov, "Relationship between defect density and charge carrier transport in amorphous and microcrystalline silicon", *Physical Review B*, vol. 79, p. 104 205, 2009.
- [268] S. Wang et al., unpublished, IEK-5 Photovoltaik, Forschungszentrum Jülich GmbH, 2016.
- [269] P. J. McElheny, J. K. Arch, H.-S. Lin, and S. J. Fonash, "Range of validity of the surface-photovoltage diffusion length measurement: A computer simulation", *Journal of Applied Physics*, vol. 64, pp. 1254–1265, 1988.
- [270] Y. Liu, Y. Sun, and A. Rockett, "A new simulation software of solar cells wx-amps", Solar Energy Materials and Solar Cells, vol. 98, pp. 124–128, 2012.
- [271] R. A. Street and K. Winer, "Defect equilibria in undoped a -Si:H", *Physical Review B*, vol. 40, pp. 6236–6249, 1989.
- [272] E. A. Schiff, "Drift-mobility measurements and mobility edges in disordered silicons", *Journal of Physics: Condensed Matter*, vol. 16, S5265–S5275, 2004.
- [273] M. Isomura, T. Kinoshita, Y. Hishikawa, and S. Tsuda, "Influence of oxygen impurity in the intrinsic layer of amorphous silicon solar cells", *Applied Physics Letters*, vol. 65, pp. 2329–2331, 1994.
- [274] T. Shimizu, T. Ishii, M. Kumeda, and A. Masuda, "Structural and conductivity change caused by N, O and C incorporation in a-Si:H", *Journal of Non-Crystalline Solids*, vol. 227-230, pp. 403–406, 1998.
- [275] J. Fahlteich, M. Fahland, W. Schönberger, and N. Schiller, "Permeation barrier properties of thin oxide films on flexible polymer substrates", *Thin Solid Films*, vol. 517, pp. 3075–3080, 2009.
- [276] K. Sato, Y. Gotoh, Y. Wakayama, Y. Hayashi, K. Adachi, and H. Nishimura, "Highly textured SnO₂:F TCO films for a-Si solar cells", *Rep. Res. Lab. Asahi Glass Co. Ltd.*, vol. 42, p. 129, 1992.
- [277] H.-L. Ma, X.-T. Hao, J. Ma, Y.-G. Yang, J. Huang, D.-H. Zhang, and X.-G. Xu, "Thickness dependence of properties of SnO₂:Sb films deposited on flexible substrates", *Applied Surface Science*, vol. 191, pp. 313–318, 2002.
- [278] J. Escarré, J. Bertomeu, J. M. Asensi, J. Andreu, V. Terrazzoni-Daudrix, F. J. Haug, and X. Niquille, "Hot Embossing of Polymer Substrates for Thin Silicon Cell Applications", in 2006 IEEE 4th World Conference on Photovoltaic Energy Conference, IEEE, 2006, pp. 1556–1559.
- [279] M. C. R. Heijna, M. J. A. A. Goris, W. J. Soppe, W. Schipper, and R. Wilde, "Roll-to-roll nanotexturisation of layers on steel soil substrates for nip silicon solar cells", in 25th Eur. Photovolt. Sol. Energy Conf. Exhib. 5th World Conf. Photovolt. Energy Convers., WIP Renewable Energies, 2010, pp. 3090–3093.
- [280] J. I. Owen, S. E. Pust, E. Bunte, and J. Hüpkes, "ZnO Etch-Feature Control via Concentration and Temperature of Various Acids", ECS Journal of Solid State Science and Technology, vol. 1, P11–P17, 2012.

- [281] W. Böttler, V. Smirnov, J. Hüpkes, and F. Finger, "Variation of back reflector morphology in n-i-p microcrystalline silicon thin film solar cells using texture-etched ZnO", *Journal of Non-Crystalline Solids*, vol. 358, pp. 2474–2477, 2012.
- [282] K. Wilken, U. W. Paetzold, M. Meier, G. M. Ablayev, E. I. Terukov, N. Prager, M. Fahland, F. Finger, and V. Smirnov, "Light management in flexible thin-film solar cells on transparent plastic substrates", *Phys. Status Solidi A*, vol. 213, pp. 1955–1963, 2016.
- [283] C. Agashe, O. Kluth, J. Hüpkes, U. Zastrow, and B. Rech, "Efforts to improve carrier mobility in radio frequency sputtered aluminum doped zinc oxide films", *Journal of Applied Physics*, vol. 95, pp. 1911–1917, 2004.
- [284] H. Schade, P. Lechner, R. Geyer, H. Stiebig, B. Rech, and O. Kluth, "Texture properties of TCO uniquely determining light trapping in thin-film silicon solar cells", in *Conference Record of the IEEE Photovoltaic Specialists Conference*, 2005, pp. 1436–1439.
- [285] H. Stiebig, M. Schulte, C. Zahren, C. Haase, B. Rech, and P. Lechner, "Light trapping in thin-film silicon solar cells by nano-textured interfaces", in *Proc. SPIE*, vol. 6197, 2006, p. 619701.
- [286] T. Söderström, "Single and multi-junction thin film silicon solar cells for flexible photovoltaics", PhD Thesis, Université de Neuchâtel, 2009.
- [287] B. Rech and H. Wagner, "Potential of amorphous silicon for solar cells", Applied Physics A: Materials Science & Processing, vol. 69, pp. 155–167, 1999.
- [288] J. C. Lee, V. Dutta, J. Yoo, J. Yi, J. Song, and K. H. Yoon, "Superstrate p-i-n a-Si:H solar cells on textured ZnO:Al front transparent conduction oxide", *Superlattices and Microstructures*, vol. 42, pp. 369–374, 2007.
- [289] J. K. Rath and R. E. I. Schropp, "Incorporation of p-type microcrystalline silicon films in amorphous silicon based solar cells in a superstrate structure", *Solar Energy Materials and Solar Cells*, vol. 53, pp. 189–203, 1998.
- [290] H. Stiebig, F. Siebke, W. Beyer, C. Beneking, B. Rech, and H. Wagner, "Interfaces in a-Si: H solar cell structures", Solar Energy Materials and Solar Cells, vol. 48, pp. 351–363, 1997.
- [291] C. Zhang, M. Meier, A. Lambertz, V. Smirnov, B. Holländer, A. Gordijn, and T. Merdzhanova, "Optical and Electrical Effects of p-type μc-SiOx:H in Thin-Film Silicon Solar Cells on Various Front Textures", International Journal of Photoenergy, vol. 2014, p. 176 965, 2014.
- [292] U. Palanchoke, V. Jovanov, H. Kurz, R. Dewan, P. Magnus, H. Stiebig, and D. Knipp, "Influence of back contact roughness on light trapping and plasmonic losses of randomly textured amorphous silicon thin film solar cells", Applied Physics Letters, vol. 102, p. 083 501, 2013.
- [293] F.-J. Haug, T. Söderstroöm, O. Cubero, V. Terrazzoni-Daudrix, and C. Ballif, "Plasmonic absorption in textured silver back reflectors of thin film solar cells", Journal of Applied Physics, vol. 104, p. 064 509, 2008.

- [294] J. Escarré, C. Battaglia, K. Söderström, C. Pahud, R. Biron, O. Cubero, F.-J. Haug, and C. Ballif, "UV imprinting for thin film solar cell application", *Journal of Optics*, vol. 14, p. 024 009, 2012.
- [295] M. A. González Lazo, R. Teuscher, Y. Leterrier, J.-A. E. Månson, C. Calderone, A. Hessler-Wyser, P. Couty, Y. Ziegler, and D. Fischer, "UV-nanoimprint lithography and large area roll-to-roll texturization with hyperbranched polymer nanocomposites for light-trapping applications", Solar Energy Materials and Solar Cells, vol. 103, pp. 147–156, 2012.
- [296] K. Wilken, U. W. Paetzold, M. Meier, N. Prager, M. Fahland, F. Finger, and V. Smirnov, "Nanoimprint texturing of transparent flexible substrates for improved light management in thin-film solar cells", *Phys. Status Solidi RRL*, vol. 9, pp. 215–219, 2015.
- [297] K. Wilken, U. W. Paetzold, M. Meier, M. Smeets, N. Prager, M. Fahland, F. Finger, and V. Smirnov, "Light Management in Flexible Thin-Film Solar Cells The Role of Nanoimprinted Textures and Tilted Surfaces", *IEEE Journal of Photovoltaics*, vol. 5, pp. 1646–1653, 2015.
- [298] W. Böttler, V. Smirnov, A. Lambertz, J. Hüpkes, and F. Finger, "Front and back contacts for microcrystalline silicon solar cells in n-i-p configuration", 25th European Photovoltaic Solar Energy Conference, pp. 3060–3063, 2010.
- [299] N. Sommer, "Conductivity and Structure of Sputtered ZnO:Al on Flat and Textured Substrates for Thin-Film Solar Cells", PhD Thesis, RWTH Aachen University, 2016.
- [300] E. Böhmer, F. Siebke, B. Rech, C. Beneking, and H. Wagner, "More Insights Into the ZnO/a-SiC:H(B) Interface An Improved TCO/p Contact", in *Materials Research Society Symposium Proceedings*, vol. 426, 1996, pp. 519–524.
- [301] M. Smeets, V. Smirnov, K. Bittkau, M. Meier, R. Carius, U. Rau, and U. W. Paetzold, "Angular dependence of light trapping in nanophotonic thin-film solar cells", Optics Express, vol. 23, pp. 1575–1588, 2015.
- [302] J. Hotovy, J. Hüpkes, W. Böttler, E. Marins, L. Spiess, T. Kups, V. Smirnov, I. Hotovy, and J. Kováč, "Sputtered ITO for application in thin-film silicon solar cells: Relationship between structural and electrical properties", Applied Surface Science, vol. 269, pp. 81–87, 2013.
- [303] R. Rößler, "Transparente leitfähige Oxide (TCO) in Silizium-Heterostruktursolarzellen: Elektronische Eigenschaften des TCO/a-Si:H Kontakts", PhD Thesis, Technische Universität Berlin, 2014.
- [304] W. Appenzeller, J. Müller, B. Rech, T. Repmann, G. Schöpe, B. Sehrbrock, and H. Siekmann, "A method for treating substrates with pre-patterned zinc oxide", Patent DE102004017680 B4, 2004.

- [305] P. Maury, D. Turkenburg, N. Stroeks, P. Giesen, I. Barbu, E. Meinders, A. van Bremen, N. Iosad, R. van der Werf, and H. Onvlee, "Roll-to-roll UV imprint lithography for flexible electronics", *Microelectronic Engineering*, vol. 88, pp. 2052–2055, 2011.
- [306] A. Luque and S. Hegedus, Eds., *Handbook of Photovoltaic Science and Engineering*. Chichester, UK: John Wiley & Sons, Ltd, 2011.
- [307] C. Lee, A. Park, Y. Cho, M. Park, W. I. Lee, and H. W. Kim, "Influence of ZnO buffer layer thickness on the electrical and optical properties of indium zinc oxide thin films deposited on PET substrates", Ceramics International, vol. 34, pp. 1093–1096, 2008.
- [308] C. Ulbrich, "Spectral and directional dependence of light-trapping in solar cells", PhD Thesis, RWTH Aachen University, 2011.
- [309] J. L. Balenzategui and F. Chenlo, "Measurement and analysis of angular response of bare and encapsulated silicon solar cells", *Solar Energy Materials and Solar Cells*, vol. 86, pp. 53–83, 2005.
- [310] P. Mialhe, S. Mouhamed, and A. Haydar, "The solar cell output power dependence on the angle of incident radiation", *Renewable Energy*, vol. 1, pp. 519–521, 1991.
- [311] C. Eisele, C. E. Nebel, and M. Stutzmann, "Periodic light coupler gratings in amorphous thin film solar cells", *Journal of Applied Physics*, vol. 89, pp. 7722–7726, 2001.
- [312] G. Dennler, K. Forberich, M. C. Scharber, C. J. Brabec, I. Tomiš, K. Hingerl, and T. Fromherz, "Angle dependence of external and internal quantum efficiencies in bulk-heterojunction organic solar cells", *Journal of Applied Physics*, vol. 102, p. 054 516, 2007.
- [313] W. R. MacCluney, *Introduction to radiometry and photometry*. Boston: Artech House, 1994.
- [314] E. I. Batzelis, P. S. Georgilakis, and S. A. Papathanassiou, "Energy models for photovoltaic systems under partial shading conditions: a comprehensive review", IET Renewable Power Generation, vol. 9, pp. 340–349, 2015.
- [315] C. Konstantopoulos and E. Koutroulis, "Global Maximum Power Point Tracking of Flexible Photovoltaic Modules", *IEEE Transactions on Power Electronics*, vol. 29, pp. 2817–2828, 2014.
- [316] B. Drevillon, S. Kumar, P. Roca i Cabarrocas, and J. M. Siefert, "In situ investigation of the optoelectronic properties of transparent conducting oxide/amorphous silicon interfaces", Applied Physics Letters, vol. 54, p. 2088, 1989.

List of Abbreviations

Common Abbreviations

Acronym Meaning

AFM atomic force microscopy

AM1.5 air mass coefficient with 1.5 path length

APCVD atmospheric pressure chemical vapor deposition

ARS angle resolved scattering

BIPV building integrated photovoltaic

c-Si crystalline silicon

CPM constant photocurrent method CVD chemical vapor deposition

Cz Czochralski DC direct current

DSR differential spectral response

FTIR Fourier transform infrared spectroscopy

HS heater station IR infrared

LED light-emitting diode

LPCVD low-pressure chemical vapor deposition

MC magazine chamber MPP maximum power point NIL nanoimprint lithography

NIR near-infrared PC process chamber

PDS photothermal deflection spectroscopy PECVD plasma enhanced chemical vapor deposition

PH₃ phosphine
PV photovoltaic
RF radio frequency
rpm revolutions per minute

sccm standard cubic centimeters per minute

SE secondary electrons

SEM scanning electron microscopy
SIMS secondary ion mass spectrometry

SSPG steady-state photocarrier grating technique

Acronym Meaning

| SWE | Staebler-Wronski-Effect |
|-----|--------------------------------|
| TC | transfer chamber |
| TCO | transparent conductive oxide |
| TO | transverse optical |
| TRJ | tunnel recombination junction |
| UHV | ultrahigh vacuum |
| UV | ultraviolet |
| VHF | very high frequency |
| VIM | variable intensity measurement |
| VIS | visible |

Formula Abbreviations

| Symbol | Description | Typical Unit |
|---------------------------|---|----------------|
| | | |
| α | absorption coefficient | ${ m cm}^{-1}$ |
| $\alpha_{1.2\mathrm{eV}}$ | sub-gap absorption at 1.2 eV | ${ m cm}^{-1}$ |
| $\alpha_{ m IR}$ | infrared absorption coefficient | ${ m cm}^{-1}$ |
| A | absorptance | - |
| A_{norm} | normalized surface area | - |
| AID | angular intensity distribution | - |
| b | length of contacts in conductivity measurements | mm |
| B | magnetic field | T |
| c_{CH4} | methane concentration | % |
| c_{H} | hydrogen content | % |
| c_{PH3} | phosphine concentration | % |
| c_{TMB} | TMB concentration | % |
| d | layer thickness | nm |
| $d_{ m el}$ | electrode distance | mm |
| E | electrical field | V/m |
| E_{04} | optical gap energy | eV |
| $E_{ m A}$ | activation energy | eV |
| $E_{ m bi}$ | built-in field | V/m |
| $E_{\rm C}$ | conduction band edge energy | eV |
| $E_{ m F}$ | Fermi level | eV |
| $E_{ m g}$ | band gap energy | eV |
| $E_{ m ph}$ | photon energy | eV |

| Symbol | Description | Typical Unit |
|-------------------------|--|-----------------------------|
| $E_{ m V}$ | valence band edge energy | eV |
| EQE | external quantum efficiency | - |
| f | excitation frequency | MHz |
| F | illumination area | $ m cm^2$ |
| FF | fill factor | % |
| γ | incident angle | 0 9 1 |
| G | generation rate | ${\rm cm}^{-3}{\rm s}^{-1}$ |
| η | efficiency | % |
| h | distance between contacts in conductivity measurements | mm |
| H_{T} | haze in transmission | - |
| θ | scattering angle | 0 |
| $	heta_{ m c}$ | angle of total internal reflection | |
| I | current | Α |
| I_{a} | integrated intensity of amorphous phase | - |
| $I_{ m c}$ | integrated intensity of crystalline phase | - |
| $I_{ m crs}$ | crystalline volume fraction | % |
| $I_{ u}$ | integrated absorption peak intensity at ν | cm^{-1} |
| $I_{ m ph}$ | photocurrent | A |
| IQE | internal quantum efficiency | - - 2 |
| J_{I} | current density | mA/cm^2 |
| J_0 | reverse saturation current density | $ m mA/cm^2$ $ m mA/cm^2$ |
| $J_{ m diode}$ | diode current density | mA/cm^2 |
| $J_{ m MPP}$ | current density at MPP photo-generated current density | mA/cm^2 |
| $J_{ m ph} \ J_{ m QE}$ | current density from EQE curve | mA/cm^2 |
| $J_{ m rec}$ | recombination current density | mA/cm^2 |
| $J_{ m SC}$ | short-circuit current density | mA/cm^2 |
| $J_{ m sh}$ | current density through physical shunts | mA/cm^2 |
| k_{2000} | absorption strength to calculate hydrogen content | cm^{-2} |
| λ | wavelength | nm |
| λ_1, λ_2 | wavelength of two neighboring extremes | nm |
| L | solar cell length | cm |
| $L_{\rm amb}$ | ambipolar diffusion length | nm |
| $L_{ m d}$ | drift length | nm |
| μ | charge carrier mobility | ${ m cm^2/Vs}$ |
| $\mu_{ m e/h}$ | mobility of electrons/holes | ${ m cm}^2/{ m Vs}$ |
| $m_{ m e}$ | effective electron mass | kg |
| ν | wave number | cm^{-1} |
| $ u_0$ | peak maximum wave number | ${ m cm^{-1}}$ |
| n | refractive index | - |
| $n_{\rm ideal}$ | ideality factor of a solar cell | - |
| N | charge carrier density | ${\rm cm}^{-3}$ |
| | | |

| Symbol | Description | Typical Unit |
|------------------------------|---|--------------------------|
| N(E) | density of states | ${ m cm^{-3}}$ |
| $N_{\rm d}$ | defect density | ${ m cm}^{-3}$ |
| $N_{ m H}$ | number of hydrogen atoms | ${ m cm^{-3}}$ |
| $N_{ m Si}$ | number of silicon atoms | ${ m cm^{-3}}$ |
| $\omega_{	ext{TO}}$ | peak width of the TO phonon mode | ${ m cm^{-1}}$ |
| p | pressure | mbar |
| P | power | W |
| $P_{ m ill}$ | incident power from illumination | W |
| P_{\max} | maximum power output | W |
| ρ | resistivity | $\Omega \mathrm{cm}$ |
| r | bending radius | mm |
| R | reflectance | - |
| $R_{ m m}$ | microstructure factor | - |
| $R_{\rm SC}$ | short-circuit resistance | $\Omega \mathrm{cm}$ |
| $R_{ m s}$ | series resistance | $\Omega \mathrm{cm}$ |
| $R_{ m sh}$ | shunt resistance | $\Omega \mathrm{cm}$ |
| R_{\square} | sheet resistance | Ω |
| σ | conductivity | S/cm |
| σ_0 | conductivity prefactor | S/cm |
| $\sigma_{ m d}$ | dark conductivity | S/cm |
| $\sigma_{ m ph}$ | photo conductivity | S/cm |
| $\sigma_{ m ill}$ | conductivity measured under illumination | S/cm |
| SC | silane concentration | % |
| au | charge carrier lifetime | S |
| $	au_{ m e/h}$ | lifetime of electrons/holes | S . |
| $	au_{ m R}$ | relaxation time | min |
| $t_{ m ann}$ | annealing time | min |
| $t_{ m depo}$ | deposition time | S |
| $t_{ m etch} \ T$ | etching time | S |
| T_0 | total transmittance | K |
| $T_{ m ann}$ | absolute temperature | °C |
| $T_{ m diff}$ | annealing temperature diffuse transmittance | C |
| $T_{ m E}$ | equilibrium temperature | $^{\circ}\mathrm{C}$ |
| $T_{ m s}$ | substrate temperature | $^{\circ}\mathrm{C}$ |
| Φ | photon flux | $\mathrm{cm^{-2}s^{-1}}$ |
| $\overset{\mathbf{\Psi}}{V}$ | voltage | V |
| $V_{ m bi}$ | built-in voltage | V |
| $V_{ m coll}$ | collection voltage | V |
| $V_{ m H}$ | Hall voltage | V |
| $V_{ m MPP}$ | voltage at MPP | V |
| $V_{ m OC}$ | open-circuit voltage | V |
| 50 | | • |

| Symbol | Description |
|--------|-------------|
|--------|-------------|

Typical Unit

| Ψ | correction factor for electrical field deformation | - |
|-----------------|--|----------------|
| x_{TO} | peak position of the TO phonon mode | ${ m cm^{-1}}$ |

Chemical Symbols

| a-Si:H | hydrogenated amorphous silicon |
|---------|---------------------------------------|
| μc-Si:H | hydrogenated microcrystalline silicon |

 $\begin{array}{ccc} Ag & silver \\ Al & aluminum \\ Al_2O_3 & aluminum \ oxide \end{array}$

Ar argon

 ${\rm CCl_4}$ carbon tetrachloride ${\rm CdTe}$ cadmium telluride

CH₄ methane

CIGS copper indium gallium selenide

 $\begin{array}{ll} Cu & copper \\ F & fluorine \\ H_2 & hydrogen \end{array}$

 $\begin{array}{ll} HCl & hydrochloric acid \\ HF & hydrofluoric acid \\ In_2O_3 & indium oxide \end{array}$

 $\begin{array}{ll} \hbox{IO:H} & \hbox{hydrogen-doped indium oxide} \\ \hbox{ITO} & \hbox{indium tin oxide } \hbox{In}_2\hbox{O}_3\hbox{:SnO}_2 \\ \end{array}$

KOH potassium hydroxide PbS lead(II) sulfide PC polycarbonate

PEDOT:PSS poly(3,4-ethylenedioxythiophene) polystyrene sulfonate

PEN polyethylene naphthalate PET polyethylene terephthalate

PH₃ phosphine PI polyimide

POP polyolefin plastomer

 $\begin{array}{ll} \text{Si} & \text{silicon} \\ \text{SiH}_4 & \text{monosilane} \\ \text{SiO}_2 & \text{silicon dioxide} \\ \text{SiO}_x N_v & \text{silicon oxynitride} \end{array}$

Sn tin

 $\begin{array}{ll} SnO_2\text{:}F & \quad \text{fluorine-doped tin oxide} \\ TMB & \quad \text{trimethylborane } B(CH_3)_3 \\ ZnSnO_x & \quad \text{zinc tin oxide (ZTO)} \end{array}$

ZnO:Al aluminum-doped zinc oxide ZnO:Al $_2$ O $_3$

Constants

e Euler's number 2.71828

 $\begin{array}{lll} h & {\rm Planck\ constant} & 4.135667662(25)\times 10^{-15}\ {\rm eV\ s} \\ k & {\rm Boltzmann\ constant} & 8.6173324(78)\times 10^{-5}\ {\rm eV\ K^{-1}} \\ q & {\rm elementary\ charge} & 1.6021766208(98)\times 10^{-19}\ {\rm C} \\ \end{array}$

 π pi 3.14159

List of Publications

Journal Publications

- <u>K. Wilken</u>, F. Finger, and V. Smirnov, Influence of ZnSnO_x barrier layer on the texturing of ZnO:Al layers for light management in flexible thin-film silicon solar cells, Phys. Status Solidi A, 2017 (accepted)
- C. Hengst, S. B. Menzel, G. K. Rane, V. Smirnov, <u>K. Wilken</u>, B. Leszczynska,
 D. Fischer, and N. Prager, *Mechanical Properties of ZTO, ITO, and a-Si:H Multilayer Films for Flexible Thin Film Solar Cells*, Materials 10, p. 245, 2017, doi: 10.3390/ma10030245
- <u>K. Wilken</u>, V. Smirnov, and F. Finger, Abschlussbericht für das Teilprojekt "Entwicklung von Solarzellen auf flexiblen Substraten" im Verbundprojekt "Entwicklung und Untersuchung der Beschichtung von Folienbändern mit Kontakten, Barrieren und Solarzellen" (FlexSol), Technische Informationsbibliothek Hannover (TIB), 2016
- <u>K. Wilken</u>, U. W. Paetzold, M. Meier, G. Ablayev, E. I. Terukov, N. Prager, M. Fahland, F. Finger, and V. Smirnov, *Light Management in Flexible Thin-Film Solar Cells on Transparent Plastic Substrates*, Phys. Status Solidi A **213**, pp. 1955-1963, 2016, doi: 10.1002/pssa.201532984
- <u>K. Wilken</u>, U. W. Paetzold, M. Meier, M. Smeets, N. Prager, M. Fahland, F. Finger, and V. Smirnov, *Light Management in Flexible Thin-Film Solar Cells The Role of Nanoimprinted Textures and Tilted Surfaces*, IEEE Journal of Photovoltaics **5**, pp. 1646-1653, 2015, doi: 10.1109/JPHOTOV.2015.2470672
- K. Wilken, U. W. Paetzold, M. Meier, N. Prager, M. Fahland, F. Finger, and V. Smirnov, Improved flexible thin-film solar cells with nanoimprinted light management textures, Proceedings of the 2015 IEEE 42nd Photovoltaic Specialists Conference (PVSC), New Orleans, LA, 2015, pp. 1-3, doi: 10.1109/PVSC.2015.7355683
- <u>K. Wilken</u>, F. Finger, V. Smirnov, Annealing Effects in Low Temperature Amorphous Silicon Flexible Solar Cells, Energy Procedia **84**, pp. 17-24, 2015, doi: 10.1016/j.egypro.2015.12.290
- <u>K. Wilken</u>, U. W. Paetzold, M. Meier, N. Prager, M. Fahland, F. Finger, and V. Smirnov, *Nanoimprint texturing of transparent flexible substrates for improved light management in thin-film solar cells*, Phys. Status Solidi RRL **9**, pp. 215-219, 2015, doi: 10.1002/pssr.201510040 (front cover publication)

- F. Urbain, <u>K. Wilken</u>, V. Smirnov, O. Astakhov, A. Lambertz, J.-P. Becker, U. Rau, J. Ziegler, B. Kaiser, W. Jaegermann, and F. Finger, *Development of Thin Film Amorphous Silicon Tandem Junction Based Photocathodes Providing High Open-Circuit Voltages for Hydrogen Production*, International Journal of Photoenergy 2014, p. 249317, 2014, doi: 10.1155/2014/249317
- <u>K. Wilken</u>, V. Smirnov, O. Astakhov, F. Finger, Thin-film silicon solar cells fabricated at low temperature: A versatile technology for application on transparent flexible plastic substrates and in integrated photoelectrochemical water splitting modules, Proceedings of the 2014 IEEE 40th Photovoltaic Specialists Conference (PVSC), Denver, CO, pp. 3051-3054, 2014, doi: 10.1109/PVSC.2014.6925579

Conference Presentations

Oral Presentations

- K. Wilken, F. Finger, <u>V. Smirnov</u>, Influence of ZnSnO_x Barrier Layer on the Texturing of ZnO:Al Layers for Light Management in Flexible Thin-Film Solar Cells, EMRS 2016 Fall Meeting Symposium K on Photonic materials and techniques for SERS and solar cell light trapping, Warsaw, Poland, Sep 2016
- <u>K. Wilken</u>, S. Wang, F. Finger and V. Smirnov, *Annealing effects in low temperature amorphous silicon flexible solar cells*, 32nd European Photovoltaic Solar Energy Conference (EU PVSEC 2016), Munich, Germany, Jun 2016
- <u>K. Wilken</u>, U. W. Paetzold, M. Meier, G. Ablayev, E. I. Terukov, N. Prager, M. Fahland, F. Finger, and V. Smirnov, *Light Management in Flexible Thin-Film Solar Cells on Transparent Plastic Substrates*, 26th International Conference on Amorphous and Nanocrystalline Semiconductors, Aachen, Germany, Sep 2015
- K. Wilken, <u>U. W. Paetzold</u>, M. Meier, N. Prager, M. Fahland, F. Finger, and V. Smirnov, *Improved flexible thin-film solar cells with nanoimprinted light management textures*, 2015 IEEE 42nd Photovoltaic Specialists Conference (PVSC-25), New Orleans, USA, Jun 2015
- K. Wilken, F. Finger, <u>V. Smirnov</u>, Annealing Effects in Low Temperature Amorphous Silicon Flexible Solar Cells, EMRS 2015 Spring Meeting Symposium C on Advanced Inorganic Materials and Structures for Photovoltaics, Lille, France, May 2015
- <u>K. Wilken</u>, U. W. Paetzold, M. Meier, N. Prager, M. Fahland, F. Finger, V. Smirnov, *Nanoimprint Texturing of Transparent Plastic Films for Flexible Thin Film Solar Cells*, 2015 MRS Spring Meeting & Exhibit, San Francisco, USA, Apr 2015

Poster Presentations

- <u>K. Wilken</u>, N. Prager, M. Fahland, F. Finger, V. Smirnov, *Thin Film Silicon Solar Cells Prepared at Low Deposition Temperature on Transparent Flexible Substrates*, 29th European Photovoltaic Solar Energy Conference (EU PVSEC 2014), Amsterdam, Netherlands, Sep. 2014
- <u>K. Wilken</u>, V. Smirnov, O. Astakhov, F. Finger, Thin-film silicon solar cells fabricated at low temperature: A versatile technology for application on transparent flexible plastic substrates and in integrated photoelectrochemical water splitting modules, IEEE 40th Photovoltaic Specialists Conference (PVSC-40), Denver, USA, Jun. 2014

Award: PVSC-40 Best Poster Award

Acknowledgment

I would like to thank all those who kindly helped and supported me during this work. I would especially like to thank:

Prof. Dr. Uwe Rau for the supervision and examination of this thesis and opportunity to work at his institution in the first place. I am thankful for his continuous support and interest in my work.

Prof. Dr. Ruud E.I. Schropp for his willingness to review this thesis.

Dr. Friedhelm Finger for being a great group leader. I deeply appreciate his guidance, encouragement, critical advice and realistic planning of time and scope. I found his frankness to be very valuable.

Dr. Vladimir Smirnov for being an untiring supervisor. The time he spent on my education is uncountable. I am deeply grateful for always having time for me, providing new ideas and spending countless hours on proof-reading manuscripts and this thesis.

Prof. Dr. Sigurd Wagner, for being my external mentor in the scope of the HITEC graduate school, and welcoming me with great hospitality during my visits at Princeton University. His expertise in the field of thin-film silicon and flexible devices was the foundation for valuable discussions during my visits. I am thankful for his extensive support and interest in my work.

Dr. Oleksandr Astakhov for the supervision during my diploma thesis and for the introduction to the world of thin-film silicon.

Dr. Wolfhard Beyer, Dr. Karsten Bittkau, Dr. Jürgen Hüpkes, Dr. Gabrielle Jost, Dr. Andreas Lambertz, Dr. Matthias Meier, Dr. Ulrich W. Paetzold and Dr. Bart Pieters for many interesting and helpful discussions throughout this work.

Gani M. Ablayev for contributing to this work and giving me the opportunity to gain first experiences in supervision.

Project partners in the FlexSol project from TU Dresden, IFW Dresden, Fraunhofer FEP, FAP GmbH and FHR Anlagenbau for a valuable collaboration.

Andreas Bauer, Alain Doumit, Ulrike Gerhards, Manuela Meyer, Sandra Moll, Lars Petter, Sven Schiffer, Andreas Schmalen, Gunnar Schöpe, Hildegard Siekmann and Johannes Wolff for sample preparation and excellent technical support.

Thomas Birrenbach, Dr. Uwe Breuer, Alain Doumit, Pascal Foucart, Dr. Gabrielle Jost, Sabine Kasper, Josef Klomfaß, Dr. Florian Köhler, Dr. Thomas C.M. Müller, Dr. Elmar Neumann, Wilfried Reetz, Oliver Thimm, Christoph Zahren, Uwe Zastrow and Brigitte Zwaygardt for helping with sample characterization.

Prof. Dr. Mehmet Günes from Mugla Sitki Kocman University in Turkey for SSPG measurements and helpful discussions regarding the annealing effect in a-Si:H.

Petra Lorbach, Andrea Mülheims and Astrid Nogga for administrative support.

the greatest imaginable office mates and friends Vito Huhn and Daniel Weigand for interesting discussions, for making me laugh, and always giving emotional support.

all my colleagues and friends at IEK-5 who helped with words and deeds and provided a comfortable working atmosphere, especially Dr. Stephan Lehnen, Jan Mock, Michael Smeets and Dr. Shuo Wang.

I would also like to acknowledge the financial support of the Bundesministerium für Wirtschaft und Energie (BMWi) within the project *Flexsol* (0325442D).

Finally my special thanks to Alexander Swagemakers and my family. They always supported and motivated me during this work and my whole studies. Especially in troubled times they would listen to me and had good advice.

Band / Volume 363

Quantitative Analyse der Lithiumverteilung in Kathoden- und Elektrolyt-Dünnschichten für Festkörperbatterien

C. Dellen (2017), vi, 161 pp ISBN: 978-3-95806-214-6

Band / Volume 364

Intragruppentrennung Seltener Erden mittels neuer phosphororganischer Liganden

S. Hadić (2017), VIII, 164 pp ISBN: 978-3-95806-215-3

Band / Volume 365

Automated Magnetic Divertor Design for Optimal Power Exhaust

M. Blommaert (2017), xxiv, 220 pp

ISBN: 978-3-95806-216-0

Band / Volume 366

PEM-Elektrolyse-Systeme zur Anwendung in Power-to-Gas Anlagen

G. Tjarks (2017), IV, 135 pp ISBN: 978-3-95806-217-7

Band / Volume 367

Fundamental Insights into the Radium Uptake into Barite by Atom Probe Tomography and Electron Microscopy

J. Weber (2017), IX, 160 pp ISBN: 978-3-95806-220-7

Band / Volume 368

Entwicklung von elektronenleitenden Schutzschichten gegen die anodische Auflösung von Stromsammlern in neuartigen "Dual-Ionen"-Energiespeichern

G. Teucher (2017), VIII, 119 pp ISBN: 978-3-95806-222-1

Band / Volume 369

Herstellung und Charakterisierung oxiddispersionsverstärkter Haftvermittlerschichten

J. Bergholz (2017), V, 133, II pp ISBN: 978-3-95806-223-8

Band / Volume 370

Performance of Plasma Facing Materials under Thermal and Plasma Exposure

I. Steudel (2017), XVI, 150 pp ISBN: 978-3-95806-226-9 Band / Volume 371

The Impact of Transient Thermal Loads on Beryllium as Plasma Facing Material

B. Spilker (2017), XII, 134 pp ISBN: 978-3-95806-227-6

Band / Volume 372

Analysis and Simulation of Macroscopic Defects in Cu(In,Ga)Se2 Photovoltaic Thin Film Modules

B. Misic (2017), iv, 147 pp ISBN: 978-3-95806-228-3

Band / Volume 373

Chemical and physical properties of sodium ionic conductors for solid-state batteries

M. Guin (2017), ix, 126 pp ISBN: 978-3-95806-229-0

Band / Volume 374

Prediction of Oxidation Induced Life Time for FCC Materials at High Temperature Operation

R. Duan (2017), vi, 180 pp ISBN: 978-3-95806-230-6

Band / Volume 375

Microstructure Evolution of Laves Phase Strengthened Ferritic Steels for High Temperature Applications

J. K. Lopez Barrilao (2017), XVI, 134 pp ISBN: 978-3-95806-231-3

Band / Volume 376

Drying front formation in topmost soil layers as evaporative restraint Non-invasive monitoring by magnetic resonance and numerical simulation

S. Merz (2017), xxii, 108 pp ISBN: 978-3-95806-234-4

Band / Volume 377

Low Temperature Thin-Film Silicon Solar Cells on Flexible Plastic Substrates

K. Wilken (2017), 194 pp ISBN: 978-3-95806-235-1

Weitere Schriften des Verlags im Forschungszentrum Jülich unter

http://wwwzb1.fz-juelich.de/verlagextern1/index.asp



Energie & Umwelt / Energy & Environment Band / Volume 377 ISBN 978-3-95806-235-1

